SYNTHESIS, FUNCTIONALIZATION AND WETTING BEHAVIOR OF CARBON NANOTUBES

A THESIS SUBMITTED TO THE

UNIVERSITY OF PUNE

FOR THE DEGREE OF DOCTOR OF PHILOSOPHY

IN

CHEMISTRY

By

BHALCHANDRA A. KAKADE

Dr. K. VIJAYAMOHANAN

(Research Guide)

PHYSICAL AND MATERIALS CHEMISTRY DIVISION

NATIONAL CHEMICAL LABORATORY

PUNE – 411 008

INDIA

May 2008

Dedicated to
my beloved
parents
& bhaiyya.....

DECLARATION

I, hereby declare that all the experiments embodied in this thesis entitled, **"SYNTHESIS, FUNCTIONALIZATION AND WETTING BEHAVIOR OF CARBON NANOTUBES"**, submitted for the degree of Doctor of Philosophy in Chemistry, to the University of Pune have been carried out by me at the Physical and Materials Chemistry Division, National Chemical Laboratory, Pune, 411 008, India, under the supervision of Dr. K. Vijayamohanan. The work is original and has not been submitted in part or full by me, for any degree or diploma to this or to any other University.

Date: 30 May 2008 **BHALCHANDRA ANAND KAKADE**

Physical and Materials Chemistry Division
National Chemical Laboratory
Pune – 411 008

Dr. K. Vijayamohanan
Scientist

Physical and Materials
Chemistry Division
National Chemical Laboratory
Pune – 411 008
INDIA

Tel: 91-020-2590 2588
Res: 91-020-2587 0307
Fax: 91-020-2590 2636
Email: vk.pillai@ncl.res.in

CERTIFICATE

This is to certify that the work incorporated in the thesis entitled, "**SYNTHESIS, FUNCTIONALIZATION AND WETTING BEHAVIOR OF CARBON NANOTUBES**" submitted by **Mr. Bhalchandra Anand Kakade,** has been carried out by him under my supervision at the Physical and Materials Chemistry Division, National Chemical Laboratory, Pune, 411 008, India. All the materials from other sources have been duly acknowledged in the thesis.

Research Guide
(K. Vijayamohanan)

Date : 30 May 2008
Place : Pune

Acknowledgements

There are so many people, whose support, encouragement & inspiration are very much essential to accomplish major achievements in life, especially, if it involves the elements of fulfilling one's cherished dreams. For me, this thesis is such an important destiny & I am indeed, indebted to lot of people for their well wishes & blessings, for completing this journey.

I would like to take this opportunity first, to pay my sincere admiration to Dr. K. Vijayamohanan, whose motivation, inspiration, encouragement & persistent guidance have lead me to bring my dream to reality. His knowledge is like an ever-expanding encyclopedia, which has all possible solutions to help me out of any problem. I must also mention that he is also a very good teacher & a wonderful research guide, which is often quite rare. His constant effort to imbue us with several, most essential habits, like weekly seminars & group meetings, monthly reports & daily planning, makes me confident to start an independent scientific carrier.

I would also like to offer my sincere admiration to Dr. I. S. Mulla for all his help, support, suggestion & advice during the course of this study.

I also extend my sincere appreciation to both Mrs. Manju (Madam) for her motherly care, blessing & constant support.

I wish to thank Dr. S. Sivaram, the Director, NCL for providing me all infrastructural facilities. I am also grateful to Dr. S. Pal, head of Physical & Materials Chemistry Division for allowing me to use all the available facilities in the division & for his constant encouragement. I also would like to extend my sincere thanks to my teachers, Profs. K. J. Patil, B.A. Ingle, K.S. Daddi, Ranade, A. Pangu, A.G. Wandre, S.P. Chavan, A.B. Gurav, S. Dhongade & G. Banadar for their gracious love & belief. A special thanks to our collaborators, Profs. M. Monthioux, H. Allouche, C.V. Dharmadhikari, & D. Joag for their precious help & valuable discussions.

My heartfelt gratitude to Drs. Anil Kumar, P. A. Joy, Satish Ogale, S.B. Halligudi, M. Sastry, B.L.V. Prasad, P. Poddar, V. Ravi, Mrs. Renu & K. Shreekumar for their advice & help. I am highly indebted to Dr. K.R. Patil, Mr. Gholap & Mr. A.B. Gaikwad for helping me a lot in characterising my samples. Timely help from Mr. Dipak & Mr. Punekar & the entire library staff for excellent facilities is gratefully acknowledged. Further, UGC & CSIR are gratefully acknowledged for the financial support.

I can never forget the help from my seniors, Drs. Aslam, Nirmal, Jadabji, Trupti, Niranjan & Murugan for their mentoring & care during my initial research days. I would like to thank Deepali & Mahima for their constant encouragement & always being with me in all sorts of situations during my stay in NCL. A special thanks to all my labmates Bhaskar, Meera, Kannan, Sanjay, Pravin, Dhanu, Dhanraj, Beena, Kuttan, Meenu, Vivek, Mukta, Roopali &

Nilesh, who have helped me in all possible ways & have been my extended family during the tenure of my work at NCL. I wish to extend my thanks to my project colleagues Shashi, Rutvik, Apurva, Anup, Jay, Srinivas, Abhay & Pravin for their love, constant efforts & enthusiasm.

I would also like to express my sincere thanks to all my divisional colleagues Suvarna, Sanju, Shekhar, Selvakannan, Sankar, Nagesh, Shraedha, Gitanjali, Sarita, Shabana, Sumit, Prathap, Deepti, Sanjay, Maggie, Sudarshan, Priyanka, Tushar, Subhas, Vijay, Sreeja & Umesh. I also extend my thanks to several other friends in NCL, Sachin, Sandeep, Mahesh, Ravi, Dushyant, Pranjal, Atul, Ankush, Khirud, Malli, Panchami, Sony, Bapu, Arun, Kishor & Smitha. A special mention of thanks to my hostel friends Mehraj, Bhaiyya, Aarif, Nilesh, Sambhuda, Patwa, Mahesh, Ravi, Deu, Ganesh, Aba, Nilesh, Prakash, Dipak, Ankush, Najrul, Prasad, Pankaj, Sachin, Asif, Shashi, Amit, Paji, Ponds, Dipika, Bhramana, Appa, Mukesh, Prabhas, Sumantra, Manoj, Ambrish, Dilip, Nishant, Rahul, Suresh, Ankur, Sahoo, Sofia & Lakshi. I have to express all my gratitude to my dearest friends Nisha, Alok, Shinya, Madhav, Sagar, Somya, Ramesh, Dilip & Viru for their constant encouragement. I also extend my special thanks to my collaborators Suman, Datta & Minakshi for their valuable help & support.

As always, it is impossible to mention everybody who had an impact on this work although there are those whose spiritual support is even more important. I find no words to express my feelings for my parents, whose moral support, love & constant encouragement have helped me to complete this journey. This thesis is also a dream for my elder brother 'Bhaiyya', whose support has always played a key role in my career. I wish to express my gratitude to my beloved brother Vinu & sister Madhu, who have always inspired me at every stage of life & my studies as well. I wish to extend my sincere gratitude to my grandmother & all other relatives for their blessings & love. Finally, a very special appreciation is due to my fiancé Anita not only for her constant encouragement but also for her patience & understanding throughout.

Bhalchandra Anand Kakade

"Any Dream Accomplished is a Fallen Angel"

List of Abbreviations

Abbreviation	Expansion
1-D	One-Dimensional
2-D	Two-Dimensional
3-D	Three-Dimensional
ac	Alternating Current
ACNT	Aligned Carbon Nanotubes
AFM	Atomic Force Microscope
BE	Binding Energy
bcc	Body Centered Cubic
CA	Contact Angle
CANAPE	Carbon Nanotubes for Applications in Electronics
CB	Conduction Band
CNLS	Complex Nonlinear Least Square
CNTs	Carbon Nanotubes
CNSs	Carbon Nanoscrolls
COSY	Correlation Spectroscopy
CV	Cyclic Voltammetry
CVD	Chemical Vapor Deposition
DAO	1,8-diamino octane
dc	Direct Current
DCM	Dichloromethane
DFT	Density Functional Theory
DRIFT	Diffused Reflectance Infrared Fourier Transform
DMS	Dimethyl sulphide
DMSO	Dimethyl sulfoxide
DOS	Density of States
DPV	Differential Pulse Voltammetry
DSC	Differential Scanning Calorimetry

DT	Differential Thermogravimetry
DWCNT	Double Wall Carbon Nanotube
ECP	Electrically Conducting Polymers
EDX or EDS	Energy Dispersive X-Ray Spectroscopy
ESCA	Electron Scanning for Chemical analysis
ET	Electron Transfer
fcc	Faced Centered Cubic
FEG	Field Emission Gun
FESEM	Field Emission Scanning Electron Microscopy
FET	Field-Effect Transistors
FFT	Fast Fourier Transform
FRA	Frequency Response Analyzer
FTIR	Fourier Transform Infrared
FWHM	Full Width at Half Maximum
hcp	Hexagonal Closed Packed
HiPCO	High pressure Carbon Monoxide Process
HOMO	Highest Occupied Molecular Orbital
HRTEM	High-Resolution Transmission Electron Microscopy
LCD	Liquid Crystal Display
LSV	Linear Sweep Voltammetry
LUMO	Lowest Unoccupied Molecular Orbital
MEMS/NEMS	Micro/Nano-Electromechanical Systems
MPCs	Monolayer Protected Nanoclusters
MW	Microwave
MWCNTs	Multi-Walled Carbon Nanotubes
NMR	Nuclear Magnetic Resonance
ODA	Octadecylamine
PL	Photoluminescence
PPy	Polypyrrole
PANI	Polyaniline
PTFE	Polytetrafluroethane

PZC	Potential at Zero Charge
QDL	Quantized Double Layer Charging
Q-dots	Quantum Dots
RBM	Radial Breathing Mode
SAED	Selected Area Electron Diffraction
SAM	Self-Assembled Monolayer
sccm	Standard cubic centimeter
SDS	Sodium dodecylsulphonate
SECM	Scanning Electrochemical Microscopy
SET	Single-Electron Transistors / Transfer
SMSI	Strong-Metal Support Interaction
SPR	Surface Plasmon Resonance
STM	Scanning Tunnelling Microscope
STS	Scanning Tunnelling Spectroscopy
SWCNTs	Single Walled Carbon Nanotubes
TBAHFP	Tetrabutyl ammoniumhexafluorophosphate
TDA	Tridecylamine
TEC	Temperature Expansion Coefficient
TEM	Transmission Electron Microscopy
TG	Thermogravimetry
THF	Tetrahydrofuran
TOF	Turn Over Frequency
TON	Turn Over Number
TTO	Total Turn Over
UV	Ultra-Violet
Uv-vis	Ultra-Violet-Visible
Uv-vis-NIR	Ultra-Violet-Visible- Near infrared
VB	Valence Band
VLS	Vapor-Liquid-Solid
XPS	X-ray Photoelectron Spectroscopy
XRD	X-ray Diffraction

Table of Contents

Chapter 1

Chapter 2

Chapter 5

CHAPTER 1

Synthesis, Functionalization and Wetting Behavior of Carbon Nanotubes

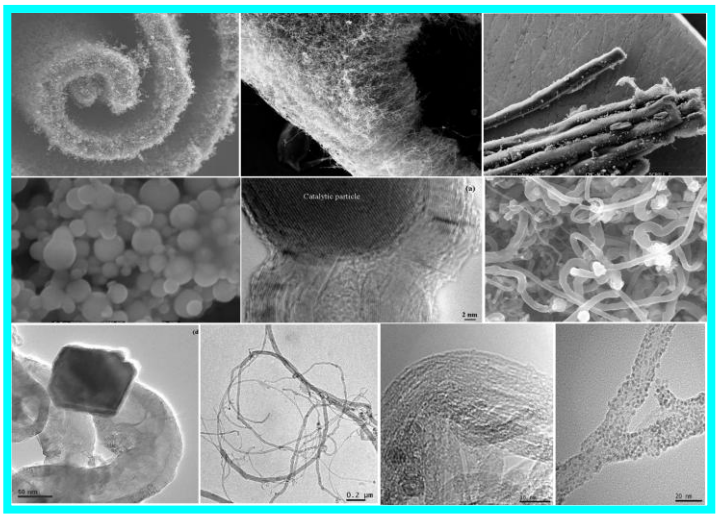

This chapter presents a critical review of literature on the synthesis, characterization, functionalization and wetting behavior of Carbon Nanotubes. The scope of these structures in nanotechnology along with several fundamental issues related to their origin and potential applications are also discussed. Particular emphasis is placed on contemporary issues related to the purification of CNT from chemical vapor deposition, nucleation and growth models, chemical functionalization strategies, modification of wetting properties and diverse applications of both single walled and multiwalled Carbon Nanotubes. Finally, the objectives of the present thesis are discussed with this perspective along with the abstract and limitations of the overall investigations at the end.

1.1 Introduction

Nanotechnology is considered by many to have just reached the status of the 21st century's leading science and technology platform to affect life of common people based on the advances revealed during the last two decades [1]. Many of these advances depend on the unique properties of nanomaterials as a function of size. One of the important features of nanotechnology is its uncanny ability to bridge the crucial dimensional gap between the atomic and molecular sciences on one hand and the microstructural scale of engineering affecting many technological landscapes on the other hand. Accordingly, it is very important to have an in-depth understanding of the synthesis of nanomaterials for the use of state-of-the-art, cutting edge technological devices like micro/nano electromechanical systems (MEMS/NEMS) and single molecule devices, often with unprecedented properties [1a]. Recently, the 'bottom-up' approach for the fabrication of nanomaterials has received a great deal of attention, primarily because of dedicated efforts of many chemists and physicists, for its simplicity and cost effectiveness [2]. However, several issues related to purity and yield still do exist with many of these materials, although tailoring various parameters during synthesis of selected nanoparticles could be routinely used in these days to fabricate many important components [1].

Among all materials used in nanotechnology, carbon nanotubes (CNTs), perhaps, occupy a preeminent position due to its unique capabilities. First, they have many remarkable electronic and mechanical properties, some stemming from the close relation between CNT and graphite, and some from their one-dimensional aspects of possessing an exotic electronic structure. It has a remarkable ability to show ballistic charge transport (current densities in the order of 10^9 A/cm^2) due to electron confinement effects in two dimensions, leading to many promising applications in future electronics. As other intriguing properties have been discovered more recently, such as their fascinating electronic transport, unique Raman spectra and unusual mechanical properties, interest has grown in their potential use in nanometer-sized electronics. Here we have what is almost certainly the strongest, stiffest and toughest molecule that can ever be produced,

one of the best possible molecular conductors of both heat and electricity. In one sense, CNT is a new man-made polymer to follow on from nylon, polypropylene and Kevlar while in another way, it could be considered as a new 'graphitic' fiber, but perhaps with highest possible strength. In yet another manner, it could be viewed as a new species in organic chemistry and potentially in molecular biology as well– a carbon molecule with the almost "alien property of electrical conductivity and super-steel strength" [3].

An ideal nanotube can be considered as a hexagonal network of carbon atoms that has been rolled up to make a seamless hollow cylinder [4a]. These hollow cylinders can be tens of micrometer long, but with diameters as small as 0.7 nm and with each end of the long cylinder "capped with half a fullerene molecule, i.e., 6 pentagons". Single wall nanotube (SWCNTs), having a cylindrical shell with only one atom in thickness, could be taken as the fundamental structural unit. Such structural units form the building blocks of both multi-wall carbon nanotubes (MWCNTs), containing multiple coaxial cylinders of ever-increasing diameters about a common axis, and nanotube ropes, comprising of ordered arrays of SWCNTs arranged on a triangular lattice.

1.2. Structure of Carbon Nanotube

One of the surprising abilities of carbon is that it can bond in different ways to create structures with dramatically opposite properties. For example, graphite and diamond, the two bulk solid phases of pure carbon, bear testimony to this. Graphite is thermodynamically stabler than diamond under ambient conditions and reverse is true at higher pressures/temperatures (the standard free energy difference is -2.90 kJ/mol at 25 ^{o}C) [5]. However, this is not the case when there is only a finite number of carbon atoms, since high density of dangling bonds dominate when the size of the graphite crystallites becomes very small (say, nanosize). At smaller sizes, the structures do energetically well by closing onto themselves to eliminate all the dangling bonds. For instance, preliminary experiments in the mid 1980s [6], which served as the precursor to the fullerene discovery [7], suggested that when the number of carbon atoms is smaller than a few hundred, curved structures (such as the fullerenes) form a planar fragment of graphite

through the introduction of a positive curvature by creating pentagons in the hexagonal lattice. Thus a greatly elongated fullerene could be produced with exactly 12 pentagons (irrespective of however big the closed structure is!) and millions of hexagons [8]. This would correspond to a carbon nanotube [8-13], as the geometry of the structure in Figure 1.1(a) reflects: a long cylinder of the hexagonal honeycomb lattice of carbon, bound by two pieces of fullerenes at both the ends.

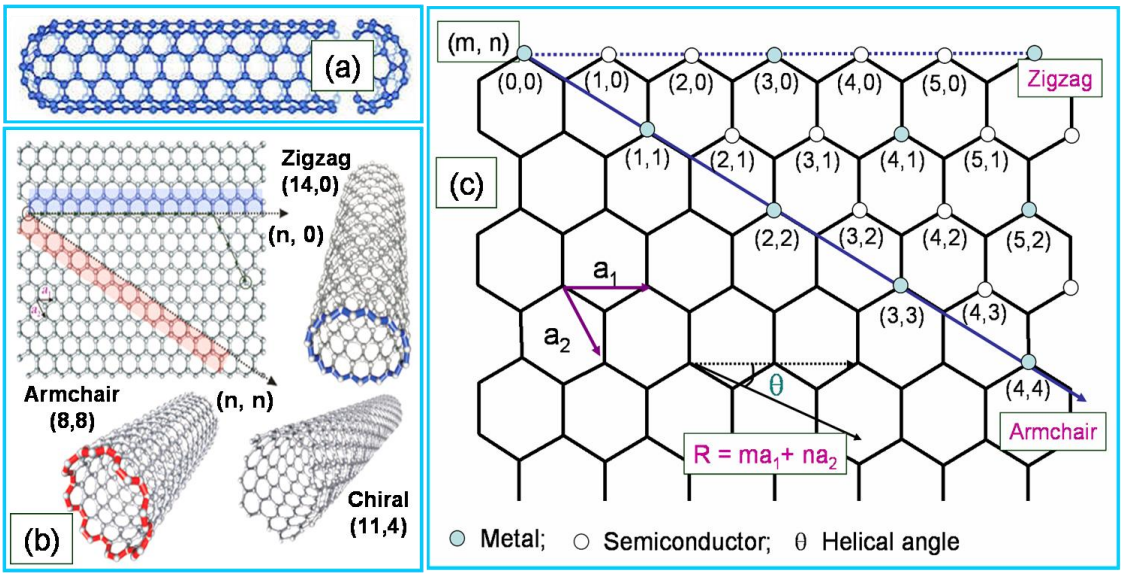

Figure 1.1. (a) honeycomb hexagonal lattice structure of a typical CNT with fullerene caps **(b)** roll-up of a graphene sheet leading to the three different types of nanotubes **(c)** possible vectors specified by the integers (m,n) for general nanotubes, including zigzag, armchair and chiral nanotubes; the green colored dots denote metallic nanotubes while white dots are semiconducting nanotubes; a_1 and a_2 are unit vectors with a chiral angle of θ resulting into a new vector as R, called Hamada vector; adopted from [14,15].

CNT can be considered as a single sheet of graphite (when this is a single atom thick 2-D sheet, it is known as graphene) that has been rolled up into a tube, having a length to diameter ratio of about 1000 (also known as aspect ratio) so that they can be considered as nearly one-dimensional (quasi 1-D) structures. As a result, one can only roll the sheet in a discrete set of directions in order to form a closed cylinder. (Figure 1.1(b)). Two atoms in the graphene sheet (two dimensional graphitic network having a honeycomb lattice) are chosen; one of which serves the role as origin and the sheet is

rolled until the two atoms coincide. The vector pointing from the first atom towards the other is called the chiral vector and its length is equal to the circumference of the nanotubes and hence the direction of the nanotube axis is perpendicular to the chiral vector [14,15].

The rolling action could be carried out in several ways, still satisfying the essential criterion that the dangling bonds present at both edges are matched. Any translational shift along the edges before fitting the dangling bonds will lead to a different orientation of the lattice with respect to an arbitrary tube axis. Thus, in a general nanotube structure, on the curved surface of the tube, the hexagonal arrays of carbon atoms can be pictured to wind around in a helical fashion, introducing *helicity* to the structure. This important variation in the graphene stacking sequence as a result of the change in bond lengths and helical angle (θ) (due to rolling of graphene) is called '*helicity*' [15]. Consequently, the boundary conditions around the cylinder during the mapping of a graphene plane (into a cylinder) can be satisfied only if one of the Bravais lattice vectors [defined in terms of the two primitive lattice vectors, (a_1, a_2) and a pair of integers (*m, n*)] of the graphene sheet conformally map on to the whole circumference of the cylinder [14-16]. This conceptual scheme is very important in correlating the properties of individual nanotubes as they provide the essential symmetry and electronic structure to the nanotube. Thus, nanotubes made from lattice translational indices of the form (*n*, 0) or (*n, n*) will have two helical symmetry operations while all other sets of nanotubes will have the three equivalent helical operations. The (*n*, 0) type of nanotubes are generally called zigzag nanotubes whereas the (*n, n*) types are called armchair nanotubes; all others will be helical or chiral nanotubes (shown in Figure 1.1(c)). Generally armchair nanotubes are metallic, zigzag are semiconducting while chiral type shows mixed properties depending on the combination of these integers and the chiral angle. It is also possible to estimate the diameter (d) of nanotube using these integers as [$d = (m^2 + n^2 + mn)^{1/2} \times 0.0783$] nm [17-19].

On the basis of the number of concentric cylinders, usually nanotubes can be divided into two categories. Multiwalled carbon nanotubes (MWCNTs), although the first

to be discovered, are close to hollow graphite fibers [20], with a much higher degree of structural perfection. They are made up of many concentric cylinders placed around a common central hollow region, with a spacing between the layers close to that of the interlayer distance in graphite (0.34 nm) (Figure 1.2(a)). This interlayer spacing in MWCNT is slightly larger than that in single-crystal graphite (0.335 nm) despite, severe geometrical constraints in forming the concentric, seamless cylinders while maintaining the graphitic spacing between them [14-20]. Undoubtedly, the three-dimensional structural correlation that prevails in single crystal graphite (ABAB stacking) is lost in this process as the layers are rotationally disordered with respect to each other. Double walled carbon nanotubes (DWCNT) belong to this type where only two graphene layers are rolled along a central axis [21].

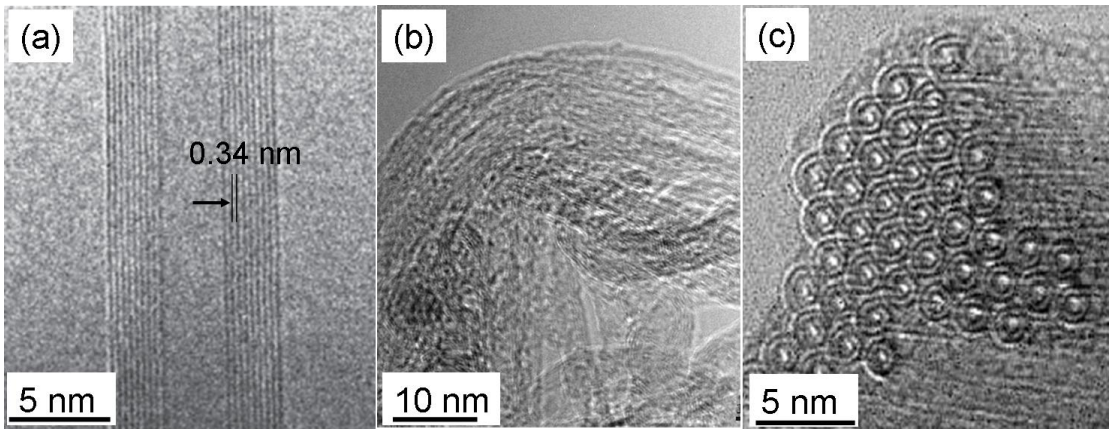

Figure 1.2. High-resolution transmission electron microscopy images of typical **(a)** MWCNT (with 9 graphitic walls), **(b)** SWCNTs in the form of ropes and bundles and (c) DWCNTs with tube ends; the inner space corresponds to the diameter of the inner hollow region in the tube (MWCNT) with a close spacing of 0.34 nm as shown between graphitic layers, whereas the SWCNT are shown in bundle form with similar spacing; adopted from [21b].

The second category of nanotubes is similar to an ideal fullerene fiber; in size they are close to fullerenes and have a single-layer of cylinder extending from one end to the other end [16,22]. These are called single walled nanotubes (SWCNTs) which possess good uniformity in diameter (1- 2 nm) (Figure 1.2(b)). During synthesis, SWCNT always self-assemble into larger bundles (ropes) that consist of several tens of nanotubes [10,23,24]. Indeed, an one-dimensional triangular lattice structure with a

lattice constant of 1.7 nm and tube-tube separation of 0.315 nm [24], is experimentally seen which is in good agreement with the theory [25]. Both varieties of nanotubes can be regarded as aggregates of units (cylinders), MWCNT consisting of concentric assembly and SWCNT ropes of close packed nanotube units. The aspect ratios of both MWCNT and SWCNT are large since their lengths are in the range of several micrometers.

1.3. Synthesis of Carbon Nanotubes

There are mainly three methods for the synthesis of Carbon nanotubes: arc discharge, laser ablation and chemical vapor deposition (CVD). Although, the report of Iijima for the production of SWCNTs is considered by many as the first [4a,16], another team from IBM California, had reported the formation of SWCNTs [22] just one day later. Interestingly, a controversial image, resembling a SWCNT, had been reported much earlier by Oberlin et al, [26], although nobody had mentioned this as SWCNTs. However, the report of growth of MWCNTs without using any metal catalyst by Iijima in 1991 could be considered as the first, although it has not cited related work by many (where graphite whiskers have been synthesized under high pressure in an arc discharge) [27]. Also, a US patent was filed almost more than a century ago, where the filamentous carbon had been reported by a thermal decomposition method (using methane as carbon source) for subsequent utilization as filament in light bulbs [28]. The popularity of this work had not reached to a sufficient level because of the lack of microscopic evidences. However, in the later century (1952) the first evidence for the tubular carbon in nanosized domain came from a Russian group [29], but again unfortunately this work had been neglected perhaps, due to the difficulty of language and also lack of scale (and resolution) in the images. Hence, in fact, Radushkevich and Lukyonovich should be credited for the discovery of hollow carbon filaments with nanometer diameters [29]. In addition, there are few other reports for the preparation of filamentous carbon [30], although nobody had mentioned the word ‘rediscovery’ despite the importance of the finding of the Russian group [29]. After these, past two decades have witnessed significant research in the field of nanotubes and their applications. More significantly,

the success in the nanotube growth using a variety of methods has led to the wide range of availability of nanotube based hybrid materials and this could be considered as the main motivation behind the recent developments.

In this chapter, we briefly discuss both arc discharge and laser ablation methods, followed by a detailed discussion on chemical vapor deposition (CVD) due to its promising features including yield, quality and user friendly nature.

1.3.1. Arc-Discharge and Laser Ablation

Both these methods have been pursued equally during the last decade for nanotube growth since interestingly both involve the condensation of carbon atoms from solid carbon source at a temperature comparable to the melting point of graphite (3000-4000 ^{o}C). In arc discharge, a carbon source is evaporated by helium plasma using a high current between an anode and cathode enabling the synthesis of high quality SWCNTs and MWCNTs with uniform diameter. For example, Ebbesen and Ajayan have first reported the arc method for the synthesis of highly crystalline, straight MWCNTs along with their purification to remove the Stone-Wales defects (presence of pentagons and heptagons in the hexagonal graphitic network) [31]. However, in the synthesis of SWCNTs it is extremely important to use suitable catalyst like Co, Ni or Fe along with the carbon source. Similarly, Bethune et al, and others have grown a good quality SWCNTs by adding a small percentage of Co with anode in a typical arc discharge synthesis [22,24].

On the other hand, laser ablation method is also employed to synthesize, mainly, SWCNTs at higher temperatures (1200 ^{o}C), where a high intense pulsed laser is used to ablate the target source containing suitable catalyst under the flow of an inert gas to form nanotubes downstream on a cold substrate [23]. For example, Smalley's group has achieved high quality synthesis of SWCNTs (at the 1-10 g scale) by using intense laser pulses to ablate a carbon target containing 0.5 at% of Ni and Co at a target temperature of 1200 ^{o}C [23]. Thus, the success of high quality growth of SWCNTs by arc discharge and

laser ablation has led to the wide availability of samples useful for exploring their applications.

CNT preparation by arc discharge and laser ablation methods is rather simple but bulk production needs controlled conditions and relatively higher temperatures (more than 1200 ^{o}C). Other limitations of these methods include the formation of impurities like fullerenes, graphitic polyhedrons with enclosed metal particles and amorphous carbon in the form of particles or overcoating on the side walls of nanotubes, thus necessitating the need for rigorous purification [8].

1.3.2. Chemical Vapor Deposition

Chemical Vapor deposition is a powerful method to prepare many nanotubes using a variety of liquid or gaseous precursors at comparatively lower temperatures than that of the above methods [32]. The only limitation of this technique is the product quality, since a lower growth temperature does not provide sufficient thermal energy to anneal nanotubes into perfectly graphitic structure.

Nanotube synthesis by CVD process has been chosen in the present work because it offers a promising route to produce high purity nanotubes commercially[#]. A variant of the CVD method has been developed particularly to meet selected criteria: low cost, bulk production, high purity, and well aligned (un-entangled) product [33]. The system is relatively simple, consisting of a quartz tube reactor within a multi-zone furnace (Figure 1.3), which involves heating a catalyst to high temperatures in a tubular furnace along with the flow of hydrocarbon source for a fixed period. For example, passing a mixture of xylene (or other hydrocarbons like toluene, benzene etc.) and ferrocene into an inert gas stream generates pure MWCNTs [34]. During the decomposition of the ferrocene-xylene mixtures in the range 625-775 °C at atmospheric pressure, Fe nanoparticles get nucleated

[#] Nanocyl Inc. (Belgium), Elicarb^{TM}SW, American Dye source, NanoNB Corp. Raymor Ind. Made-in-China.com. Pyrograph products (USA), Carbon Nanomaterials Tecnology (South Korea) and Nanothinx Nanotubes Inc. are few of the leading CNT manufacturers by CVD method.

to begin the deposition of carbon (from source) as pure MWCNT arrays on the quartz surfaces (reactor walls and substrates).

The control of tube diameter and length is a key feature of this nanotube synthesis using CVD. Therefore, nanotube growth mechanisms and those factors determining the geometry of the product within the operating parameters of the reactor have been studied by many groups. The growth of the MWCNT begins soon after the deposition of a catalyst particle on the quartz substrate, and hence the rate of deposition of carbon is directly proportional to the amount of surface area presented to the decomposing hydrocarbons. Many of these studies show that a very short-duration (typically 2- 10 min) is required to grow the MWCNTs rapidly to a maximum length, typically of 50 μm [32].

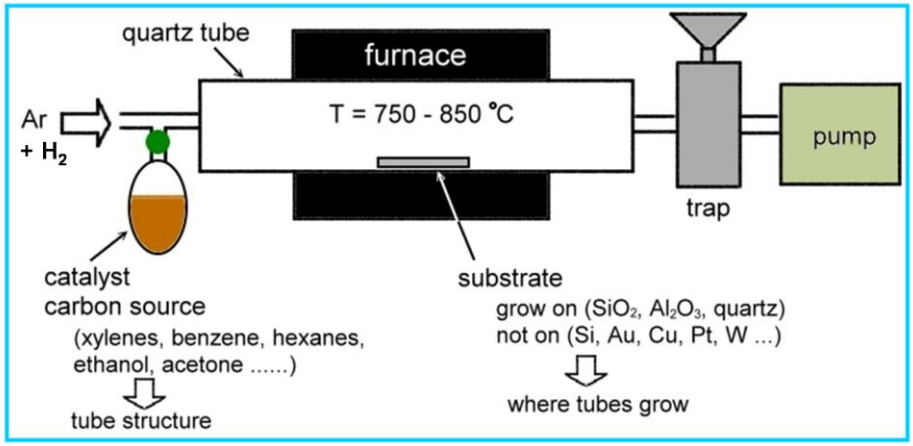

Figure 1.3. Schematic of catalytic CVD set up for the synthesis of MWCNTs using various carbon precursors in presence of a suitable catalyst along with a support for CNT growth; adopted from [33].

Several methods have been reported for the synthesis of aligned MWCNTs on mesoporous silica, using iron oxide nanoparticles as catalysts with 9% acetylene as a feed stock at 600 ^{o}C using 180 torr pressure [35]. Nanotubes with millimeter length have been grown in this process. Ren et al, have also grown forests of MWCNTs at 660 ^{o}C using nickel as a catalyst on glass [36a] and thick mats of densely packed, well-aligned nanotubes have been grown by continuous insertion of precursors with slow rates at 850 ^{o}C [36b]. Several other reports are available for the synthesis of MWCNTs by CVD

growth along with their growth mechanism [37-39] illustrating the role played by various key factors like the nature of hydrocarbon source, catalyst and growth temperature [40].

Table 1.1. Comparison of three different methods of preparation of CNTs along with their advantages and disadvantages [41d].

Method	Arc discharge	Laser Ablation	CVD
Process and carbon feed-stock	CNT growth on graphite electrodes during direct current arc-discharge evaporation of carbon in presence of an inert gas	Vaporization of a mixture of carbon (graphite) and transition metals located on a target to form CNTs	Fixed bed method: hydrocarbon decomposition over suitable support using transition metal catalysts at 700 – 1200 ^{o}C
Yield	< 75 %	< 75 %	> 75%
SWCNT or MWCNT	Both	Only SWCNTs	Both
Advantages	Inexpensive, defect-free crystalline nanotubes	high purity CNTs, crystalline nanotubes	Inexpensive, Low temperature, High purity and yield, aligned growth, fluidized bed technique for large-scale
Disadvantages	Purification of crude product, cannot be scaled up, high temperature	Cannot produce MWCNTs, lab-scale, Purification of crude product	usually MWCNTs, parameters to obtain SWCNTs, less crystalline nanotubes

Similarly, plenty of studies are available on the mechanistic aspects of SWCNT growth by the CVD process. For instance, earlier reports by Kong et al, have suggested the formation of high quality SWCNTs at 850-1000 ^{o}C using methane as a feed-stock in presence of a suitable metal catalyst [37,41], despite having low yield. Comparatively higher temperature is necessary to form SWCNTs that have small diameters and thus high strain energies, which allow nearly defect-free crystalline nanotubes. Among all hydrocarbons, methane is perhaps the most stable carbon source which gives good quality SWCNTs in presence of transition metals. Hence the selection of carbon feed-stock is one of the important key parameters to grow high quality SWCNTs, containing

no defects and also without any amorphous carbon. Further, in order to achieve high yield and better quality, several supports like, silica, alumina and MgO are essential. For example, a catalyst consisting of Fe/Mo bimetallic species on sol-gel derived alumina-silica support (using methane source) gives SWCNTs with diameter range of 0.7-3 nm with a yield of 0.45 g per gram of catalysts [41], although the yield and purity are normally the functions of catalyst properties; stronger the metal-support interactions, better will be the yield and purity and these interactions are normally invariant with temperature [41c]. Other recent reports also provide important information for the synthesis of SWCNTs by CVD growth [42]. A comparison of all three methods of synthesis is presented in Table 1.1, along with their main advantages and disadvantages. Although, every method has its own benefits, CVD process is more promising due to its ability to have the bulk synthesis of defect free, high purity and high aspect ratio nanotubes.

Although a significant amount of work has been focused on the production of nanotubes, only catalytic decomposition by CVD process is promising for actual commercialization (~50 kg/day) [43]. However, despite the remarkable progress made in this during the last 3–4 years, the cost is still too high for large-scale applications. Current price for SWCNTs is around 50–100 Euros per gram [44], although the purity of such samples lags behind that of other standard laboratory reagents. The product usually contains amorphous carbon, fullerenes, and catalytic metal particles (e.g., Co or Ni) as impurities. Consequently, effective purification of the nanotubes is a prerequisite for further processing [45]. However, there are major concerns in the bulk production of CNTs including (1) growth with precisely controlled diameters (thus chirality) and length (2) difficulty of achieving highly crystalline, defect free nanotubes and (3) cost effectiveness, which require further technological innovations.

1.3.3. Growth Mechanism

General growth mechanism in a CVD process involves the dissociation of hydrocarbon catalyzed by a suitable catalyst and subsequent dissolution/ saturation of carbon atoms in

the metal nanoparticles [46]. The precipitation of the carbon from saturated metal particles leads to the formation of tubular carbon. Consequently, carbon growth occurs in the open edges of the sheets in order to avoid the dangling valencies on the tubular structure. At higher temperatures carbon has finite solubility in transition metals to form metal-carbon solutions, which leads to two different growth mechanisms, i.e. Root growth and Top growth as shown in Figure 1.4.

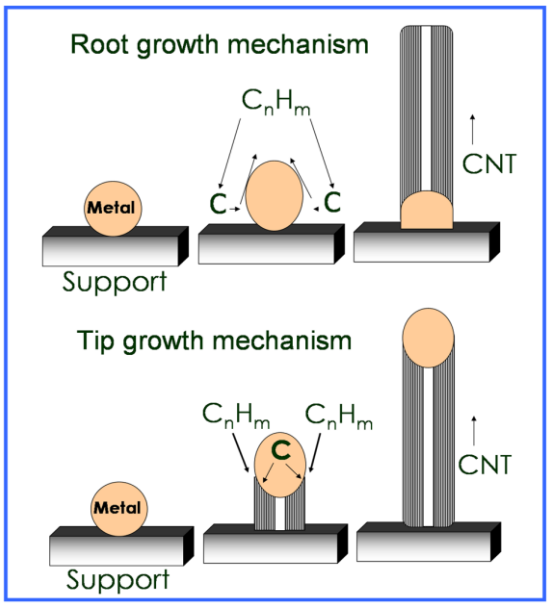

Figure 1.4. Two general modes of growth mechanism in CVD including Root growth and Tip growth.

One of the important features of this mechanism is that the form of graphite produced is closely related to the physical dimensions of the metal catalysts. This hypothesis builds on a considerable amount of results that have been collected over the past two to three decades using diverse techniques on the formation of graphitic carbon over various substrates [32f,47] in presence of most effective metal catalysts like iron, nickel or cobalt. The ability of these metals to form ordered carbon is thought to be related to a combination of factors, including (1) their catalytic activity for the decomposition of volatile carbon compounds, (2) the fact that they form metastable carbides, and (3) the ability of carbon to diffuse through and over these metals at a rapid rate [32f,48]. The latter property allows ordered carbon to be produced by a mechanism

of diffusion followed by precipitation and consequently a variety of distinct mechanisms have been proposed till date [49]. This also means that graphitic structures are formed only in close proximity to the metal surface. If the reaction occurs away from the metal, other undesirable forms of carbon, such as amorphous nanoparticles, could become side products. Restriction of the reaction to the surface is controlled through the choice of the carbon precursor, its partial pressure, and the reaction temperature [40].

Although *in situ* investigations along with DFT calculations have suggested that CNT growth catalyzed by Ni particles is a surface-diffusion process [50], there is still not enough evidence for this at the atomic scale [51]. Furthermore, it is not yet clear whether carbon dissolves and diffuses through the metal catalyst particle and then precipitates as a carbon filament, or whether carbon diffuses on the catalyst surface, or whether bulk and surface diffusions compete with each other. Therefore complementary experimental and theoretical studies are essential for improving our understanding of growth mechanisms based on models postulated after 1970s [52].

1.4. Purification and Covalent Functionalization of Carbon Nanotubes

Purification of CNTs is one of the important steps in order to eliminate catalyst particles and amorphous carbon or nontubular carbonaceous species from the sample. In the first step, the amorphous carbon is removed by oxidation upon heating to ~350 ^{o}C in air. Following this, the free metal is removed by heating in an acid solution. Through a final annealing above 1000 ^{o}C in vacuum, most of the defects created in the earlier steps can be removed. Another effective method as summarized in scheme 1.1 is the oxidation of SWCNTs using extensive ultrasonic treatment in a mixture of concentrated nitric and sulfuric acid [53,53a]. However, such drastic conditions could also lead to the opening of the tube caps as well as the formation of holes in the sidewalls, followed by an oxidative etching along the walls with concomitant release of carbon dioxide. The final products are nanotube fragments with lengths in the range of 100 to 300 nm, whose ends and sidewalls are decorated with a high density of various oxygen containing groups (like –COOH, -OH). Under less vigorous conditions, such as refluxing in nitric acid, the

shortening of the tubes can be minimized. The chemical modification is then limited mostly to the opening of tube caps and the formation of functional groups at defect sites along the sidewalls. More importantly, nanotubes functionalized in this manner basically retain their pristine electronic and mechanical properties, since there is no major change in the band structure [53b].

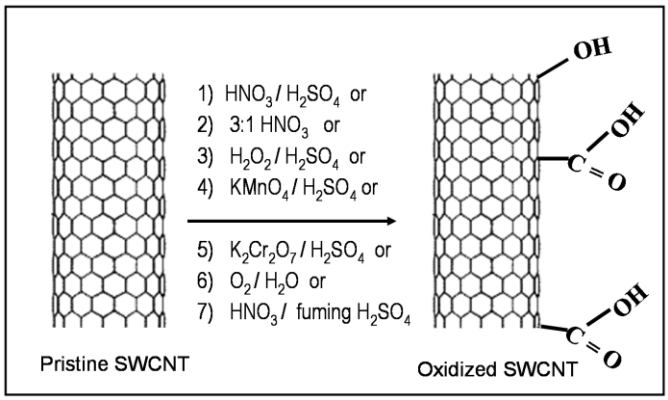

Scheme 1.1. Various routes for oxidation and subsequent purification methods for SWCNTs, which generate various oxygenated functional groups on the side walls along with the separation of deleterious impurities like metal particles and amorphous carbon; the seven routes create oxygen containing functional groups to different extent on the side walls.

In particular other oxidizing environments like $KMnO_4/H_2SO_4$ [51b], Oxygen [51c], $K_2Cr_2O_7/H_2SO_4$, ozone [54d] or OsO_4 [54e] could be used for oxidation (end opening) with subsequent purification of the nanotubes for further processing (as shown in Scheme 1.1). More effective purification of both SWCNTs and MWCNTs could be carried out by acid treatment (HNO_3 for 3 h) followed by hydrogen treatment at 700 – 1000 ^oC, where the metal impurities are removed by acid and the amorphous carbon could be eliminated by the reaction with hydrogen at high temperature [54f].

Chemical functionalization, on the other hand, plays a preeminent role in many areas of research like fabrication of high-strength polymer nanocomposites [55a,b], optics [15,55c] and bio-technology [55d,e] to energy storage. This is mainly because, in order to take the full advantage of potential applications of CNTs, the inert surface of nanotubes with intrinsic van der Waals forces must be overcome by linking them to appropriate molecules, which in turn, can make them more adaptable/soluble in various solvents.

Mainly, functionalization of nanotubes has been divided into two categories including covalent and non-covalent functionalization. Covalent functionalization is based on covalent linkage of functional entities onto the nanotube's carbon scaffolding at the termini of the tubes or at their side walls. Covalent functionalization is accompanied by a change in the hybridization from sp^2 to sp^3 and disruption of intrinsic electronic structure of nanotube. Defect functionalization takes the advantage of oxygenated sites and structural defects such as pentagon and heptagon in the hexagonal lattice.

Few important covalent reactions of SWCNTs are summarized in Scheme 1.3, where side-wall groups are functionalized with various organic reagents using 'name reactions'. This kind of a covalent reactivity of SWCNTs is due to two factors, (1) pyramidalization (increased angle between sp^2 carbon atoms due to curvature effects, shown in Scheme 1.2) at the carbon atom and (2) π-orbital misalignment between adjacent carbon atoms [53h]. Comparatively, pyramidalization in case of nanotubes is not severe as it is present in fullerenes (due to more strained walls), whereas, π-orbital misalignment is much more effective to cause addition reactions for CNTs [53i]. Non-covalent functionalization is mainly based on supramolecular organization although it interestingly, retains the original electronic structure. A special case of this type is the endohedral/exohedral functionalization of CNTs, i.e., filling of the tubes with atoms or smaller molecules.

Many of such chemical approaches eventually lead to the separation of metallic and semiconducting nanotubes. For example, diazotization of SWCNTs enables the separation of metallic SWCNTs from semiconducting type as illustrated by Smalley and co-workers [56], although only a limited success has been realized in this direction. Also, several methods have been subsequently attempted recently to functionalize SWCNTs [57], with the primary objectives of tuning their electronic properties for exploiting their potential applications along with alleviating common processing obstacles like bundling or flocculation while using the pristine form.

More recent studies reveal that, the solubility of SWCNTs in water can be enhanced along with efficient exfoliation of nanotube bundles due to special

functionalization methods like superacid/surfactant treatment [58], attachment of arylsulphonated groups [59] and microwave treatment in presence of oleum and nitric acid at elevated pressures [60]**.** However, several issues regarding the extent of functionalization, chopping of nanotubes under strong oxidative treatment and contamination affecting their purity have not been adequately investigated. For example, it is not clear how the low extent of –COOH group attachment (less than 5 wt% of oxygenated side groups) on the sidewalls/ends, generates such a highly unusual amount of amine functionalization (up to 70 wt%) [61a]. Whether, the present methods of acid functionalization of CNTs are sufficient or not to produce adequate amount of –COOH groups for further processing is also not clear. The effect of functionalization on band structure is also not well understood. More significantly, the purification of SWCNTs-COCl by repeated centrifugation and washing with solvents could deactivate (due to moisture sensitive –COCl groups) the acyl moieties, which is not well explained in all these reports. Hence, there is an immediate need to explore alternative synthetic procedures in order to achieve greater efficiency and high purity using covalent functionalization strategies due to its preeminent role in all application of SWCNTs.

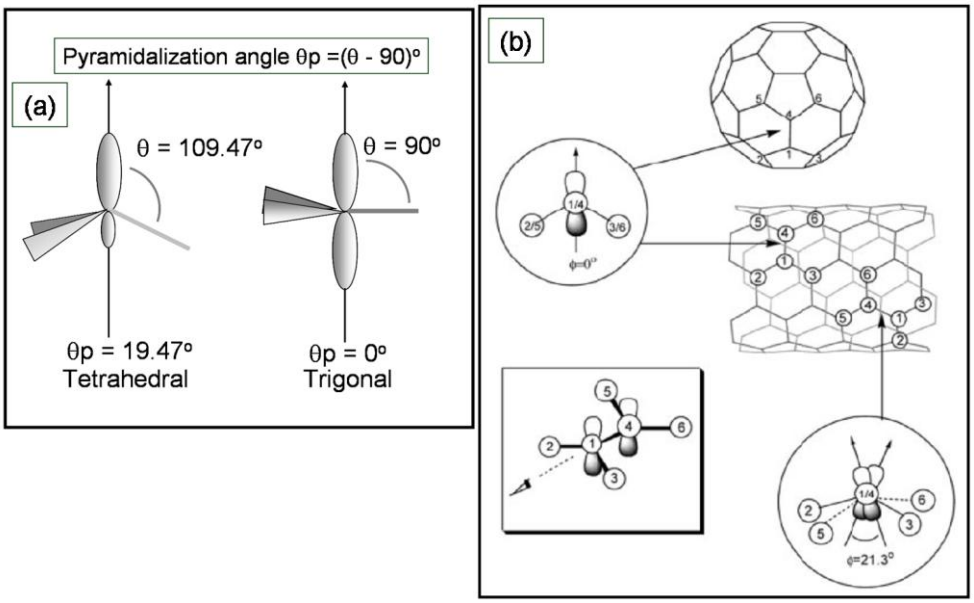

Scheme 1.2. (a) Pyramidalization angle (θp), and **(b)** the π-orbital misalignment angles (ϕ) along the C1-C4 bond in the metallic SWCNT and its capping fullerene, C_{60}, responsible for chemical reactivities of nanotubes; schemes are adopted from [61].

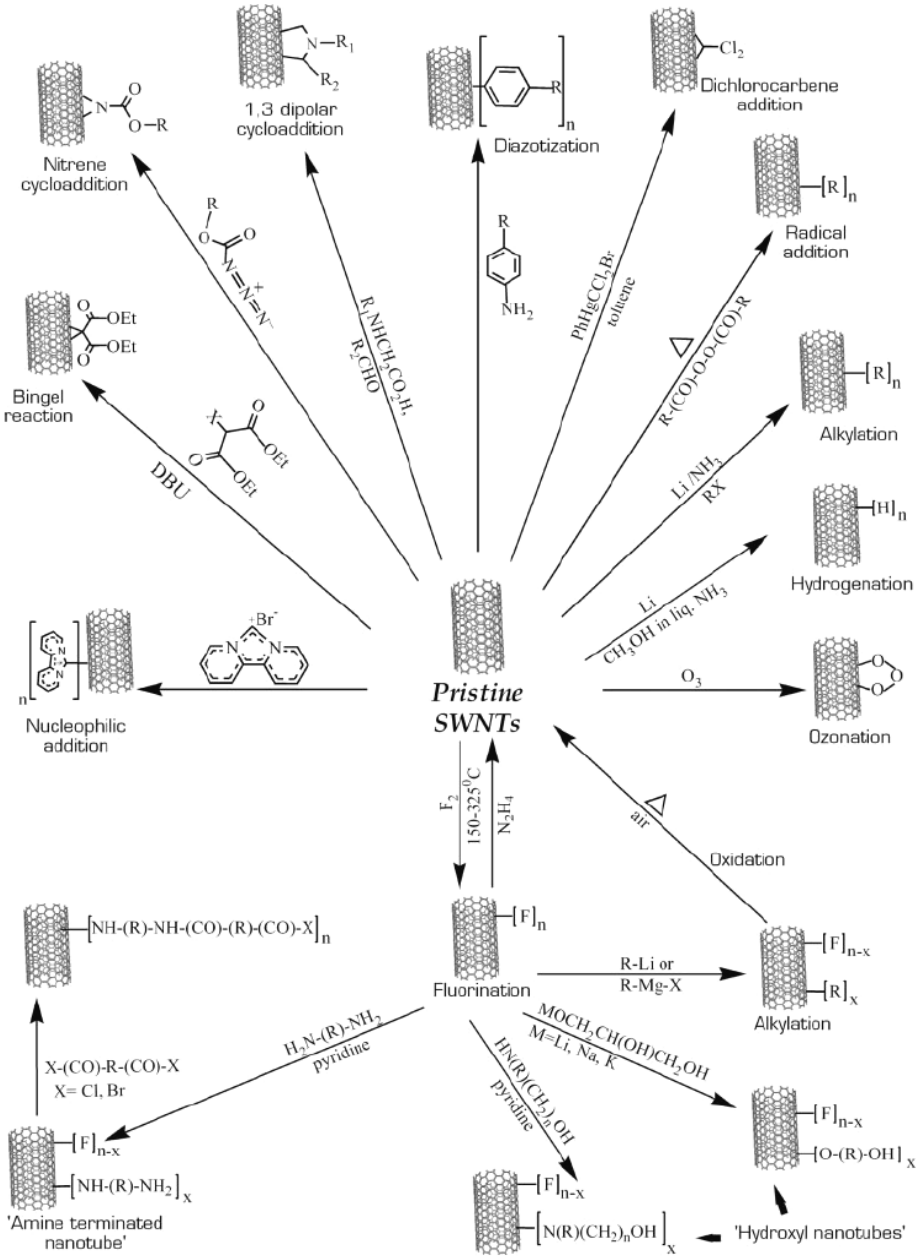

Scheme 1.3. Schematic of various methods of side wall covalent functionalization of SWCNTs where, the side walls could be selectively manipulated using simple chemical approach; scheme is adopted from [55f].

The fabrication of bucky papers is one of the important breakthroughs from the functionalization of nanotubes [63], since it shows tremendous application potential. It

has been made first by obtaining a stable suspension of CNTs using a non-ionic surfactant. This solution is ultra-sonicated to get a homogeneous dispersion of nanotubes and then filtered through a nanoporous membranes (generally polycarbonate or PTFE) using high vacuum. Thin film formed on the membrane is dried and used directly as the bucky paper with characteristic features and properties.

Applications of bucky paper as actuators are numerous, which include artificial muscles in humans, mechanical sensors, energy conversion devices and airflow control in jet engines. The reasons for the use of bucky paper as an actuator rather than the conventional ferroelectrics and electrostrictive actuators are its operating temperatures of 350 ^{o}C and its ability of using low operation voltage to produce higher output currents.

More importantly, all existing preparative methods for SWCNTs give rise to polydispersity in the sample, containing catalysts and amorphous carbon. In addition, this raw soot of nanotubes always contains the mixture of semiconducting and metallic SWCNTs [56]. One of the daunting challenge is to separate them into individual forms for further applications like field emission probes, scanning probes etc. Many chemical methods have been reported to alleviate this issue, although a complete separation without any loss of nanotubes is still a major challenge [64]. The unique electronic structure with electron rich sp^2 carbon atoms in the metallic SWCNTs leads to the formation of strong covalent bond in presence of electrophilic groups, which enhances the solubility of nanotubes to a remarkable extent resulting into effective separation (semiconducting nanotubes remain unaffected upon such treatment). Chemical methods show more promising effect for the bulk separation of tubes, as compared with techniques associated with (i) alternating current dielectrophoresis and (ii) the current-induced oxidation of metallic nanotubes, which have recently been reported as alternative methods for achieving chiral separations of nanotubes [65].

In recent years the advances in the solution-phase dispersion [66] along with spectroscopic identification using band-gap fluorescence [67] and Raman spectroscopy [68], have greatly improved the ability to monitor electrically distinct nanotubes as suspended mixtures. This has led to definitive assignments of the optical features of

semiconducting [67] as well as metallic and semimetallic distinct species [68]. More significantly, Strano and co-workers have shown a controlled method of functionalization based on the electronic structure of SWCNTs, where the diazonium reagent extracts electrons, thereby leaving a stable C-C covalent bond along with the evolution of N_2 [56]. Due to the addition of such electron deficient groups in nanotube mixture, under controlled conditions, only metallic nanotubes get affected leaving behind semiconducting as insoluble residue, which is confirmed by Uv-vis-NIR spectrum (disappearance of Van-Hove singularities due to discrete density of states, which is selectively affected in case of metallic nanotubes rather than that of semiconducting ones as shown in Figure 1.5) [56].

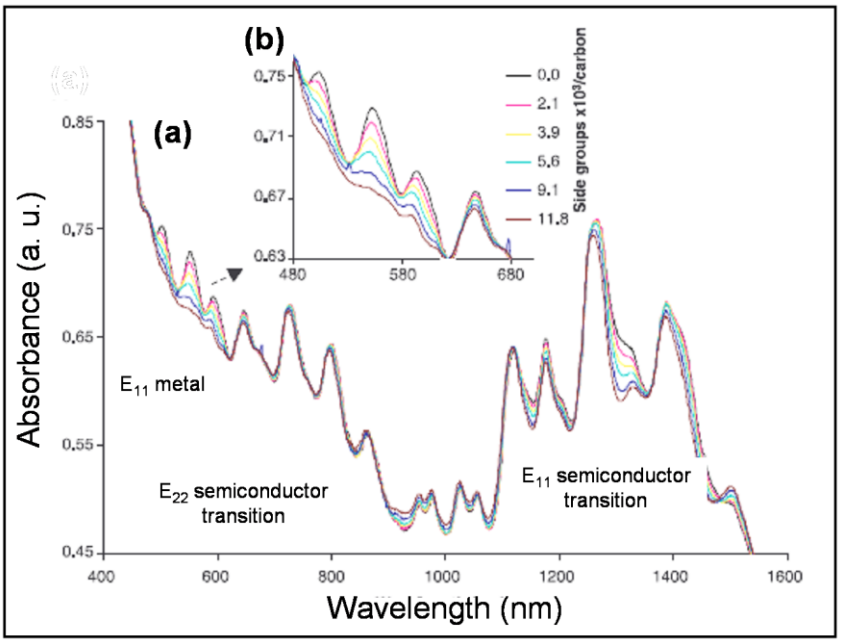

Figure 1.5. (a) Uv-vis-NIR spectrum of SWCNTs after the addition of various amounts of 4-chlorobenzenediazonium tetrafluoborate, showing changes in the van-Hove singularities of metallic nanotubes while, semiconducting remain unaffected and **(b)** expanded region of metallic transition along with some bathochromic shift due to changes in the surfactant adsorbed phase; E_{11}, E_{22} are quantized excitations for metallic and semiconducting nanotubes respectively; figure is adopted from [56].

Raman analysis is one of the important and widely used techniques to diagnose the electronic changes in the nanotubes. Raman spectrum (especially the radial breathing

mode (RBM); 100-300 cm^{-1}) of such functionalized CNTs gets severely affected in the intensities of RBM bands corresponding to metallic nanotubes although there could be some difficulty in detecting Raman spectrum of functionalized CNTs due to strong luminescent background and the dependence on the excitation wavelength [56,69]. The luminescent interference apparently depends on how well the CNTs are dispersed in the soluble sample, since better dispersion causes stronger interference of luminescence. For example, the functionalization via amidation with acylchloride route is more effective than that using diimide-activated coupling for a better dispersion [70]. Consequently, the spectrum obtained after amidation using 1-ethyl 3,(3-diamethylaminopropyl) carbodimide (EDAC) as a coupling agent exhibits less interference [70]. However, if this sample that contains more bundled nanotubes is refunctionalized to improve nanotube dispersion, the Raman spectrum of resulting sample would show a strong and broad luminescence [70]. Hence the inverse correlation between the Raman response and luminescence properties as a function of nanotube dispersion is very interesting, although needs further investigations in order to understand the mechanism of such a trend.

Solubilization of CNTs provides excellent opportunity for NMR studies, where it could be possible to understand the generation of various functional groups on the side walls by both ^{1}H and ^{13}C NMR [70]. For example, the attachment of long chain amine like octadecylamine could be confirmed by ^{13}C NMR using CNT solution in $CDCl_3$ [70b]. A COSY ^{1}H NMR has been shown for 4-chlorophenyl-SWCNTs when 4-chlorophenylamine reacts with SWCNTs in presence of isoamylnitrite [70c].

Functionalized CNTs from solution can be deposited directly onto a surface by electrophoresis for various microscopies like scanning electron microscopy (SEM or FESEM), transmission electron microscopy (TEM or HRTEM) and optical microscopy. Such a kind of analysis offers a direct evidence for the functionalization as TEM analysis is especially useful in providing both an overview at lower magnification and details of structural and morphological changes after functionalization examination at high resolution. Of course, the electron beam could damage the nanotubes during analysis, especially if it has energy more than 100 keV, which is sufficient to distort the graphitic

arrangement [68]. However, recently Iijima and co-workers have shown the chiral indices of SWCNT with a diameter of ~ 0.4 nm [(5,1) (3,3) and (4,3)] under 120 keV capable of achieving a resolution of 0.14 nm, under specific conditions [72].

Scanning probe microscopies have contributed significantly to understand a wide range of properties of carbon nanotubes. For example, scanning tunneling microscopy (STM) and spectroscopy (STS) have been used to characterize the atomic structure and tunneling density of states of individual SWCNTs and SWCNT ropes [73]. Studies of defect-free SWCNTs show semiconducting and metallic behavior that depends on the helicity and diameter of the nanotube. It is possible to define the one dimensional van-Hove singularities in the density of states for both the types of nanotubes.

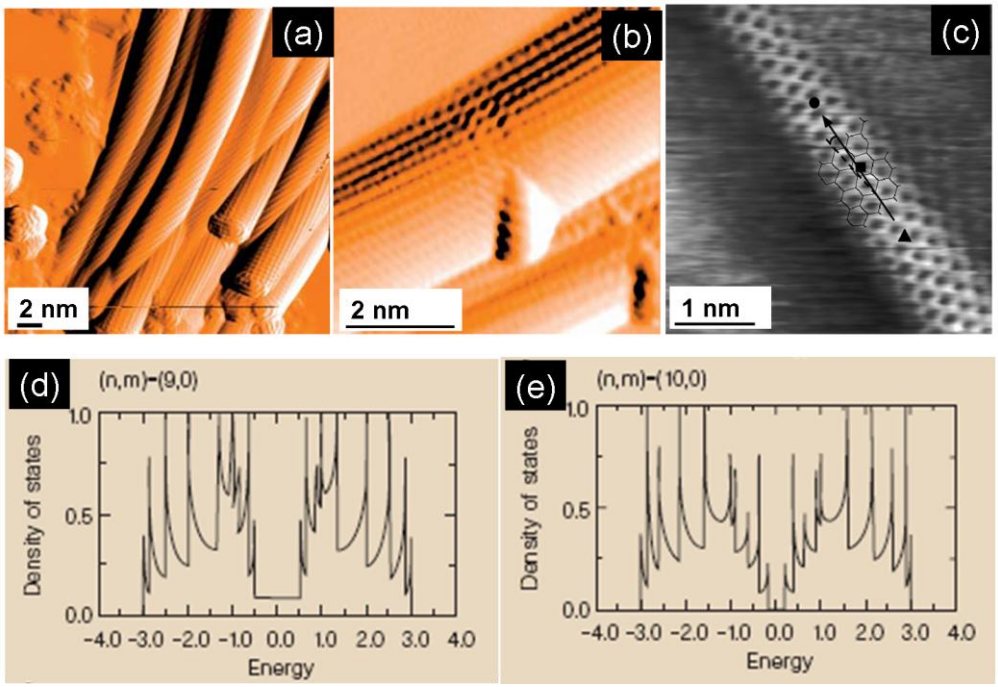

Figure 1.6. (a) Atomically resolved image of laser ablated SWCNTs; **(b)** functional molecule appearing as single protrusion on the SWCNT's sidewall and is oriented with the molecular plane parallel to the SWCNT sidewall as expected for π-stacking functionalization **(c)** atomic structure of metallic SWCNTs, showing the surface of a rope, recorded in the constant-current mode with bias voltages of 50 mV and tunnelling current of 150 pA; electronic structure of **(d)** armchair (9,0) metallic SWCNT and **(e)** zigzag (10,0) semiconducting SWCNT showing enormous difference in their properties with a small difference in the geometry; figures are adopted from [19,74a,b].

Further, the functionalization of nanotubes with their probable interaction with organic molecule could be well studied by STM/STS. For example, the π-stacking interaction between aromatic molecules (9-aminoanthracene and 4-(pyren-1-yl)butanoic acid) and nanotubes after functionalization has been demonstrated using STM/STS (as shown in Figure 1.6), where the aromatic molecules lie parallel to the SWCNT side wall [74].

Atomic force microscopy (AFM) is also a valuable tool for assessing the mechanical properties of nanotubes and for manipulating nanotubes into new structures [75]. AFM has been used to assess fundamental energetics of nanotube-surface interactions and frictional properties as nanotubes slid and/or roll on surfaces. High force sensitive tips could be used to determine the mechanical properties of nanotubes. In addition, the chemically modified tips have been employed for force measurements [75b]. Interestingly, chemical species at the ends of nanotube tips can be studied with great sensitivity by measuring the adhesion of a nanotube tip on chemically well defined self-assembled monolayers (SAMs) [76]. For example, the force titration between carboxylic groups on the tip of MWCNT / SWCNT and the SAM molecules has been studied as a function of pH [76]. Finally, AFM studies using such functionalized nanotube tips demonstrate their robustness and high resolution, although there could be important limitations like (1) resolution being constrained by probe tip dimensions and (2) artifacts generated due to repeated CNT bending–adhesion–separation process [76d].

Other techniques like x-ray photoelectron spectroscopy (XPS), thermogravimetry (TG), and Fourier transform infrared spectroscopy (FTIR) have been used to characterize the extent of functionalization of nanotubes [57].

Thus, rational functionalization methods provide unique opportunity for the manipulation of CNT properties in a predictive manner. The surface chemistry of both SWCNTs and MWCNTs plays a vital role in enabling the dispersability, purification, solubilization and diameter (more precisely aspect ratio dependent) and chirality based separation of these unique nanostructures. Thus, site selective functionalization is critical for the hierarchical design of these nanostructures into functional architectures, such as nanocomposites and electronic devices with unique applications.

1.5. Wetting Behavior of Carbon Nanotubes

1.5.1. Hydrophobicity / Hydrophilicity

Solid surfaces can be classified as hydrophobic or hydrophilic based on their ability to repel a water drop or be wetted by it. More specifically, surfaces having water contact angles greater than 150° and lower than 30° are described by many as superhydrophobic and superhydrophilic respectively, although other diagnostic criteria such as hysteresis and low rolling angle are also important to describe the extent of hydrophobicity [77]. Lotus leaf and many other leaves have hierarchical surface structures that prevent dirt and even bacteria from sticking. This "Lotus leaf effect" is related to superhydrophobicity and has attracted tremendous attention due to its wide applications related to the development of water-repellent and stainless coatings, self-cleaning and anti-fouling surface design and lab-on-a-chip devices [78]. In many of these applications, it would be of immense importance to externally control the interaction of liquids with a superhydrophobic surface, including the modification of contact angle, droplet mobility, and degree of penetration of liquid.

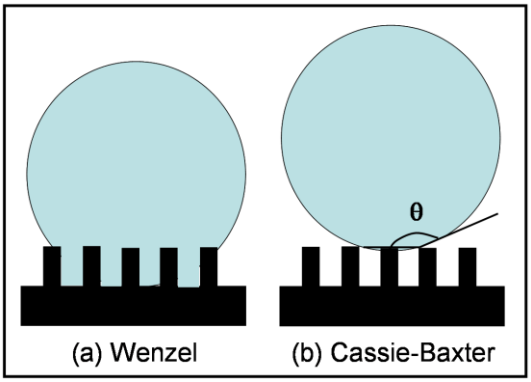

Figure 1.7. Wetting on hydrophobic rough surfaces showing **(a)** Homogenous (Wenzel form) wetting that wets the surface through capillaries and **(b)** Heterogeneous (Cassie-Baxter form) wetting, where air is trapped between droplet and solid surface.

From a thermodynamic perspective, the shape of a liquid drop is affected by the free energy of the surface, which forms an angle with the surface, known as the contact angle (CA), which in turn, is a function of the surface free energy as defined by the Young –Dupre equation,

$\gamma_{LV} \cos\theta = \gamma_{SL} - \gamma_{SV}$ …….. (1.1)

where, θ is the angle between the tangent to the droplet and the surface and $\gamma_{SV,}$ γ_{LV} and γ_{SL} are the surface tension at solid-vapor interface, liquid-vapor interface and solid-liquid interfaces respectively.

It is important, however, to understand the effect of surface roughness on the wetting behavior, which could be explained on the basis of two different theories, i.e., the Wenzel and Cassie-Baxter models. According to the former, the space between the protrusions on the surface is assumed to be completely filled by the liquid (Figure 1.7(a)) [79]; this model predicts that both hydrophobicity and hydrophilicity are reinforced by the roughness, according to the following relation-

$\cos\theta_w = r \cos\theta_Y$ ……(1.2)

where, θ_w and θ_Y are Wenzel apparent and ideal Young angle (ideal contact angle) respectively and 'r' is the surface roughness, which is defined as the ratio of the actual area of the solid surface to the projected area on the horizontal plane.

The approach developed by Cassie and Baxter, however, assumes that air is trapped by the asperities [80] so that the drop sits on a composite surface made of air and solid (Figure 1.7(b)); the relation between the apparent contact angle θ_C and the ideal angle θ_Y in this case is,

$\cos\theta_C = \phi_S \cos\theta_Y + \phi_S - 1$ ..... (1.3)

where, θ_C is the Cassie apparent contact angle and ϕ_S is the fraction of the projected area of the solid surface wetted by the liquid.

Both Wenzel and Cassie-Baxter relations were originally formulated for static drops at equilibrium; however, since the low-rate advancing angles and static angles are essentially identical [81], equations 1.2 and 1.3 could be applied to advancing angles also. Few attempts have been made to model the receding angles [82] and it has been shown that a droplet can be in either a Cassie-Baxter or a Wenzel state on a rough hydrophobic surface depending on how it is formed [83]. Because the advancing angles predicted by both the Cassie- Baxter and Wenzel theories can be very close to the experimental values, the receding angles can be used as a qualitative indication of the

state of the drop: if θrec is high (i.e., the hysteresis is low), then the drop will be in a Cassie- Baxter (slippy) mode; if θrec is low, then the drop will be in a Wenzel (sticky) state. Therefore, obtaining a stable Cassie-Baxter drop is the ultimate goal for achieving superhydrophobicity by tailoring surface topography. The adhesive behavior of water on rough surfaces can also be assessed by rolling-angle measurements [84] The rolling angle is defined as the critical angle where a water droplet begins to roll down in an inclined plate: a high rolling angle indicates a sticky Wenzel state, whereas a low sliding angle suggests a Cassie-Baxter regime (i.e., the drop will easily roll off a slightly tilted substrate) [84] Much less work has been carried out to the study of superhydrophilic (or more generally, superwetting) surfaces [85]. Assuming that no air is trapped in the roughness gaps of the hydrophilic surface, the exactly opposite situation has been described by Abdelsalam et al. [86], the Wenzel model still applies, along with the hemi-wicking or "composite-drop" (propagation of a drop inside the texture of solid surface with the development of liquid-vapor interface) model [77,87,88], where the drop is assumed to sit on a composite surface made up of solid and water.

1.5.2. Theoretical Models

1.5.2.1. Hydrophobic Surfaces

Since chemical composition is an intrinsic property of materials, wettability is usually enhanced by the increase of surface roughness (three-dimensional microgeometry), especially by fractal structures [87b-d]. In order to observe the effect of surface texture on the wetting behavior of hydrophobic as well as hydrophilic surfaces, several theoretical models based on their geometries have been discussed. For vertical structures with a flat top, assuming that the water does not occupy the roughness, then r = 1 and ϕ_S = *f*. Here, ϕ_S always refers to the solid fraction of cylindrical pillars and is given by $\phi_S = \pi d^2/4l^2$, where *d* is the base diameter of the cylinders, and *l* is their center-to-center pitch [77,87,88]. The Cassie-Baxter formulae for two different geometries now become,

$\cos\theta_C = -1 + \phi_S (1+ \cos\theta_Y)$ …….. (1.4) for cylindrical geometry and

$\cos \theta_C = -1 + \phi_B (1+ \cos \theta_Y)^2$ …….. (1.5) for hemispherical- pillar geometry

where, ϕ_B is the ratio of the area of geometry over the total area.

Similarly, Wenzel formula in two different geometries could be written as,

$\cos \theta_W = [1 + 4\phi_S (h/d – 0.25)] \cos \theta_Y$ ……(1.6) for the case of hemispherical - pillar geometry, whereas the equation for Wenzel form for cylindrical geometry is similar to that of equation 1.2. Thus, the two-dimensional geometry of the superhydrophobic surface determines the mode of wetting.

1.5.2.2. Hydrophilic Surfaces

Hydrophilic surfaces, on the other hand, also render an interesting relationship with respect to the geometry (texture) of the surface. Wettability in such cases could entirely be explained in terms of Wenzel formalism (sticky state), due to the filling of grooves. Therefore, wetting angles for both, hemi-wicking drop (propagation of liquid through texture creating liquid-vapor interface) and Wenzel form have been given for two different geometries of surface [77,87,88]. First, the relation for hemi-wicking drop is given as,

$\cos \theta_{Comp} = 1 + \phi_S (\cos \theta_Y - 1)$ ……. (1.7) for cylindrical geometry and

$\cos \theta_{Comp} = \phi_S (2 + 2\cos \theta_Y + 3\cos^2 \theta_Y - 1) + 1$ …… (1.8) for hemispherical-pillar geometry. However, the Wenzel formalism for such hydrophilic surfaces is similar to equation 1.2, where the space between protrusions is completely filled by liquid (homogeneous wetting) in all possible geometries.

Thus the wettability of a solid surface is a very important property for practical applications, especially since it depends on several parameters controlling its surface energy including the geometrical structure [89]. In particular, research on surface modification of CNTs is initiated due to the need for controlling their wettability. Although the preparation of superhydrophobic surfaces has been extensively studied for various materials [90], only a few attempts have been successful in controlling the wettability of CNTs. For example, Lau *et al.* [91] have reported the creation of superhydrophobic CNT forests with the water contact angle (CA) of 168° by modifying

the surface of vertically aligned nanotubes with a hydrophobic poly-tetrafluoroethylene (PTFE) coating although it requires many standard parameters to get optimum density of nanotubes, tedious growth steps and difficulty in applications. Also, Li *et al.* [92] have created honeycomb-like patterns composed of vertically aligned CNTs with diameter ranging from 3 to 15 μm, revealing superhydrophobic surface with CA of about 163.4°, although similar limitations would preclude their practical utilization; thus more studies are desired to resolve these issues.

One of the important limitations of contact angles measurements is the assumption of negligible time dependant changes. Several recent reports have been attempted to achieve a dynamic control over the wettability of superhydrophobic surfaces [93]. For example, the application of electric field to aligned CNT surface (in parallel direction) has been shown to reduce the interfacial tension between solid and liquid [94]. More recently, a dynamic electrical control of the whole range of wetting behavior (from hydrophilic to superhydrophobic) of liquids on nanostructured surfaces has been reported [95]. This way of modulation of the wetting of carbon nanotubes, indeed, has many profound implications in nano-fluidic transport, irrespective of the nature of the application. More interestingly, controlling the wetting behavior of low-melting metals like Ga and In could be favorably utilized to crystallize them into continuous nanowires, which would further facilitate fundamental investigations in determining their unusual electrical and magnetic properties like Luttinger liquid behavior [96].

Arrays of CNTs are usually hydrophobic (due to geometrical effects) though their wetting characteristics can be modulated between the extremes by changing functionalization strategies, so that one could prepare papers which are wetted selectively with unique behavior [97]. This applies equally important to other liquids such as oil and by a proper preparation and functionalization, one could even create solid surfaces that coexist both hydrophobic and amphiphilic domains facilitating the separation of the two [98]. Also, the forests of aligned carbon nanotubes show superhydrophobic behavior due to a higher degree of surface roughness as a result of microdomains between nanotubes

grown on a substrate [22]. Generally, superhydrophobicity requires both low surface energy and high surface roughness [97,98].

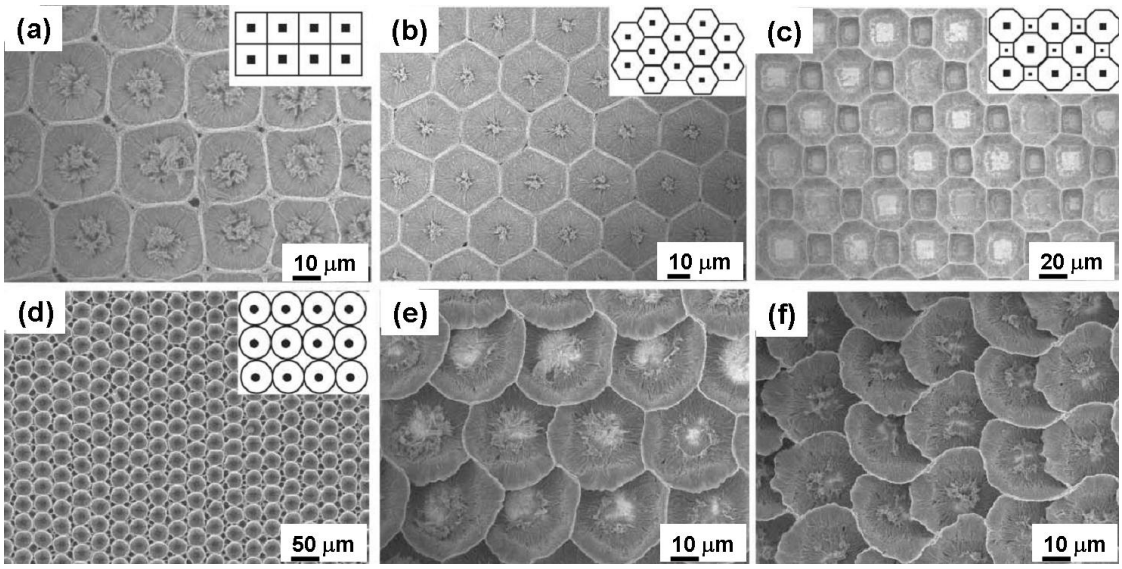

Figure 1.8. SEM images of highly ordered micro-patterned aligned CNT with different morphologies, **(a–d)** micro-patterns (cubic, the hexagon, the alteration of octagon and cubic, and the circle) self-assembled from aligned CNT; **(e and f)** are the micro-patterns originated from aligned CNT; the 'walls' bent, forming wave-like patterns after water spreading due to wetting; figure is adopted from [97].

Carbon nanotubes are inherently somewhat hydrophilic, with a water contact angle of less than 86^{o} [99], which is confrmed based on theoretical calculations [99e]. When they are arranged in a textured manner on substrates having different surface topographies, different wettabilities are exhibited. This ranges from hydrophilic to hydrophobic, and even superhydrophobic, and with isotropic to anisotropic with varying extent of contact angle hysteresis. If chemical modification is involved, the wettability could be adjusted from superhydrophobic to superhydrophilic on structured aligned CNTs [97,100]. The structural influence of isotropic roughness on this effect (including nano-structures and hierarchical structures) has been observed, where isotropic wetting shows an interesting transition from superhydrophobic behavior (for a very small period) and finally spreads, with a pinning action even beyond 30^{o} [101]. This is because of the triple phase (solid-liquid-vapor) contact line [102]. Water can wet the nanostructured CNT aligned surface (with different micro-patterns), resulting in self-organization due to

capillary effects, as shown in Figure 1.8, where patterned CNTs change their geometry after wetting measurements. However, hierarchically modified nano-structured materials show remarkable, superhydrophobic behavior. Secondly, the effect of anisotropic roughness on wetting behavior is well studied, although some of the challenges in this field need more detailed investigations [97].

The above discussion clearly illustrates that minute variations in the surface topography (roughness) of CNTs in a textured form impart tremendous changes in the wetting behavior. Thus chemical tuning of the wetting characteristics of CNT surfaces implies that the fabrication of nanotube composites with an amazing range of superhydrophobic to superhydrophilic properties could be realized by improving the surface functionalization strategies. Practical utilization of such tunable nanotube surfaces to make high performance polymer composites would significantly open up new perspectives in their possible applications. Such capabilities would allow one to construct much more sophisticated architectures from nanotubes, including electronic interconnects, robust nanocomposites and structured thin films.

1.6. Recent Developments in the Applications of Carbon Nanotubes

Many potential applications have recently been found for carbon nanotubes, including conducting and high-strength composites, energy storage and energy conversion devices, chemical and biological sensors, field emission displays and radiation sources, hydrogen storage media, and nanometer-sized semiconductor devices, probes, and interconnects [100]. However, the cost of nanotube, polydispersity and limitations in large scale processing and assembly methods are important barriers for realizing some of these applications.

Some of the fascinating dual identity (metal and semiconductor) of such one dimensional carbon nanostructures could serve as a wire, transporting current from one place to another, and it could also act as a transistor, using changes in current to store information. This promising structure could also be the secret to extending Moore's Law, which predicts that the number of transistors on the fastest CPUs will double every 18

months, beyond the limits of today's silicon microprocessors and thus, this could be our best hope for the next generation electronics. It is also the basic building block for future devices ranging from flat-panel displays and long-lasting batteries to fishing poles and satellite cables (in accordance with the lower density of nanotubes since, nanotubes are 30 to 100 times stronger than steel of same diameter).

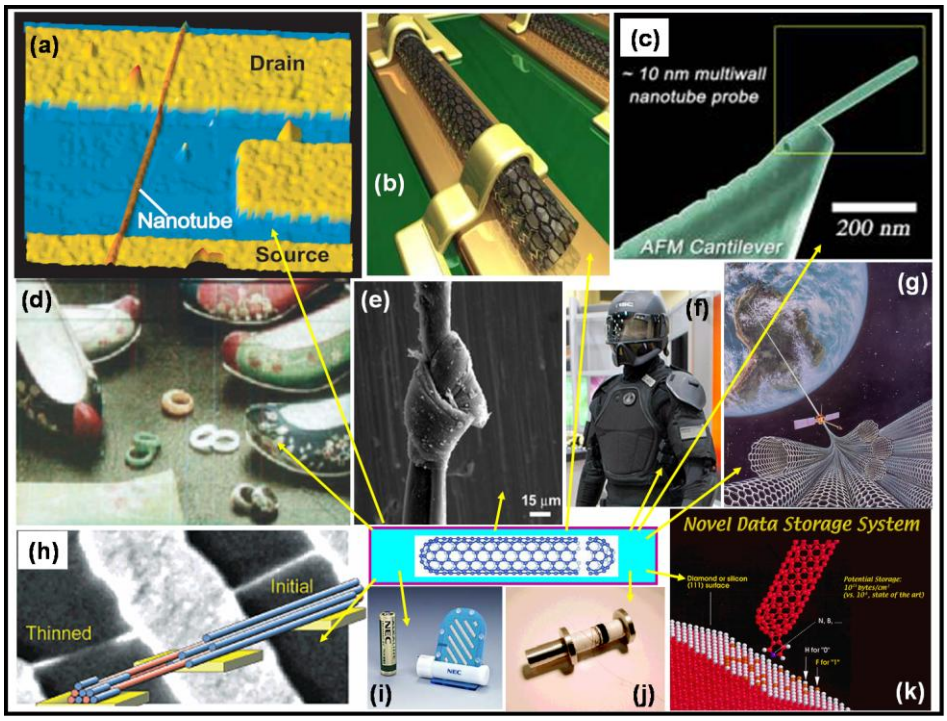

Figure 1.9. Various applications of carbon nanotubes including **(a)** nanotube based FET **(b)** a prototype for STM **(c)** MWCNT for AFM tip **(d)** flat panel display made by CNT **(e)** super-strong fibre made by CNT **(f)** CNT based composite for armor **(g)** a model for earth elevator by CNT **(h)** removal of number of layers from MWCNT to obtain desired electronic property **(i)** batteries **(j)** super -strong SWCNT/PVA composite **(k)** novel data storage system from CNT; figures are adopted from [103,108].

On the other hand, the silicon-based CPUs are being developed by Advanced Micro Devices (AMD), International Business Machine Corporation (IBM), and Intel (using extreme ultraviolet lithography) and this usage will be continued until the present technology would be unable to shrink silicon transistors any further, moving on to materials like CNTs. Semiconductors conduct current at certain voltages but not others.

They are used to build transistors, in which processors store information. When one voltage is applied, current flows freely through the nanotube, and the transistor turns on and when a different voltage is applied, the current stops, and the transistor turns off. Metals that conduct at any voltage are used to build the wires that connect transistors. In theory, one could build an entire microprocessor from carbon nanotubes. Its parts would be far smaller, and thus far faster than the copper wires and silicon transistors used today. Some of the promising applications are briefly illustrated in Figure 1.9.

For realizing above applications of CNTs, controlling their growth direction is extremely important. Individually addressable nanotubes are to be grown orthogonal to the substrate plane and this is accomplished by exploring patterned catalyst using different approaches. Further, researchers still seek answers for questions like "how do you control their physical properties? How do you grow them in the right place? How do you connect them?" Carbon nanotubes also show promise for an extraordinary variety of products such as infra red sources, flat-panel displays, batteries with twice as much energy as conventional ones and so on. Apart from these exciting developments in this field, CNTs have plethora of applications in various fields of science and technology; some of them are summarized in the following sections.

1.6.1. Nanocomposites

One of the first major commercial applications of MWCNTs is their use as electrically conducting polymer composites. Incorporation of nanotubes into plastics (or polymer) can potentially provide structural materials with a dramatically increased modulus and strength [104]. The critical challenges lie in uniformly dispersing the nanotubes, achieving nanotube-matrix adhesion that provides effective stress transfer, and avoiding intra-tube sliding between concentric tubes within MWCNTs and intra-bundle sliding within SWCNT ropes. Some promising results have been reported, for example by Biercuk and others [105], where a monotonic increase of resistance to indentation (Vickers hardness) by 3.5 times has been observed on loading up to 2% SWCNTs along with a doubling of thermal conductivity with 1% SWCNTs. Also, 1% MWCNT loading

in polystyrene has increased the modulus and breaking stress by up to ~40% and 25%, respectively [106]. Baughman et al have reported one of the transparent and toughest materials by spinning fibers of SWCNTs with polyvinyl alcohol [104]. Beating the previous contender, spider silk, by a factor of four, these fibers interestingly, require 600 J/g to break (in comparison, the bullet-resistant fiber Kevlar is 27–33 J/g) [107]. A method for producing transparent carbon nanotube sheets of $1/1000^{th}$ the thickness of a human hair capable of supporting 50,000 times their own mass is now possible. More significantly, a continuous, conducting and strong fibre of 100 m length has been fabricated at the speed of several centimetres per second. [108-109].

1.6.2. Field Emission Devices

Carbon nanotubes show excellent emission characteristics at a field lower than 1 V/μm along with high current densities of more than 1 A/cm^2. Consequently, CNT emitters can be fabricated in variety of configurations depending on the type of nanotube, their microscopic arrangement, synthetic procedure and the desired emitter source [110]. The largest potential market for CNT field emitters is for field emission display (FED), a technology that could replace most of today's monitors in desktop, laptop computers and televisions. The major current technologies applied in the display industry are cathode ray tube (CRT), liquid crystal display (LCD) and plasma display panel (PDP) all of which can perform unique functions [111].

1.6.3. Scanning Probe Microscopes

Scanning probe microscopy (SPM) has shown tremendous benefits in the past two decades in analyzing many nanomaterials [112a]. The smaller dimension of CNTs along with its high aspect ratio is desirable for its application in SPM. One of the most advantageous factors for the use of CNT as a probe is its mechanical property, which renders the tip very robust. Using MWCNT as a probe, a three dimensional imaging of a line and space array of a photoresist pattern has been produced by a 193 nm lithographic tool, although the use of SWCNT enhances the resolution [112b]. More interestingly, the

robustness of the nanotubes and the low buckling force dramatically increase the probe life concomitantly minimizing the sample damage during repeated hard crashes into the substrate. The cylindrical shape and small tube diameter also enable imaging in narrow, deep crevices allowing improved resolution in comparison to conventional nanoprobes, especially for higher sample feature heights [113].

1.6.4. Chemical and Bio-Sensors

Pristine SWCNTs may be used as miniaturized chemical sensors [40,111]. On exposure to environments, which contain NO_2, NH_3 or O_2, the electrical resistance changes, indicating the sensing ability of CNTs. In addition, sheets of SWCNTs could be used as electromechanical actuators, mimicking the actuator mechanism present in natural muscles. For example, a pair of nanotubes could be used as tweezers to move nanoscale structures on surfaces [114]. Nanotube tips can be modified by attaching various functional groups in order to use them as molecular probes, with potential applications in chemistry and biology. CNTs with well defined nanoscale dimension and unique molecular structures could be used as bridges linking biomolecules to macro-micro solid-state devices so that the information of bioevents can be transduced into measurable signals. Exciting new biosensing concepts and devices with extremely high sensitivities still being demonstrated using various types of CNTs [115].

1.7. Conclusions and Perspectives

Thus some of the most recent developments in the field of Carbon nanotubes have been presented in this chapter with particular emphasis on their preparation, functionalization, wetting properties and various applications. Both theory and experiment clearly show extraordinary structures and properties of CNTs. The smaller dimensions, high strength and remarkable chemical and physical properties of these carbon nanostructures enable a broad range of promising applications. Also, having vast tunability with respect to their structure and property, these applications are expected to lead the prospect of this field

for continuing decades with immense benefits in many areas like energy, healthcare, nanoelectronics and environmental monitoring. More specifically, these nanostructures act as indispensable building blocks for creating designer materials, devices and especially in robust polymer composites. Although there are many well-established methods to synthesize and understand the properties, several daunting challenges of these materials such as control of aspect ratio, difficulty of complete separation of metallic-semiconducting nanotubes, issue of scale-up and cost effectiveness, require breakthrough results to utilize these technological benefits.

1.8. Motivation, Scope and Organization of the Thesis

Various synthetic procedures such as Laser ablation, Arc discharge, High pressure carbon monoxide (HiPCO) process and thermal chemical vapor deposition (CVD) have been developed for the production of CNTs. Among these, CVD has been extensively used to grow a variety of carbon nanostructures. One of the important prerequisite during CNT synthesis is the precise control of temperature of the reaction zone because of its direct influence on the CNT diameter-distribution. Conventional synthetic procedures for CNT growth by CVD and its variants enable researchers to deal at relatively lower temperature range, viz. 700 – 1200 ^{o}C, using various hydrocarbons in presence of suitable catalysts. Accordingly, several methods have been developed, in order to explain the growth mechanism under different synthetic conditions. Nevertheless, no report exists on the preparation of carbon nanostructures under a constant temperature ramp, which could be helpful in understanding possible transformations in the growth mechanism. Hence the present thesis addresses this important issue, where the morphology of CNTs could be tuned under a constant temperature ramp facilitating scroll formation.

Although, considerable efforts have been expended in functionalizing carbon nanotubes, several important aspects related to their extent of selective functionalization, purity, and its relation to the wetting behavior remain unaddressed. One of the daunting challenges of tailoring CNTs, for several special applications, is its poor solubility in many solvents necessitating functionalization to be an unavoidable route before

engineering them into a proper geometry. Many previous studies have undoubtedly revealed that, the solubility of SWCNTs in water could be enhanced along with efficient exfoliation of nanotube bundles due to special methods like superacid treatment, attachment of arylsulphonated groups, and microwave treatment in presence of oleum and nitric acid at elevated pressures. However, several issues regarding the extent of functionalization and contamination affecting their purity have not been adequately addressed in this context. For example, it is not clear how the low extent of –COOH group attachment on the sidewalls/ends, generates such an unusual amount of amine functionalization (up to 70 wt%). Whether, the present methods of functionalization of CNTs are sufficient or not to produce adequate amount of –COOH groups for further efficient derivatization is also not clear. Hence, there is an immediate need to explore alternative synthetic procedures in order to achieve greater efficiency and high purity using functionalization strategies due to its preeminent role in all applications.

1.9. Objective of the Present Thesis

The foregoing critical review of carbon nanotubes shows several important methods for their synthesis, purification, functionalization, wetting property and applications; although several lacunae are still present for their wide utilization for various applications. For example, most of the nanostructures synthesized by CVD (and other methods as well) contain other unwanted structures along with the desired materials or structures, whose removal is very troublesome. Also, the effect of temperature on the preparation methods is rather crucial to design these nanostructures in a desired manner. Since the nanostructures of CNTs are very important as a backbone for fabrication of composite materials including bullet-proof jackets, electrochemical devices and flat panel displays, it is of immense importance to understand the effect of functionalization of their chemical as well as physical properties. Further, wetting behavior of nanotubes, especially, when they are present in the form of bucky papers are extremely important in order to understand the interfacial interactions with liquid. Furthermore, the use of CNTs as a support in heterogeneous catalysis has tremendous utility due to their favorable

characteristics such as high surface area, mechanical strength, inert carbon network and chemically tunable topography. Hence, it will be interesting to explore the catalytic properties of nanotubes after making their hybrid materials with metal nanoparticles like rhodium, where the effect of substrate plays an important role. The specific objectives of the work embodied in this thesis are set out in this perspective as follows:

(a) To synthesize MWCNTs using CVD process under a continuous temperature ramp;

(b) To explore the effect of microwave treatment on purification and solubility of SWCNTs and MWCNTs;

(c) To accomplish the effective covalent functionalization of water-soluble SWCNTs using unique techniques;

(d) To elucidate the effect of surface functionalization on wetting behavior of bucky papers of MWCNTs, thus demonstrating the possibility of tuning their wetting behavior;

(e) To illustrate the effect of electric field on the wetting properties of bucky papers;

(f) To synthesize and characterize the monodispersed Rhodium nanoparticles revealing some of their unique behavior like single electron transfer;

(g) To synthesize Rh/MWCNT hybrid materials for catalytic hydrogenation of various arenes.

Present thesis attempts to address some of these issues by carrying out specific functionalization methods using both SWCNTs and MWCNTs. In particular, many types of chemical treatments have been carried out on CNT surfaces to correlate the wetting behavior of MWCNT bucky papers using sessile drop contact angle (CA) measurements. Similarly the design of hybrid nanostructures like Rhodium/MWCNTs has helped to

illustrate the promising catalytic activity of these materials in many reactions like the hydrogenation of arene.

First chapter represents a critical review on synthesis, functionalization, characterization, and various properties of CNTs relative to other carbonaceous materials. Their detailed synthetic methods, especially utilizing CVD have been discussed in relation to their precise control over selective growth of nanotubes. The impact of these materials on nanotechnology for diverse applications such as multifunctional catalysts, optical, electronic and magnetic device fabrication, medical diagnostics, have been discussed along with the issues regarding environmental and pollution control. In the end, specific objectives of the present study are explained with special relevance to their surface manipulation by chemical functionalization. Finally, few of the major existing limitations with respect to the synthesis and processing of CNTs are also highlighted.

In **second chapter**, we explain a method for synthesizing scrolls of MWCNTs, by subjecting a reaction mixture of toluene and ferrocene in hydrogen-argon environment to a dynamic temperature gradient facilitating the formation of scrolls of felt-like carbonaceous layers. These few micron-thick layers comprising of intertwined MWCNTs with very low catalyst content have been characterized by many techniques including Scanning electron microscopy (SEM), High resolution transmission electron microscopy (HRTEM), X-ray photoelectron spectroscopy (XPS), Thermogravimetry (TG), Raman Spectroscopy, dc conductivity, cyclic voltammetry and electrochemical impedance measurements. A tentative growth mechanism has been discussed in order to explore the effect of dynamic temperature on the morphology of carbon nanostructures.

In **third chapter**, we discuss a simple and novel method of solubilizing SWCNTs using microwave treatment. This also includes a strategy for an efficient phase transfer of SWCNTs from an aqueous to non-aqueous media using a unique amino functionalization route, where the water soluble SWCNTs (2.6 mg/mL) could be transferred to solvents like chloroform, toluene and carbon disulphide (CS_2). A comparative study on two amine functionalization routes for SWCNTs is also provided. These functionalized SWCNTs have been characterized by techniques including SEM, TEM, XPS, TG, Raman

spectroscopy, cyclic voltammetry and electrochemical **i**mpedance measurements. The chapter concludes by providing a comparison of microwave functionalization with other reported methods in terms of the extent of functionalization, purity and solubility.

In **Fourth chapter**, we discuss a strategy for controlling the wettability of MWCNT films (bucky papers) from superhydorphobic (156^o) to nearly hydrophilic (40^o), which further shows superhydrophilicity with water CA approaching 0^o within 2 seconds. Since CNT has a perfect graphitic network of sp^2 carbon, it exhibits intrinsic hydrophilic behavior (with water CA< 90^o), where further functionalization could facilitate easy control of their wetting properties. Accordingly, various methods of acid functionalization have been employed to render effective modification of nanotube surfaces and the effect has been monitored by CA measurements. In addition, the wetting properties of such superhydrophobic nanotube surfaces have also been controlled using external electric field. A tentative mechanism for electrowetting of CNT paper has been discussed with respect to pH, ionic strength and size of cations/anions.

The use of CNT as a substrate in heterogeneous catalysis has garnered much attention due to their favorable characteristics such as high surface area, mechanical stability and inert carbon network and chemically tunable topography. They also show catalytic properties superior to those of many conventional catalysts prepared on activated carbon, soot or graphite. If such high aspect ratio carbon nanostructures coupled with metal nanoparticles like Rhodium, an improved catalytic activity in the hydrogenation of olefin and arenes could be achieved. Consequently, in **chapter five**, a novel synthetic procedure has been demonstrated to get monodispersed nanoclusters of Rh due to their importance in size and shape dependent catalytic properties. More significantly, a unique electron transfer behavior has been discussed in case of these Rhodium nanoparticles stabilized by TDA (4.9± 0.2 nm) using data from electrochemical measurements. A series of evenly spaced redox peaks have been observed at room temperature (298 K). The later part of this chapter deals with the synthesis and characterization of Rh/MWCNT hybrid materials. These nanomaterials are characterized by different techniques such as FTIR, TEM, TGA, XPS, XRD and EDX. It also includes

the catalytic activity of such hybrid materials in heterogeneous hydrogenation of several arenes under selected conditions. The results indicate that Rh/MWCNTs could be a good option for hydrogenation of arenes since it selectively forms thermodynamically less favorable products with enhanced turn over number.

A summary of all major conclusions of the present study with respect to synthesis, functionalization, their characterization and various properties like electron transfer properties of functionalized CNTs have been discussed in **chapter six**. One of the major findings is an efficient method of chemical functionalization of both SWCNTs and MWCNTs. Significantly, the variations in the wetting behavior of bucky papers have been addressed based on both chemical functionalization and electric field to explore the interfacial properties. This chapter also outlines some of the limitations of these studies including the lack of microscopic information at the interface along with their probable hazardous effects on environment and plausible precautions needed during the synthesis and processing. Finally, long term future prospects of these materials are outlined within the broad perspective of both fundamental and technological interest in different interdisciplinary areas like chemistry, physics, biology and engineering.

These studies clearly show the usefulness of surface functionalization, thus demonstrating the significance of tuning the surface properties of CNTs for various applications. However, several limitations such as purity of nanotubes and difficulty of separating mixture of both metallic and semiconducting nanotubes, could restrict their wide spread commercial applications and further work is desired to alleviate these disadvantages. Various other barriers such as cost effective bulk synthesis and impact on environment need to be addressed. Despite these limitations, the results of present study are believed to be useful to understand several fundamental phenomena of CNTs for fabricating future devices.

1.10. References

1. (a) *Springer Handbook of Nanotechnology*, Bharat Bushan (Ed.) Springer-Verlag Berlin Heidelberg, New York **2004**. (b) Amato, I. Nanotechnology, www.ostp.gov/nstc/html/iwgn.iwgn.public.brocure/welcome.htm or www.nsf.gov.home/crssprgm/nano/nsfnnireport.htm (2000). (c) Anonymous: *National nanotechnology initiative*, www.ostp.gov/nstc/html/iwgn.fy01budsuppl/nni.pdf or www.nsf.gov/home/crssprgm/nano/nsfnnireports.htm (2000).
2. Feynman, R. P. *There is plenty of room at the bottom*, *Eng. Sci.* (February **1960**) 22.
3. (a) White, C. T.; Todorov, T. N. *Nature* **1998**, *393*, 240. (b) Frank, S.; Ponchoral, P.; Wang, Z. L.; de Heer, W. A. *Science* **1998**, *280*, 1744. (c) Yu, M. F.; Lourie, O.; Dyer, M. J.; Moloni, K.; Keley, T. F. ; Ruoff, R. S. *Science* **2000**, *287*, 637. (d) Hall, L. J.; Coluci, V. R.; Galvão, D. S.; Kozlov, M. E.; Zhang, M.; Dantas, S. O.; Baughman, R. H. *Science* **2008**, *320*, 504.
4. (a) Iijima, S. *Nature* **1991**, *354*, 56. (b) Monthioux, M.; Kuznetsov, V. L. *Carbon* **2006**, *44*, 1621.
5. *Carbon Materials for Advanced Technologies*, Edited by Burchell, T. D. (Pergamon, An Imprint of Elsevier Science, UK **1999**).
6. Rohlfing, E. A.; Cox, D. M.; Kaldor, A. *J. Chem. Phys.* **1984**, *81*, 3322
7. Kroto, H. W.; Heath, J. R.; O'Brien, S. C.; Curl, S. C.; Smalley, R. E. *Nature* **1985**, *318*, 162.
8. Ebbesen, T. W. *Carbon Nanotubes: Preparation and Properties*; CRC Press: Boca Raton, FL, **1997**.
9. Dresselhaus, M. S.; Dresselhaus, G.; Eklund, P. C. *Science of Fullerenes and Carbon Nanotubes*; Academic Press: New York, **1996**.
10. Kiang, C. H.; Goddard, W. A.; Beyers, R.; Bethune, D. S. *Carbon* **1995**, *33*, 903.
11. (a) Ajayan, P. M.; Ebbesen, T. W. *Rep. Prog. Phys.* **1997**, *60*, 1025. (b) Yakabson, B. I.; Smalley, R. E. *Am. Sci.* **1997**, July-August, 324.

12. Yakabson, B. I.; Smalley, R. E. *Am. Sci*. **1997**, July-August, 324.
13. Saito, R.; Dresselhaus, M. S.; Dresselhaus, G. *Physical Properties of Carbon Nanotubes*; World Scientific: New York, **1998**.
14. Mintmire, J. W.; Dunlap, B. I.; Carter, C. T. *Phys. Rev. Lett.* **1992**, *68*, 631.
15. (a) Hamada, N.; Sawada, S.; Oshiyama, A. *Phys. Rev. Lett.* **1992**, *68*, 1579. (b) Dressselhaus, M. S.; Dresselhaus, G.; Saito, R. *Phys. Rev. B* **1992**, *45*, 6234. (c) (d) Balasubramanian, K.; Burghard, M. *Small* **2005**, *1*, 180.
16. Iijima, S.; Ichihashi, T. *Nature* **1993**, *363*, 603.
17. Ge, M.; Sattler, K. *Science* **1993**, *260*, 515.
18. Wildoer, J. W. G.; Venema, L. C.; Rinzler, A. G.; Smalley, R. E.; Dekker, C. *Nature* **1998**, *391*, 59.
19. Odom, T.; Huang, J.; Kim, P.; Lieber, C. *Nature* **1998**, *391*, 62.
20. Dresselhaus, M. S.; Dresselhaus, G.; Sugihara, K.; Spain, I. L.; Goldberg, H. A. *Graphite Fibers and Filaments*; Springer- Verlag: New York, **1988**.
21. (a) Hutchison J. et al, *Carbon* **2001**, *39*, 761. (b) Endo, M.; Muramatsu, H.; Hayashi, T.; Kim, Y. A.; Terrones, M.; Dresselhaus, M. S. *Nature* **2005**, *433*, 476.
22. Bethune, D. S.; Kiang, C. H.; de Vries, M. S.; Gorman, G.; Savoy, R.; Vazquez, J.; Beyers, R. *Nature* **1993**, *363*, 605.
23. Thess, A.; Lee, R.; Nikolaev, P.; Dai, H.; Petit, P.; Robert, J.; Xu, C.; Lee, Y. H.; Kim, S. G.; Rinzler, A. G.; Colbert, D. T.; Scuseria, G. E.; Tomanek, D.; Fischer, J. E.; Smalley, R. E. *Science* **1996**, *273*, 483.
24. Journet, C.; Maser, W. K.; Bernier, P.; Loiseau, A.; Lamy de la Chappelle, M.; Lefrant, S.; Deniard, P.; Lee, R.; Fischer, J. E. *Nature* **1997**, *388*, 756.
25. Charlier, J.-C.; Gonze, X.; Michenaud, J.-P. *Europhys. Lett.* **1995**, *29*, 43.
26. Oberlin, A.; Endo, M. Koyama, T. *J. Cryst. Growth* **1976**, *32*, 335.
27. Bacon, R.; Bowman, J. C. *Bull. Amer. Phys. Soc.* **1957**, *2*, 13.
28. Hughes, T. V.; Chambers, C. R. US patent 405480, **1889**.
29. Radushkevich, L. V.; Lukyanovich, V. M. *Zurn. Fisic. Chim.* **1952**, *26*, 88.

30. (a) Hillert, M.; Lange, N. *Z. Kristallogr* **1958**, *111*, 24. (b) Baker, R. T. K. Harris, P. S.; Thomas, R. B.; Waite, R. J. *J. Catal.* **1973**, *30*, 86. (c) Boehm, H. P. *Carbon* **1973**, *11*, 583.
31. (a) Ebbesen, T. W.; Ajayan, P. M. *Nature* **1992**, *358*, 220. (b) J. Zhao, H. Park, J. Han, J. P. Lu, *J. Phys. Chem. B* **2004**, *108*, 4227.
32. (a) Tibbetts, G. G. *J. Cryst. Growth* **1984**, *66*, 632. (b) Tibbetts, G. G. *Carbon* **1989**, *27*, 745. (c) Tibbetts, G. G. *Filaments and Composites, in Carbon Fibres* (Cluwer Academic, Amsterdam **1990**) pp. 73. (d) Tibbetts, G. G. *J. Cryst. Growth* **1985**, *73*, 431. (e) Baker, R. T. K.; *Physic and Chemistry of Carbon*, Vol. 14, Walker, P.; Thrower, P. (Eds.) (Dekker New York **1978**) pp. 83. (f) Baker, R. T. K.; Carbon **1989**, *27*, 315. (g) Baker, R. T. K.; Murrell, L. L. (Eds.) *Novel Materials in Heterogeneous Catalysis* (Washington, DC **1990**). (h) Snyder, C. E.; Mandeville, W. H.; Tennent, H. G.; Truesdale, L. K.; *Hyperion Catalysis International*, US patent, (**1989**).
33. Andrews, R.; Jacques, D.; Rao, A. M.; Derbyshire, F.; Qian, D.; Fan, X.; Dickey, E. C.; Chen, J. *Chem. Phys. Lett.* **1999**, 303, 467-474.
34. (a) Sen, R.; Govindaraj A.; Rao, C. N. R. *Chem. Phys. Lett.* **1997**, *267*, 276. (b) Rao, C. N. R.; Sen, R.; Satishkumar, B. C.; Govindaraj A.; *Chem. Commun.* **1998**, 1525.
35. (a) Li, W. Z.; Xie, S. S.; Qian, L. X.; Chang, B. H.; Zou, B. S.; Zhou, W. Y.; Zhao, R. A.; Wang, G. *Science* **1996**, *274*, 1701. (b) Pan, Z. ; Xie, S. S. ; Chang, B. ; Wang, C. *Nature* **1998**, *394*, 631. (c) Hinds, B. J.; Chopra, N.; Rantell, T.; Andrews, R.; Gavalas, V. Bachas, L. G. *Science* **2004**, *303*, 62.
36. (a) Ren, Z. F.; Huang, Z. P.; Xu, J. W.; Wang, J. H.; *Science* **1998**, *282*, 1105. (b) Deck, C. P. ; Vecchio, K. S. *J. Phys. Chem. B* **2005**, *109*, 12353.
37. Dai, H.; Kong, J.; Zhou, C.; Franklin, N.; Tombler, T.; Cassell, A.; Fan, S.; Chapline, N. *J. Phys. Chem.* **1999**, *103*, 11246.
38. Dai, H. *Phys. World* (**2000**).
39. (a) Fan, S.; Chapline, M.; Franklin, N.; Tombler, T.; Cassell, A.; Dai, H. *Science*

1999, *283*, 512. (b) Endo, M. ; Takeuchi, K. ; Igarashi, S. ; Kobori, K. ; Shiraishi, M. ; Kroto, H. W. *J. Phys. Che. Solids* **1993**, *54*, 1841. (c) Zhu, L. B.; Xiu, Y. H.; Hess, D. W.; Wong, C. P. *Nano Lett.* **2005**, *5*, 2641. (d) Allouche, H.; Monthioux, M.; Jacobsen, R. L. *Carbon* **2003**, *41*, 2897. (e) Allouche, H.; Monthioux, M. *Carbon* **2005**, *43*, 1265. (f) Singh, C; Shaffer, M; Kinloch, I; Windle, A; *Physica B: Condensed Matter* **2002**, *323*, 339. (g) Delzeit, L; Nguyen, C.V.; Chen, B.; Stevens, R.; Cassell, A.; Han, J.; et al. *J. Phys. Chem. B* **2002,** *106*, 5629. (h) Hoffmann, S.; Ducati, C.; Robertson, J.; Kleinsorge, B. *Appl. Phys. Lett.* **2003**, *83*, 135. (i) Singh, C.; Shaffer, M. S.; Kozial, K. K.; Kinloch, I. A.; Windle, A. H. *Chem. Phys. Lett.* **2003**, *372*, 860. (j) Meng, G.; Jung, Y. J.; Cao, A.; Vajtai, R.; Ajayan P. M. *Proc. Am. Chem. Soc.* **2005**, *102*, 7074. (k) Xiang, R.; Yang, Z.; Zhang, Q.; Luo, G.; Qian, W.; Wei, F.; Kadowaki, M.; Einarsson, E.; Maruyama, S. *J. Phys. Chem. C*. **2008**, *112*, 4892. (l) Andrews, R.; Jacques, D.; Qian, D.; Rantell, T. *Acc. Chem. Res*. **2002**; *35*, 1008. (m) Peng, H.; Jain, M.; Li, Q.; Peterson, D. E.; Zhu, Y.; Jia, Q. *J. Am. Chem. Soc.* **2008**; *130*, 1130. (n) Zhang, Z.; Wei, B. Q.; Ramanath, G.; Ajayan, P. M. *Appl. Phys. Lett.* **2000**, *77*, 23. (o) Wei, B. Q.; Vajtai, R.; Jung, Y.; Ward, J.; Zhang, R.; Ramanath, G.; Ajayan, P. M. *Nature* **2002**, *416*, 495. (p) Li, X.; Cao, A.; Jung, Y. J.; Vajtai, R.; Ajayan, P. M. *Nano Lett* **2005,** *5*, 1997.

40. Dresselhaus, M. S.; Dresselhaus, G.; Avouris, Ph. (Eds.) *Carbon Nanotubes Synthesis, Structure, Properties and Applications* (Springer-Verlag Berlin Heidelberg, Germany) 2001

41. (a) Kong, J.; Cassell, A. M.; Dai, H. *Chem. Phys. Lett.* **1998**, *292*, 567. (b) Kong, J.; Soh, H.; Cassell, A. M.; Quate, C. F.; Dai, H. *Nature* **1998**, *395*, 878. (c) Cassell, A.; Raymakers, J.; Kong, J.; Dai, H. *J. Phys. Chem.* **1999**, *103*, 6484. (d) *The Wondrous World of Carbon Nanotubes* 'a review of current carbon nanotube technologies' Niessen R. A. H. Eindhoven University of Technology, Feb **2003**.

42. (a) Iwasaki, T.; Zhong, G.; Aikawa, T.; Yoshida, T.; Kawarada, H. *J. Phys. Chem. B.* **2005,** *109*, 19556. (b) Zhou, W.; Zhang, Y.; Li, X.; Yuan, S.; Jin, Z.;

Xu, J.; Li, Y. *J. Phys. Chem. B.* **2005,** *109,* 6963. (c) Li, X.; Tu, X.; Zaric, S.; Welsher, K.; Seo, W. S.; Zhao, W.; Dai, H. *J. Am. Chem. Soc.;* **2007**; *129*(51); 15770. (d) Jung, Y. J.; Homma, Y.; Ogino, T.; Kobayashi, Y.; Takagi, D.; Wei, B.; Vajtai, R.; Ajayan, P. M. *J. Phys. Chem. B* **2003,** *107,* 6859. (e) Ago, H.; Ohshima, S.; Uchida, K.; Yumura, M. *J. Phys. Chem. B.* **2001,** *105,* 10453. (f) Ago, H.; Ohshima, S.; Uchida, K.; Yumura, M. *J. Phys. Chem. B* **2001,** *105,* 10453. (g) Liao, H.; Hafner, J. H. *J. Phys. Chem. B.* **2004,** *108,* 6941. (h) Su, M.; Li, Y.; Maynor, B.; Buldum, A.; Lu, J. P.; Liu, J. *J. Phys. Chem. B.* **2000,** *104,* 6505. (i) Hornyak, G. L.; Grigorian, L.; Dillon, A. C.; Parilla, P. A.; Jones, K. M.; Heben, M. J. *J. Phys. Chem. B.* **2002,** *106,* 2821. (j) Fu, Q.; Huang, S.; Liu, J. *J. Phys. Chem. B.* **2004,** *108,* 6124. (k) Bhaviripudi, S.; Mile, E.; Steiner, S. A., III; Zare, A. T.; Dresselhaus, M. S.; Belcher, A. M.; Kong, J. *J. Am. Chem. Soc*.; **2007,** *129,* 1516. (l) Huang, L.; Cui, X.; White, B.; O'Brien, S. P. *J. Phys. Chem. B.;* **2004,** *108,* 16451. (m) Nishino, H.; Yasuda, S.; Namai, T.; Futaba, D. N.; Yamada, T.; Yumura, M.; Iijima, S.; Hata, K. *J. Phys. Chem. C.* **2007,** *111*, 17961. (n) Li, Y.; Kim, W.; Zhang, Y.; Rolandi, M.; Wang, D.; Dai, H. *J. Phys. Chem. B.* **2001**; *105*, 11424. (o) Li, Y.; Kim, W.; Zhang, Y.; Rolandi, M.; Wang, D.; Dai, H. *J. Phys. Chem. B.* **2001,** *105,* 11424. (p) Iwasaki, T.; Robertson, J.; Kawarada, H. *Nano Lett.* **2008,** *8,* 886.

43. B. Zheng, C. G. Lu, G. Gu, A. Makarovski, G. Finkelstein, J. Liu, *Nano Lett.* **2002**, *2*, 895.
44. http://www.nanotech-now.com/nanotube-survey-april2003.htm
45. C. A. Furtado, U. J. Kim, H. R. Gutierrez, L. Pan, E. C. Dickey, P. C. Eklund, *J. Am. Chem. Soc.* **2004**, *126*, 6095.
46. Sinnott, S. B.; Andrews, R.; Qian, D.; Rao, A. M.; Mao, Z.; Dickey, E. C.; Derbyshire, F. *Chem. Phys. Lett.* **1999**, *315*, 25-30.
47. Baker, R. T. K.; Harris, P. S. In Chemistry and Physics of Carbon; Walker, P. L., Thrower, P. A., Eds.; Marcel Dekker: New York, **1978**; Vol. 14, p 83.
48. Derbyshire, F.; Presland, A. E. B.; Trimm, D. L. *Carbon* **1975**, *13*, 111.

49. (a) Lin, M.; Ying Tan, J. P.; Boothroyd, C.; Loh, K. P.; Tok, E. S.; Foo, Y.-L. *Nano Lett.* **2006,** *6*, 449. (b) Ding, F.; Rosen, A.; Campbell, E. E. B.; Falk, L. K. L.; Bolton, K. *J. Phys. Chem. B* **2006,** *110*, 7666. (c) Lin, M.; Tan, J. P. Y.; Boothroyd, C.; Loh, K. P.; Tok, E. S.; Foo, Y.-L. *Nano Lett.* **2007**, *7* 2234. (d) Zhu, L.; Hess, D. W.; Wong, C.-P. *J. Phys. Chem. B.* **2006**, *110*, 5445. (e) Takagi, D.; Hibino, H.; Suzuki, S.; Kobayashi, Y.; Homma, Y. *Nano Lett.* **2007,** *7*, 2272. (f) Yun, Y.; Shanov, V.; Tu, Y.; Subramaniam, S.; Schulz, M. J. *J. Phys. Chem. B* **2006,** *110*, 23920. (g) Reina, A.; Hofmann, M.; Zhu, D.; Kong, J. *J. Phys. Chem. C.* **2007**, *111*, 7292. (h) Qi, H.; Yuan, D.; Liu, J. *J. Phys. Chem. C.* **2007**, *111*, 6158. (i) Lin, M.; Tan, J. P. Y.; Boothroyd, C.; Loh, K. P.; Tok, E. S.; Foo, Y.-L. *Nano Lett.* **2007,** *7*, 2234. (j) Jung, Y. J.; Wei, B. Q.; Vajtai, R.; Ajayan, P. M.; Homma, Y.; Prabhakaran, K.; Ogino, T. *Nano Lett.* **2003,** *3*, 561.

50. (a) Abild-Pedersen, F.; Nørskov, J. K.; Rostrup-Nielsen, J. R.; Sehested, J.; Helveg, S. *Phys. Rev. B* **2006,** *73*, 115419. (b) Helveg, S.; L'pez-Cartes, C.; Sehested, J.; Hansen, P. L.; Clausen, B. S.; Rostrup-Nielsen, J. R.; Abild-Pedersen, F.; Nørskov J. K. *Nature* **2004,** *427*, 426.

51. (a)Amara, H.; Bichara, C.; Ducastelle, F. *Phys. Rev. B* **2006,** *73*, 113404. (b) Raty, J. –Y.; Gygi, F.; Galli1, G. *Phys. Rrv. Lett.* **2005,** *95***,** 096103.

52. (a) Hayashi, T.; Muramatsu, H.; Kim, Y. A.; Kajitani, H.; Imai, S.; Kawakami, H.; Kobayashi, M.; Matoba, T.; Endo, M.; Dresselhaus M. S. *Carbon* **2006**, *44*, 1130. (b) Helveg, S.; L'pez-Cartes, C.; Sehested, J.; Hansen, P. L.; Clausen, B. S.; Rostrup-Nielsen, J. R.; Abild-Pedersen, F.; Nørskov J. K. *Nature* **2004,** *427*, 426.

53. (a) J. Chen, M. A. Hamon, H. Hu, Y. Chen, A. M. Rao, P. C. Eklund, R. C. Haddon, *Science* **1998**, *282*, 95. (b) J. Zhang, H. Zou, Q. Qing, Y. Yang, Q. Li, Z. Liu, X. Guo, Z. Du, *J. Phys. Chem. B* **2003**, *107*, 3712. (c) Rinzler, A. G.; Liu, J.; Dai, H.; Nikolaev, P.; Huffman, C. B.; Rodriguez-Macias, F. J.; Boul, P. J.; Lu, A. H.; Heymann, D.; Colbert, D. T.; Lee, R. S.; Fischer, J. E.; Rao, A. M.; Eklund, P. C.; Smalley, R. E. *Appl. Phys. A* **1998,** *67*, 29. (d) Shelimov, K. B.;

Esenaliev, R. O.; Rinzler, A. G.; Huffman, C. B. Smalley, R. E. *Chem. Phys. Lett.* **1998,** *282*, 429. (e) Mawhinney, D. B.; Naumenko, V.; Kuznetsova, A.; Yates Jr., J. T.; Liu, J.; Smalley, R. E. *Chem. Phys. Lett.* **2000,** *324*, 213. (f) Shaffer, M. S. P.; Fan, X.; Windle, A. H. *Carbon* **1998,** *36*, 1603. (g) Harutyunyan, A. R.; Pradhan, B. K.; Chang, J. P.; Chen, G. G.; Eklund, P. C. J. Phys. Chem. B **2002**, *106*, 8671. (h) Haddon, R. C. *Acc. Chem. Res.* **1998**, *21*, 243. (i) Hamon, M. A.; Itkis, M. E.; Niyogi, S.; Alvaraez, T.; Kuper, C.; Menon, M.; Haddon, R. C. *J. Am. Chem. Soc.* **2001**, *123*, 11292.

54. (a) Liu, J.; Rinzler, A. G.; Dai, H.; Hafner, J. H.; Bradley, R. K.; Boul, P. J.; Lu, A.; Iverson, T.; Shelimov, K.; Huffman, C.B.; Rodriguez-Macias, F. Shon, Y. S.; Lee, T. R.; Colbert, D. T.; Smalley, R. E. *Science*, **1998**, *280*, 1253. (b) Hiura, H.; Ebbesen, T. W.; Tanigaki, K. *Adv. Mater.* **1995**, *7*, 275. (c) Ajayan, P. M.; Ebbesen, T. W.; Ichihashi, T. Iijima, S.; Hiura, H. *Nature* **1993**, *361*, 333. (d) Banerjee, S.; Benny, T.H.; Balasubramanian, M.; Fischer, D.A.; Misewich, J.A.; Wong, S. S. *Chem. Phys. Chem.* **2004**, *5*, 1416. (e) Hwang, K. C. *J. Chem. Soc. Chem. Commun.* **1995**, *173*. (f) Vivekchand, S. R. C.; Govindraj, A.; Seikh, Md. M.; Rao, C. N. R. *J. Phys. Chem. B* **2004**, *108*, 6935.

55. (a) Salvetat, J. -P.; Bonard, J. –M.; Thomson, N. H.; Kulik, A. J.; Forro, L.; Benoit, W.; Zuppiroli, L. *Appl. Phys. A: Mater. Sci. Process.* **1999**, *69*, 255. (b) Calvert, P. *Nature* **1999**, *399*, 210. (c) Dai, H. *Acc. Chem. Res.* **2002**, *35*, 1035. (d) Pantarotto, D.; Partidos, C. D.; Hoebeke, J.; Brown, F.; Kramer, E.; Briand, J-P.; Muller, S.; Prato, M.; Bianco, A. *Chem. Biol.* **2003**, *10*, 961. (e) Chen, R. J.; Zhang, Y.; Wang, D.; Dai, H. J. *J. Am. Chem. Soc.* **2001**, *123*, 3838. (f) Banerjee, S. Benny, T. H.; Wong, S. S. *Adv. Mater.* **2005**, *17*, 17.

56. (a) Strano, P. J.; Dyke, C. A.; Usrey, M. L.; Barone, P. W.; Allen, M. J.; Shan, H.; Kittrell, C.; Hauge, R. H.; Tour, J. M.; Smalley, R. E. *Science* **2003**, *301*, 1519. (b) Dyke, C. A.; Tour, J. *J. Phys. Chem. A* **2004**, *108*, 11151.

57. (a) Bahr, J. L.; Tour, J. M. *J. Mater. Chem.* **2002,** *12*, 1952. (b) Banerjee, S.; Kahn, M. G. C.; Wong, S. S. *Chem. Eur. J.* **2003**, *9*, 1898. (c) Liu T.; Kumar, S.

Nano Lett. **2003,** *5*, 647. (d) Liang, F.; Sadana, A. K.; Peera, A.; Chattopadhyay, J.; Gu, Z.; Hauge R. H.; Billups, W. E. *Nano Lett.* **2004**, *4*, 1257. (e) Zhao, W.; Song C.; Pehrsson, P. E. *J. Am. Chem. Soc.* **2002**, *124*, 12418. (f) Qin, S.; Qin, D.; Ford, W. T.; Herrera, J. E.; Resasco, D. E.; Bachilo, S. M.; Weisman, R. B. *Macromolecules,* **2004**, *37*, 3965. (g) Zhao, B.; Hu H.; Haddon, R. C. *Adv. Funct. Mater*. **2004**, 14, 71. (h) Georgakilas, V.; Tagmatarchis, N.; Pantarotto, D.; Bianco, A.; Briand J.-P.; Prato, M. *Chem. Commun.* **2002**, 3050. (i) Pompeo F.; Resasco, D. E. *Nano Lett.* **2002**, *2*, 369. (j) Takahashi, T.; Tsunoda, K.; Yajima H.; Ishii, T. *Chem. Lett.* **2002**, 690. (k) Hirsch A. *Angew Chem. In. Ed.* **2002**, *41*, 1853. (l) Tasis, D. Tagmatarchis, N.; Bianco, A.; Prato, M. *Chem. Rev.* **2006**, *106*, 1105. (m) Stephenson, J.; Hudson, J. L.; Leonard, A. D.; Price, B. K.; Tour, J. M. *Chem. Mater.* **2007**, *19*, 3491.

58. Davis, V. A.; Ericson, L. M.; Parra-Vasquez, A. N.; Fan, H.; Wang, Y.; Prieto, V.; Longoria, J. A.; Ramesh, S.; Saini, R. K.; Kittrell, C.; Billups, W. E.; Adams, W. W.; Hauge, R. H.; Smalley R. E.; Pasquali, M. *Macromolecule*, **2004**, 37, 154.
59. Hudson, J. L.; Casavant, M. J.; Tour, J. M. *J. Am. Chem. Soc.* **2004**, 126, 11158.
60. (a) Wang, Y.; Iqbal Z.; Mitra, S. *J. Am. Chem. Soc.* **2006**, 128, 95. (b) Wang, Y.; Iqbal Z.; Mitra, S. *Carbon,* **2005**, *43*, 1015.
61. (a) Saini R. K.; Chiang, I. W.; Peng, H.; Smalley, R. E.; Billups, W. E.; Hauge, R. H.; Margrave , J. L. *J. Am. Chem. Soc.* **2003**, *125*, 3617. (b) Hamon, M. A.; Hu, H.; Bhowmik, P.; Niyogi, S.; Zhao, B.; Itkis, M. E.; Haddon, R. C. *Chem. Phys. Lett.* **2001**, *347*, 8. (c) Mark, A. H.; Chen, J.; Hu, H.; Chen, Y.; Itkis, M. E.; Rao, A. M.; Eklund, P. C.; Haddon, R. C. *Adv. Mater*. **1999**, *11*, 834.
62. Niyogi, S.; Hamon, M. A.; Hu, H.; Zhao, B.; Bhowmik, P.; Sen, R.; Itkis, M. E.; Haddon, R. C. *Acc. Chem. Res.* **2002**, *35*, 1105.
63. (a) Minett, A.I.; Fraysse, J.; Gu, G.; Roth, S. Practical considerations for the demonstration of a single walled carbon nanotube actuator. In: Kuzmany H et al., editors. Electronic properties of molecular nanostructures. *American Institute of*

Physics; **2001**, 585. (b) Mazzoldi, A.; De Rossi, D.; Baughman, R. H. Electro-mechanical behavior of carbon nanotube sheets in electrochemical actuators. In: Bar-Cohen Y, editor. Smart structures and materials **2000**: electroactive polymer actuators and devices: *Proceedings of SPIE*, **2000**, *3987*, 25. (c) Spinks, G. M.; Wallace, G. G.; Carter, C.; Zhou, D.; Fifield, L.S.; Kincaid, C.; Baughman, R. H. *Conducting polymer, carbon nanotube and hybrid actuator materials.* In: Bar-Cohen Y, editor. Smart structures and materials **2001**: electroactive polymer actuators and devices: *Proceedings of SPIE*, **2001,** *4329*, 199. (d) Vohrer, U.; Kolaric, I.; Haque, M. H.; Roth, S. Detlaff-Weglikowska, U. *Carbon* **2004**, *42*, 1159.

64. (a) Baik, S.; Usrey, M.; Rotkina, L.; Strano, M. *J. Phys. Chem. B.* **2004,** *108*, 15560 (b) Li, H.; Zhou, B.; Lin, Y.; Gu, L.; Wang, W.; Fernando, K. A. S.; Kumar, S.; Allard, L. F.; Sun, Y.-P. *J. Am. Chem. Soc.* **2004,** *126*, 1014. (c) An, L.; Fu, Q.; Lu, C.; Liu, J. *J. Am. Chem. Soc.* **2004,** *126*, 10520. (d) Lustig, S. R.; Jagota, A.; Khripin, C.; Zheng, M. *J. Phys. Chem. B.* **2005,** *109*, 2559. (e) Huang, H.; Maruyama, R.; Noda, K.; Kajiura, H.; Kadono, K. *J. Phys. Chem. B* **2006,** *110*, 7316. (f) Menard-Moyon, C.; Izard, N.; Doris, E.; Mioskowski, C. *J. Am. Chem. Soc.* **2006,** *128*, 6552 (g) Li, X.; Tu, X.; Zaric, S.; Welsher, K.; Seo, W. S.; Zhao, W.; Dai, H. *J. Am. Chem. Soc.* **2007,** *129*, 15770. (h) Li, H.; Zhou, B.; Lin, Y.; Gu, L.; Wang, W.; Fernando, K. A. S.; Kumar, S.; Allard, L. F.; Sun, Y.-P. *J. Am. Chem. Soc.* **2004,** *126*, 1014. (i) Chen, Z.; Du, X.; Du, M.-H.; Rancken, C. D.; Cheng, H.-P.; Rinzler, A. G. *Nano Lett.* **2003**, *3*, 1245. (j) Chattopadhyay, D.; Galeska, I.; Papadimitrakopoulos, F. *J. Am. Chem. Soc.* **2003**, *125*, 3370. (k) Strano, M. S. *J. Am. Chem. Soc.* **2003**, *125*, 16148. (l) Strano, M. S.; Dyke, C. A.; Usrey, M. L.; Barone, P. W.; Allen, M. J.; Shan, H.; Kittrell, C.; Hauge, R. H.; Tour, J. M.; Smalley, R. E. *Science* **2003**, *301*, 1519. (m) Banerjee, S.; Wong, S. S. *J. Am. Chem. Soc.* **2004**; *126*, 2073. (n) Kim, W.-J.; Usrey, M. L.; Strano, M. S. *Chem. Mater.* **2007,** *19*, 1571.

65. (a) Collins, P. G.; Arnold, M. S.; Avouris, P. *Science* **2001**, *292*, 706. (b) Krupke,

R.; Hennrich, F.; Lohneysen, H. V.; Kappes, M. M. *Science* **2003**, *301*, 344.

66. (a) M. S. Strano *et al., J. Nanosci. Nanotechnol* **2003**, *3*, 81. (b) O'Connell, M. J.; Bachilo, S. M.; Huffman, C. B.; Moore, V. C.; Strano, M. S.; Haroz, E. H.; Rialon, K. L.; Boul, P. J.; Noon, W. H.; Kittrell, C.; Ma, J.; Hauge, R. H.; Weisman, R. B.; Smalley, R. E. *Science* **2002**, *297*, 593.
67. Bachilo, S. M.; Strano, M. S.; Kittrell, C.; Hauge, R. H.; Smalley, R. E.; Weisman, R. B. *Science* **2002**, *298*, 2361.
68. Strano, M. S.; Doorn, S. K.; Haroz, E. H.; Kittrell, C.; Hauge, R. H.; Smalley, R. E. *Nanoletters* **2003**, *3*, 1091.
69. (a) Sun, Y. –P.; Huang, W. ; Lin, Y. ; Fu, K.; Kitaygorodsky, A.; Riddle, L.A. ; Yu, Y. J. ; Carroll, D. L. *Chem. Mater.* **2001**, *13*, 2864. (b) Lin, Y.; Rao, A. M.; Sadanadan, B.; Kenik, E. A.; Sun, Y. –P.; *J. Phys. Che. B* **2002**, *106*, 1294. (c) Huang, W.; Lin, Y.; Taylor, S.; Gaillard, J. Rao, A. M.; Sun, Y. –P. *Nano. Lett.* **2002**, *2*, 231.
70. (a) Sun, Y. ; Fu, K. ; Lin, Y. ; Huang, W. *Acc. Chem. Res.* **2002**, *35*, 1096. (b) Xu, M. Huang, Q.; Chen, Q. ; Guo, P. ; Sun, Z. *Chem. Phys. Lett.* **2003**, *375*, 598. (c) Nelson, D. ; Rhoads, H. ; Brammer, C. *J. Phys. Chem. C* **2007**, *111*, 17872.
71. (a) Chopra, N. G.; Ross, F. M.; Zettl, A. *Chem. Phys. Lett*. **1996**, *256*, 241. (b) Crespi, V. H.; Chopra, N. G.; Cohen, M. L.; Zettl, A.; Louie, S. G. *Phys. Rev. B: Condens. Mater*. **1996**, *54*, 5927.
72. Guan, L. Suenaga, K. ; Iijima, S. *Nano. Lett.* **2008**, *8*, 459.
73. (a) Charlier, J. C.; Lambin, Ph. *Phys. Rev. B.* **1998**, *57*, R15037. (b) Odom, T. W.; Huang, J. –L.; Kim, P.; Lieber, C. M. *J. Phys. Chem. B* **2000**, *104*, 2794.
74. (a) Lauffer, P.; Jung, A. ; Graupner, R.; Hirsch, A. ; Ley, L. *Phys. stat. sol.* **2006**, *243*, 3213. (b) Dresslehaus, M. S. *Nature* **1998**, *391*, 19.
75. (a) Frisbie, C. D.; Rozsnyai, L. F.; Noy, A.; Wrighton, M. S.; Lieber, C. M. *Science* **1994**, *265*, 2071. (b) Noy, A.; Sanders, C. H.; Vezenov, D. V.; Wong, S. S.; Lieber, C. M.; *Langmuir*, **1998**, *14*, 1508. (c) Green, J. B. D.; McDermot, M. T.; Porter, M. D.; Siperko, L. M. *J. Phys. Chem.* **1995**, *99*, 10960. (d) Noy, A.;

Frisbie, C. D.; Rozsnyai, L. F.; Wrighton, M. S.; Lieber, C. M. *J. Am. Chem. Soc.* **1995**, *117*, 7943. (e) Noy, A.; Vezenov, D. V.; Lieber, C. M. *Annu. Rev. Mater. Sci.* **1997**, *27*, 381. (f) Walters, D. A.; Ericson, L. M.; Casavant, M. J.; Liu, J.; Colbert, D. T. ; Smith, K. A. ; Smalley, R. E. *Appl. Phys. Lett.* **1999**, *75*, 3803.

76. (a) Wong, S. S.; Joselevich, E.; Woolley, A. T.; Cheung, C. –L.; Lieber, C. M.; *Nature*, **1998**, *394*, 52. (b) Wong, S. S.; Joselevich, E.; Woolley, A. T.; Cheung, C. –L.; Lieber, C. M.; *J. Am. Chem. Soc.*, **1998**, *120*, 8557. (c) Noy, A. Vezenov, D. V.; Kayyem, J. F.; Meade, T. J.; Lieber, T. J. *Chem. Biol.* **1997**, *4*, 519. (d) *Methods in Molecular Biology, vol. 283: Bioconjugation Protocols: Strategies and Methods* Edited by: C. M. Niemeyer © Humana Press Inc., Totowa, NJ.
77. (a) Martines, E.; Seunarine, K.; Morgan, H.; Gadegaard, N.; Wilkinson, C. D. W.; Riehle M. O. *Nano Lett.* **2005**, *5*, 2097. (b) Extrand, C. W. *Langmuir* **2004**, *20*, 4017. (c) Gao, L.; McCarthy, T. J. *Langmuir* **2006**, *22*, 6234. (d) McHale, G.; Shirtcliffe, N. J.; Newton, M. I. *Langmuir* **2004**, *20*, 10146. (e) He, B.; Lee, J.; Patankar, N. A. *Colloids and Surfaces A: Physicochem. Eng. Aspects* **2004**, *248*, 101. (f) Li, W.; Amirfazli, A. *J. Coll. Inter. Sci*. 2005, *292*, 195. (g) McHale, G.; Shirtcliffe, N. J.; Aqil, S.; Perry, C. C.; Newton. M. I. *Phys. Rev. Lett.* **2004**, *93*, 036102-1. (h) Rio, E.; Daerr, A.; Andreotti, B.; Limat, L. *Phys. Rev. Lett.* **2005**, *94*, 024503. (i) Baret, J.-C. *Phys. Rev. Lett.* **2006**, *96*, 016106. (j) Dorrer, C.; Ru¨he, J. *Langmuir* **2006**, *22*, 7652. (k) Extrand, C. W.; Kumagai, Y. *J. Coll. Inter. Sci.* **1997**, *191*, 378. (l) Baret, J. –C.; Brinkmann, M. *Phys. Rev. Lett.* **2006,** *96*, 146106.
78. Feng, L.; Li, S. H.; Li, Y. S.; Li, H. J.; Zhang, L. J.; Zhai, J.; Song, Y. L.; Liu, B. Q.; Jiang, L.; Zhu, D. B. *Adv. Mater.* **2002**, *14*, 1857.
79. Wenzel, R. N. *Ind. Eng. Chem.* **1936**, *28*, 988.
80. Cassie, A. B. D.; Baxter, S. *Trans. Faraday Soc.* **1944**, *40*, 546.
81. Kwok, D. Y.; Lin, R.; Neumann, A. W. *Colloids Surf. A* **1996**, *116*, 63.
82. (a) Patankar, N. A. *Langmuir* **2003**, *19*, 1249. (b) Roura, P.; Fort, J. *Langmuir* **2002**, *18*, 566.

83. (a) Yoshimitsu, Z.; Nakajima, A.; Watanabe, T.; Hashimoto, K. *Langmuir* **2002**, *18*, 5818. (b) Shibuichi, S.; Onda, T.; Satoh, N.; Tsujii, K. *J. Phys. Chem.* **1996**, *100*, 19512. (c) Miwa, M.; Nakajima, A.; Fujishima, A.; Hashimoto, K.; Watanabe, T. *Langmuir* **2000**, *16*, 5754.

84. Quere, D.; Lafuma, A.; Bico, J. *Nanotechnology* **2003**, *14*, 1109.

85. (a) Bico, J.; Thiele, U.; Quere, D. *Colloids Surf., A* **2002**, *206*, 41. (b) Bico, J.; Tordeux, C.; Quere, D. *Europhys. Lett.* **2001**, *55*, 214. (c) McHale, G.; Shirtcliffe, N. J.; Aqil, S.; Perry, C. C.; Newton, M. I. *Phys. Rev. Lett.* **2004**, *93*, 036102.

86. Abdelsalam, M. E.; Bartlett, P. N.; Kelf, T.; Baumberg, J. *Langmuir* **2005**, *21*, 1753.

87. (a) Quere, D. *Physica A* **2002**, *313*, 32. (b) Shibuichi, S.; Onda, T.; Satoh, N.; Tsujii, K. *J. Phys. Chem.* **1996**, *100*, 19512. (c) Shibuichi, S.; Yamamoto, T.; Onda, T.; Tsujii, K. *J. Colloid Interface Sci.* **1998**, *208*, 287. (d) Miwa, M.; Nakajima, A.; Fujishima, A.; Hashimoto, K.; Watanabe, T. *Langmuir* **2000**, *16*, 5754.

88. (a) Martines, E.; Seunarine, K.; Morgan, H.; Gadegaard, N.; Wilkinson, C. D. W.; Riehle M. O. *Nano Lett.* **2005**, *5*, 2057. (b) Yang, C.; Tartaglino, U.; Persson, B. N. J. *Eur. Phys. J. E.* **2006**, *19*, 47. (c) Yang, C.; Tartaglino, U.; Persson, B. N. J. *J. Phys. Cond. Mater.* **2006**, 0604052-v3.

89. Öner, D.; McCarthy, T. J. *Langmuir* **2000,** *1*6, 7777.

90. (a) Ogawa, K.; Soga, M.; Takada, Y.; Nakayama, I. *Jpn. J. Appl. Phys. Part 2* **1993**, *32*, L614. (b) Yabu, H.; Takebayashi, M.; Tanaka, M.; Shimomura, M. *Langmuir* **2005**, *21*, 3235.

91. Lau, K. K. S.; Bico, J.; Teo, K. B. K.; Chhowalla, M.; Amaratunga, G. A. J.; Milne, W. I.; Mckinley, G. H.; Gleason, K. K. *Nano Lett.* **2003**, *3*, 1701.

92. Li, S.; Li, H.; Wang, X.; Song, Y.; Liu, Y.; Jiang, L.; Zhu, D. J. *J. Phys. Chem. B* **2002,** *106*, 9274.

93. (a) Ichimura, K.; Oh, S.-K.; Nakagawa, M. *Science* **2000**, *288*, 1624. (b) Lahann, J.; Mitragotri, S.; Tran, T.-N.; Kaido, H.; Sundaram, J.; Choi, I. S.; Hoffer, S.;

Somorjai, G.; Langer, R. *Science* **2003**, *299*, 371. (c) Isaakson, J.; Tengstedt, C.; Fahlman, M.; Robinson, N.; Berggren, M. *Adv. Mater.* **2004**, *16*, 316.

94. Zhu, L.; Xu, J.; Xiu, Y.; Sun, Y.; Hess, D. W.; Wong, C. *J. Phys. Chem. B* **2006**, *110*, 15945.
95. Krupenkin, T.; Taylor, J.; Schneider, T.; Yang, S. *Langmuir* **2004**, *20*, 3824.
96. (a) Chen, J. Y.; Kutana, A.; Collier, C. P.; Giapis. K. P. *Science* **2005**, *310*, 1480. (b) Bockrath, M.; Cobden, D. H.; Lu, J.; Rinzler, A G.; Smalley, R. E.; Balents, L.; McEuen. P. L. *Nature* **1999**, *397*, 598. (c) Electronic transport in CNTs is strongly influenced by the electron-electron interaction unlike in higher dimensions where Fermi liquid theory provides a one-to-one correspondence between the free electrons and the quasi-particles of the interacting system. Transport in one dimensional system is often studied within the framework of the Tomonaga-Luttinger liquid. Characteristic predictions like power-law scaled conductance on bias voltage or temperature and spin-charge separation have been confirmed in experiments where the one dimensional system is well separated from the higher dimensional source and drain reservoirs.
97. Liu, H.; Zhai, J.; Jiang, L. *Soft Matter* **2006**, *2*, 811 and the references therein.
98. Feng, X.; Jiang, L. *Adv. Mater.* **2006**, *18*, 3063.
99. (a) Fowkes F. M.; Harkins, W. D. *J. Am. Chem. Soc.*, **1940**, *62*, 3377 (b) Morcos, I. *J. Chem. Phys.* **1972**, *57*, 1801. (c) Fowhes F. M.; Sawyer, W. M. *J. Chem. Phys.* **1952**, *20*, 1650 (d) Boyd G. E.; Livingston, H. K. *J. Am. Chem. Soc.* **1942**, *64*, 2383. (e) Dujardin, E.; Ebbesen, T. W.; Krishnan A.; Treacy, M. M. J. *Adv. Mater.* **1998,** *10*, 1472.
100. (a) Kong, H.; Gao C.; Yan, D. *J. Am. Chem. Soc.* **2004**, *126*, 412. (b) Baskaran, D.; Mays, J. W.; Bratcher, M. S. *Angew. Chem., Int. Ed.*, **2004**, *43*, 2138.
101. Lau, K. K. S.; Bico, J.; Teo, K. B. K.; Chhowalla, M.; Amaratunga, G. A. J.; Milne, W. I.; McKinley G. H.; Gleason, K. K. *Nano Lett.* **2003**, *3*, 1701.
102. Chen, W.; Fadeev, A. Y.; Hsieh, M. C.; O¨ner, D.; Youngblood J.; McCarthy, T. J. *Langmuir*, **1999**, *15*, 3395.

103. (a) http://news.bbc.co.uk/2/hi/science/nature/7038686.stm (b) http://www.technologyreview.com/Nanotech/19730/#comment-200368. (c) Cover page of *American Scientific*, July 1997. (d) www.technologyreview.com/nanotech/19730. (e) www.nec.co.jp/rd/Eng/Topics/data/r010830. (f) www.rpt.arc.nasa.gov/gallery.html.
104. Baughman, R. H.; Zakidov, A. A.; de Heer, W. A. *Science* **2002**, *297*, 787.
105. Biercuk M. J.; Rodosavijevic, M.; Hyun, J. K.; Johnson, A. T. Fischer, J. E. *Appl. Phys. Lett.* **2002,** *80*, 2767.
106. Qian, D.; Dickey, E. C.; Andrews, R.; Rantell, T. *Appl. Phys. Lett.* **2000,** *76*, 2868.
107. Srivastava, N.; Joshi, R.V.; Banerjee, K. *"Carbon Nanotube Interconnects: Implications for Performance, Power Dissipation and Thermal Management,"* IEDM, 2005, pp. 257-260.
108. (a) Banerjee K.; Srivastava, N. *"Are Carbon Nanotubes the future of VLSI Interconnections?"*, ACM Design Automation Conference, **2006**, pp. 809-814. (b) Cover page of '*American Scientist*', July-August 1997, The magazine of Sigma XI (Scientific Research Society) (c) www.ipt.arc.nasa.gov. (d) www.nec.co.jp/rd/Eng/overview.
109. (a) Banerjee, K.; Im, S.; Srivastava, N. *"Can Carbon Nanotubes Extend the Lifetime of On-Chip Electrical Interconnections?"* IEEE Nano Networks Conference, 2006. (b) Avouris, P. et al., *"Carbon Nanotube Electronics,"* Proc. IEEE, **2003,** *91*, 1772.
110. (a) Saito, Y.; Uemura, S. *Carbon* **2000**, *38*, 169. (b) Bonard, J. –M.; Kind, H.; Stockli, T.; Nilsson, L. –O. *Solid-State Electron* **2001**, *45*, 893. (c) Bachtold, *Science* **2001**, *294*, 1314.
111. (a) Meyyappen, M. *Carbon Nanotubes, Science and Applications*, CRC press (2000, N. W.). (b) Choi, W. B.; Chung, D. S.; Kang, J. H.; Kim, H. Y.; Jin,Y. W.; Han, I. T.; Lee, Y. H.; Jung, J. E.; Lee, N. S.; Park, G. S.; Kim, J. M. *Appl. Phys.*

Lett. **1999**, *75*, 3129.

112. (a) Binnig, G.; Quate, C. S.; Gerber, C. *Phys. Rev. Lett.* **1986**, *59*, 930. (b) Stevens, R. M.; Nguyen, C.; Cassell, A.; Delzeit, L.; Meyyappan, M.; Han, J. *Appl. Phys. Lett.* **2000**, *77*, 3453.
113. (a) Hafner, J. H.; Cheung, C. L.; Leiber, C. M. *Nature* **1999,** *398*, 761. (b) Dai, H.; Hafner, J. H.; Rinzler, A. G.; Colbert, D. T.; R. E. Smalley, *Nature* **1996**, *384*, 147.
114. Farhat, S.; La Chapelle, M. L.; Loiseau, A.; Scott, C. D.; Lefrant, S.; Journet, C.; Bernier, P. *J. Chem. Phys.* **2001**, *115*, 6752.
115. (a) Li, J.; Ng, H. T.; Chen, H. *Carbon nanotubes and nanowires for biological sensing, in protein Nanotechnology: Protocols, Instrumentation and Applications*, T. Vo-Dinh, Ed., Humana Press, Totowa, NJ (**2003**). (b) Wong, S. S.; Woolley, A. T.; Joselevich, E.; Cheung, C. L.; Lieber, C. M. *J. Am. Chem. Soc.* **1998**, *120*, 8557. (c) Taton, A. T.; Mirkin, C. A. *Nat. Biotechnol.* **2000**, *18*, 713. (d) Campbell, J. K.; Sun, L.; Crooks, R. M. *J. Am. Chem. Soc.* **1999**, *121*, 3779. (e) Sotiropoulou, S.; Chaniotakis, N. A. *Anal. Bioanal. Chem.* **2003**, *375*, 103. (f) Dieckmann, G. R.; Dalton, A. B.; Johnson, P. A.; Razal, J.; Chen, J.; Giordano, G. M.; Muñoz, E.; Musselman, I. H.; Baughman, R. H.; Draper, R. K. *J. Am. Chem. Soc.* **2003**, *125*, 1770.

CHAPTER 2

Synthesis of High-Purity Scrolled Mats of Multi Walled Carbon Nanotubes using Temperature Modulation*

Felt-like mats (6-7 micron thickness) of multiwalled carbon nanotubes wrapped into scrolls have been synthesized by chemical vapor deposition from a toluene-ferrocene mixture using a temperature ramp from 680 ^{o}C to 550 ^{o}C in hydrogen-argon atmosphere. Considering both, different time scales of various reactions and the diffusion of reactants and products, a tentative growth mechanism has been proposed as per the available characterization data in conjunction with possible scrolling effects. A plausible mechanism has been provided for the rolling action of sheets based on the thermal expansion effects. Interestingly, electrical conductivity measurements as a function of temperature suggest a semiconducting behavior of these scrolls, in contrast to the multitude of electron transport possibilities expected for such carbon nanostructures.

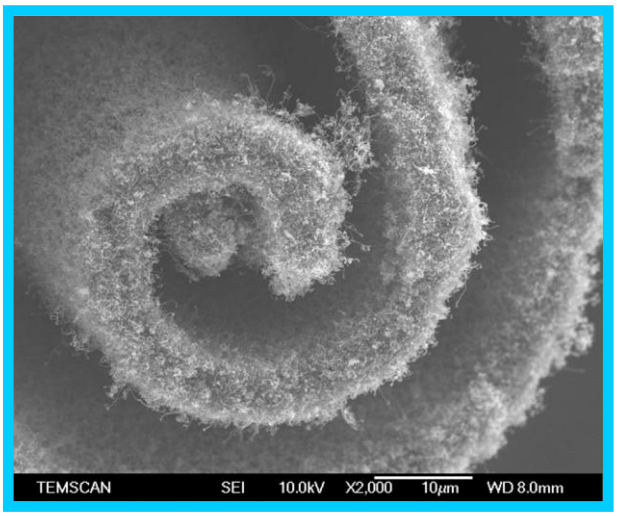

---

* A part of the work discussed in this chapter has been published in "*Carbon* **2008,** *46***,** 567**.**"

2.1. Introduction

After a landmark report by Iijima [1], Carbon nanotubes (CNTs) have attracted tremendous attention due to their unique structural, electronic, mechanical and optical properties [2], tunable at various levels. Consequently, CNTs have been considered as promising materials for a variety of applications such as field effect transistor [3-5], random access memory [6], and atomic force microscopy [7] as explained in chapter 1. While most of the efforts are focused on the production of single walled carbon nanotubes (SWCNTs), there are enumerable difficulties to reproduce them into a proper geometry, high purity and consistent chirality since their synthesis needs an accurate control of many parameters like temperature, nature and extent of catalysts, partial pressures of gaseous reactants, etc. On the other hand, considerable progress has been made in the synthesis of multi-walled carbon nanotubes (MWCNTs), which comprise several graphene sheets rolled into concentric cylinders leading to a stiffer and robust carbon structure, due to its reproducible nature at relatively low temperatures.

One of the important prerequisites during CNT synthesis is the precise control of temperature of the reaction zone because of its direct influence on the CNT diameter-distribution [8]. Conventional synthetic procedures for CNT growth by chemical vapor deposition (CVD) and its variants enable researchers to deal at relatively lower temperature range, viz. 700-1200 ^{o}C, using various gaseous/liquid hydrocarbons in presence of suitable catalysts [9-12]. For example, Andrews et al. [10] have reported an efficient and selective growth of aligned MWCNTs at 675 ^{o}C rather than at elevated temperature although the hydrocarbon conversion was only 25%. Similarly, Singh et al. have suggested a perpendicular growth of aligned MWCNTs on micron sized quartz flakes at 760 ^{o}C using a toluene-ferrocene mixture [13]. More interesting is a report on tree-like structures of carbon by Ajayan et al, achieved by a flash CVD method using methane as a source, demonstrating the effect of rapid heating and cooling cycles on CNT morphology [14]. In addition, maintaining a constant temperature gradient throughout the duration of synthesis has been proven to be effective to obtain carbon nanostructures with varying morphology like trees [14] cones [15], onions [16], and filaments [17]. A "kite-mechanism" has been proposed recently during a 'fast-heating'

CVD process to synthesize long and oriented SWCNTs on a surface, where different heating rates, both on the surface and in the surroundings, play a crucial role for controlling the growth [18]. On the contrary, despite the well-demonstrated importance of temperature in controlling the morphology, no report exists on the synthesis of carbon nanostructures under a constant temperature ramp.

In the first chapter we have given a critical review on synthesis, functionalization, characterization, and various properties (like wettability) of CNTs along with more details on their mechanistic features. All preparation methods, including CVD have been discussed in relation to their precise control over selective growth of nanotubes and few of the major limitations highlighting the importance of maintaining an accurate temperature profile during the synthesis.

Accordingly in this chapter, we describe a simple method for synthesizing pure scrolls of MWCNTs, by subjecting a reaction mixture of toluene and ferrocene in a hydrogen-argon environment under a dynamic temperature gradient, facilitating the formation of scrolls of felt-like carbonaceous layers. These few micron thick layers comprising intertwined MWCNTs (outer diameter of 10-150 nm) with a very low catalyst content (less than ca. 2 wt%) have been characterized by many techniques including scanning electron microscopy (SEM), high resolution transmission electron microscopy (HRTEM) X-ray photoelectron spectroscopy (XPS), Thermogravimetry (TG), Raman Spectroscopy and low temperature dc conductivity measurements. Based on these results a tentative growth mechanism has been discussed in order to explore the effect of dynamic temperature ramp on the morphology of these carbon nanostructures. The results of these investigations are presented below with the help of plausible models describing the growth mechanism.

2.2. Experimental Section

2.2.1. Materials

Ferrocene was used as received from Aldrich (99.99%) without any further purification, while toluene, acetone, and sulphuric acid were used as received from Merck (AR grade); deionized water (16 MΩ) from Milli-Q system was used for all experiments.

2.2.2. Experimental Set-up

An in-house fabricated CVD set-up, capable of attaining 1200 ^{o}C (with a dual zone) was used to synthesize the scrolls of MWCNTs, similar to the one used by Andrews et al, except for a few minor features like separate precursor heating zone and no separate accessories like Cu coolant or pressure gauze [10]. The precursor zone was connected to the carrier gas unit and Sage syringe pump (which could facilitate the usage of various flow rates from 0.1 mL/min to 1 mL/min) in order to pass the carbon source. The end of the main reaction zone was connected to the exhaust system through a cooling condenser, where the unreacted hot gases were trapped (Figure 2.1). In the beginning, a stream of argon was passed through the quartz tube (inner diameter 34 mm) at 100 sccm to expel all the impurities till both the zones achieved their respective temperatures (preheater zone; 200 ^{o}C, main zone; 680 ^{o}C). A solution of approximately 6 mol% of ferrocene in toluene was used as the precursor. This precursor solution was injected at a flow rate of 1.5 ml/hr for 16 min into the first zone of the dual furnace, maintaining the temperature at 200 ^{o}C to ensure complete sublimation of ferrocene and vaporization of toluene. The sublimed precursors were then passed into the main zone by means of a mixture of hydrogen and argon (ratio 1:9) as a carrier gas at 200 sccm. The temperature of the main furnace was programmed in such a way that it starts decreasing as soon as the vaporized gases entered the reaction zone without any external cooling aid. The scrolls were obtained by subjecting the system to a temperature ramp from 680-550 ^{o}C at a natural cooling rate (~ 8 ^{o}C/min). Almost 5 cm of the inner wall of quartz tube was spread by plenty of needles like (length: 0.5 - 2.0 cm, wall thickness: ~ 6-7 μm) scrolls of MWCNTs. The experimental conditions were quite different from the usual CVD conditions, particularly in two main aspects. First, during our CVD process, the cooling of the reactor was started at the same time when the nanotubes started to grow

(concomitant to the entry of the vaporized gases), unlike the usual CVD reactor, wherein the cooling starts right after the nanotube formation (after stopping the flow of the vaporized gases). Secondly, the injection of precursor was stopped when the temperature reached 550 ^{o}C (within 16 min) while, **g**enerally, MWCNTs produced by CVD are grown at a constant temperature. Hence, the formation of scrolls in our case could be attributed to the very specific experimental conditions and probably may not be related to the chemical or the mechanical removal of the MWCNTs from the wall of the reactor.

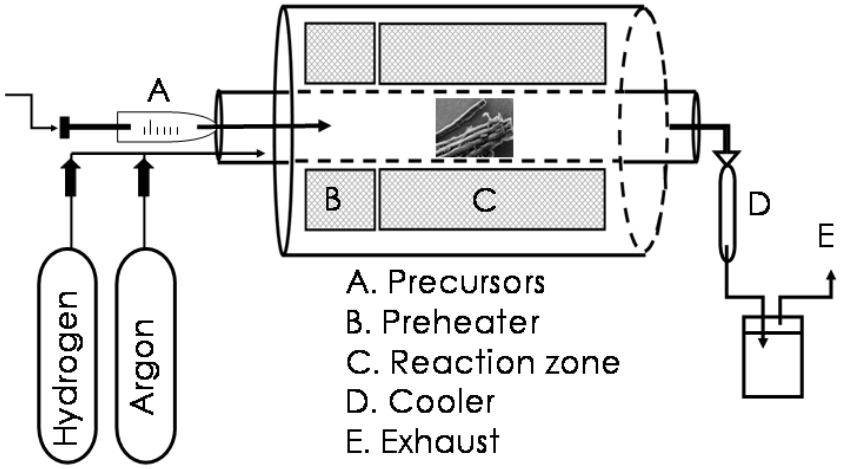

Figure 2.1. Experimental set-up used for the synthesis of scrolled mats of MWCNTs showing various components including dual zone heating arrangement, precursors, carrier gas and exhaust assembly.

2.3. Structural and Morphological Characterization

2.3.1. X-ray Diffraction (XRD)

X-ray powder diffraction studies were performed in order to understand the crystallinity and diameter distribution of nanotubes and also to estimate the presence of catalyst using CuK_{α} (λ = 1.54 Å) radiation on a Philips PW1830 instrument operating at 40 kV and a current of 30 mA at room temperature. Diffraction patterns were collected at a step of 0.02° (2θ) using a fixed CuKα radiation. The background was subtracted with the linear interpolation method.

2.3.2. Field-Emission Scanning Electron Microscopy (FESEM) and Energy Dispersive X-ray Analysis (EDX)

The morphology of these felt-like structures was examined by a JEOL JSM-6700F SEM having a field emission source and exhibiting a resolution of about ~2–3 nm, with no metal deposition on the scrolled mats. A selected amount of scrolled mat sample was put into ethanol to prepare a sonicated suspension. The surface morphology was also characterized by Kevex model EDX system (with Lieca Stereoscan 440 model SEM). For comparative studies, the energy of the electron beam was kept constant while analyzing all the samples. The micrographs of the samples were recorded with a 20 kV electrical high tension and 25 pA camera attached on the high-resolution recording unit.

2.3.3. High-resolution Transmission Electron Microscopy (HRTEM)

A selected amount of scrolled mat sample was put into ethanol to prepare a sonicated suspension. A drop of this suspension was cast on lacey carbon film-coated copper micro-grids. After drying, these grids were then used for structural investigation using a transmission electron microscope (HRTEM) of Philips CM12, equipped with a high resolution objective stage, operating at 120 kV, and providing a point resolution better than 0.3 nm, the coefficient of spherical aberration being 1.35 mm. The images were digitized in the size of 256×256 pixels with a pixel size of 0.03994 nm and thus atomically resolved images were possible. These images were stored in the computer after digitization and power spectra were calculated to enable detailed structural analysis in terms of interplanar distances, angle between planes etc.

2.3.4. X-ray Photoelectron Spectroscopy (XPS)

XPS measurements were carried out on a VG MicroTech ESCA 3000 instrument at a pressure of $>1 \times 10^{-9}$ Torr (pass energy of 50 eV, electron takeoff angle 60^{o}, and overall resolution ~1 eV using monochromatic Mg Kα (source, $h\nu = 1253.6$ eV). The core level spectra of the C1s and S2p orbitals were recorded with an overall instrumental resolution of ~1 eV. The alignment of binding energy (BE) was carried out using Au 4f BE of

84 eV as the reference. The X-ray flux (power 70 W) was kept deliberately low to reduce the beam-induced damage. The Spectra were fitted using a combined polynomial and Shirley type background function [19,20].

2.3.5. Thermogravimetric and Differential Thermal Analysis (TG-DTA)

Inadvertent impurities like amorphous carbon and metallic residues can be easily traced out by using TG-DT measurements. About 2-3 mg of the nanotube sample was heated in pure oxygen in order to detect the purity of the sample. TG-DT analysis was carried out on a Perkin-Elmer TGA 7 thermal analyzer by heating about 5 mg of carbon sample from 50 ^{o}C to 900 ^{o}C at a rate of 10 °C/min.

2.3.6. Raman Analysis

Raman analysis is a fundamental tool to understand the surface defects and electronic structure of nanotubes, where the tangential mode (G-band) and defect mode (D-bands) of vibrations change systematically after surface functionalization. Accordingly, Raman analysis of scroll sample was performed on a Witec GMBH confocal Raman spectrometer using 532 nm green laser in order to obtain valuable information regarding defects and the extent of graphitization.

2.3.7. Conductivity Measurements

Electrical conductivity measurement was performed along 1cm^2 thin film of "as grown" sample using KEITHLY 220 Programmable current source and KEITHLY 181 Nanovoltmeter coupled with an OXFORD Intelligent temperature controller ITC-4. A thin film of sample was made by drop-coating on a glass slide after making a good dispersion in toluene and the four point electrical conductivity was measured as a function of temperature.

2.3.8. Electrochemical Measurements

All the electrochemical measurements were carried out in 0.1 M H_2SO_4 using a standard three electrode cell comprising modified glassy electrode (3 mm) as the working electrode, a Pt wire as counter electrode and Hg/Hg_2SO_4 as a reference electrode. Cyclic voltammetric experiments were performed on an Autolab PGSTAT30 (ECO CHEMIE) instrument, whereas electrochemical impedance measurements were carried out in an impedance analyzer (Autolab PGSTAT 30 with FRA software). The ac signal amplitude was 10 mV, and the frequency range employed was 0.1 Hz–25 kHz and the data recorded with averaging over five cycles for each frequency.

2.4. Results and Discussion

2.4.1. FESEM / EDX

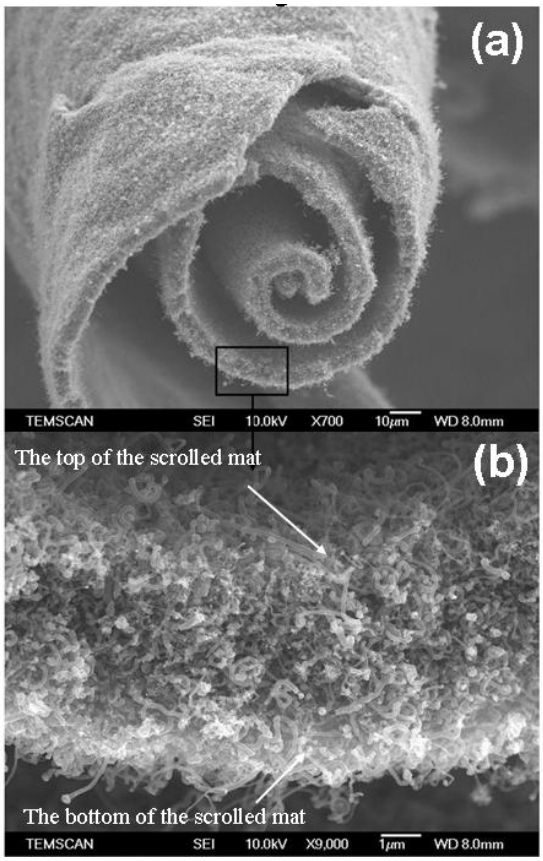

Figure 2.2. (a) Low resolution scanning electron micrographs of "as synthesized" scrolls of MWCNTs, clearly indicating the thickness of 6-7 microns; **(b)** SEM of the magnified portion of (a) that shows plenty of MWCNTs.

Figure 2.2(a-b) shows a comparison of low-resolution SEM images of as-synthesized scrolls of MWCNTs with an average thickness of 6-7 μm for the mats mounted on a copper substrate using a conducting carbon tape.

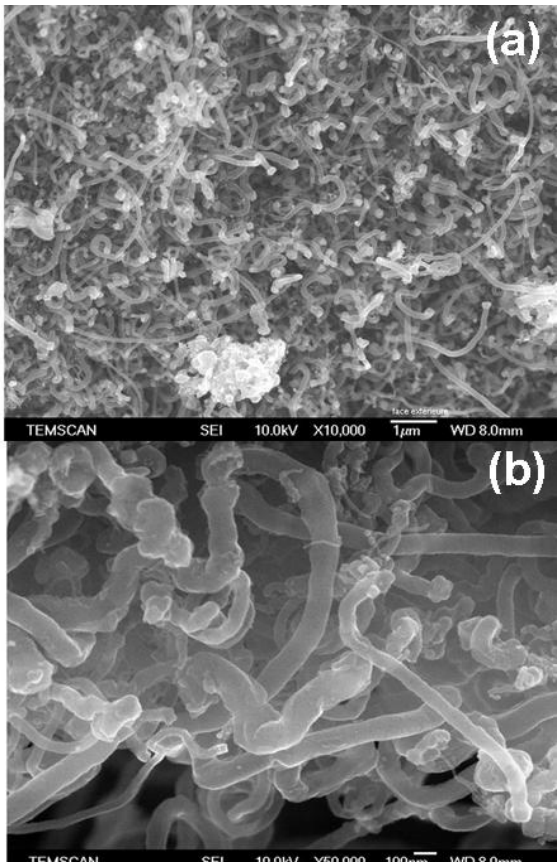

Figure 2.3. FESEM images of the multi-wall carbon nanotubes located **(a)** at the bottom surface of the scrolled mat **(b)** at the bottom of the scrolled mat cross-section which exhibits a larger diameter distribution as a result of thermal expansion effect.

Figure 2.2(b) is a magnified cross-sectional image of the edge of the scrolled mat, where both the bottom and top portion of the mats have been indicated. The curvature effect has been clearly seen as a consequence of the variations of diameter differences in the diameter distribution at top and bottom of the mat. Figure 2.3 and 2.4 are Field emission scanning electron microscopy (FESEM) images of the MWCNTs located at the bottom and at the top of the scrolled mat. Interestingly, these figures show a variation in the MWCNT diameter distribution between the bottom and the top of the mat (compare Figures 2.3(a) and 2.4(a) respectively). A large dispersion in outer diameter of the

MWCNTs is evident, varying generally from 10 to 150 nm either at the top or at the bottom of the scrolled mat respectively. However, it appears that the average diameter of the MWCNTs at the top is lower than that at the bottom. In addition, the FESEM images show that MWCNTs with large diameters are often distorted at the surface perhaps, due to dynamic temperature variations. The nut-like ends with catalyst at the tip suggests the possibility of a "top growth" mechanism (more favorable in the present case) and the formation of scrolls could be attributed to the nuclei that grew at surprisingly high growth rates.

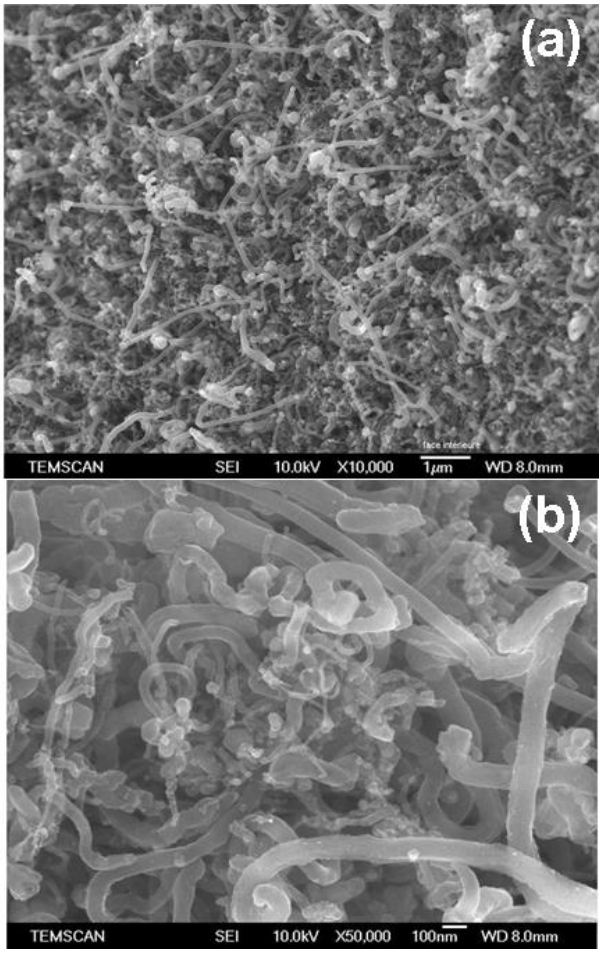

Figure 2.4. FESEM images of the MWCNTs located **(a)** at the top surface of the scrolled mat and **(b)** at the top of the scrolled mat cross-section which exhibit a relatively smaller diameter distribution as a result of decreased thermal expansion effect.

Also, the dynamic temperature conditions might play an important role during the synthesis in order to extend it into large microstructures with concomitant scrolling effects. The catalyst particles involved in the process also determine the cross section of the individual nanotubes in the microstructure. For example, the Oberlin model suggests that carbon diffuses over the surface of metal catalyst and forms a tubular structure from the circumference of the catalyst [20].

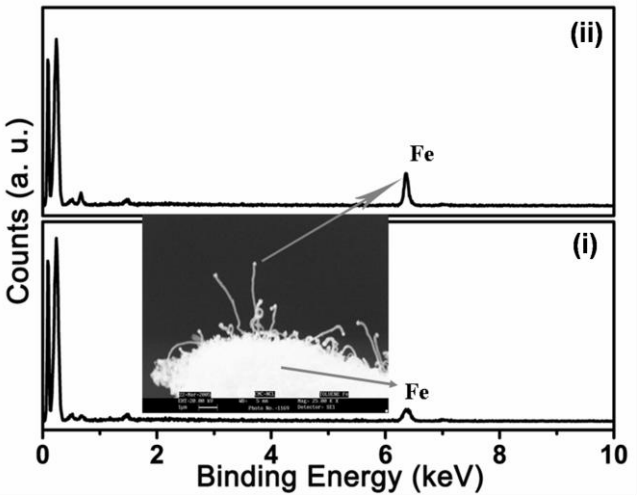

Figure 2.5. EDX spectrum of scrolls of MWCNTs indicating **(i)** low Fe content all over the sample and **(ii)** comparatively higher concentration of Fe at the tip of nanotubes revealing "top growth" mechanism.

Further, EDX analysis reveals the presence of Fe (less than 2 wt %) all over the surface of scrolls except at the tip, wherein an enhancement of about 6 wt %, indicates perhaps a catalyst-assisted growth (Figure 2.5). More interestingly, a closer observation of the micrographs suggests the rolling of the mat into a truncated Archimedean type of spiral scroll [21]. The mechanism of formation of such type of scrolls could be well understood by comparing it with similar results in a report on jelly-like wrapping of a single graphene sheet into a nanotube resulting in the formation of carbon nanoscrolls (CNSs) [21]. The mechanism could also be compared with that proposed for rolling of SWCNT bundles into carbon nanorings based on growth-induced stress between the outer and inner nanotubes inside the bundles [22].

2.4.2. TEM

Figure 2.6(a) depicts the low-resolution TEM image of as-synthesized MWCNTs after ultrasonication in toluene for 10 min. A detailed investigation of this image reveals a comparatively wide diameter distribution of MWCNTs (10-150 nm). However, these MWCNTs exhibit always a central tube with a diameter ranging from 4 to 50 nm. Generally, the diameter of the inner tube varies locally within the same MWCNT**.** These images also reveal that some of the nanotubes contain Fe nanoparticles at the tip in addition to their presence in the walls of few other tubes.

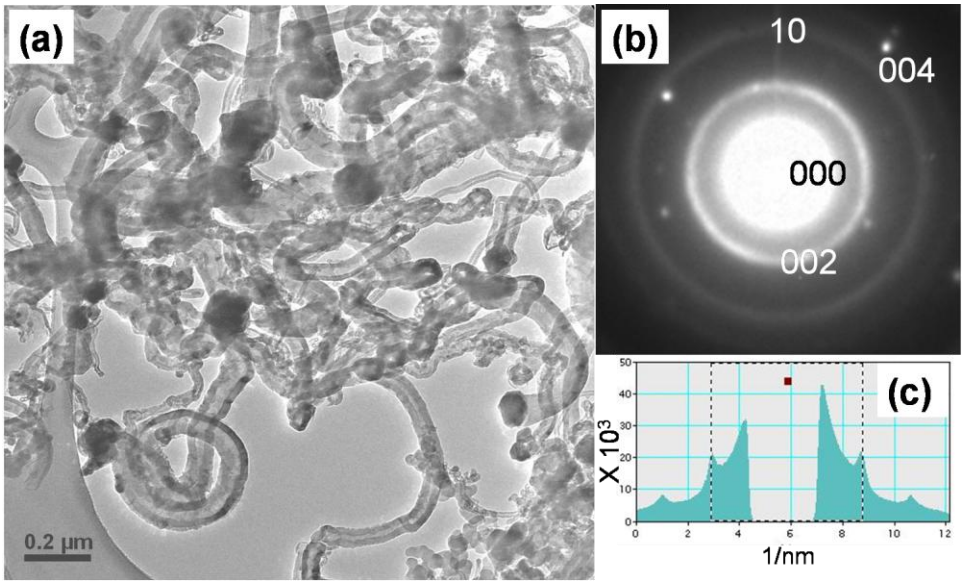

Figure 2.6. (a) Low resolution transmission electron micrographs of MWCNTs in scrolls with a wider outer diameter distribution, where catalyst particles are abundantly present, **(b)** selected area electron diffraction (SAED) pattern showing the turbostratic structure of the MWCNTs forming the scrolled mats, and **(c)** profile of the single MWCNT exhibiting interplanar distance of 0.34 nm, corresponding to the graphitic (002) plane.

The purity of the sample is found to be relatively high based on TEM observations by scanning almost every region of the sample on the copper grid. Although, catalyst particles have appeared throughout the sample, the extent of graphitization is observed to be unusually high. Selected area electron diffraction (SAED) pattern (Figure 2.6(b)) clearly shows a reflection at (002) lattice plane consistent with the interlayer graphitic distance of 0.34 nm and supports the idea of co-axial as well as the

familiar herringbone texture (more precisely stacked cone geometry) of graphitic tubules [23]. However, other reflections are rather insignificant, which could be due to the smaller number of effective graphene layers that give rise to *hk0* reflections, corresponding to turbostratic characteristics. In other words, they also exhibit 10 and 11 bands in addition to the 002 and 004 reflections.

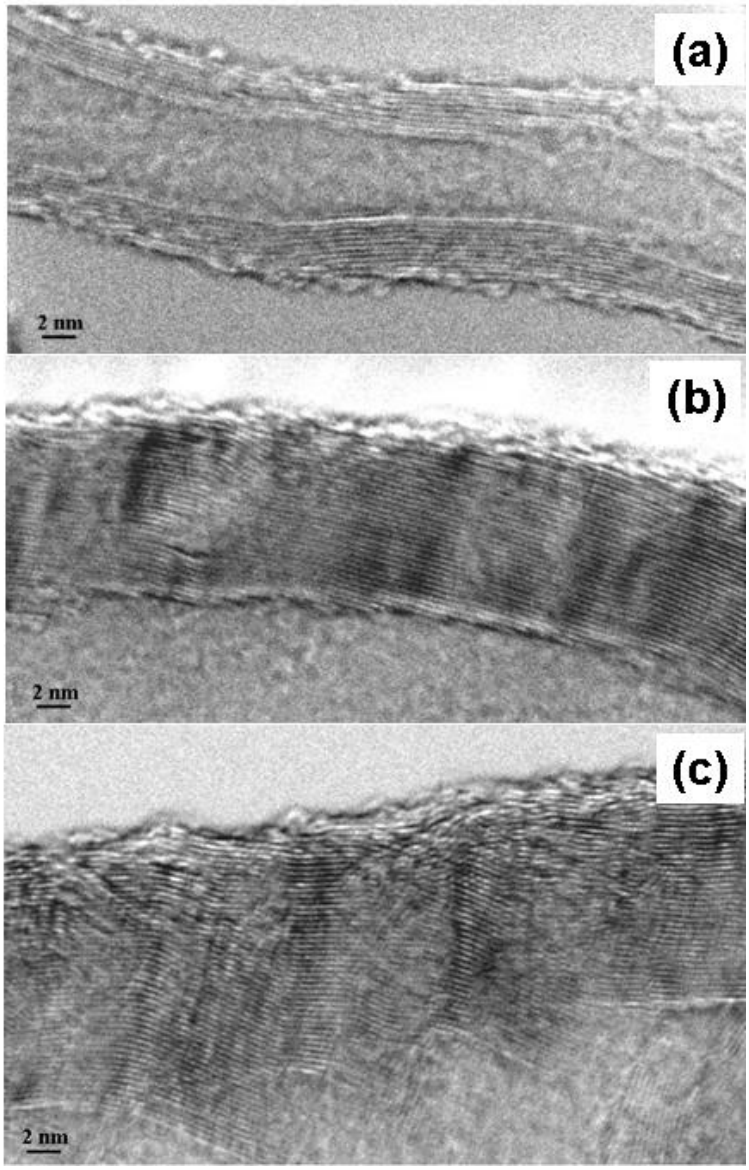

Figure 2.7. (a-c) HRTEM images showing herringbone texture (more precisely stacked cone geometry) of the MWCNTs forming the scrolled mat.

The presence of the 004 reflections shows that the MWCNTs are of a good nanotextural quality. The 002 reflection appear as circles instead of being narrow arcs because the MWCNTs are randomly oriented on the copper micro-grid. This also suggests that, the scrolls are formed by herringbone structure “carbon nanotubes" and not "nanofibers”, which is confirmed by the TEM analysis after high temperature annealing (1000 ^{o}C in argon).

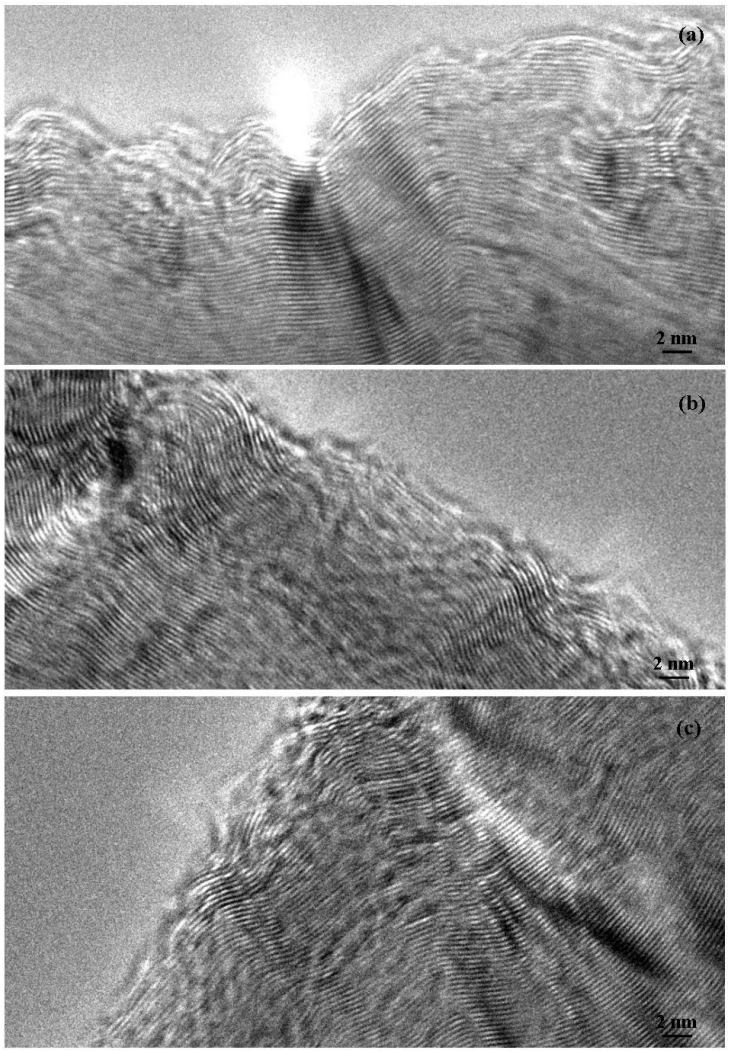

Figure 2.8. (a-c) HRTEM micrographs showing the distortion of the graphenes close to the large diameter MWCNT surfaces.

HRTEM investigation (Figure 2.7(a-c)) shows that majority of the MWCNTs exhibit a herringbone texture in which all graphenes are oblique to the tubular axis. The

angle between the graphene orientations and the nanotube axis is generally small and is of about ~5-10° indicating that the MWCNT surfaces are constituted of successive and free graphene edges. However, no significant difference has been observed between the bottom and the top of the MWCNTs according to the graphene display.

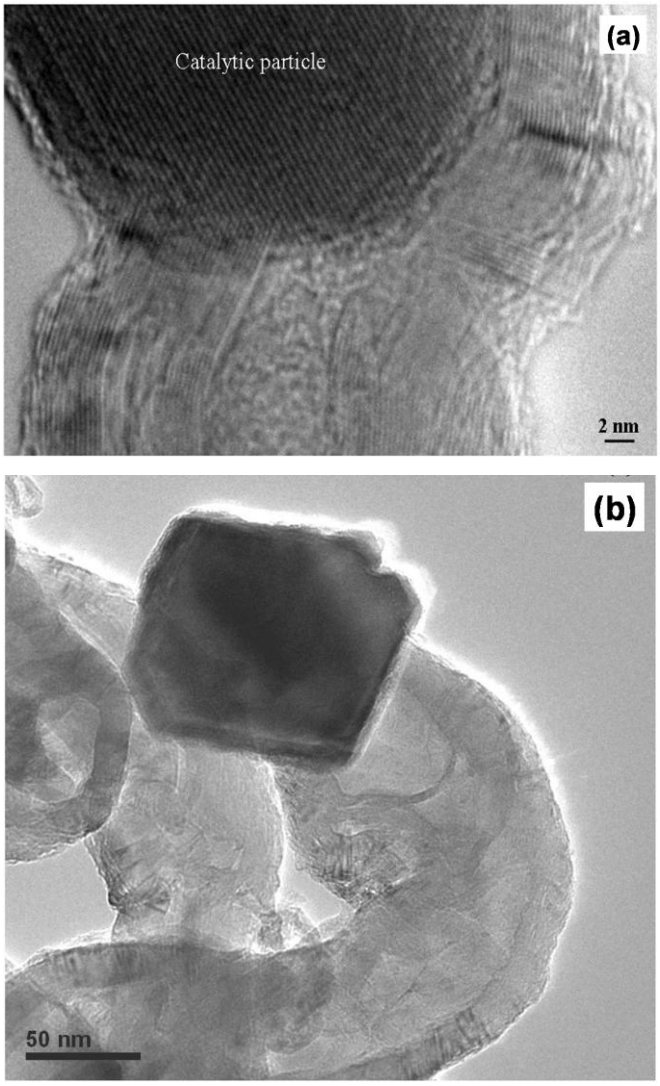

Figure 2.9. (a) Lattice fringes of the catalyst particles located at the MWCNT tips; catalyst particles are not facetted for MWCNTs exhibiting ~20 nm in diameter; **(b)** TEM images of the catalyst particles located at the MWCNTs tips; catalyst particles are facetted for MWCNTs exhibiting ~120 nm in diameter.

On the other hand, HRTEM images in Figure 2.8(a-c) clearly reveal the distortion of the graphenes close to the larger diameter MWCNT surfaces. Interestingly, catalyst particles

contributing to the growth of the large diameter MWNTs (Φ > 40 nm) are generally facetted (see Figure 2.9(a)) while, those contributing to the growth of the small diameter MWNTs (Φ < 40-60 nm) are generally not as shown in Figure 2.9(b).

2.4.3. Scrolling Mechanism

Several reports are available for the synthesis of MWCNTs by CVD growth along with their distinct growth mechanism [8-13,24]. It has often been observed that the, key parameters in nanotube growth by CVD are the hydrocarbon, catalyst and growth temperature [25]. In order to explain the scrolling mechanism two effects are presumably responsible in our experimental conditions of growth. Both effects, namely the variation in the (i) average diameter of nanotubes and (ii) thermal expansion between the top and the bottom of the mat due to temperature modulation are induced by the specific cooling step from 680 to 550 °C. Because, the initial growth of nanotubes at the bottom of mat occurs at a higher temperature than that at the top, the MWCNTs constituting the bottom exhibit higher average diameter compared to those at the top (for example, see Figures 2.3 and 2.4), since the cracking rate of the carbon species is directly proportional to the prevailing temperature. This will make the top surface of the mats smaller than the bottom surface.

On the other hand, since in the present case growth is predominantly through the tip growth mechanism, the bottom of the MWCNT mats corresponding to the growth already had taken place at the early stages, (i.e. at the highest temperature) means that the MWCNT diameters are at maximum due to thermal expansion coefficient (TEC). As long as the MWCNTs proceed towards the top of the mat corresponding to the end of the growing event, (i.e. which had occurred at the lowest temperature), these tubes could get closer and closer to each other because of the decreasing effect of TEC. Then, because the amount of tubes is obviously the same at top and at bottom of the mat, the effect of TEC upon the decreasing temperature ramp makes the top surface of the mat to be smaller inducing the scrolling effect.

HRTEM images reveal that a single atomic layer is present at the Fe surface, where it seems that a graphene sheet ends at each of these steps. Such free edges of catalyst fringes play an important role in the nucleation and growth of graphene sheets in opposite directions. An additional graphene sheet layer grows between a pair of such free edges with subsequent movement of Fe particle towards the tip. This process clearly indicates the diffusion of carbon atoms through Fe particles, leading to a tip growth mechanism.

Further, it is also important to note that, in the case of SWCNTs, the growth rate could easily be estimated since, the majority of nanotubes exhibit almost the same diameter (for example the diameter is about ~ 1.0 - 1.4 nm for SWCNTs produced by the arc discharge technique) and they are formed by only one graphene. But, in the case of MWCNTs, the growth rate depends on (1) the outer diameter, (2) the diameter of the central tube, and (3) on the MWCNT texture (graphene display). Hence it is difficult to estimate the MWCNT growth rate in our reactor because the nanotubes constituting the scrolled mat are very heterogeneous either according to the outer diameter (which vary from 10 to 150 nm) or according to the diameter of the central tube (which vary from 4 to 50 nm). This also depends on the number and the length of graphenes forming the nanotubes walls (see HRTEM- Figure 2.7).

A better understanding of the role played by various process parameters in controlling the morphology can be obtained by an accurate comparison of yields under different conditions (i.e., carrier gas flow, temperature of the preheater zone, flow rate of precursors and deposition temperature). In the present case, we have employed the process after keeping all parameters constant except the temperature of the main zone, where a gradual decrease in the temperature (8^{o} C/min) could cause enormous variations in the time scales of various processes. Although, a smaller process time (usually few milliseconds) is required for product formation when compared to the overall processing time (few minutes in the present case), it is difficult to comment on the rate-controlling step, since the system is under a continuous temperature ramp, rather than at a constant temperature. The scrolls would have been formed within few milliseconds and at a temperature well above the graphitization point.

2.4.4. XRD Analysis

X-ray diffraction studies help to clarify the graphitic nature of these scrolled samples. Accordingly, Figure 2.10 shows a very broad peak with spikes corresponding to 002 reflection of the graphene stacking (similar to polyaromatic solids) along with a small shift from its original position attributed to the tubular curvature. A slight shift in the (002) peak position ($2\theta = 26.7^{o}$) also reveals clear evidence for the increased interlayer separation in CNTs as compared to that in an ideal graphite crystal, perhaps due to turbostratic stacking of graphene sheets. Interestingly, other distinct reflections (starred positions in Figure 2.10) corresponding to both the α-Fe phase and Fe_3C (cementite phase) originating from the ferrocene although a less intense peak at 44.38^{o} could be attributed to other reflections (perhaps turbostratic 10 reflections) from carbon structure [25].

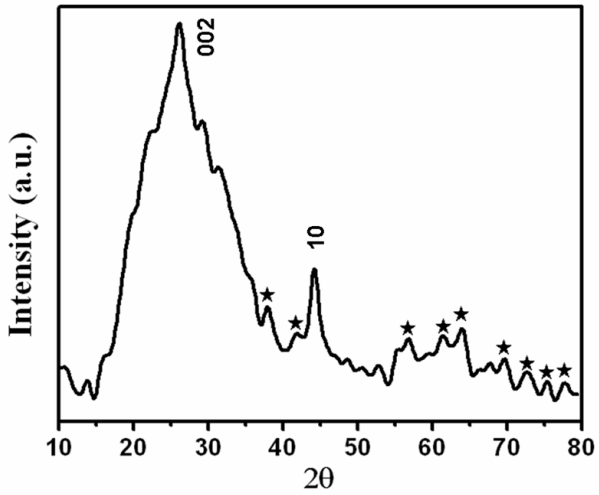

Figure 2.10. X-ray diffraction pattern of as-synthesized scrolls of MWCNTs, showing 002 reflections corresponding to graphene stacking along with all possible reflections (starred) of the Fe catalyst.

2.4.5. TG-DT Analysis

Effect of thermal treatment on the carbon scrolls is important for validating the purity of these samples [26,27]. Accordingly, Figure 2.11 exhibits the thermogram and differential thermogram of as-synthesized product in air at 10 ^{o}C/min. Initial weight loss at around 290 ^{o}C is attributed to adsorbed water or molecular oxygen, whereas, the one at 680 ^{o}C

could be attributed to the actual decomposition of carbon. However, the observed decomposition temperature of carbon is still presumably lower than that of the MWNTs (700 ^{o}C) [26], although greater than that of SWCNT (550 ^{o}C) prepared by the CVD method [27]. This sharp and distinct single weight loss at 680 ^{o}C suggests a clear evidence for negligible amorphous carbon content in the as-synthesized sample. In addition, a final residue of only ca. 1-2 wt%, corresponding to the Fe catalyst, demonstrates the relative purity of the sample, reported to date [28].

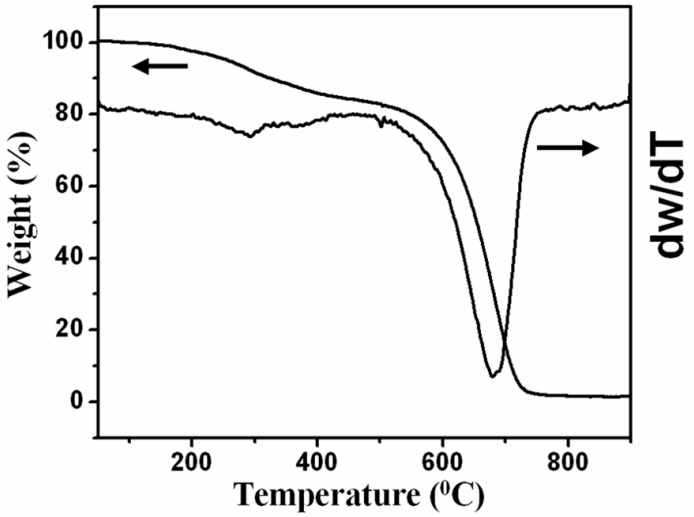

Figure 2.11. Superimposed TG/DT curves of as-synthesized scrolls of MWCNTs performed in air atmosphere at the rate of 10 ^{o}C/min.

2.4.6. XPS Analysis

The presence of surface functionalities on the "as-synthesized" carbon sample is confirmed by XPS analysis especially when the results are compared with those available for MWCNTs. Accordingly, Figure 2.12 shows the XP spectrum of as-synthesized carbon sample where, the C 1s spectrum has been (Figure 2.12(a)) deconvoluted to four peaks; a major peak at 284.6 eV is assigned to C-C bonds [29] while three minor contributions at 286.8, 288.0 and 290.8 eV could be attributed to the carbon atoms attached to oxygen atoms in three different environments such as -C-OH, -C=O and -COOH. Minor contributions from three different oxygen functionalities as compared to the major C-C peak also supplement the results of the TG studies (only 15% weight loss),

revealing the presence of oxygenated functional groups generated during the synthesis. The oxygen spectra also give four peaks (Figure 2.12b) after a similar fitting procedure; a peak at a binding energy of 531.6 eV corresponds to the double bonded oxygen (like –C=O group) while another peak at 533.1 eV could be attributed to single bonded oxygen atom (like –C-OH). Similarly, two peaks at 534.6 and 536.7 eV could be attributed to the presence of adsorbed moisture and oxygen respectively [30].

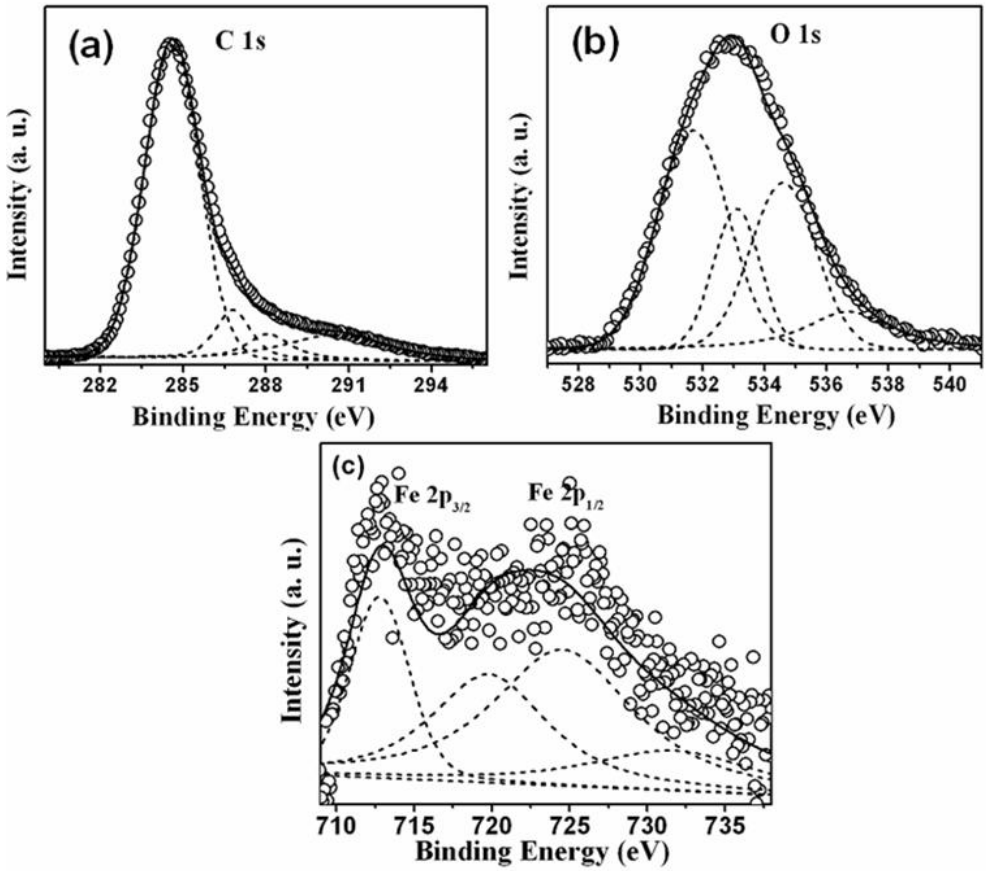

Figure 2.12. X-ray photoelectron spectra of **(a)** C 1s **(b)** O 1s and **(c)** Fe $2P_{3/2,1/2}$ core levels of 'as synthesized' carbon sample; the circles represent the experimental data, thick lines represent the fitting data for overall signal and the dotted lines are the deconvoluted individual peaks for different species in the sample.

In addition, two low intensity peaks for Fe (Figure 2.12c) corresponding to core level $2p_{3/2}$ and $2p_{1/2}$ are observed at 712.8 and 724.5 eV respectively with a peak separation of 11.7 eV, which is in close agreement with the data in earlier reports [31-32]. The binding energy of 711.8 eV corresponding to the $2p_{3/2}$ peak is consistent with typical

values for ferric oxide with a slight shift towards the higher energy region [33]. Interestingly, both the main peaks ($2p_{3/2}$ and $2p_{1/2}$) show their satellite peaks on their higher binding energy side with an energy separation of 7.7 and 9.0 eV respectively, which could be due to systematic variations in the hybridization of Fe 3d and O 2*p* levels as well as due to the d-d electron correlation energy [34].

2.4.7. Raman Analysis

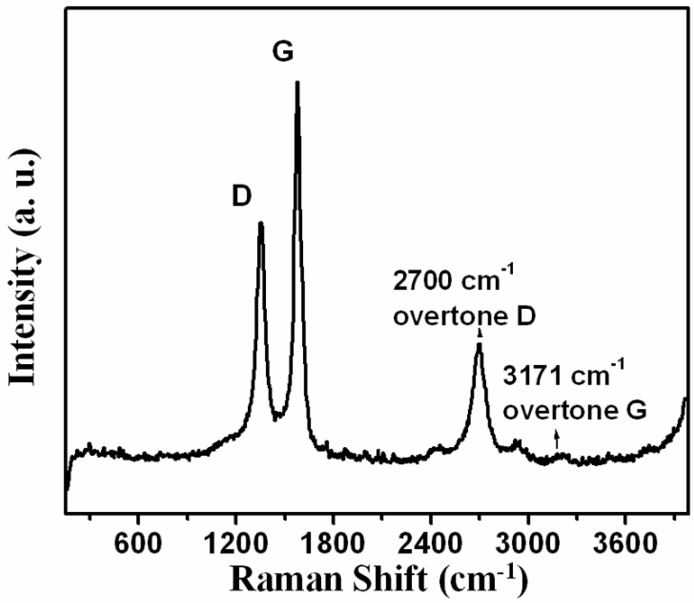

Figure 2.13. Raman spectrum of as grown sample taken using an argon ion laser with wavelength of 514.5 nm, which clearly shows distinct D and G bands corresponding to defect induced double resonant scattering and ordered graphitic carbon.

In order to interrogate the defect sites present on the "as synthesized" carbon sample, Raman studies have been performed using a 514.5 nm argon ion laser for excitation. Most of the graphitic materials show a sharp and distinct band at 1350 cm^{-1} (D band), which is perceptible in accordance with some defect-induced double resonant Raman scattering [25]. Figure 2.13 exhibits the Raman spectra of as synthesized scrolls of CNTs, which show two characteristic peaks at 1350 cm^{-1} and 1572 cm^{-1} corresponding to D and G bands respectively. The intensity ratio I_D/I_G could be used to diagnose wall-defects and disorder in the graphitic structure. For example, a comparatively larger I_D/I_G

(~0.85) indicates more strain on the sidewalls of CNTs as compared to that of ideal defect-free CNT, which is in agreement with the observations from XRD studies. Although, the D band depends on the number of defects and quality of the nanotubes, even higher quality tubes show a sharp and strong D band [31,35]. In addition, Raman peaks at 3152 and 2700 cm^{-1} correspond to the combination bands (overtones) due to D with G and D with D bands respectively.

2.4.8. Conductivity Measurements

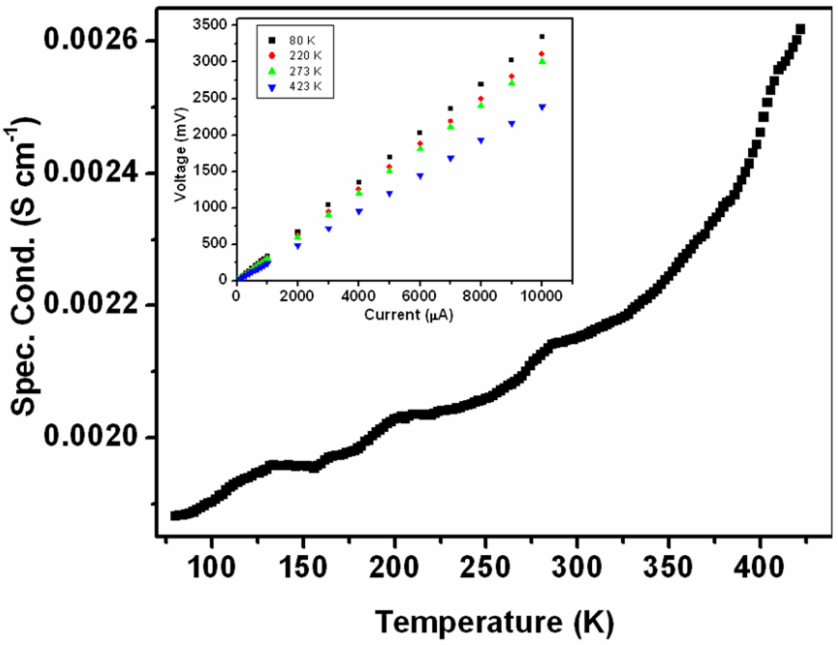

Figure 2.14. Conductivity variations with temperature suggest a semiconducting behavior of mats of MWCNTs; inset shows linear I-V curves at different temperatures exhibiting ohmic contact throughout the measurements.

Figure 2.14 exhibits the variation of dc conductivity with temperature for these samples and the decrease in resistivity from 531 Ω cm to 380 Ω cm corresponding to 80 to 423 K undoubtedly indicating the semiconducting behavior. The reproducibility has been verified by repeating the experiment more than five times. The important parameter of the I-V measurements is the ohmic contact, which has been confirmed by carrying out I-V measurements at different temperatures as shown in the inset of Figure 2.14. In

addition, the variation of conductivity with temperature exhibits two distinct slopes revealing a two-step electron transfer mechanism. An initial gradual increase in the conductivity up to 310 K gives the activation energy of about 0.33 meV, followed by a sudden increase in the conductivity (intrinsic part). The lower value of activation energy perhaps suggests the reduced effect of Coulomb blockade with smaller number of multiple islands as explained by Ruzin et al. [36]. Further, the observed values of activation energies are slightly lower compared to the reported values for single SWCNT measured using multiprobe electrodes, which could be explained on the basis of a multiple island model [37]. Films of MWCNTs, in comparison, reveal slightly higher activation energy attributed, perhaps, to both contributions of activation barrier and tunneling band gap [38]**.** Interestingly, extrapolation of conductivity data from Figure 2.13 to absolute zero gives a value of 1.8×10^{-3} Scm^{-1} suggesting a very high carrier concentration although it might have unknown contributions from adsorbed moisture and intertubular tunneling band gap.

2.4.9. Electrochemical Measurements

Figure 2.15 shows superimposed cyclic voltammograms of "as-grown" scrolled carbon sample (thick line), after 100 cycles (dashed line) along with that of blank glassy carbon electrode (dotted line) at 0.1 V/s scan rate in 0.1 M H_2SO_4. A quasi-reversible redox peak at -0.372 V (anodic scan) and -0.553 V (cathodic scan) is attributed to the redox behavior of the Fe catalyst present in the "as synthesized" sample. Interestingly, an initial Fe content of ca. 0.1% (as inferred from area under the anodic peak) has been found to decrease upon cycling, as shown in dashed line of Figure 2.15, indicating an irreversible etching of Fe.

A prominent cathodic peak, even after 100^{th} cycle, reveals the diffusion of reduced species from the solution, whereas, reduced anodic peak suggests an irreversible dissolution of Fe, eventually capable of making Fe-free carbon sample. A minor reversible peak observed at -0.045 V and -0.075 V respectively in both the cases, is perceptible to the generation of oxygenated functional groups [39] on the side walls

during cycling. The capacitance of this sample is estimated to be ~3 F/g, which is comparable to that of graphitized carbon black (~6 F/g) [40].

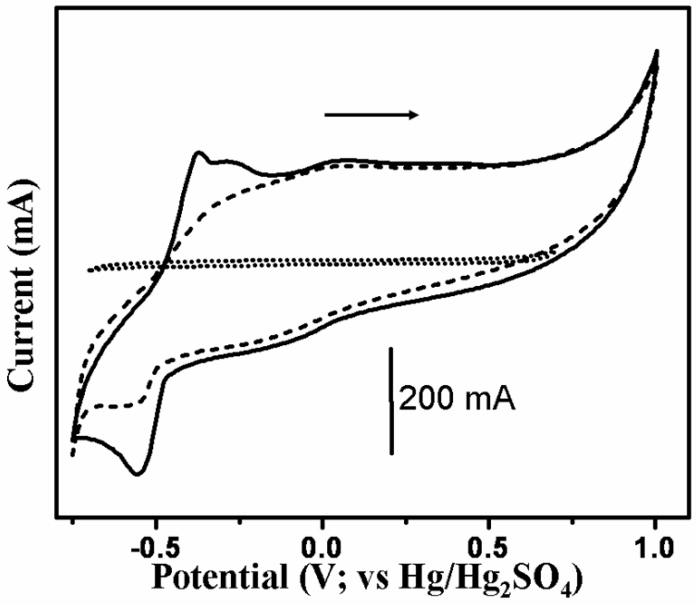

Figure 2.15. Superimposed cyclic voltammograms of scrolled carbon sample (thick line), carbon sample after 100 cycles (dashed line) and blank glassy carbon electrode (dotted line) at 0.1 V/s scan rate in 0.1 M H_2SO_4.

Figure 2.16 shows the superimposed complex plane impedance plots of scrolled carbon sample (**O**) and that of CNTs purified in nitric acid treatment for 8 hrs (Δ), where the suppressed semicircle in case of scrolled sample at the higher frequency domain is fitted to a semicircle and analyzed with Randles equivalent circuit shown in the inset of Figure 2.16. Impedance analysis of as synthesized scrolled sample suggests an initial charge transfer process at a higher frequency domain, attributable to the signature of redox active Fe in the pristine sample, which reveals a double layer capacitance of 90 $\mu F/cm^2$ and exhibits an exchange current density [i_o = RT / F Rct, where, R = gas constant; 8.314 J, T = absolute temperature, F = Faraday constant; 96500 C and Rct = charge transfer resistance deduced from diameter of fitted semicircle] of 40 $\mu A/cm^2$. Interestingly, upon oxidation in presence of 1:1 HNO_3 solution for 8 hrs, the scrolled carbon sample exhibits a curve almost parallel to the imaginary (-Z") axis in the complex plane impedance plot, indicating the removal of catalyst with concomitant enhancement

in its capacitance. The combined analysis of electrochemical results suggests an enhancement in the capacitive feature of scrolled carbon sample after an irreversible etching of Fe during several cycling or due to oxidative treatment prior to measurements.

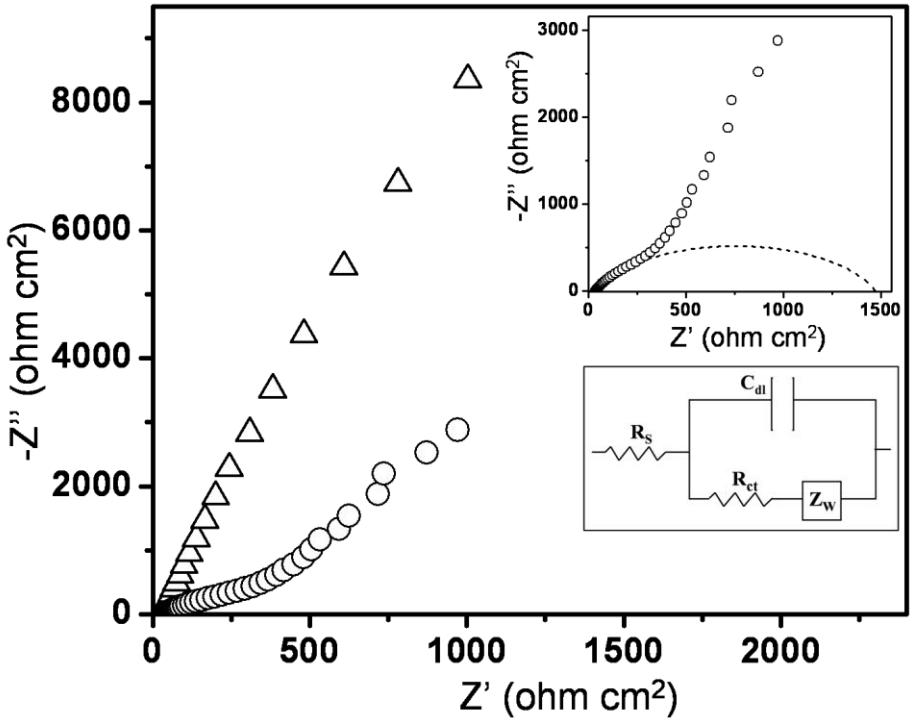

Figure 2.16. Superimposed complex plane impedance plots of scrolled carbon sample (**O**) and that of after nitric acid treatment for 8 hrs (Δ), where the suppressed semicircle in case of scrolled sample at the higher frequency domain is fitted to a semicircle and analyzed with Randles equivalent circuit shown in the inset (where, Rs: solution resistance, Cdl: double layer capacitance, Rct: charge transfer resistance and Zw: warburg impedance).

A tentative mechanism of "top growth" of MWCNTs could be proposed based on the above evidences. The low catalyst content in the product suggests a growth mechanism in which initial few nucleation sites cause a continuous growth resulting into large microstructure of scrolls. The formation of these types of scrolls could be well understood by comparing it with the carbon nanoscrolls (CNSs) [21], which might be produced by the jelly-like wrapping of a single graphene sheet into a nanotube. There are two conflicting parameters like the elastic energy increase due to bending of sheet and the van der Waals interaction energy between overlapping regions of the sheet governing the formation of CNSs. In case of scrolls of MWNTs, the intertubular interaction (due to the

decreasing effect of temperature expansion coefficient with time) would play an important role in enhancing the stability of the rolled structure. Usually two growth mechanisms have been proposed previously for the nanotube growth in CVD process, viz. 'top growth' and 'root growth', where, the latter mechanism has been well studied in case of both SWCNTs and MWCNTs [41] although the former one has been well demonstrated for certain MWCNTs [42]. In the present case, a 'top growth' is preferentially demonstrated based on electron microscopic analysis, where the presence of Fe at the tip of few tubes clearly supports the growth hypothesis.

2.5. Conclusions

MWCNTs in the form of micron sized felt-like mats have been synthesized from a mixture of toluene and ferrocene using a temperature ramp from 680 °C to 550 °C under a hydrogen - argon atmosphere. Since the properties of carbon nanostructures depend on the local reaction temperature, it is possible to tune their morphology by this simple approach of using a controlled temperature gradient. These experimental conditions would result in high yield and pure MWCNTs in the form of thick scrolls, despite higher interlayer separation than that in graphite. High-resolution electron microscopy investigations show that the majority of the MWCNTs exhibit the herringbone texture along with concentric tubules. Thermal expansion effects could help to explain a tentative mechanism for rolling action of sheets, although it is rather difficult to comment on the rate controlling process for the scroll formation due to a continuous decrease in the temperature. A relatively high value of the intensity ratio of D and G bands in the Raman signals suggests that the walls of the nanotubes within the scrolls are more strained compared to those of ideal defect free nanotubes. Low temperature dc conductivity however, show that the carbon sample is semiconducting while cyclic voltammetric and electrochemical impedance results reveal a redox behavior of 0.1% Fe content which can be etched out irreversibly by cycling for 100 cycles or by an extensive acid treatment.

2.6. References

1. Iijima, S. *Nature* **1991,** *354*, 56.
2. Baughman, R. H.; Zakhidov, A. A.; Heer, W. A. *Science* **2002**, *297*, 787.
3. Heer, W.A.; Chatelain, A.; Ugarte, D. A. *Science* **1995**, *270*, 1179.
4. Shim, M.; Javey, A.; Kam, N.; Dai, H. J. *J. Am. Chem. Soc*. **2001**, *123*, 11512.
5. Wang, Q. H.; Sethur, A. A.; Lauerhaas, J. M.; Dai, J. Y.; Seeling, E. W.; Chang, R. P. *Appl. Phys. Lett.* **1998**, *72*, 2912.
6. Rueckes, T.; Kim, K.; Joselevich, E.; Tseng, G. Y.; Cheung, C.L.; Lieber, C. M.; *Science* **2000**, *289*, 94.
7. Hafner, J. H.; Cheung, C. L.; Woolley, A.T.; Lieber, C. M.; *Prog. Biophys. Mole. Biol.* **2001**, *77*, 73.
8. Singh, C.; Shaffer, M.; Kinloch, I.; Windle, A. *Physica B: Condensed Matter* **2002**, *323*, 339.
9. Dai, H.; Kong, J.; Zhou, C.; Franklin, N.; Tombler, T.; Cassell, A; Fan, S.; Chapline, N. *J. Phys. Chem. B* **1999,** *103*, 11246.
10. Andrews, R.; Jacques, D.; Rao, A. M.; Derbyshire, F.; Qian, D.; Fan, X.; Dickey, E. C.; Chen, J. *Chem. Phys. Lett.* **1999**, 303, 467-474.
11. Delzeit, L; Nguyen, C.V.; Chen, B.; Stevens, R.; Cassell, A.; Han, J.; et al. *J. Phys. Chem. B* **2002,** *106*, 5629.
12. Hoffmann, S.; Ducati, C.; Robertson, J.; Kleinsorge, B. *Appl. Phys. Lett.* **2003**, *83*, 135.
13. Singh, C.; Shaffer, M. S.; Kozial, K. K.; Kinloch, I. A.; Windle, A. H. *Chem. Phys. Lett.* **2003**, *372*, 860.
14. Ajayan, P. M.; Nugent, J. M.; Siegel, R. W.; Wei, B.; Kohler-Redlich Ph, *Nature* **2000**, *404*, 243.
15. Blanck, V. D.; Polyakov, E. V.; Kulnitskiy, B. A.; Nuzhdin, A. A.; Alshevskiy, Y. L.; Bangert et al., *Thin Solid Films* **1999,** *346*, 86.
16. Ugarte, D. *Nature* **1992**, *359*, 707.
17. Motojima, S.; Kawaguchi, M.; Nozaki, K.; Iwanaga, H. *Appl. Phys. Lett.* **1990**,

56, 321.

18. Huang, S.; Woodson, M.; Smalley, R.; Liu, J. *Nano Lett.* **2004**, *4*, 1025.
19. Shirley, D. A. *Phys. Rev. B* **1972,** *5*, 4709.
20. Oberlin, A.; Endo, M.; Koyama, T. *J. Crystal Growth* **1976**, *32*, 335.
21. Braga, S. F.; Coluci, V. R.; Legoas, S. B.; Giro, R.; Galvao, D. S.; Baughman, R. H. *NanoLetters* **2004**, *4*, 881.
22. Song, L.; Ci, L.; Sun, L.; Jin, C.; Liu, L.; Ma, W.; et al. *Adv. Mater.* **2006**, *18*, 1817.
23. (a) Endo, M.; Kim, Y. A.; Hayashi, T.; Fukai, Y.; Oshida, K.; Terrones, M.; Yanagisava, T.; Higaki, S.; Dresselhaus, M. S. *Appl. Phys. Lett.* **2002**, *80*, 1267. (b) Sun, X. ; Li, R. ; Stanfield, B.; Dodelet, J. –P.; Menard, G.; Deslites, S. *Carbon* **2007**, *45*, 732. (c) Monthoux, M. ; Noe, L. ; Dussault, L. ; Dupin, J. -C. ; Latorre, N. ; Ubieto, T. ; Romeo, E. ; Royo, C. ; Monzon, A. ; Guimon, C. *J. Mater. Chem.* **2007**, *17*, 4611.
24. (a) Fan, S.; Chapline, M.; Franklin, N.; Tombler, T.; Cassell, A.; Dai, H. *Science* **1999**, *283*, 512. (b) Endo, M. ; Takeuchi, K. ; Igarashi, S. ; Kobori, K. ; Shiraishi, M. ; Kroto, H. W. *J. Phys. Che. Solids* **1993**, *54*, 1841. (c) Zhu, L. B.; Xiu, Y. H.; Hess, D. W.; Wong, C. P. *Nano Lett.* **2005**, *5*, 2641. (d) Allouche, H.; Monthioux, M.; Jacobsen, R. L. *Carbon* **2003**, *41*, 2897. (e) Allouche, H.; Monthioux, M. *Carbon* **2005**, *43*, 1265. (f) Li, W. Z.; Xie, S. S.; Qian, L. X.; Chang, B. H.; Zou, B. S.; Zhou, W. Y.; Zhao, R. A.; Wang, G. *Science* **1996**, *274*, 1701. (g) Pan, Z.; Xie, S S.; Chang, B.; Wang, C. *Nature* **1998**, *394*, 631. (h) Ren, Z. F.; Huang, Z. P.; Xu, J. W.; Wang, J. H. *Science* **1998**, *282*, 1105. (i) Nasibulin, A. G.; Queipo, P.; Shandakov, S. D.; Brown, D. P.; Jiang, H.; Pikhitsa, P. V.; Tolochko, O, V.; Kauppinen, E. I. *J. Nanosci. Nanotechnol.* **2006**, *6*, 1233. (j) Meng, G.; Jung, Y. J.; Cao, A.; Vajtai, R.; Ajayan P. M. *Proc. Am. Chem. Soc.* **2005**, *102*, 7074. (k) Xiang, R.; Yang, Z.; Zhang, Q.; Luo, G.; Qian, W.; Wei, F.; Kadowaki, M.; Einarsson, E.; Maruyama, S. *J. Phys. Chem. C*. **2008**, *112*, 4892. (l) Andrews, R.; Jacques, D.; Qian, D.; Rantell, T. *Acc.*

Chem. Res. **2002**; *35,* 1008. (m) Peng, H.; Jain, M.; Li, Q.; Peterson, D. E.; Zhu, Y.; Jia, Q. *J. Am. Chem. Soc.* **2008**; *130*, 1130. (n) Zhang, Z.; Wei, B. Q.; Ramanath, G.; Ajayan, P. M. *Appl. Phys. Lett.* **2000**, *77*, 23. (o) Wei, B. Q.; Vajtai, R.; Jung, Y.; Ward, J.; Zhang, R.; Ramanath, G.; Ajayan, P. M. *Nature* **2002**, *416,* 495. (p) Li, X.; Cao, A.; Jung, Y. J.; Vajtai, R.; Ajayan, P. M. *Nano Lett* **2005,** *5,* 1997. (q) Dai, H. *Phys. World* (**2000**). (r) Cojocaru, C. S. ; Larijani, M. ; Misrea, D. S. ; Singh, M. K.; Veis, P.; Le Noramnd, F. *Diamond and Realted Materials* **2004**, *13*, 270. (s) Cojocaru, C. S.; Senger, A.; Le Normand, F. *J. Nanosci. Nanotechnol.* **2006**, *6*, 1331. (t) ren, W.; Li, F. ; Bai, S. ; Cheng, H. –M. *J. Nanosci. Nanotechnol.* **2006**, *6*, 1339.

25. (a) Dresselhaus, M. S.; Dresselhaus, G.; Avouris, Ph. (Eds.) *Carbon Nanotubes Synthesis, Structure, Properties and Applications* (Springer-Verlag Berlin Heidelberg, Germany) **2001**. (b) Meyyappan, M. *Carbon Nanotubes, Science and Applications* (CRC press, Florida, **2004**) pp. 133
26. Lee, C. J.; Park, J. H.; Huh, Y.; Lee, J. Y. *Chem. Phys. Lett.* **2001**, *343,* 33.
27. Chiang, I. W.; Brinson, B. E.; Huang, A. Y.; Willis, P. A.; Bronikowski, M. J.; Margrave, J. L.; Smalley, R. E.; Hauge, R. H. *J. Phys. Chem. B* **2001**, *105,* 8297.
28. Murukami, Y.; Miyauchi,Y.; Maruyama, S.C.S. *Chem. Phys. Lett.* **2003**, *374,* 53.
29. Desimoni, E.; Cassella, G. I.; Morone, A.; Salvi, A. M. *Surface Interface Anal.* **1990**, *15*, 627.
30. Xie, Y.; Sherwood, P.M . A. *Applied Spectrosc.* **1989**, *43,* 1153.
31. Tan, B. J.; Klabunde, K. J.; Sherwood, P. M. A. *Chem. Mater.* **1990**, *2,* 186.
32. Langevoort, I. J. C.; Sutherland, L. I.; Hanekamp, L. J.; Gellings, P. J. *Appl. Surf. Sci.* **1987,** *28*, 167.
33. Brundle, C. R.; Chuang, T. J.; Wandelt, K. *Surf. Sci.* **1977**, *68,* 459.
34. Fujii, T.; de Groot, F. M. F.; Sawatzky, G. A.; Voogt, F. C.; Hibma, T.; Okada, K. *Phys. Rev. B* **1999**, *59*, 3195.
35. Bacsa, R. R.; Flahaut, E.; Laurent, Ch.; Peigney, A.; Aloni, S.; Puech, P. *New J. Phys.* **2003**, *5*: 131.1- 1.9.

36. Ruzin, I. M.; Chandrasekhar, V.; Levin, E. I. Glazman, L. I. *Phys. Rev. B* **1990**, *45*, 13469.
37. Bezryadin, A.; Verschueren, A. R.; Tans, S. J.; Dekker, C. *Phys. Rev. Lett.* **1998**, *80*, 4036.
38. Hu, C. G.; Wang, W. L.; Liao, K. J.; Liu, G. B.; Wang, Y. T. *J. Phys. Chem. Sol.* **2004**, *65*, 1731.
39. (a) Gong, K.; Yan, Y.; Zhang, M.; Su, L.; Xiong, S.; Mao, L. *Analytical Sciences* **2005**, *21*, 1383.. (b) Xing, Y.; Li, L.; Chusuei, C. C.; Hull, R. V. *Langmuir* **2005**, *21*, 4185. (c) Liu, J.; Rinzler, G.; Dai, H.; Hafner, J. H.; Bradley, R. K.; Boul, P. J.; Lu, A.; Iverson, T.; shelimov, K.; Huffman, C. B.; Rodriguez-Macias, F.; Shon, Y. S.; Lee, T. R.; Colbert, D. T.; Smalley, R. E. *Science* **1998**, *280*, 1253. (d) Kneller, J. M.; Soto, R. J.; Surber, S. E.; Colomer, J. F.; Fonseca, A.; Nagy, J. B.; Van Tendeloo, G.; Pietrass, T. *J. Am. Chem. Soc.* **2000**, *122*, 10591. (e) Kuznetsova, A.; Mawhinney, D. B.; Naumenko, V.; Yates, J. T.; Liu, Jr. J.; Smalley, R. E. *Chem. Phys. Lett.* **2000**, *321*, 292. (f) Hou, P. X.; Bai, S.; Yang, Q. H.; Liu, C.; Cheng, H. M. *Carbon* **2002**, *40*,81. (g) Bendjemil, B.; Borowiak-Palen, E.; Graff, A.; Pichler, T.; Guerioune, M.; Fink, J.; Knupfer, M. *Appl. Phys. A* **2004**, *78*, 311. (h) Zhang, J.; Zou, H.; Qing, Q.; Yang, Y.; Li, Q.; Liu, Z.; Guo, X.; du, Z. *J. Phys. Chem. B* **2003**, *107*, 3712.
40. (a) Kinoshita, K. Carbon: Electrochemical and Physical Properties; Wiley: New York, 1988. (b) Banks, C. E.; Davies, T. J.; Wildgoose, G. G.; Compton, R. G. *Chem Commun.* **2005**, 829 and the references therein.
41. Li, Y. M.; Kim, W.; Zhang, Y. G.; Rolandi, M.; Wang, D. W.; Dai, H. J.; *J. Phys. Chem. B* **2001**, *105*, 11424.
42. (a) Baker, R. T. K. *Carbon* **1989,** *27*, 315. (b) Sinnott, S. B.; Andrews, R.; Qian, D.; Rao, A. M.; Mao, Z.; Dickey, E. C.; Derbyshire, F. *Chem. Phys. Lett.* **1999**, *315*, 25. (c) Han, J.; Yoo, J. B.; Park, C. Y.; Kim, H. J.; Park, G. S.; Yang, M.; Han, I. T.; Lee, N.; Yi, W.; Yu, S. G. Kim, J. M. J. *Appl. Phys.* **2002**, *91*, 483.

CHAPTER 3

A Novel Route towards Covalent Functionalization of Single Walled Carbon Nanotubes*

This chapter describes an efficient phase transfer of Single-wall carbon nanotubes (SWCNTs) from aqueous to nonaqueous media using a unique amide functionalization route, where water soluble SWCNTs (2.6 mg/mL) are effectively transferred to solvents like chloroform, toluene and CS_2. A maximum of 30 wt% of oxygenated surface groups have been generated on the side walls by clean and rapid microwave treatment, leading to a solubility of more than 3 mg/mL in water. An approximate surface amine coverage of 50% has been accomplished after oxalyl chloride treatment as inferred from thermogravimetry and X-ray photoelectron spectroscopy by controlling several key parameters associated with the extent of functionalization including purity of the sample, temperature and time. A comparative surface functionalization using various amines including tridecylamine, octadecylamine and aniline has been discussed along with their unique electrochemical behavior and possible applications.

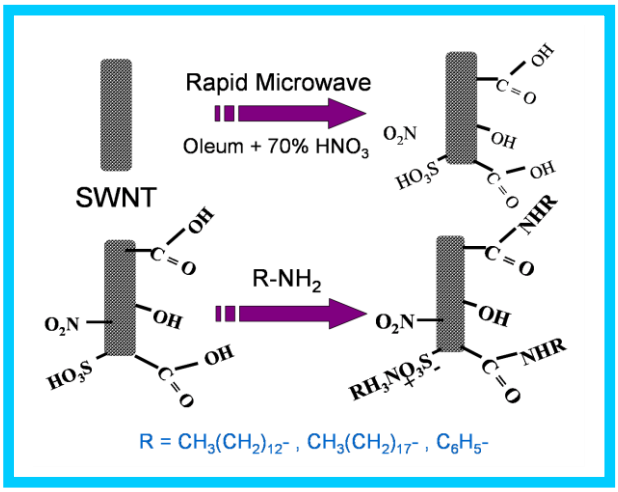

---

* A part of the work discussed in this chapter has been published in "*Appl. Surf. Sci.* **2008,** *254*, 4936"

3.1. Introduction

Recently, functionalization of single walled carbon nanotubes has attracted great interest in numerous areas of research, ranging from high-strength polymer nanocomposites [1,2], optics [3] and bio-technology [4,5] to energy storage. This is mainly because, in order to take the full advantage of potential applications of CNTs, the inert surface of nanotubes with intrinsic van der Waals forces must be overcome by linking them to appropriate molecules, which in turn, could make them more effective. Consequently, controlled chemical modification of carbon nanotubes is required for applications that are based on the specific interaction of nanotubes with other molecules. These applications include chemical sensors in the gas or liquid phase, mechanically reinforced composite materials, atomic force microscopy tips of tailored chemical sensitivity, as well as electrical contacts for biological systems like nerve cells. There are, however, several barriers which prevent many of these applications including, (1) difficulty of separating the mixtures of CNTs with different diameters, and chiralities with both metallic and semiconducting nanotubes, (2) presence of impurities like catalyst and amorphous carbon and (3) lack of solubility in common solvents as illustrated in first chapter. More importantly, the chemistry of carbon nanotubes, however, is far less developed than the chemistry of their smaller counterparts, namely the fullerenes, despite their structural similarities. Nevertheless, chemical modifications have been performed only on bulk nanotubes to date, which hardly allow any control over the degree of functionalization.

One way to alleviate these processing difficulties is by using chemical functionalization (post-synthesis chemical processing protocols) or alternatively to explore the possibility of using CNT-polymer composites where hopefully, some of the attractive features of polymer processing can be brought in. Unfortunately, many studies of polymer-CNT nanocomposites, however, reveal segregation and non-uniform mixing behavior often causing serious concerns of reproducibility in their electrical, mechanical and thermal behavior. Many composites show different types of threshold behavior in terms of change in electrical, thermal or mechanical properties with the amount of CNT and the properties of composites critically depend on the miscibility, compatibility, and

adhesion. For example, recently a remarkable *in situ* preparation of Nylon-CNT composites has been reported to show that tailoring of the CNT-polymer interfacial interaction could alter the morphology and properties [6]. However, in all these cases chemical functionalization is an essential prerequisite to get uniform properties of the composites. Thus, in order to exploit the advantages of the remarkable geometrical structure of CNT in various applications, especially in the form of many robust polymer composites, CNTs need to be solubilized or derivatized with inorganic or organic functional groups that facilitate a strong bonding and selectivity through either hydrogen or covalent bonds.

Many approaches have been tried so far to carry out chemical functionalization of carbon nanotubes. For example, the generation of surface hydrophilic substituents such as carboxylic, hydroxyl or sulphonic acid groups by a suitable chemical method is rather easy for their wide use in medical and biological applications [5,7], since these functional groups provide necessary sites for covalent or noncovalent coupling of SWCNTs. In addition, a majority of recent reports deal with a variety of chemical treatments such as fluorination [8], alkylation [9], diazotization [10,11,12] etc, for sidewall functionalization although many methods still need greater efforts in order to improve the yield and selectivity of the products. For instance, acid functionalization has been extensively explored through many oxidation routes to open the ends of SWCNTs and to develop hydrophilic functional groups [13-16]. However, several difficulties, during such treatments, would thwart their wide applications in CNT processing.

For example, for carboxylation or hydroxylation, the reaction mixture is typically refluxed in concentrated HNO_3 or acid mixture for 10-50 h, which is a tedious and time consuming process. To avoid this time consuming carboxylation of SWCNTs, recently Wang et al [16], have demonstrated a rapid functionalization using microwave (MW) radiation in presence of concentrated acid mixture under pressure. A considerably higher value of the solubility of SWCNTs (more than 2 mg/mL) has been observed in aqueous media within a period of 3 min by this approach. Although the extent of surface damage or defect creation by this process has not been analyzed critically, more studies on new functionalization methods are desired to improve our understanding on site-specific

functionalization and also to enable further accurate control. More significantly, diazotization of SWCNTs enables the separation of metallic SWCNTs from semiconducting type as illustrated by Smalley and co-workers [17a]. Also, several methods have been subsequently attempted recently to functionalize SWCNTs [18], with the primary objective of tuning their electronic properties for exploiting their potential applications along with alleviating common processing obstacles like bundling or flocculation while using the pristine form. More recent studies reveal that, the solubility of SWCNTs in water can be enhanced along with efficient exfoliation of nanotube bundles due to special methods like superacid treatment [19], attachment of arylsulphonated groups [20] and microwave treatment in presence of oleum and nitric acid at elevated pressures [16].

However, several issues regarding the extent of functionalization and contamination affecting their purity have not been adequately analyzed in these cases. For example, it is not clear how the low extent of –COOH group attachment (less than 5 wt% of oxygenated side groups) on the sidewalls/ends, generates such an unusual amount of amine functionalization (up to 70 wt%) [21]. Whether the present methods of acid functionalization of CNTs are sufficient or not to produce adequate amount of –COOH groups for further efficient derivatization is not clear to date. More significantly, the purification of SWCNTs-COCl by repeated centrifugation and washing with solvents could deactivate (due to moisture sensitive –COCl groups) the acyl moieties, which is not again well understood. Hence, there is an immediate need to explore alternative synthetic procedures in order to achieve greater efficiency and high purity using covalent functionalization strategies due to the preeminent role in all application of SWCNTs.

In the previous chapter we have described a novel morphology of MWCNTs in the form of scrolled mats prepared under a constant temperature ramp. However, such "as-synthesized" nanotubes have many impurities like metal nanoparticles and amorphous carbon and thus there is a strong need for purification and functionalization prior to investigating their fundamental properties. Therefore in this chapter, we describe a novel functionalization strategy to increase the solubility of SWCNTs/MWCNTs in water using a simple and rapid microwave treatment in acid mixture. Also, a covalent

amide formation method of SWCNTs with tridecylamine through oxalyl chloride treatment is discussed, which enables a higher, yet quantitative, degree of functionalization facilitating complete phase transfer from aqueous to non-aqueous media. The use of oxalyl chloride gives remarkable purity in the final product along with easy processing characteristics due to its lower boiling point, whereas, thionyl chloride [15] or dicyclohexylcarbodiimide [18g] requires many rigorous purification steps to remove excess reagents or unwanted by-products. Finally, these results have been compared with those of tridecylamine functionalized SWCNTs obtained by using $SOCl_2$.

This chapter also includes the comparative results obtained after functionalization by using two different aliphatic amines viz., tridecylamine and octadecylamine along with an aromatic amine as aniline. Such a simple and efficient method of functionalization with aniline also provides a remarkable degree of amidation, where the formation of polyaniline has been avoided. Also, the direct mixing of aniline and s-SWCNTs in presence of an acid shows an evidence for the electrostatic interaction between aniline and s-SWCNTs, where the proton plays catalytic role to form such interactions at ambient conditions. On the other hand, the electrochemical response of these functionalized SWCNTs shows remarkable variations in their redox properties. Interestingly, a monolayer functionalization of aniline would lead to an electrochemical coating of polyaniline on the SWCNT surface, which has been demonstrated by cyclic voltammetric and electrochemical Impedance studies.

3.2. Experimental Section

3.2.1. Materials

SWCNTs were obtained from Aldrich (purity > 60%; diameter: 0.7-1.3 nm; synthesized by CVD method), while MWCNTs were prepared by CVD method [22] using a ferrocene-xylene mixture at 700 ^{o}C as mentioned in the previous chapter. Ferrocene, tridecylamine (TDA), octadecylamine (ODA), sodium dodecyl sulphonate (SDS), potassium bromide (KBr; spectroscopy grade) oxalyl chloride and thionyl chloride were used as received from Aldrich (99.99%), while xylene, acetone, tetrahydrofuran (THF),

chloroform ($CHCl_3$), carbon disulphide (CS_2), sodium hydroxide and nitric acid were used as received from Merck (AR grade); deionized water (16 MΩ) from Milli-Q system was used for all experiments. Aniline was purchased from Merck and used after distillation. Fuming sulphuric acid (oleum) was obtained from s.d. fine chemicals and used as received.

3.2.2. Surface Modification

3.2.2.1. Preparation of Water-soluble SWCNTs

In a typical experiment, 50 mg of SWCNT was taken in a teflon cylinder with a grooved stopper containing an 1:1 mixture of oleum and 70% HNO_3. This was subjected to microwave (MW) irradiation in a domestic oven for 4 min (separated by 60 s off-time interval) using 60% of its total power of 700 W. No external pressure was applied in these studies The rigorous conditions imposed by the microwave render rapid breaking of graphitic -C=C- bonds to develop a large amount of –OH, -COO-, $-NO_2$ and $–SO_3H$ groups on the sidewalls of the SWCNTs. Soluble residue was first filtered through a 0.2 μm PTFE membrane and separated out from the unfiltered carbon matrix. Nanotubes which passed through the membrane were collected separately after a thorough purification by dialysis to yield shorter analogues. The unfiltered residue was again dispersed in 2 M HCl and sonicated for 30 min to develop –COOH groups rather than –COO-, which perhaps could hinder further functionalization. CNTs collected on the filter paper were transferred to a dialysis bag with a cut-off molecular weight of 12 kDa. The bag was filled with 100 mL deionized water and subjected to dialysis for 48 h. Deionized water used for the dialysis was frequently replaced in order to completely eliminate all acidic residues from the CNT sample (till pH changes to 7). The suspension was removed from the bag and rota-evaporated under vacuum to isolate the solid material for further characterization. SWCNTs obtained through such microwave treatment show a remarkable solubility (of 2.6 mg/mL) in water. The CNTs present in the filtrate have a much higher solubility (3-4 mg/mL) without any serious damage on the sidewalls. An irradiation time of 4 min is systematically chosen in this study in order to achieve better side wall functionalization as well as to restrict further damaging/cutting of nanotubes

that might lead to loss in weight. Interestingly, the solubility of s-SWCNTs is found to decrease with the addition of an acid (four different acids viz, HCl, H_2SO_4, HNO_3 and $HClO_4$ were used to check the effect), which is in sharp contradiction to an earlier report [16]. Such suppression in water-solubility of the SWCNTs could be attributed to the protonation of $–COO^-$ moieties on the side-walls to form comparatively less soluble –COOH groups. On the other hand, the solubility is found to be less enhanced with increase in pH, perhaps due to the formation of soluble salt of $–COO^-Na^+/K^+$.

3.2.2.2. Preparation of Water-soluble MWCNTs

A similar procedure has been employed to disperse MWCNTs in water, as discussed in section 3.2.2.1. A maximum solubility of 0.1 mg/mL was observed in the case of MWCNTs. Irradiation of microwave for 4 min to SWCNTs gives optimal solubility with a minimal loss of nanotubes, while MWCNTs require 5 min for their appreciable dispersion and solubility. SWCNTs and MWCNTs functionalized by such microwave irradiation are symbolized as s-SWCNTs and s-MWCNTs respectively in this thesis for the convenience of representation.

3.2.2.3. Amine Functionalization

3.2.2.3.1. Functionalization of s-SWCNTs using oxalyl chloride

About 40 mg of water-soluble SWCNTs (s-SWCNTs) having 2.6 mg/mL was ultrasonicated for 10 min in presence of 10 mL of oxalyl chloride, (taking extreme care during the handling of oxalyl chloride, since symptoms like burning and itching would be seen on exposure to skin [23]) and the reaction was carried out in an argon atmosphere. The mixture was then refluxed for 24 h at 60 ^oC to obtain a higher degree of acylchloride functionalization (SWCNTs-COCl); excess of oxalyl chloride was removed under vacuum using rota-evaporation. SWCNTs-COCl was then mixed with 1 g solid tridecylamine (TDA; $CH_3(CH_2)_{12}NH_2$) and refluxed at 40 ^oC (m. p. of TDA: ~30 ^oC) for 40 h. Excess of TDA was then removed by washing with copious amount of THF with

successive sonication and centrifugation. The resultant SWCNTs modified by TDA (37 mg) were found to be highly soluble in $CHCl_3$ and CS_2, as revealed in Scheme 3.1.

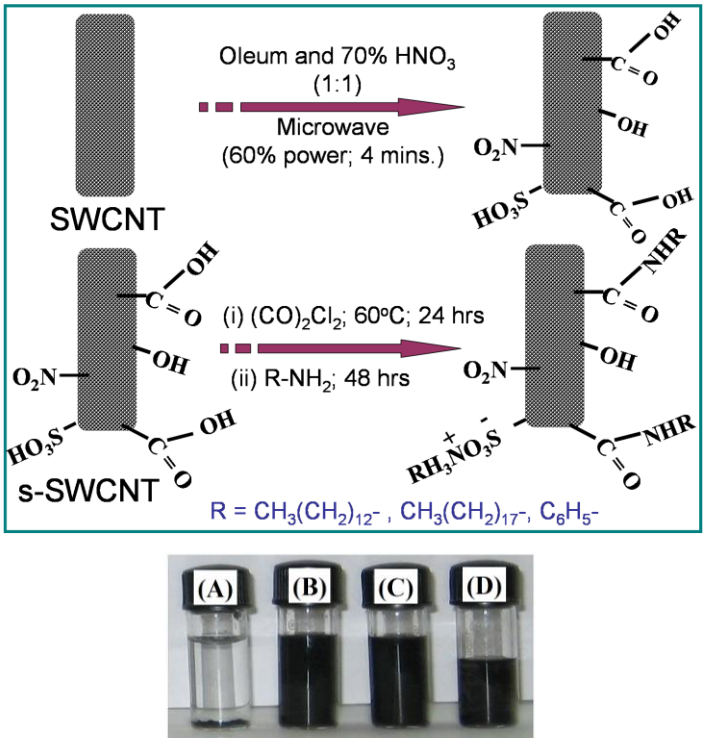

Scheme 3.1. Schematic depiction of the formation of water-soluble s-SWCNTs using microwave treatment followed by tridecylamine functionalization via oxalyl chloride; photographs corresponds to (A) pristine SWCNTs (B) s-SWCNTs (in water; 2.6 mg/mL) and after amide formation SWCNTs (C) in $CHCl_3$ (D) in CS_2.

3.2.2.3.2. Functionalization of s-SWCNTs using thionyl chloride

About 40 mg of water-soluble SWCNTs (s-SWCNTs) having 2.6 mg/mL was ultrasonicated for 10 min in presence of 10 mL of thionyl chloride and the reaction was carried out in an argon atmosphere. The mixture was then refluxed for 24 h at 80 ^{o}C to obtain an acylchloride derivative of SWCNTs (SWCNTs-COCl); excess of thionyl chloride was removed under vacuum using rota-evaporation at 40 ^{o}C. SWCNTs-COCl was then mixed with 1 g solid tridecylamine (TDA; $CH_3(CH_2)_{12}NH_2$) and refluxed at 40 ^{o}C (m. p. of TDA: ~30 ^{o}C) for 40 h. Excess of TDA was then removed by washing with copious amount of THF followed by successive sonication and centrifugation.

A similar procedure has been adopted for the functionalization of s-SWCNTs using octadecylamine and aniline (as discussed in above sections). Briefly, the aniline functionalization has been carried out as follows.

About 20 mg of s-SWCNTs having 2-3 mg/mL solubility was ultrasonicated for 10 min in presence of 10 mL of oxalyl chloride, and the reaction was carried out in an argon atmosphere. The mixture was then refluxed for 24 h at 60 ^{o}C to obtain a higher degree of acylchloride functionalization (SWCNTs-COCl); excess of oxalyl chloride was removed under vacuum using rota-evaporation. SWCNTs-COCl was then mixed with 5 mL of pure and distilled aniline and refluxed at 190 ^{o}C (b. p. of aniline: 186 ^{o}C) for 40 h. The reaction was carried out in a closed and inert condition in order to avoid the oxidation of aniline. Excess of aniline was then removed by washing with copious amount of toluene followed by successive ultrasonication and centrifugation, finally giving rise to 15 mg of aniline derivatized SWCNTs [SWCNT-COHNC_6H_5].

Furthermore, upon the addition of amine to such s-SWCNTs, the solubility of nanotubes gets suppressed due to the formation of linkages like SWCNT-$COO^-H_3N^+R$. This kind of bonding is rather different from the usual amide linkages. In order to obtain such electrostatically, amine functionalized SWCNTs, 10 mg of s-SWCNTs in 12 mL of deionized water was ultrasonicated for 10 min to form a clear black solution. To this, 1 mL of aniline hydrochloride was added and stirred gently and then ultrasonicated for 2 min. A black precipitate of SWCNT-$COO^-H_3N^+C_6H_5$ settled down within few seconds, which was then washed thoroughly with deionized water and characterized further.

3.2.3. Material Characterization

3.2.3.1. Uv-visible Spectroscopy

A Varian model Cary50 Dual Beam Uv-vis spectrophotometer was used to monitor the changes in the density of states of SWCNTs before and after functionalization. The pristine SWCNT sample was ultrasonicated in 1 mM sodium dodecylsulphate (SDS) in water to get a good dispersion of SWCNTs, whereas the SWCNTs-CONH$(CH_2)_{12}CH_3$ sample was dissolved in toluene before recording the spectra.

3.2.3.2. Fourier Transform Infrared Spectroscopy (FTIR)

In order to understand the presence of various functional groups on the side walls of nanotubes, before and after functionalization, FTIR studies have been performed using a Perkin Elmer Instruments- Spectrum One FTIR spectrometer in the Diffused reflectance (DRIFT) mode, after a thorough mixing of a small amount of sample in dry spectroscopic grade KBr followed by drying in a desiccator for 24 h.

3.2.3.3. Thermogravimetry

Since an analysis of the weight loss as a function temperatures could give valuable information on of the amount (%) of organic molecules anchored on the side walls of nanotubes, thermogravimetric (TG) analysis was carried out on a TGA Q5000 TA Instruments-Thermal Analysis and Rheology analyzer by heating about 0.2 mg of carbon sample from 50^{o}C to 900^{o}C at a rate of 10 °C/min in air.

3.2.3.4. Proton Nuclear Magnetic Resonance Spectroscopy

In order to understand the surface functionality present on water-soluble and amine functionalized SWCNTs samples, proton NMR (^{1}H NMR) studies have been performed on a Bruker MSL400 MHz instrument using DMSO (d_6) as a dispersing solvent to detect magnetically different protons after functionalization.

3.2.3.5. Raman Spectroscopy

Raman analysis is a fundamental tool to understand the surface defects and electronic structure of nanotubes, where the tangential mode (G-band) and defect mode (D-bands) of vibrations change systematically after surface functionalization. Accordingly, Raman analysis of various nanotube sample was performed on a JASCO confocal Raman spectrometer using 532 nm green laser (NRS 1500 W) in order to obtain the effect of functionalization.

3.2.3.6. X-ray Photoelectron Spectroscopy

X-ray photoelectron spectroscopic (XPS) measurements were carried out on a VG Micro Tech ESCA 3000 instrument at a pressure of > $1x10^{-9}$ Torr (pass energy of 50 eV with an electron take off angle 60^{o} and an overall resolution of 1 eV) using MgK_{α} radiation (1253.6 eV). The binding energy of C1s peak was fixed to 284.5 eV and all peaks were calibrated with reference to this graphitic C1s peak. The background was subtracted by Shirley method.

3.2.3.7. Scanning Electron Microscopy

The morphology of the MWCNTs was examined by a LEICA Stereoscan 440 scanning electron microscope (SEM) equipped with Phoenix energy dispersive analysis of X-ray (EDX).

3.2.3.8. Transmission Electron Microscopy

The morphology of the SWCNTs was examined by a JEOL JEM 1200 EX transmission electron microscope (TEM) operated at an accelerating voltage of 120 kV with a resolution of not less than 3-4 nm. However, high resolution (lattice resolution) images have been obtained from a FEI, Tecnai $F30G^2$, 300 kV HRTEM with FE gun with a resolution of 0.14 nm.

3.2.3.9. Cyclic voltammetry and Impedance Measurements

Cyclic voltammetry was performed using an Autolab PGSTAT30 (ECO CHEMIE) instrument, whereas electrochemical impedance measurements were carried out in an impedance analyzer (Autolab PGSTAT 30 with Frequency Response Analyzer operated by FRA software). A 10 mV rms ac signal was applied in the frequency range, 0.1 Hz – 1 kHz and the impedance values were averaged over five cycles for each frequency.

3.3. Results and Discussion

3.3.1. Uv-visible Spectroscopy

The diversity in the electronic structure of the nanotubes arises from the quantization of the electronic wave vector in the one-dimensional (1D) system through the conceptual rolling of graphene sheet into cylinder forming a nanotube [17b,c]. Such subtle differences in the electronic structure (geometry dependant) of nanotubes lead to remarkable changes in solution-phase reactivities of these species [17a]. As a consequence, pristine SWCNTs show typical van Hove's singularities in the Uv-Vis-NIR spectra, which are lost upon covalent functionalization [11,18b,l-o]. Basically, these singularities arising due to extended π-conjugation in SWCNTs can be disrupted by defects as well as by covalent functionalization [18p-r].

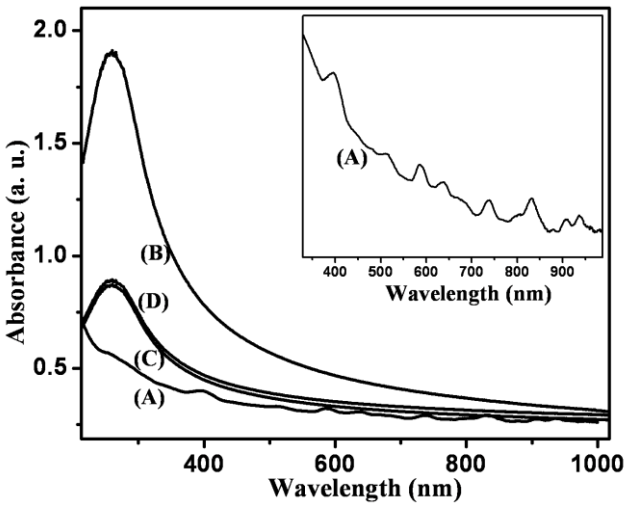

Figure 3.1. Uv-vis absorption spectra of (A) pristine SWCNTs dispersed in 1 mM SDS solution in water (B) microwave treated water soluble SWCNTs (C) SWCNTs-$CONH(CH_2)_{12}CH_3$ prepared by oxalyl chloride and (D) SWCNTs- $CONH(CH_2)_{12}CH_3$ prepared by thionyl chloride in toluene, which show a complete loss of the fine spectral features (van Hove singularities) upon chemical treatments, revealing the formation of defects due to conversion of sp^2 to sp^3 carbon; inset shows the expanded spectrum of pristine SWCNTs with distinct singularities.

Accordingly, a comparison of absorption spectra in Figure 3.1, for both pristine as well as functionalized SWCNTs, clearly shows the disappearance of the van Hove singularities both after microwave treatment as well as amine functionalization, indicating the breaking of electronic structure due to the generation of defect sites (along

with the formation of functional groups) on the sidewalls. In pristine SWCNT, the presence of both semiconducting and metallic SWCNTs shows individual absorption peaks that allow the monitoring of valence electrons. Further, the functionalization with tridecylamine gives localization of these valence electrons resulting into the decay of such maxima in the spectrum.

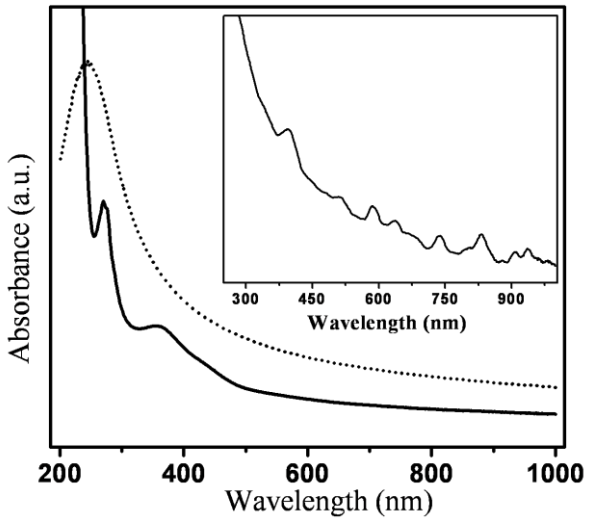

Figure 3.2. Uv-vis spectra of s-SWCNTs (dashed line) in water and SWCNT-$COHNC_6H_5$ (thick line in toluene); inset shows the Van-Hove singularities of pristine sample (prepared in 1 mM SDS in water), which have vanished after aniline functionalization.

In addition, the modification of the sidewalls by aniline (aromatic amine) is also evidenced by the results of Uv-vis absorption spectra. For example, Figure 3.2 indicates the superimposed Uv-vis spectra of s-SWCNTs (dashed line) and SWCNT-$COHNC_6H_5$ (thick line) in toluene where discernible features allow us to have a critical comparison. The inset of Figure 3.2 shows the expanded Uv-vis spectrum of pristine SWCNTs in water with SDS, which clearly demonstrates the Van-Hove singularities due to electronic structure of the nanotubes. The disappearance of these singularities on microwave irradiation indicates a significant alteration in the electronic structure and properties of the nanotubes. However, a strong absorption peak at 243 nm has been observed, perhaps due to the presence of $–COO^-$ or –C=O functional groups on the nanotubes. The amine bonding alters the Uv-vis spectra with the appearance of two new absorption peaks at 260 and 370 nm respectively, which could be attributed to the π-π^* (K band) transitions due

to the covalent modifications with aniline. However, the possibility of polymerization (to form polyaniline) has been ruled out, since the peaks corresponding to the benzenoid and quinoid segments of the polyemeraldine chain [24,25] are not found in the Uv-vis spectrum, which is a prerequisite for the conducting polymer formation.

3.3.2. FTIR Analysis

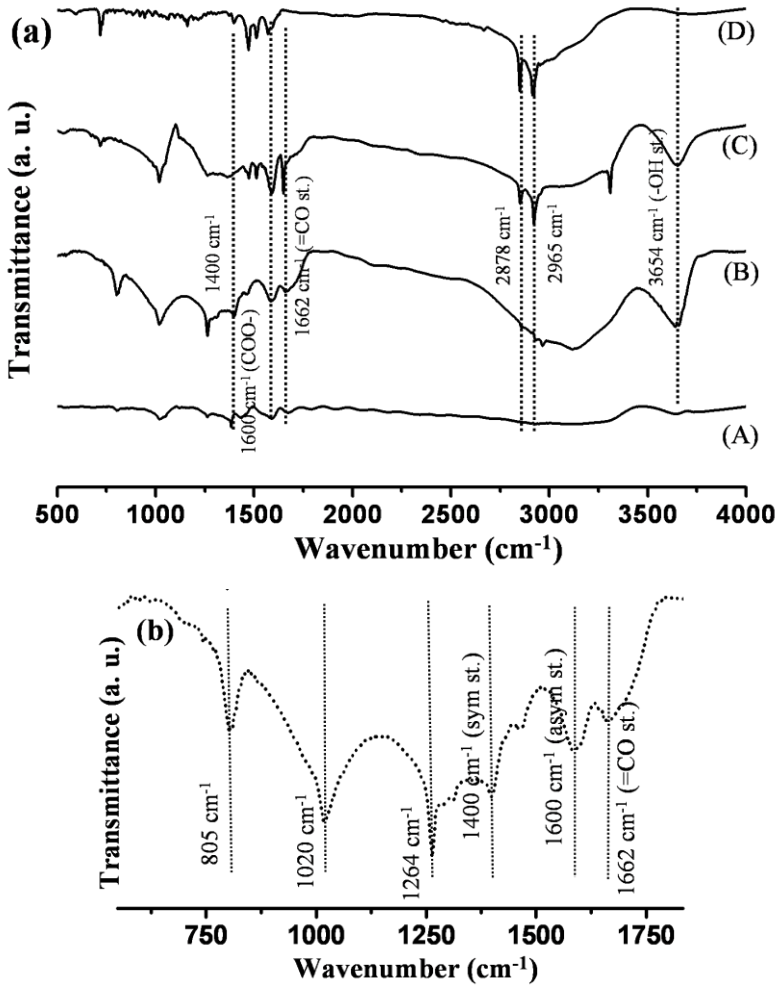

Figure 3.3. (a) A comparison of DRIFT spectrum of (A) pristine SWCNTs (B) s-SWCNTs (C) SWCNTs- $CONH(CH_2)_{12}CH_3$ prepared by oxalyl chloride and (D) SWCNTs- $CONH(CH_2)_{12}CH_3$ prepared by thionyl chloride; **(b)** magnified DRIFT spectrum for s-SWCNTs performed after making a pellet using KBr.

DRIFT spectra (Figure 3.3) of all samples, including pristine SWCNTs, s-SWCNTs and SWCNTs-$CONH(CH_2)_{12}CH_3$ show a peak at 1580 cm^{-1} corresponding to

the active carbon stretching mode of the nanotubes. A new peak at 1600 cm^{-1} in the case of s-SWCNTs is attributed to the $–COO^-$ groups (asymmetric stretching), which facilitates the solubility of SWCNTs. It also shows the appearance of an additional peak at 1400 cm^{-1} supporting the presence of COO- (symmetric stretching mode) groups in the DRIFT spectrum of s-SWCNTs. In addition, the presence of a broad and intense band at 3654 cm^{-1} suggests the attachment of –COOH groups (not H-bonded) on the sidewall. Thus the hydrophilic groups like –COOH and –OH are also likely to be generated in addition to the carboxylate groups. Further, strong bonding among SWCNTs (intertubular bonding) could be possible due to the $–COO^-$ groups, which has not been explained well in earlier reports [15,16]. The microwave irradiation in presence of such fuming acid mixture produces sulphonic groups (unlike in presence of usual nitrating mixture) on the side walls, perhaps due to the excess SO_3 present in oleum. Figure 3.3(b), for example, shows the presence of three strong peaks at 805, 1020 and 1264 cm^{-1} corresponding to S-O, $–SO_3H$ and –S=O respectively, indicating the formation of sulphonic functional groups on the side-walls. Typical –C-H stretching frequencies present on benzene rings of nanotubes have been observed at 2878 and 2965 cm^{-1} respectively. Also a sharp peak at 1662 cm^{-1} has been observed corresponding to a stretching frequency of carbonyl ($\nu_{C=O}$) group. A sharp peak at 1650 cm^{-1} has been observed corresponding to a stretching frequency of carbonyl ($\nu_{C=O}$) after amide formation.

Similarly, Figure 3.4(b) indicates the DRIFT spectrum of SWCNT-$CONHC_6H_5$, where the covalent linkage between SWCNTs and aniline could clearly be illustrated, especially at the finger print region. Interestingly, the peak at 3654 cm^{-1} becomes broader and gets shifted towards higher wavenumbers after the amide functionalization. The deconvolution of this peak shows an additional small hump at 3750 cm^{-1} perhaps, corresponding to the –N-H stretching (adjacent to sp^2 carbon in phenyl ring; higher energy as compared to –OH stretching and -NH) due to amide formation.

Although, a previous report [13] suggests that, the presence of ionic carboxylate groups can block further amine functionalization due to its inactive nature towards reagents like thionyl chloride or oxalyl chloride, the present results (aniline derivative)

indicate an enhancement in SWCNT-$COO^-H_3N^+C_6H_5$ functionalization in presence of -COO^- groups.

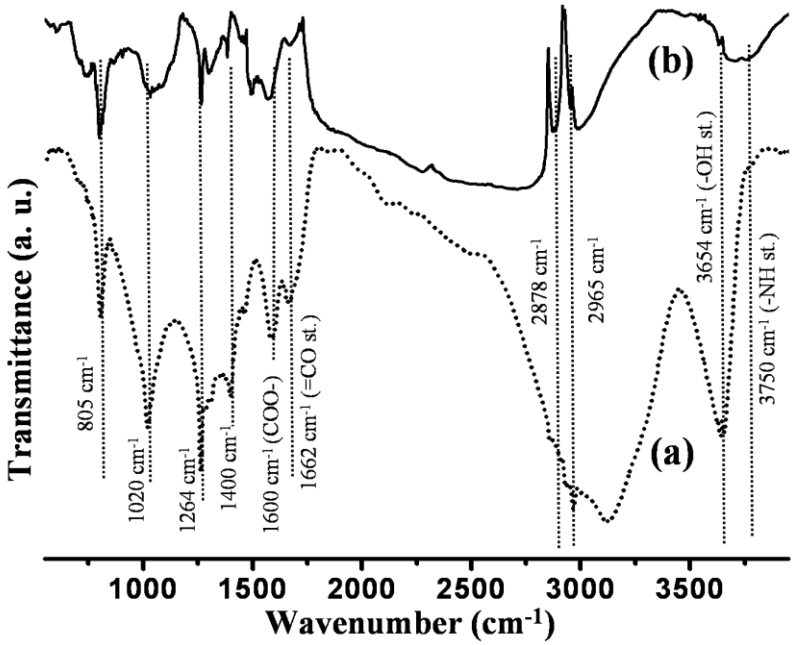

Figure 3.4. DRIFT spectra of **(a)** s-SWCNTs and **(b)** SWCNT-$COHNC_6H_5$ indicating amide functionalization.

3.3.3. NMR Analysis

^{1}H NMR (400 MHz, DMSO (d_6)) of SWCNTs-$CONH(CH_2)_{12}CH_3$ shows the presence of a long aliphatic chain on the sidewalls as well as on the ends of SWCNTs, from the chemical shift data δ 0.89 (t, 3H, CH_3), 1.33 (s, 2H, CH_2). The CH_2 group directly attached to the amide group at the ends of the SWCNTs shows several broad signals in the range of δ 2.8 to 3.2; the integral of all of these signals corresponds to 2H, which suggests the existence of magnetically different types of protons α- to the amide group in our SWCNTs. In addition, the signals ranging from δ 6.94 to 7.20 indicate the development of few –C-H bonds on benzene rings (aromatic H) of SWCNTs, creating wall defects. Also, the presence of a peak at δ 7.71 indicates amido proton, although the weak intensity could contradict subsequent description of extensive amidation (Figure 3.5).

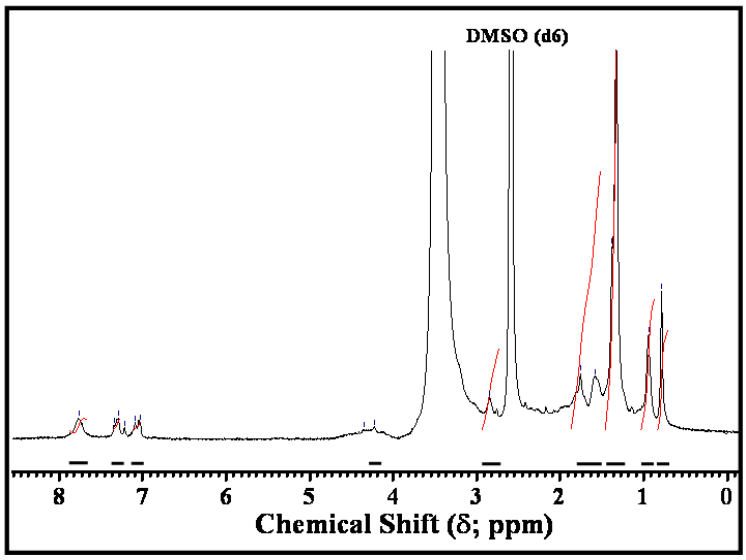

Figure 3.5. ^{1}H NMR spectrum of SWCNTs-$CONH(CH_2)_{12}CH_3$ performed in DMSO (d_6), showing the presence of magnetically different protons due to covalent bonding of TDA through amidation.

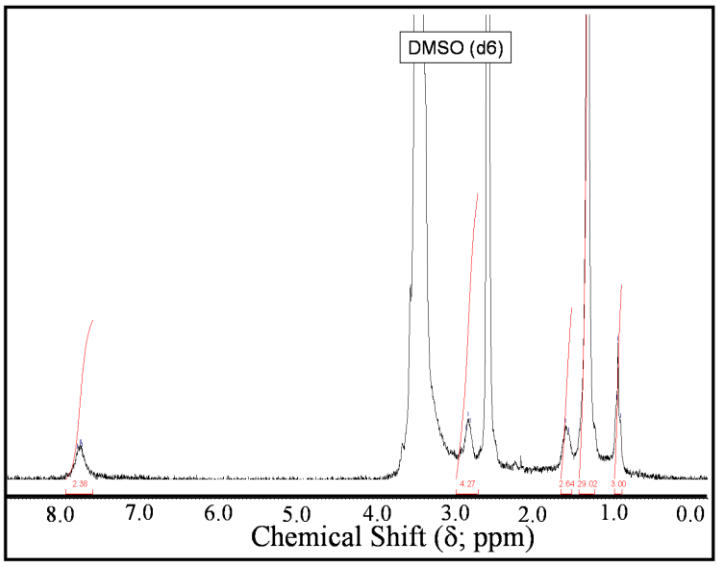

Figure 3.6. ^{1}H NMR spectrum of SWCNTs-$CONH(CH_2)_{17}CH_3$ performed in DMSO (d_6), showing the presence of magnetically different protons due to covalent bonding of ODA through amidation.

Protons in the SWCNTs-$CONH(CH_2)_{12}CH_3$, in which the tridecylamine is covalently attached to the SWCNTs, are much more affected by the backbone of SWCNTs network, and it is the strong amidation that is responsible for the drastic

changes in the ^{1}H NMR spectrum of the tridecylamine. This also indicates that, no free tridecylamine is present in the sample.

Similarly, ^{1}H NMR spectrum (at 400 MHz, DMSO(d_6)) of SWCNTs-$CONH(CH_2)_{17}CH_3$ also shows (Figure 3.6) the presence of a long aliphatic chain of octadecylamine on the sidewalls as well as on the ends of SWCNTs, from the chemical shift data δ 0.89 (t, 3H; CH_3), 1.27 (s, 28H; CH_2), 1.57-1.58 (m, 2H), 2.76- 2.82 (m, 4H) and the peak at 7.72 (s, 2H) indicates the protons from amido group or sp^3 defect-sites of SWCNTs. All other peaks are indexed in similar way as that of SWCNTs-$CONH(CH_2)_{12}CH_3$.

3.3.4. TG / DT Analysis

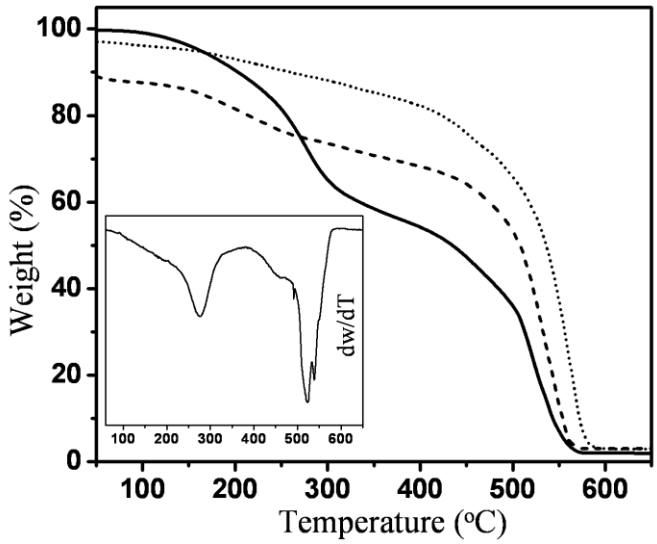

Figure 3.7. TG analysis of s-SWCNTs (dotted line) and SWCNTs-$CONH(CH_2)_{12}CH_3$ prepared by oxalyl chloride (thick line) in dry oxygen, showing 50% loss in weight implying a higher degree of amidation on defect walls; SWCNTs-$CONH(CH_2)_{12}CH_3$ prepared by thionyl chloride (dashed line) shows only 15% of weight loss, although an initial weight loss of 10% could be attributed to volatile impurities. Inset exhibits a DT curve for SWCNTs-$CONH(CH_2)_{12}CH_3$ (corresponding to thick line), clearly indicating two step weight loss.

TGA can determine the degree of SWCNT functionalization by sufficiently heating the material in pure oxygen atmosphere in order to remove the functional moiety, leaving the pristine SWCNTs and hence measuring the weight loss. In the present case, more than 50% of the TDA attached to SWCNTs is confirmed by the weight loss from

the TG analysis. A single inflection in the weight loss (Figure 3.7; thick line) pattern up to 300 ^{o}C indicates the presence of only covalently bonded TDA, revealing the purity of our functionalized SWCNTs.

One of the key reasons in the enhancement of such a large amidation might be the abundance (~ 8 wt%) of carboxylic groups generated during the microwave treatment and consequently a considerably higher degree of acylation with oxalyl chloride. However, this weight loss of TDA is quite lower when SWCNTs-CONH$(CH_2)_{12}CH_3$ prepared by thionyl chloride, which shows only 15% weight loss (dashed line). Inset of Figure 3.7 shows a differential thermal analysis curve for SWCNTs-CONH$(CH_2)_{12}CH_3$ that gives a smaller hump at 460 ^{o}C (corresponding to other stronger functional moieties on the side walls) in addition to two sharp inflexions, revealing a clear evidence for TDA functionalization. Also, it is consistent with the fact that, other reactive sites like $–SO_3H$ are produced during the oxidative treatments along the tubular walls and at the ends. The volume of the SWCNTs is also found to expand (approximately 30%) after the functionalization due to the exfoliation of nanotube bundles forming shorter analogues.

Figure 3.8(a) summarizes a comparison of main TG features for both s-SWCNTs (dotted line) and SWCNT-$COHNC_6H_5$ (thick line). TG curves clearly show two distinct weight loss regions in case of SWCNT-$COHNC_6H_5$, revealing the decomposition of organic side chain of aniline around 130-250 ^{o}C**.** DT curve (shown in inset of Figure 3.8(a)) demonstrates the stepwise loss in weight, where three distinct weight losses have been observed at 134, 184 and 218 ^{o}C respectively. First two weight losses could be assigned to the moisture or solvent and unbound aniline present in the sample. The loss at 184 ^{o}C could also be attributed to the decomposition of aniline molecules present due to π $–\pi$ interaction (aromatic) with basal plane of nanotubes, which would remain even after rigorous washings. This suggests that a non-covalent attachment of aniline is also possible perhaps, due to π $–\pi$ interaction between aromatic molecules and nanotubes and requires more energy to break such bonds. However, the latter weight loss at 218 ^{o}C has been assigned to the decomposition of amide linkages between aniline and nanotubes. These results also suggest the absence of any polyaniline structures on the nanotube surface.

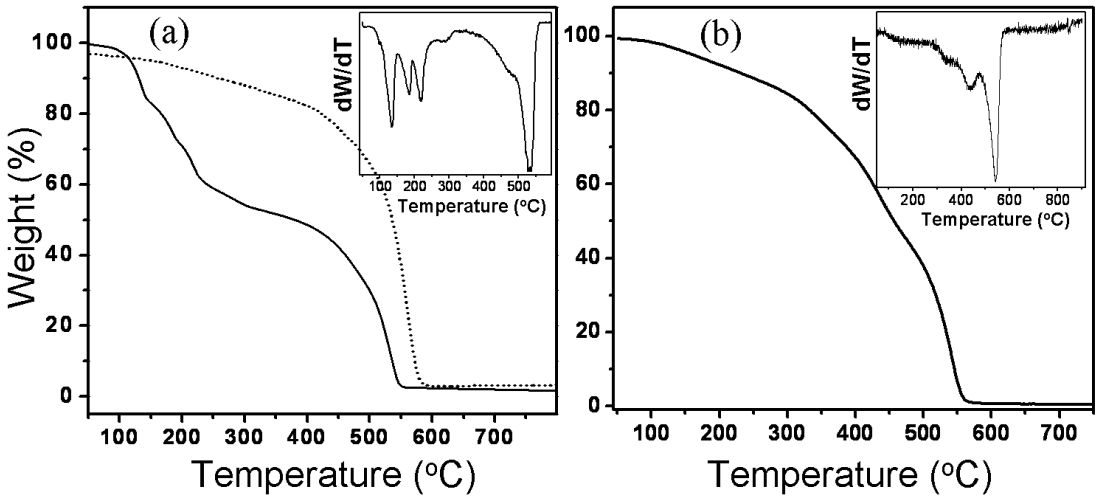

Figure 3.8. (a) Superimposed TG curve of s-SWCNTs (dotted line) and SWCNT-$COHNC_6H_5$ (thick line) exhibiting stepwise decomposition of organic molecules along with a decrease in the thermal stability of nanotubes; inset shows DT curve of SWCNT-$COHNC_6H_5$ clearly indicating the stepwise weight loss and **(b)** TG curve for SWCNT-$COO^-H_3N^+C_6H_5$, showing a gradual weight loss; inset shows the DT curve with two prominent inflections.

In addition, a simple strategy of linking SWCNTs to aniline has been carried out at room temperature. The addition of aniline hydrochloride to the s-SWCNTs in water shows settling of nanotubes within 60 s, indicating a strong suppression in the solubility due to the formation of zwitterionic species like SWCNT-$COO^-H_3N^+C_6H_5$, However, Hamon et. al, [26] have shown a dissolution of shortened SWCNTs-COOH with addition of amine at 90 ^oC. TG analysis (Figure of 3.8(b)) of SWCNT-$COO^-H_3N^+C_6H_5$ summarizes a continuous and gradual decrease of weight during heating in air with an onset temperature of 142 ^oC suggesting the decomposition of organic molecules produced after amine functionalization. More interestingly, the decomposition temperature for SWCNT-$COO^-H_3N^+C_6H_5$ is found to increase to 556 ^oC as compared to 540 ^oC of s-SWCNTs. A sharp weight loss of 40% is observed in case of amine modified SWCNTs after 495 ^oC, which could be attributed to the decomposition of sp^2 carbon to carbon dioxide.

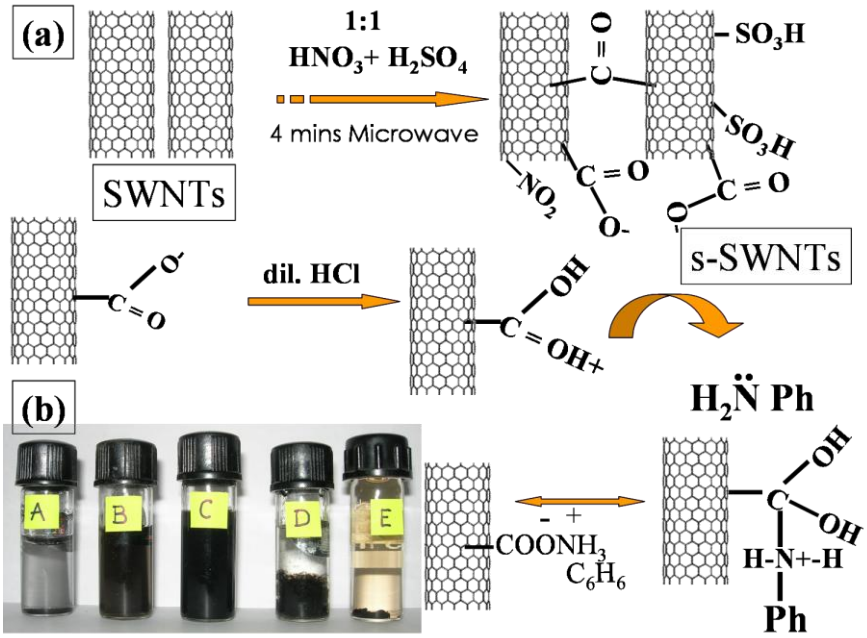

Scheme 3.2. (a) A schematic representation of generation of $–COO^-$ groups on sidewalls of SWCNTs upon microwave irradiation, which further undergoes covalent coupling with amine (aniline) through acid catalytic mechanism at room temperature; **(b)** Photographs of (A) as-received SWCNTs in water after 30 min ultrasonication (B) s-MWCNTs (0.1 mg/mL) (C) s-SWCNTs produced by 4 min exposure to microwave (3 mg/mL) (D) SWCNT-$CONHC_6H_6$ in water settles down (E) SWCNT-$COO^-H_3N^+C_6H_5$ formation shows immediate precipitation in water due to zwitterionic linkages.

Based on this experimental data, we now propose a tentative acid catalyzed mechanism of functionalization of CNTs at ambient conditions, as demonstrated in Scheme 3.2. Here, pH is an important parameter, since protons can play an important role to form SWCNT-$COO^-H_3N^+C_6H_5$ linkages. Although, clear changes with respect to pH have been observed (these species are formed only in acidic pH), the exact reason is not clear.

3.3.5. XPS Analysis

Structural variations could also be clarified by XPS analysis (Figure 3.9), where the presence of a reduced peak corresponding to the C1s core shell directly indicates a remarkable extent of functionalization.

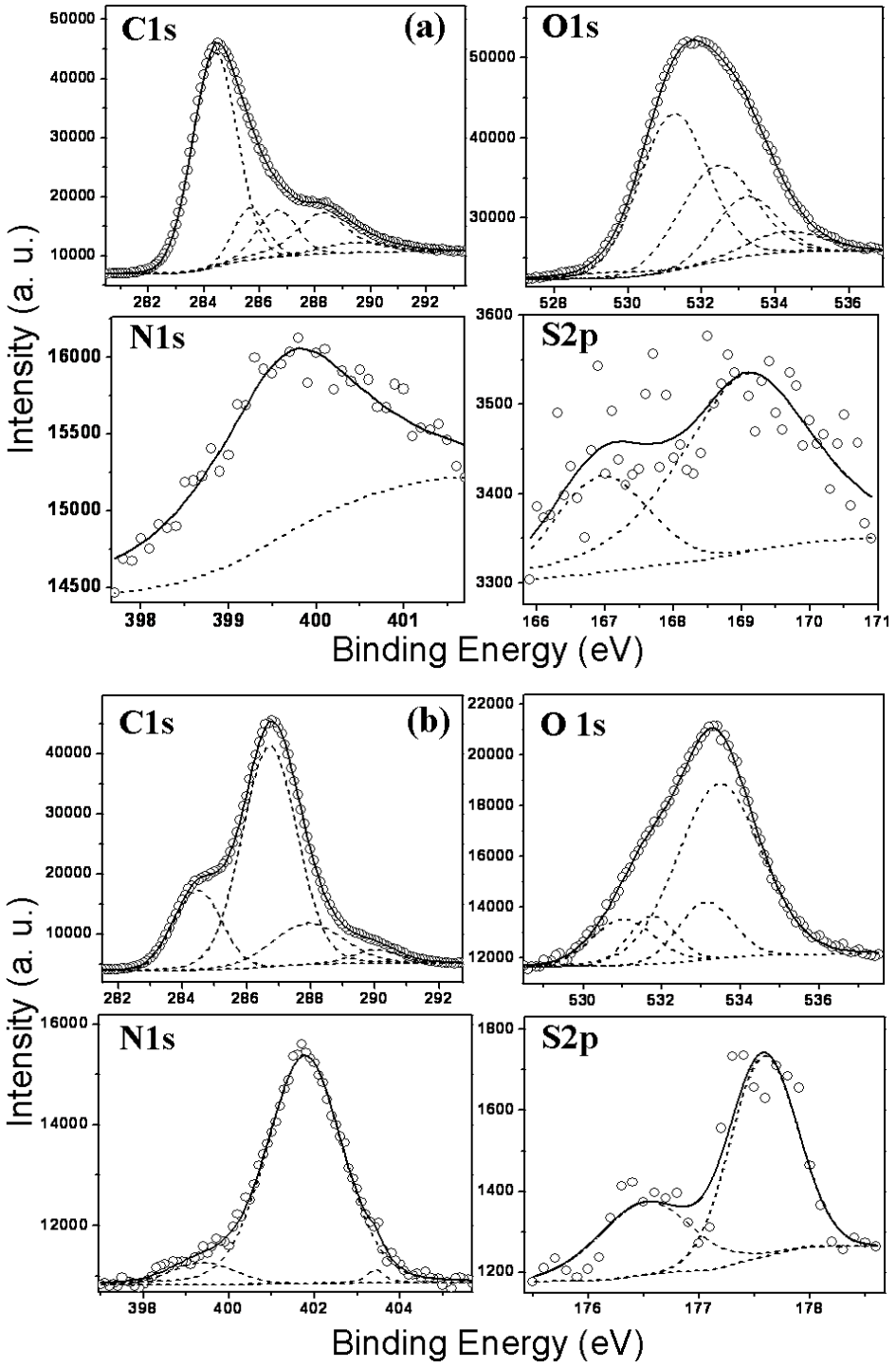

Figure 3.9. XP spectra of **(a)** water soluble SWCNTs (s-SWCNTs) and **(b)** SWCNTs-$CONH(CH_2)_{12}CH_3$ where core levels of (A) C1s (B) O1s and (C) N1s and (D) S $2p_{3/2}$ and S $2p_{1/2}$ are deconvulated separately; the circles represent the experimental data; thick lines represent the fitting data for overall signal; the dotted lines are the deconvoluted individual peaks for different species present in the sample.

For example, the surface functionalities on the SWCNTs are also confirmed by XPS analysis especially when the results are compared with those for pristine CNTs. In addition, using relative amounts of C, N and S present in the sample and normalizing to the S, we find that there are 16 N atoms (form amide bonds) per 1 S atom (from sulphonate). This means that approximately 7 wt% of N and 1 wt% of S are present on the side walls after TDA amidation, which is in excellent agreement with the results of the TG analysis. The quantitative analysis of elements has been carried out using formula given in [27]. Accordingly, Figure 3.9(a) shows the XP spectrum of s-SWCNTs where, the C1s spectrum has been deconvoluted to four peaks; a major peak at 284.4 eV is assigned to graphitic C-C bonds, while four minor contributions at 285.6, 286.6, 288.5 and 289.5 eV could be attributed to the carbon atoms attached to other atoms in three different environments such as, OH, NO_2, COOH and SO_3H respectively.

In addition to a major (~74092; after background subtraction) peak at 284.4 eV corresponding to graphitic C-C bond, a relatively intense (~20868: after background subtraction, FWHM: 2.19) peak at 288.5 eV is observed due to COOH groups, which are utilized for the formation of –CONH functionalization with TDA. By normalizing with respect to oxygen the composition of oxygen on the side wall after microwave treatment is found to be 30 wt% (~4.3 C atoms per 1 O atom), which is higher than that reported earlier [14,18,26,28]. However, interestingly, five different oxygen functionalities, interestingly, are observed corresponding to various groups on the sidewalls generated during the synthesis. Accordingly, Figure 3.9a (O1s) shows five different peaks after a similar fitting procedure; a peak at a binding energy of 529.5 eV corresponds to the oxygen in $–SO_3H$ group, while intense peaks at 531.2 eV and 532.4 eV could be attributed to the double bonded oxygenated group like –COOH and group like $–NO_2$ respectively. Similarly, a peak at 533.2 eV could be assigned to the single bonded oxygenated groups like –OH whereas, a smaller peak at 534.3 eV might be due to adsorbed moisture or molecular oxygen. In addition, a broad and less intense peak at 399.8 eV in Figure 3.9a (N1s) is assigned to the N1s core level of $–NO_2$ group. A doublet at 166.9 and 168.0 eV (Figure 3.9a (S 2p**)**) has been assigned to the S $2p_{3/2}$ and S $2p_{1/2}$ level of $–SO_3H$ groups respectively, which are developed during the treatment.

Figure 3.9(b) illustrates the XP spectra of SWCNTs after the covalent bonding with tridecylamine due to several environmental changes. Interestingly, the C1s peak is found to be affected after amidation, which is evident in Figure 3.9(b) (C1s)**,** where the peak (284.5 eV) due to graphitic C-C bonding is reduced appreciably and a new peak at 286.7 eV could be attributed to C1s of alkyl chain of amine. This enhanced and unusually intense peak (intensity: ~82820; FWHM: 2.02) corresponding to alkyl carbon indicates a remarkable degree of amidation. In addition, two peaks at 287.9 and 290.1 eV are assigned to C-OH and –CONH linkages, although a slight shift is observed in both the cases that might be due to several complex interactions with other functional groups.

On normalizing with respect to N, the atomic ratio C: N of 8.6:1 (6.8 wt% of N with respect to total C) is observed which is in an excellent agreement with that of C: COOH of s-SWCNTs. This ratio is also verified by comparing the C1s (290.1 eV) and N1s (401.8 eV) of amide linkages, which is found to be 1:1. Also, an atomic ratio of 16:1 for N:S (and C:S as 175:1 i.e. 0.76 wt% of S) as observed, indicates a lesser extent of -SO_3H groups developed during the microwave treatment. Further, appreciable changes have been observed in case of O1s peaks after amide formation. For example, Figure 3.9(b) (O1s) indicates the deconvoluted spectra for O1s, which shows four peaks corresponding to –SO_3H, -OH, –NO_2, and -CONH bonding at 531.1, 532.0 and 533.1 and 533.45 eV respectively. Minor contribution from adsorbed oxygen is not observed even after fitting up to standard deviation (χ^2) of less than unity. Also, an extra peak at 401.8 eV (intensity: ~10716; FWHM: 2.06) observed in the case of N1s might be due to –CONH- linkages, which is shown in Figure 3.9(b) (N1s). Interestingly, two minor peaks observed at 176.5 and 177.5 eV in the case of S $2p_{3/2}$ after amidation, could be due to –SO- moieties attached to halides like chloride ions or due to the formation of salt like SWCNTs- $\bar{S}O_3{}^{\oplus}NH_2(CH_2)_{12}CH_3$ (Figure 3.9(b) S2p). Consequently, a remarkable solubility ranging from 2.6 to 5 mg/mL observed after microwave treatment could be explained due to the presence of a higher concentration (~30 %) of oxygenated species including –COOH, -OH, -SO_3H and -NO_2 groups developed during microwave

irradiation. All the data including the binding energies of species present are given in Table 3.1.

Table 3.1. All the binding energy positions of the elements present in different nanotube samples.

Species	Binding Energy (eV)		
	'As received' SWCNT	**s-SWCNTs**	**SWCNT-$CONH(CH_2)_{12}CH_3$**
C1s	284.5	284.4	284.4
	286.0	285.6	286.7
	287.5	286.6	287.9
	289.3	288.2	290.0
	291.0	289.5	
O1s	530.5	531.2	531.0
	531.8	534.3	531.7
	532.9	529.5	533.1
	534.2	532.4	533.4
		533.2	
S2p	-	166.9	176.5
		169.0	177.5
N1s			399.4
	-	399.6	401.8
			403.4
Fe	710.6	-	-
	713.3	-	-

In addition, Figure 3.10 illustrates the XP spectra for the elements in the SWCNT-$CONHC_6H_5$. The C1s peak affected by amidation, as evident in Figure 3.10 (C1s), where the intensity of peak (~94784; after background subtraction to 284.5 eV) due to graphitic C-C bonding is enhanced appreciably and it could be attributed to the addition of more sp^2 carbons from the aniline side chain. In addition, four peaks at 285.8, 286.6, 288.3 and 290.4 eV are assigned to C-OH, –CONH, C-NO_2 and C-$SO3^-$ linkages, although a slight shift is observed in both the cases that might be due to several complex interactions with other functional groups. Further, appreciable changes have been observed in case of O1s peaks after amide formation. Figure 3.10 (O1s) indicates the deconvulated spectra for O1s, which shows four peaks corresponding to –SO_3H, -OH, –NO_2, and -CONH bonding

at 531.1, 532.0 and 533.1 and 533.45 eV respectively. Minor contribution from adsorbed oxygen is not observed even after fitting up to standard deviation (χ^2) of less than unity. Also, an extra peak at 400.7 eV (intensity: ~1812; FWHM: 2.3) is observed in case of N1s might be due to –CONH- linkages, which is shown in Figure 3.10 (N1s). Interestingly, two minor peaks observed at 163.7 and 165 eV in case of S $2p_{3/2}$ after amidation, could be due to –SO- moieties attached to halide like chloride ions or due to the formation of salt like SWCNTs- $\bar{S}O3^{\oplus}NH_2\ (CH_2)_{12}CH_3$ (Figure 3.10 (S2p)), perhaps attributable to the charge localization.

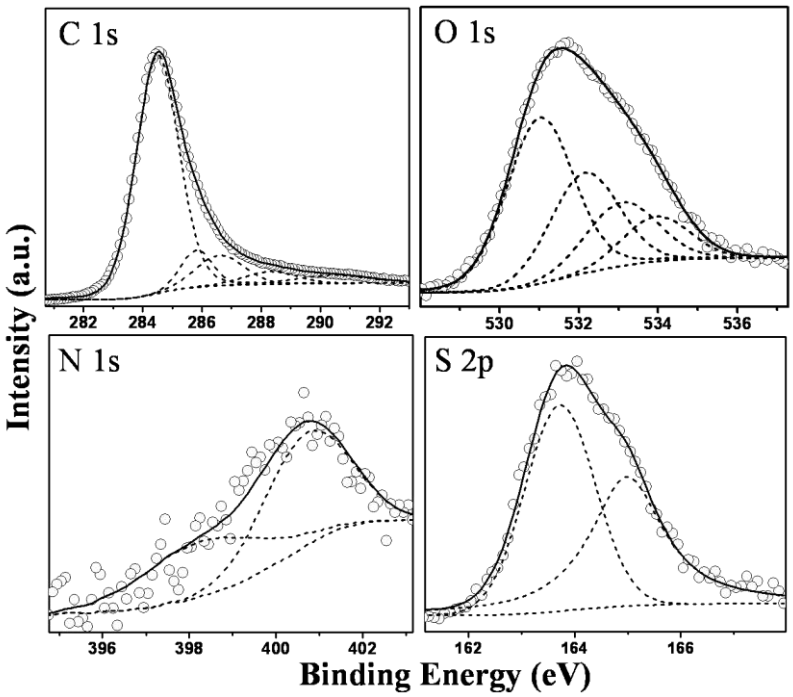

Figure 3.10. XP spectra of SWCNT-$COHNC_6H_5$ where core levels of C1s, O1s, N1s and $S2p_{3/2,1/2}$ are deconvulated separately. The circles represent the experimental data; thick lines represent the fitting data for the overall signal; the dotted lines are the deconvulated individual peaks for different species.

In order to support the XPS analysis, the microanalysis (C, H, N analysis) results have been documented in Table 3.2, although these results would not be used for quantitative information due to its limitations. Nevertheless, Table 3.2 in combination with the XPS analysis clearly indicates the generation of plenty of oxygenated functional groups after acid treatment along with microwave irradiation. It also suggests an efficient

TDA-functionalization using oxalyl chloride (~2.97% of N) as compared to that using thionyl chloride (~1.66% of N), while ODA shows an unusually higher degree of functionalization (containing ~4.46% of N). This could be attributed to the geometry of the long chain amine, since the cage like structure of TDA might lead to comparatively lesser amidation.

Table 3.2. Composition of various elements present in different nanotube samples.

Sample	Carbon	Hydrogen	Oxygen	Nitrogen	Sulphur
Pristine SWCNT	91.11	0.6	8.29	-	-
s-SWCNT	73.81	0.611	24.83	0.362	0.387
SWCNT-$CONH(CH_2)_{12}CH_3$ prepared using oxalyl chloride	71.40	5.05	19.93	2.97	0.65
SWCNT-$CONH(CH_2)_{12}CH_3$ prepared using thionyl chloride	66.35	2.35	28.64	1.66	1
SWCNT-$CONH(CH_2)_{17}CH_3$	68.54	13.60	12.97	4.46	0.425
SWCNT-$COHNC_6H_5$	65.62	3.72	22.58	8.076	-

3.3.6. Raman Analysis

Raman spectroscopy is one of the important tools to determine the properties and structure of a single carbon nanotube, since the density of electronic states is very large for some energy ranges in SWCNTs. The density of states is an indication for the number of energy states, ΔN, per energy difference, ΔE. Every different nanotube geometry, i.e. a different (*n*,*m*) pair, results in a unique pattern for the density distribution of states which could also be calculated theoretically. If the photon energy is (almost) equal to the energy needed for the valence to conduction band transition, an intense Raman signal is found as a direct result of the strong coupling between the electrons and phonons of a nanotube under resonance conditions [29].

Hence, Raman spectroscopy has also been employed to strengthen our interpretation of clean and efficient functionalization. Accordingly, Figure 3.11(a) shows superimposed Raman spectra of pristine-SWCNTs (black curve), s-SWCNTs (blue curve) and tridecylamine derivatized SWCNTs prepared by oxalyl chloride (green line) and thionyl chloride methods (red line) respectively. Shifts in the characteristic D (disorder or defect sites in the sample) and G-bands (tangential mode) after the microwave treatment and eventually by tridecylamine functionalization, clearly suggest an enormous side-wall damage resulting into effective functionalization of sp^2 carbon.

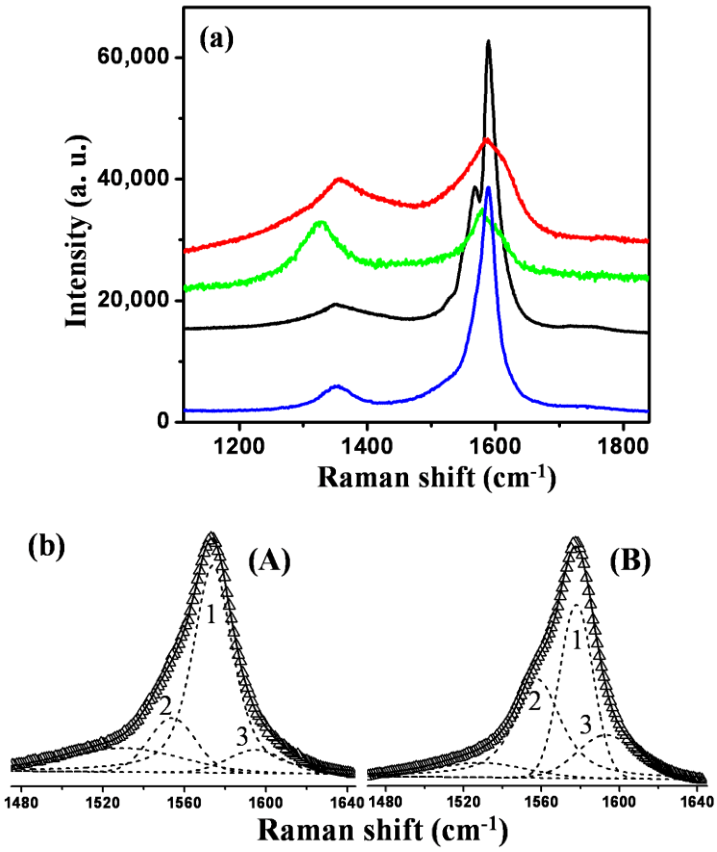

Figure 3.11. (a) Superimposed Raman spectra of pristine-SWCNTs (black line), s-SWCNTs (blue line), SWCNTs-$CONH(CH_2)_{12}CH_3$ prepared by oxalyl chloride (green line) and SWCNTs-$CONH(CH_2)_{12}CH_3$ prepared by thionyl chloride (red line) respectively, which indicate a relative decrease in I_G/I_D ratio revealing amine functionalization **(b)** G-band splitting of (A) pristine-SWCNTs and (B) s-SWCNTs revealing an increase in the peak at 1558 cm^{-1} causing much damage to the side-walls after the microwave treatment.

The microwave treatment on SWCNTs in presence of such concentrated acid mixture gives a remarkable degree of solubilization and debundling, facilitating the narrow distribution of nanotube diameter. Interestingly, this has been found to be less feasible in the case of a single acid treatment. Most importantly, an increase in the ratio I_G/I_D in the case of s-SWCNTs appears to contradict the findings from previous reports, where a chemical functionalization adds to a defect site contribution [28]. This is quite acceptable in the present case, since removal of non-graphitic carbon impurities and catalyst particles after the microwave treatment could indeed, reduce the D-band intensity, and hence logically, such treatment would cause an enhancement to the purity of the sample. Further, the RBM peaks are absent in case of SWCNTs-$CONH(CH_2)_{12}CH_3$, perhaps due to strong covalent wrapping of tridecylamine on the nanotubes. Significantly, the G-band has been seriously affected and shifted to the higher wavenumbers by 4 cm^{-1}, which could further be clarified by looking at the splitting after the microwave treatment. The deconvolution of this G-band gives a decrease of peak ratio (marked as 1 and 2 in Figure 3.11(b)) suggesting a higher degree of sidewall functionalization or debundling of SWCNTs leading to the defect site formation, which could further facilitate the amine functionalization.

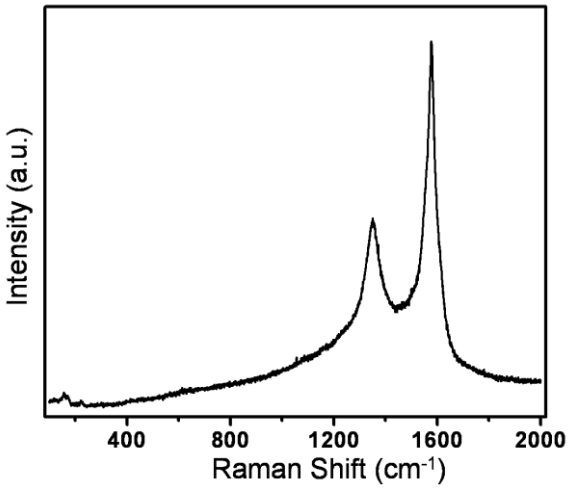

Figure 3.12. Raman spectra of SWCNT-$COHNC_6H_5$, revealing the considerable increase in the I_D/I_G ratio.

In addition, Figure 3.11(a) (green curve) shows a Raman spectrum of tridecylamine functionalized SWCNTs, revealing a decreased I_G/I_D ratio presumably indicating a remarkable extent of amide linkages on the side walls as well as on the broken ends. Interestingly, a comparison of SWCNTs-$CONH(CH_2)_{12}CH_3$ prepared by two different methods viz., oxalyl chloride and thionyl chloride clearly shows increased I_G/I_D ratio in case of former, indicating a more efficient and higher degree of amidation.

Similarly, Raman spectrum of SWCNT-$COHNC_6H_5$ also shows (as shown in Figure 3.12) an increase in the I_D/I_G ratio due to a stronger covalent functionalization. Interestingly, features related to the rest of the nanotube network and its electronic structure, except the side wall functionalization, have been preserved during such functionalization, which are evidenced by FTIR and Raman spectroscopy.

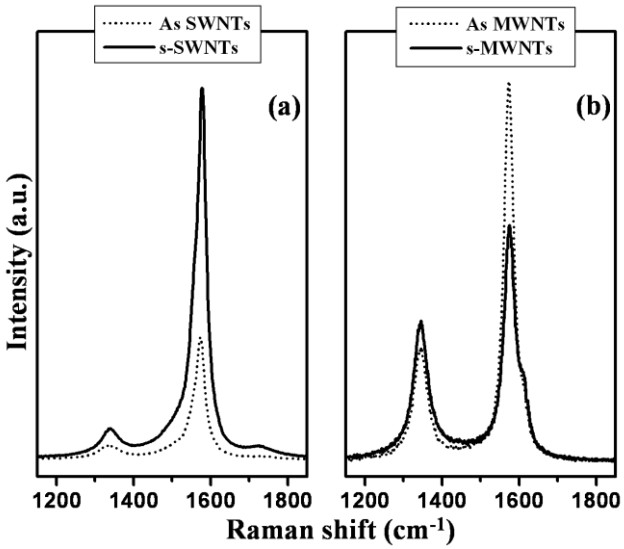

Figure 3.13. Raman spectra for **(a)** SWCNTs and **(b)** MWCNTs before and after microwave treatment respectively, showing enormous variations in the G-band due to sidewall functionalization.

More significantly, the loss of weight in case of s-SWCNTs after microwave treatment perhaps arises due to the dissolution of nontubular contents or amorphous carbon in the sample. This leads to the purification of the sample with more than 95%, with concomitant damage of the side-walls. This could be confirmed with the results of Raman studies, where the intensity ratio I_G/I_D decreases in case of s-MWCNTs, whereas the ratio has been increased in case of s-SWCNTs. Accordingly, Figure 3.13(a) and

3.13(b) show comparative Raman spectra for SWCNTs and MWCNTs respectively, before and after the microwave treatment. It indicates that, the formation of graphitic nanoparticles in case of MWCNTs leads to the generation of defect sites on the side walls after microwave treatment, whereas the removal of amorphous /nontubular carbon in case of SWCNTs adds to the purity of the sample [28,30].

3.3.2. Surface Topography after Functionalization

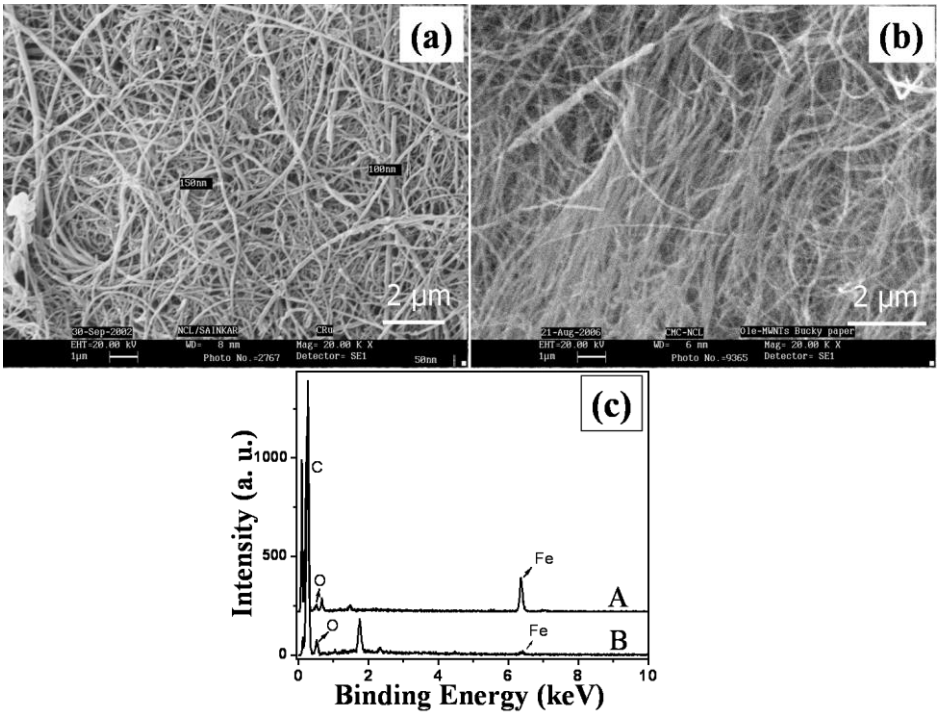

Figure 3.14. Scanning electron micrographs of **(a)** pristine MWCNTs and **(b)** s-MWCNTs showing alignment due to intertubular interaction **(c)** superimposed EDX spectra exhibiting the presence of more than 6 wt% of oxygen along with a decrease in Fe content after microwave irradiation (see in B).

Figure 3.14 exhibits a comparison of the SEM images of 'as-synthesized' MWCNTs (a) and s-MWCNTs (b) revealing a compact structure of the resultant nanotubes after functionalization despite the use of these harsh experimental conditions. Importantly, the MWCNTs are found to be unperturbed with respect to their length, which means that the cutting of nanotubes has not occurred during irradiation [18c,r].

Figure 3.14(b) also reveals that, most of the nanotubes are aligned parallel to one another perhaps, due to strong intertubular electrostatic interactions (Vs. weak van der Waals interactions for the pristine nanotubes) among surface functional groups. However, this kind of interaction is absent in case of pristine MWCNTs as shown in Figure 3.14(a), since the hydrophobic surface of MWCNTs (with sp^2 graphene stacking) leading to repulsion among tubes, results into the random orientation of nanotubes. Interestingly, no change in its diameter is observed after microwave treatment, which could be due to the exceptionally high structural stability attributed to several graphitic layers.

Presence of less than 2-3% catalyst content in the "as-synthesized" sample of MWCNT gets reduced substantially during the microwave irradiation, since no peak corresponding to Fe catalyst is detected in the EDX spectrum (as shown in Figure 3.14c(B)). EDX spectrum also shows the peaks corresponding to carbon and oxygen with ca, 6 wt% latter suggesting an appreciably higher extent of oxygenation. However, XPS analysis (as discussed in section 3.3.5) shows an unusual extent of functionalization (containing groups like –COOH, $-SO_3H$, -OH and $–NO_2$) with more than 30 wt% of oxygen after the microwave treatment, which could perhaps render a remarkable degree of solubilization in aqueous media.

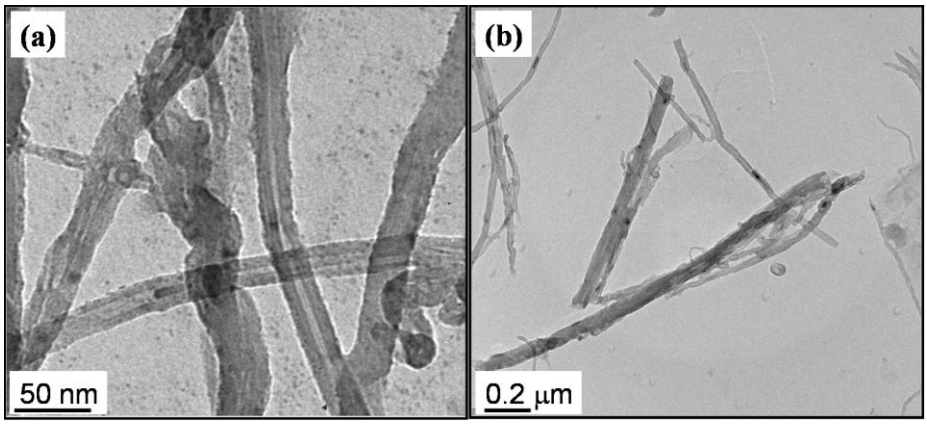

Figure 3.15. Low resolution TEM images of s-MWCNTs showing **(a)** the formation of carbon nanoparticles in the range of 2-4 nm **(b)** tube openings due to breaking of fullerene caps after microwave irradiation.

The topographical changes are explicit from their TEM images, where microwave produces an abundance of defect sites, leading occasionally even to the opening of

fullerene caps of the nanotubes. Accordingly, the TEM image (Figure 3.15(a)) of s-MWCNTs shows carbon nanoparticles ranging from 2-4 nm (produced due to the breaking / chopping of tubular carbon as well as amorphous impurities [30d]), whereas the existence of such nanoparticles in s-SWCNTs is not observed indicating a true solution of s-SWCNTs after microwave irradiation. However, Wang et al, have reported the existence of such carbon nanoparticles (100-300 nm) at a concentration of 0.1 mg/mL in presence of a surfactant [16]. This could be possibly due to severe damaging of tubular carbon along with amorphous impurities observed in their studies. Figure 3.15(b) also shows the opening of fullerene caps after the microwave treatment, eventually facilitating the removal of catalyst impurities.

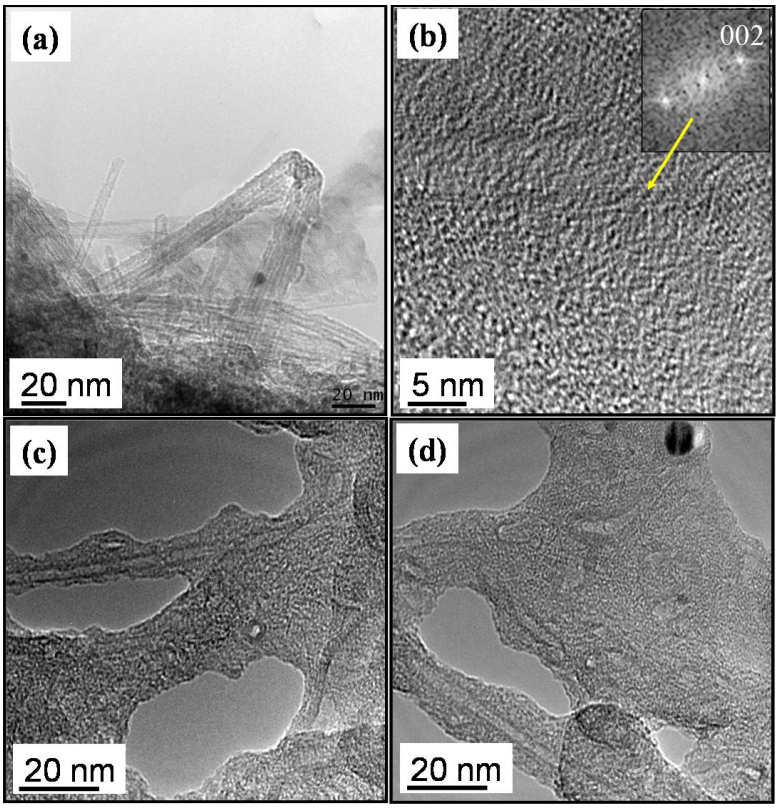

Figure 3.16. High resolution TEM images of **(a)** pristine SWCNTs **(b)** s-SWCNTs **(c)** SWCNTs-$CONH(CH_2)_{12}CH_3$ and **(d)** SWCNTs-$CONH(CH_2)_{17}CH_3$, which clearly show morphological differences after functionalization; s-SWCNTs show the debundling to certain extent, while the 002 reflection if Fast Fourier Transform (FFT) image in the inset of (b) clearly shows strong van der Waal's interaction among individual nanotubes; amine functionalized SWCNTs show a large amount of organic molecules around nanotubes, hence precluding resolved images of the nanotubes.

On the other hand, Figure 3.16 indicates high resolution TEM images of pristine-SWCNTs, s-SWCNTs, SWCNTs-CONH$(CH_2)_{12}CH_3$ and SWCNTs-CONH$(CH_2)_{17}CH_3$, showing copious sites of defects (damaged walls) after the microwave processing and amine functionalization. This unresolved image (but still graphitic fringes are seen) of s-SWCNTs also indicates some electrostatic interactions among nanotube bundles. In fact, an effective debundling would lead to enhanced solubility, although the bundles are still clearly seen in Figure 3.16(b). This could be clarified by the Fast Fourier Transform (FFT) image of the Figure 3.16(b), shown in the inset, where the strong 002 reflection reveals the presence of graphitic interactions (intertubular). Amine functionalized SWCNTs show a large amount of wrapping of organic molecules around nanotubes (as shown in Figure 3.16(c and d), thus precluding high resolution images, which reveal a higher extent of functionalization.

Similarly, Figure 3.17 reveals the TEM image of the SWCNT-COHNC_6H_5 sample, indicating the debundling of the SWCNTs upto a certain extent. The presence of few nanoparticles/aggregates in the micrograph could be due to non-tubular carbon present in the sample, even after a rigorous microwave treatment.

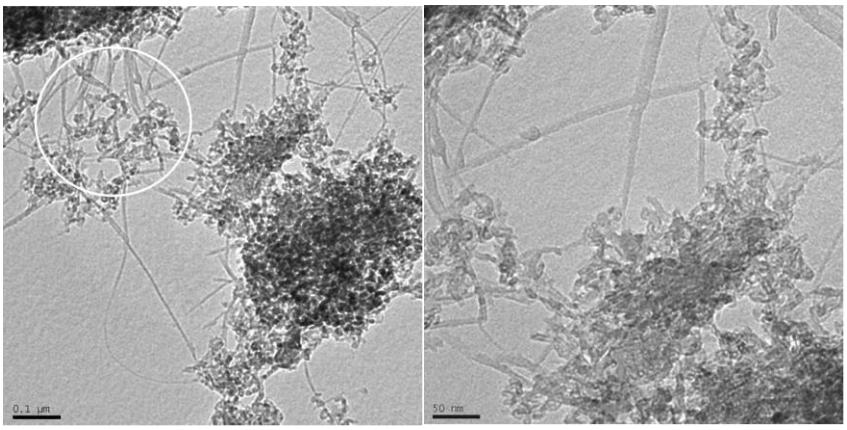

Figure 3.17. TEM images of SWCNT-COHNC_6H_5 showing the non-tubular carbon content with aggregates; encircled portion of the image shows the organic coating of the nanotubes, although a clear image of separate SWCNT is difficult.

An aqueous solution with concentration of s-SWCNTs more than 2-3 mg/mL remains stable without any precipitation even up to 6 months, while SWCNTs-CONH$(CH_2)_{12}CH_3$ and SWCNTs-CONH$(CH_2)_{17}CH_3$ form stable solutions in toluene,

CS_2, CH_2Cl_2 and $CHCl_3$ which remain same for more than 6 months. In addition, the unusual solubility of both s-SWCNTs and SWCNTs-$CONH(CH_2)_{12}CH_3$ in their respective solvents might be due to the covalent functionalization rather than non-covalent [29]. However, the solubility of SWCNT-$COHNC_6H_5$ is very poor in CH_2Cl_2, $CHCl_3$ and CS_2 although it is completely insoluble in water. However, a very little solubility (less than 0.05 mg/mL) has been also observed in solvents like toluene and dimethylformamide (DMF), where a stable suspension could be obtained for a longer period. This means that, despite the absence of alkyl side chain on the aniline ring, a better dispersion of SWCNTs can be obtained due to a remarkable degree of covalent functionalization after the microwave solubilization. Hence, the microwave treatment in presence of acid mixture could furnish a better pre-treatment strategy towards the nanotube engineering to tune their solubility and wetting behavior.

3.5.3. Electrochemical Behavior

Functionalized CNTs are of great interest as electrodes for many applications including fuel cells, electrocatalysis and chemical/biological sensing [31,32]. This is because of the ease with which the carbon nanotube surface can be modified either by physisorption or by covalent functionalization. Several approaches have been reported, where the covalent linkages have been activated using electrochemical oxidation of amines in presence of carbon [33,34]. However our understanding on the electrochemical behavior of SWCNT is incomplete and many more studies are necessary with respect to functionalization.

Accordingly, Figure 3.18(a) shows superimposed cyclic voltammograms of pristine SWCNTs (green line), s-SWCNTs (black line) and SWCNT-$CONH(CH_2)_{12}CH_3$ (red line) at 100 mV/s in 0.1 M H_2SO_4. Figure 3.18(b) and (c) exhibit a scan rate dependent voltammograms for s-SWCNTs and SWCNT-$CONH(CH_2)_{12}CH_3$ respectively. A set of broad quasi-reversible peaks for s-SWCNTs at 0.382 V (anodic) and 0.196 V (cathodic) respectively is observed at 100 mV/s, which is attributed to the redox behavior of the oxygenated functional groups generated on the side-walls after microwave treatment. This is in good agreement with the earlier reports, where a pair of redox peaks

has been assigned to some oxygenated groups developed during the pretreatment [35]. The peak-to-peak separation (ΔEp) is found to increase with scan rate along with appreciable peak broadening effects, indicating a broad and random distribution of oxygenated carboxylic groups. A pair of similar peaks is observed in case of oxygenated GC electrode in highly acidic media revealing the oxidation of graphitic surface [35].

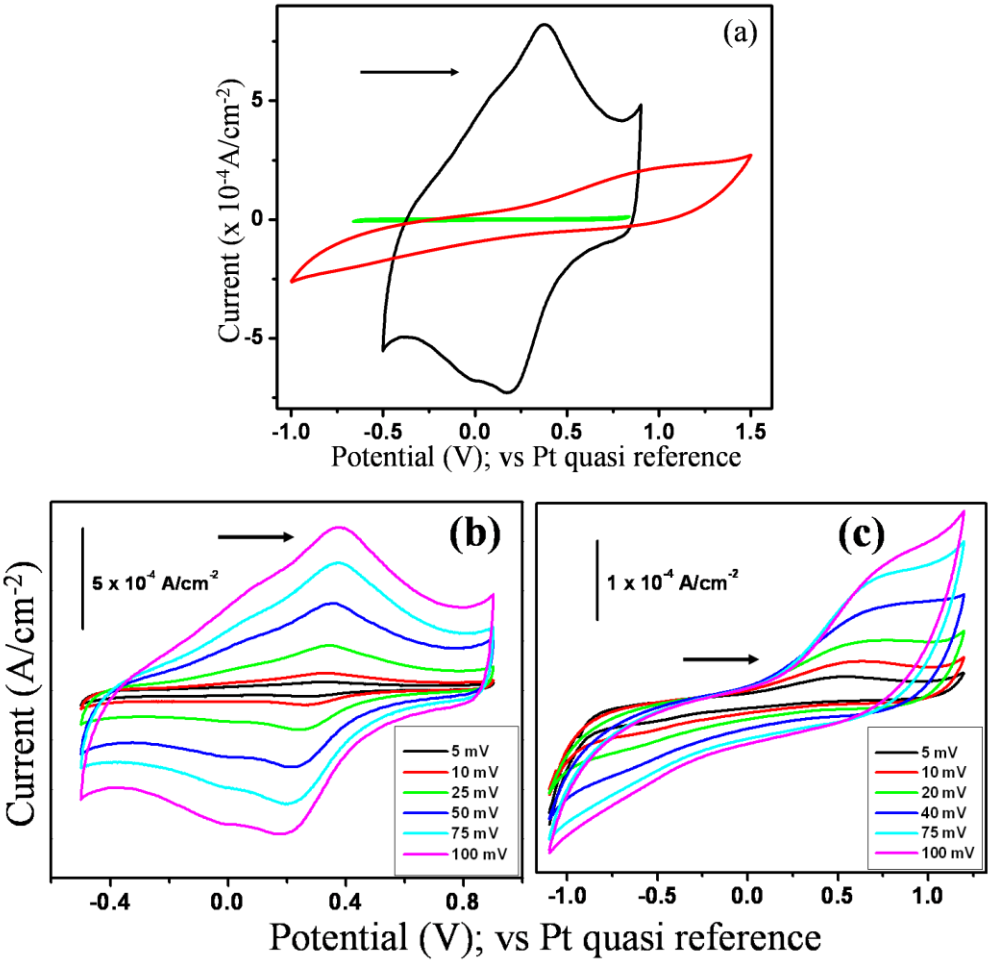

Figure 3.18. (a) Superimposed cyclic voltammograms of pristine SWCNTs (green line), s-SWCNTs (black line) and SWCNT-$CONH(CH_2)_{12}CH_3$ (red line) at 100 mV/s in 0.1 M H_2SO_4 ;**(b)** scan rate dependent CV of s-SWCNTs, revealing an unperturbed reversible redox peak corresponding to oxygenated groups, and **(c)** scan rate dependent CV of SWCNT-$CONH(CH_2)_{12}CH_3$, showing no special features except a decrease in the capacitance after functionalization; arrow indicates the direction of scan.

In addition, a minor reversible peak at 0.089 V (anodic) and -0.015 V (cathodic) in the case of s-SWCNTs is also perceptible to the oxygenated functional groups. The

capacitance of this sample is estimated to be ~110 F/g, which is higher compared to that of graphitized carbon black (~6 F/g) [36] perhaps due to exfoliated side-walls of nanotubes generated during the pretreatment [18c]. In addition, SWCNT-$CONH(CH_2)_{12}CH_3$ shows a rather different charge transfer behavior in its electrochemical studies, where the double layer capacitance (~8 F/g) has been decreased on amidation perhaps could be due to resistive long chain amine.

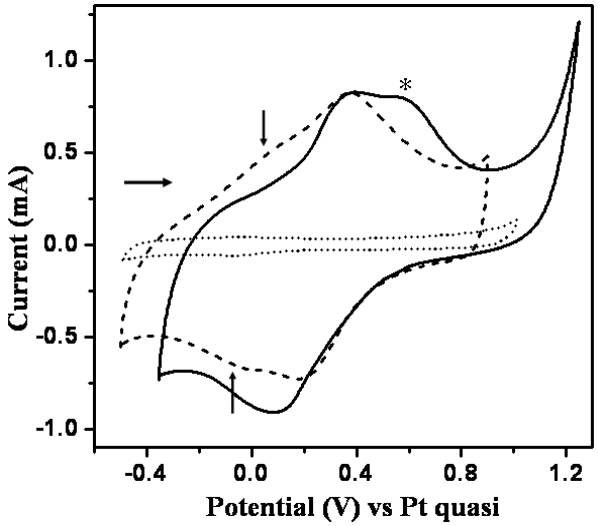

Figure 3.19. Superimposed cyclic voltammograms of as-received SWCNTs (dotted line), s-SWCNTs **(**thick line**)** and SWCNT-$COHNC_6H_5$ **(**dashed line**)** at 0.1 V/s scan rate in 0.1 M H_2SO_4.

In order to increase the capacitance of nanotubes, it is essential to either enhance the surface area or to utilize the pseudocapacitance effects obtained by the addition of special oxides or electrically conducting polymers (ECP) like polypyrrole (PPy), polyaniline (PANI) or by other appropriate functionalization techniques. Accordingly, we have studied the electrochemical responses of SWCNTs after anchoring aniline covalently on the sidewalls.

Thus, Figure 3.19 shows superimposed cyclic voltammograms of pristine SWCNTs (dotted line), s-SWCNTs (dashed line) and SWCNT-$COHNC_6H_5$ (thick line) at 100 mV/s in 0.1 M H_2SO_4. Interestingly, the voltammetric behavior of s-SWCNT remains the same even after aniline attachment except few minor changes. For example, an additional irreversible anodic peak is observed at 0.586 V (marked as star in Figure

3.19), perhaps corresponding to the oxidation of adsorbed aniline on the side-walls, although its position remain unaffected with respect to the scan rate and with the number of cycles. This indicates strong adsorption of aniline molecules on the nanotube surface, despite the presence of H_2SO_4.

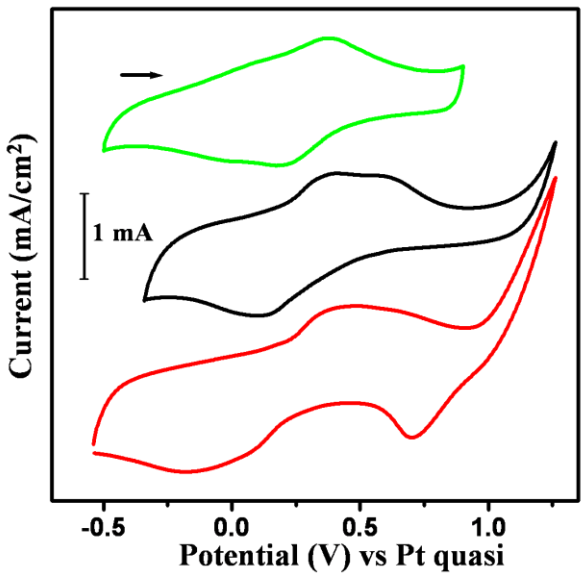

Figure 3.20. Cyclic voltammograms of s-SWCNTs (green line), SWCNT-$COHNC_6H_5$ (black line) in 0.1 M H_2SO_4 and SWCNT-$COHNC_6H_5$ (red line) in 0.1 M HCl at 0.1 V/s scan rate, where a prominent peak corresponding to polymerization is clearly seen in case of HCl (thick line).

However, the voltammetric response in presence of HCl shows a reversible redox behavior at 0.727 V, indicating doping of HCl (shown in Figure 3.20) to form a dynamic layer of polyaniline, which is in agreement with that present in many available reports [37]. The cathodic peak corresponding to the nanotubes has been shifted towards negative direction by 90 mV after several cycles, perhaps due to the formation of a thin polymer layer with subsequent covering of nanotubes [37]. More studies are needed to unravel this change, especially since the thin polyaniline film does not seem to grow further.

Figure 3.21 shows superimposed complex plane impedance plots of s-SWCNTs (O) and that of SWCNT-$COHNC_6H_5$ (□), where the higher frequency domain is fitted to a semicircle for analysis using with a Randles equivalent circuit as shown in the inset of Figure 3.21. Impedance analysis of s-SWCNT suggests an initial charge transfer process

at higher frequency domain, attributable to the signature of redox active oxygenated functional groups, which reveals a double layer capacitance (C_{dl}) of 140 F/g exhibiting an exchange current density [i_o = RT / F Rct, where, R = gas constant; 8.314 J, T = absolute temperature, F = Faraday constant; 96500 C and Rct = charge transfer resistance] of 6 $\mu A/cm^2$. However, the complex plane impedance plot for SWCNT-$COHNC_6H_5$ shows a shift in sample resistance (Rs) by 25 ohm cm^{-2} (due to enhanced resistance of sample perceptible to the amidation).

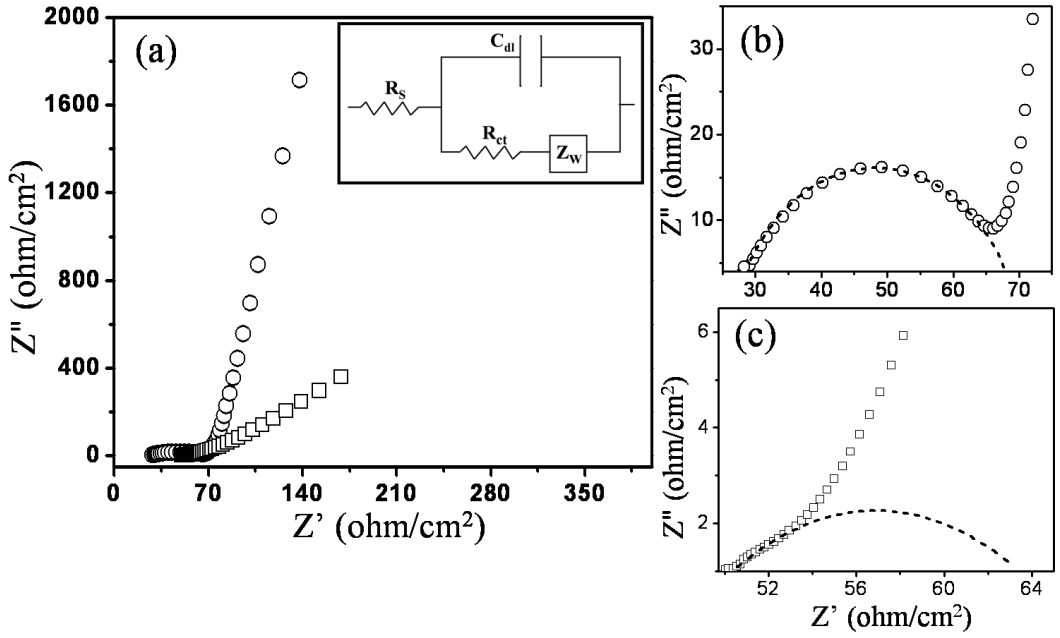

Figure 3.21. (a) Superimposed complex plane impedance plots of s-SWCNTs (O) and that of SWCNT-$COHNC_6H_5$ (□), where the higher frequency domain is fitted to a semicircle in **(b)** and **(c)** respectively for analysis using Randles equivalent circuit shown in inset of (a); dotted line indicates the fitting curve (with $\chi 2$ = 0.99) based on Randles circuit (where, Rs: solution resistance, Cdl: double layer capacitance, Rct: charge transfer resistance and Zw: warburg impedance).

A suppressed semicircle with decreased capacitance shows a C_{dl} of ~20 F/g and an exchange current density of 2.4 $\mu A/cm^2$. The formation of a dynamic polymer layer on the SWCNTs surface has been confirmed by the addition of 10 μL (in 10 mL) of pure and distilled aniline during cyclic voltammetric measurements in presence of H_2SO_4. This kind of hybrid materials with 'metal-semiconductor' or 'metal-metal' core-shell systems would be of immense interest in developing smart materials including chemical sensors,

actuators, photovoltaic cells and various electronic devices to emission probes. The combined analysis of electrochemical results suggests a covalent functionalization of aniline on the SWCNT surface after microwave treatment in acid mixture.

3.6. Conclusions

In conclusion, this chapter deals with a novel technique for the complete phase transformation of SWCNTs from aqueous to organic media, facilitating a new generation of CNT composites capable of controlling their unique properties in a determinable manner. A maximum of 30 wt% of oxygenated groups have been generated on the side walls by rapid microwave treatment, leading to a solubility of more than 2.6 mg/mL in water. A clean and higher, yet quantitative, degree of amidation is achieved by oxalyl chloride preceded by microwave treatment in acid media. Uv-vis analysis shows the disappearance of singularities after microwave treatment and covalent amidation, indicating the blockage for valence electrons due to functionalization. ^{1}H NMR and Raman studies also reveal interesting features that support for a covalent functionalization of SWCNTs with various amines where the formation of polyaniline could be avoided. Electrochemical analysis suggests possible variations on the nanotube topography with the concomitant formation of a polymer layer. The practical utilization of such tunable CNT surfaces, both in aqueous as well as in non-aqueous media, to make high performance polymer composites (e.g., controlling the interfacial adhesion between CNT surface and polymer) would significantly open up new perspectives in the preparation of various polymer composites extending the range of their possible applications including electrocatalysis, chemical/bio-sensing and developing electronic devices such as FETs and SETs.

3.7. References

1. Salvetat, J. P.; Bonard, J. M.; Thomson, N. H.; Kulik, A. J.; Forro, L.; Benoit, W.; Zuppiroli, L. *Appl. Phys. A: Mater. Sci. Process.* **1999**, *69*, 255.
2. Calvert, P. *Nature* **1999**, *399*, 210.
3. Dai, H. *Acc. Chem. Res.* **2002**, *35*, 1035.
4. Pantarotto, D.; Partidos, C. D.; Hoebeke, J.; Brown, F.; Kramer, E.; Briand, J. P.; Muller, S.; Prato, M.; Bianco, A. *Chem. Biol*. **2003**, *10*, 961.
5. (a) Chen, R. J.; Zhang, Y.; Wang, D.; Dai, H. J. *J. Am. Chem. Soc.* **2001**, *123*, 3838. (b) Dresselhaus, M.S.; Dresselhaus, G.; Avouris, P. *Eds. Carbon Nanotubes: Synthesis, Structure Properties, and Applications*, Springer-Verlag: Berlin, Germany, **2001**. (c) Baughman, R.H.; Zakhidov, A.A.; Heer, W. A. *Science* **2002**, *297*, 787. (d) Avouris, P. *Acc. Chem. Res.* **2002**, *35*, 1026.
6. Gao, J.; Zhao, B.; Itkis, M. E.; Bekyarova, E.; Hu, H.; Kranak, V.; Yu, A.; Haddon, R. C. *J. Am. Chem. Soc.* **2006**, *128*, 7492.
7. Pantarotto, D.; Partidos, C.D.; Hoebeke, J.; Brown, F.; Kramer, E.; Briand, J. - P.; Muller, S.; Prato, M. *A. Bianco, Chem. Biol.* **2003**, *10*, 961.
8. Mickelson, E. T.; Huffman, C. B.; Rinzler, A. G.; Smalley, R. E.; Hauge, R. H.; Margrave, J. L. *Chem. Phys. Lett.* **1998**, *296*, 188.
9. Saini, R. K.; Chiang, I. W.; Peng, H.; Smalley, R. E.; Billups, W. E.; Hauge, R. H.; Margrave, J. L. *J. Am. Chem. Soc.* **2003**, *125*, 3617.
10. Bahr, J. L.; Yang, J.; Kosynkin, D.V.; Bronikowski, M. J.; Smalley, R.E.; Tour, J. M. *J. Am. Chem. Soc.* **2001,** *123*, 6536.
11. Holzinger, M.; Abraham, J.; Whelan, P.; Graupner, R.; Ley, L.; Hennrich, F.; Kappes, M.; Hirsch, A. *J. Am. Chem. Soc.* **2003,** *125*, 8566.
12. Holzinger, M.; Vostrowsky, O.; Hirsch, A.; Hennrich, F.; Kappes, M.; Weiss, R.; Jellen, F. *Angew. Chem. Int. Ed.* **2001,** *40*, 4002.
13. Banerjee, S.; Wong, S.S. *Nano Lett.* **2002,** *2*, 49.
14. Chen, J.; Hamon, M. A.; Hu, H.; Chen, Y.; Rao, A. M.; Eklund, P. C.; Haddon, R.C. *Science* **1998,** *282*, 95.

15. Niyogi, S.; Hamon, M. A.; Hu, H.; Zhao, B.; Bhowmik, P.; Sen, R.; Itkis, M. E.; Haddon, R. *Acc. Chem. Res.* **2002**, *35*, 1105.
16. 17Wang, Y.; Iqbal, Z.; Mitra, S. *J. Am. Chem. Soc.* **2006,** *128*, 95.
17. (a) Strano, P. J.; Dyke, C. A.; Usrey, M. L.; Barone, P. W.; Allen, M. J.; Shan, H.; Kittrell, C.; Hauge, R. H.; Tour, J. M.; Smalley, R. E. *Science* **2003**, *301*, 1519. (b) Bronikowaski, M. J.; Willis, P. A.; Colbert, D. T.; Smith, K. A.; Smalley, R. E. *J. Vac. Sci. Technol.* **2001**, *19*, 1800. (c) Saito, A.; Dresselhaus, G.; dresselhaus, M. G. *Physical Properties of Carbon Nanotubes* (Imperial College Press, London, **1998**).
18. (a) Liu, J.; Rinzler, A. G.; Dai, H.; Hafner, J. H.; Bradley, R. K.; Boul, P. J.; Lu, A.; Lverson, T.; Shelimov, K.; Huffman, C. B.; Rodriguez-Macias, F.; Shon, Y. S.; Lee, T. R.; Colbert, D. T.; Smalley, R. E. *Science*, **1998**, *280*, 1253. (b) Bahr, J. L. ; Tour, J. M. *J. Mater. Chem.* **2002**, *12*, 1952. (c) Banerjee, S.; Kahn, M. G. C.; Wong, S. S. *Chem. Eur. J.* **2003**, *9*, 1898. (d) Liu, T.; Kumar, S. *Nano Lett.* **2003**, *5*, 647. (e) Liang, F.; Sadana, A. K.; Peera, A.; Chattopadhyay, J.; Gu, Z.; Hauge, R. H.; Billups, W. E. *Nano Lett.* **2004**, *4*, 1257. (f) Zhao, W.; Song, C.; Pehrsson, P. E. *J. Am. Chem. Soc.* **2002**, *124*, 12418. (g) Qin, S.; Qin, D.; Ford, W. T.; Herrera, J. E.; Resasco, D. E.; Bachilo, S. M.; Weisman, R. B. *Macromolecules,* **2004**, *37*, 3965. (h) Zhao, B.; Hu, H.; Haddon, R. C. *Adv. Funct. Mater.* **2004**, *14*, 71. (i) Georgakilas, V.; Tagmatarchis, N.; Pantarotto, D.; Bianco, A.; Briand, J. P.; Prato, M. *Chem. Commun.* **2002**, 3050. (j) Pompeo, F.; Resasco, D. E. *Nano Lett.* **2002**, *2*, 369. (k) Takahashi, T.; Tsunoda, K.; Yajima, H.; Ishii, T. *Chem. Lett.* **2002**, 690. (l) Dyke, C.; Tour, J. *J. Am. Chem. Soc.* **2003**, *125*, 1156. (m) Bahr, J. Tour, J. *Chem. Mater.* **2001**, *13*, 3823. (n) Dyke, C.; Tour, J. *Nano Lett.* **2003**, *3*, 1215. (o) Nelson, D.; Rhoads, H.; Brammer, C. *J. Phys. Chem. C* **2007**, DOI. 10.1021/jp071326y. (p) Kim, P.; Odom, T.; Huang, J.; Lieber, C. *Phys. Rev. Lett.* **1999**, *82*, 1225. (q) Moniruzzaman, M.; Winey, K. *Macromolecules* **2006**, *39*, 5194. (r) Wang, S. ; Liang, Z. ; Wang, B. ; Zhang, C. ; Rahman, Z. *Nanotechnology* **2007**, *18*,

055301.

19. Davis, V. A.; Ericson, L. M.; Parra-Vasquez, A. N.; Fan, H.; Wang, Y.; Prieto, V.; Longoria, J. A.; Ramesh, S.; Saini, R. K.; Kittrell, C.; Billups, W. E.; Adams, W. W.; Hauge, R. H.; Smalley, R. E.; Pasquali, M. *Macromolecule,* **2004**, *37*, 154.
20. Hudson, J. L.; Casavant, M. J.; Tour, J. M. *J. Am. Chem. Soc.* **2004**, *126*, 11158.
21. (a) Saini, R. K.; Chiang, I. W.; Peng, H.; Smalley, R. E.; Billups, W. E.; Hauge, R. H.; Margrave, J. L. *J. Am. Chem. Soc.* **2003**, *125*, 3617. (b) Hamon, M. A.; Hu, H.; Bhowmik, P.; Niyogi, S.; Zhao, B.; Itkis, M. E.; Haddon, R. C. *Chem. Phys. Lett.* **2001**, *347*, 8. (c) Mark, A. H.; Chen, J.; Hu, H.; Chen, Y.; Itkis, M. E.; Rao, A. M.; Eklund, P. C.; Haddon, R. C. *Adv. Mater*. **1999**, *11*, 834.
22. Andrews, R.; Jacques, D.; Rao, A. M.; Derbyshire, F.; Qian, D.; Fan, X.; Dickey, E. C.; Chen, J. *Chem. Phys. Lett.* **1999**, 303, 467.
23. MSDS of oxalyl chloride http://www.jtbaker.com/msds/englishhtml/o6180.htm. OR http://msds.chem.ox.ac.uk/OX/oxalyl_chloride.html.
24. Do Nascimento, G. M.; Corio, P.; Novickis, R. W.; Temperini, M. L. A.; Dresselhaus, M. S. *J. Poly. Sci.: Part A: Polymer Chemistry*, **2005**, *43*, 815.
25. Zhang, X.; Zhang, J.; Liu, Z. *Appl. Phys. A.* **2005,** *80*, 1813.
26. Hamon, M. A.; Chen, J.; Hu, H.; Chen, Y.; Itkis, M. E.; Rao, A. M.; Eklund, P. C.; Haddon, R. C. *Adv. Mater*. **1999**, *11*, 834.
27. Using the atomic sensitivity factors the ratio of C:O is calculated using the relation- C1s / O1s = $[I_C / I_O] \times [\sigma_O / \sigma_C] \times [K.E._C / K.E._O]^{1/2}$

    where, I_C is the area under the curve of deconvulated C1s, I_O is the area under the curve of deconvulated O1s, σ_O and σ_C are the atomic sensitivity factors for O(=2.85) and C(=1) respectively and $K.E._C$ and $K.E._O$ are the kinetic energies of the electron of C and O respectively.

    K.E. = [Source energy – Binding energy of element],

    The atomic sensitivity factors (σ) for N1s, $S2p_{3/2}$, $S2p_{1/2}$, $Fe2p_{3/2}$ and $Fe2p_{1/2}$ are 1.15, 0.1302, 10.54 and 5.43 respectively.

28. (a) Gu, Z.; Peng, H.; Hauge, R. H.; Smalley, R. E.; Margrave, J. L. *Nano Lett.* **2002**, *2*, 1009. (b) Chen, C. M.; Dai, Y. M.; Huang, J.G.; Jehng, J. M. *Carbon* **2006,** *44*, 1808.
29. Dresselhaus, M. S.; Dresselhaus, G.; Jorio, A.; Souza Filho, A. G.; Pimenta, M. A.; Saito, R. *Acc. Chem. Res.* **2002**, *35*, 1070.
30. (a) Banerjee, S.; Benny, T. H.; Balasubramanian, M.; Fischer, D. A.; Misewich, J. A.; Wong, S. S. *Chem. Phys. Chem.* **2004**, *5*, 1416. (b) Hentschke, R.; Winkler, R. G. *J. Chem. Phys.* **1993**, *99*, 5528. (c) Park, C.; Engel, A.; Crowe, E. S.; Rodriguez, N. M. *Langmuir* **2000**, *16*, 8050. (d) Liang, Z.; Wang, Z.; Wang, B.; Zhang, C. *Methods for mechanically chopping carbon nanotube and nanoscale fibrous materials*, US patent No. 20060017191, Class 264140000.
31. Leventis, H.C.; Streeter, I.; Wildgoose, G.G.; Lawarence, N.S.; Jiang, L.; Jones, T. G. J.; Compton, R.G. *Talanta* **2004**, *63*, 1039.
32. Wildgoose, G.G.; Leventis, H.C.; Streeter, I.; Lawarence, N.S;. Wilkins, S. J.; Jiang, L.; Jones, T. G. J.; Compton, R.G. *Chem. Phys. Chem.* **2004**, 5, 669.
33. (a) Dawnard, A. J. *Electroanalysis* **2000**, *12*, 1085. (b) Barbier, B.; Pinson, J.; Desormot, G.; Sanchez, M. J. *Electrochem. Soc.* **1990**, *137*, 1757.
34. Delamar, M.; Hitimi, R.; Pinson, J.; Saveant, J.–M. *J. Am. Chem. Soc.* **1992**, *114*, 5883.
35. (a) Luo, H.; Shi, Z.; Li, N.; Gu, Z.; Zhuang, Q. *Anal. Chem.* **2001**, *73*, 915. (b) Barisci, J. N.; Wallace, G. G.; Baughman, R. H. *J. Electroanal. Chem.* **2000**, *488*, 92. (c) Barisci, J. N.; Wallace, G. G.; Baughman, R. H. *J. Electrochim. Acta* **2000**, *46*, 509. (d) Barisci, J. N.; Wallace, G. G.; MacFarlane, D. R.; Baughman, R. H. *J. Electrochem. Comm.* **2004**, *6*, 22.
36. Kinoshita, K. *Carbon: Electrochemical and Physical Properties*, Wiley: New York, **1988**.
37. (a) Fujita, I.; Ishiguchi, M.; Shiota, H; Danjo, T.; Kosai, K. *J. Appl. Poly. Sci.* **1992**, *44*, 987. (b) Downs, C.; Nugent, J.; Ajayan, P. M.; Duquette, D. J.; Santhanam, K. S. V. *Adv. Mater.* **1999**, *11*, 1028.

CHAPTER 4

Tuning the Wetting Properties of Multiwall Carbon Nanotube based Bucky Papers*

A simple strategy of chemical functionalization is employed here for controlling the wettability of multiwalled carbon nanotube films from superhydorphobic (CA ≥ 156°) to nearly hydrophilic (CA < 40°), which further shows a water contact angle of about 0° within 2 seconds. Functionalized bucky paper (with CA 145°) shows an unusual pinning action even at a tilt angle of 45°, following Wenzel behavior of the surface. The variation in wetting properties of MWCNT bucky paper using such surface functionalization strategies provides controlled heterogeneity on the surface with no or minimal effect of surface roughness. Further, the superhydrophobic MWCNT bucky paper, synthesized by ozonolysis shows fascinating wetting behavior as a result of the application of electric field. The electrowetting of such bucky paper has been studied as a function of ionic strength, nature of electrolyte and pH of the liquid droplet. Droplet behavior can be reversibly switched between superhydrophobic, Cassie-Baxter state to hydrophilic, Wenzel state by the application of electric field, especially below a threshold value.

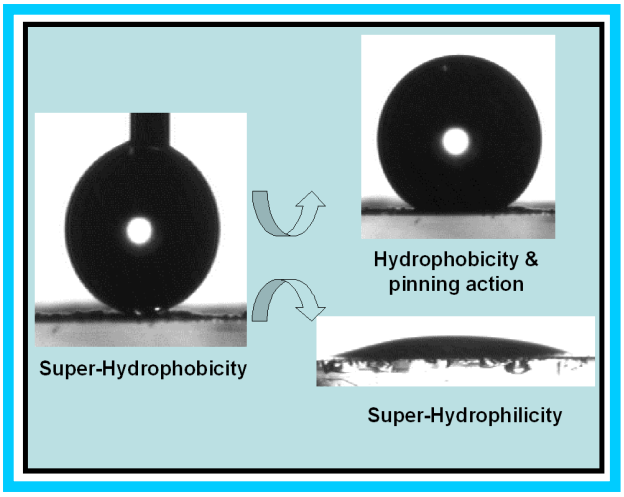

---

* A part of the work discussed in this chapter has been published in: *J. Phys. Chem. C* **2008,** *112,* 3183.

4.1. Introduction

Variation of both chemical composition and the geometrical structure of solid surfaces[1,2] to control the wetting behavior is of enormous importance for many processes in living organisms [3-5] and for numerous industrial applications such as design of self cleaning glass, smart windows and adhesive fixtures. As a result, many superhydrophobic surfaces have been designed by a wide variety of methods ranging from lithographic fabrication to the transformation of a simple plastic substrate by surface functionalization [6-8] as well as by surface roughening [9-16]. For example, a temperature induced fine control over wettability of colloidal-crystal films of latex spheres has been reported recently, where the surface roughness is indeed tuned by temperature [17]. Similarly, a fluoroalkylsilane coated aligned CNT forest has been more recently shown to be super-amphiphobic with water and oil due to chemical interactions pertaining to the fluoroalkylsilyl groups [2]. Since carbon nanotubes have a perfect graphitic network of sp^2 carbon, they exhibit intrinsic hydrophillic behavior (contact angle $< 90^o$), where further functionalization or texture-change could facilitate easy control of their wetting properties [18].

Although many chemical functionalizations have been recently carried out on both single and multiwalled CNTs, no report is available to date, on their functionalization-dependent tuning of wetting behavior despite the importance. On the other hand, surface properties of CNTs especially if they are in the form of paper or mat, offer the possibility of using them in more compact form for easy processing. Finally the interactions of CNTs (both pristine as well as functionalized) with various liquids are also important for understanding a variety of new phenomena including voltage generation up on liquid flow for developing flow sensors [19]. Wetting properties of single shell CNTs have effectively been shown to be crucial for understanding the capillary action and the transition from wetting to nonwetting using various liquids, which could in principle, facilitate to do the solution chemistry inside the open ends of nanotubes [20-22]. Indeed, the wetting properties of fibers may differ significantly from those of plane solid surfaces and the effect of curvature (diameter dependence) can be important [23]. For example,

Mattia et al, have recently shown a disordered wetting of CVD grown carbon films and nanopipes using both polar and non-polar liquids [24].

All the above results undoubtedly, demonstrate the significance of tuning the surface properties of CNTs for various applications. For instance, a combination of surface roughness/inhomogeneity (geometrical or fractal surfaces) and surface energy (chemical) can make CNT surface superhydrophobic, if they are aligned vertically with a diameter of few microns [25]. As explained in the first chapter, tuning of hydrophobicity/hydrophilicity of CNT surface is one of the daunting challenges in order to engineer them into proper geometry and also to formulate composite coatings due to a lower value of surface tension (~27 mN/m). Unfortunately, no one has demonstrated the ability to control the hydrophobicity/hydrophilicity of MWCNTs in the form of bucky paper, on the basis of chemical functionalization. Hence, a correlation between the surface functionalization and externally manifested wetting characteristics of a surface is of tremendous utility in order to understand a variety of phenomena including anti-fogging, self cleaning and water repellent behavior which might be important to develop novel and robust hybrid coatings.

In many of these applications, it would also be of immense importance to externally control the interaction of liquids with the superhydrophobic surface, including the modification of contact angle, droplet mobility, and degree of penetration. Consequently, several recent reports have attempted to achieve a dynamic control over wettability of superhydrophobic solid surfaces [26]. For example, the application of electric field to aligned CNT surface has been shown to reduce the interfacial tension between solid and liquid [26]. More recently, a dynamic electrical control of the whole range of wetting behavior (from hydrophilic to superhydrophobic) of liquids on nanostructured surfaces has been reported [28]. This way of electrical modulation of the wetting of carbon nanotubes, indeed, has many profound implications in nano-fluidic transport, irrespective of the nature of the application. More interestingly, controlling the wetting behavior of low-melting metals like Ga and In could be favorably utilized to crystallize them into continuous nanowires, which would further facilitate fundamental

investigations in determining their unusual electrical and magnetic properties like Luttinger liquid behavior [29,30].

Buckypapers are usually thin films of carbon nanotubes with layered structure, their wetting characteristics could be modulated between the extremes by changing the surface roughness [31]. As such, one can prepare papers which are wetted selectively by water with unique behavior. This applies equally important to other liquids such as oil and by a proper preparation and functionalization one could even create solid surfaces that have coexisting hydrophobic and amphiphilic domains facilitating the separation of the two [31]. Interesting report of the forests of aligned carbon nanotubes show superhydrophobic behavior due to a higher degree of surface roughness as a result of microdomains between nanotubes grown on a substrate [27], although superhydrophobicity, generally, requires both low surface energy and high surface roughness [25,31].

The wetting properties of such superhydrophobic nanotube surfaces could also be effectively controlled using external forces like electric and magnetic field. For example, Froumkine and co-workers have shown a wetting of polarized metal surface by electrolyte [32], similar to the one used by Lippman [33]. This effect has been made clearer by studying a thiol self-assembled monolayer on a metal surface [34]. For example, nanostructured parylene films deposited on the arrays of aligned MWCNTs have shown effective electrowetting without any saturation limit upto 80 V [35]. However, aligned growth of nanotubes on any solid substrate is practically a tedious process as this needs a stringent control over various parameters such as selection of catalysts, precursor gas/liquid, and carrier gas (and its flow rate) during the synthesis. In order to achieve flexibility in such superhydrophobic nanotube films, fabrication of bucky paper could be an alternative with concomitant control over their wetting properties by suitable functionalization strategy. Surprisingly, there are no reports on the electrowetting behavior of continuous film of MWCNTs despite its significance in many aforementioned applications. Hence, a correlation of electric field on the wetting behavior of nanotube paper as a function of ionic strength, nature of electrolyte and pH is

of immense importance to understand the fundamental chemistry and physics of nanotube surface.

Consequently, in this chapter, first we describe a method of tuning the hydrophobicity of MWCNTs in the form of bucky paper using unique functionalization strategies. In chapter 3 we had already discussed a strategy to get soluble nanotubes using microwave treatment followed by a unique covalent functionalization for their efficient phase-transformation and these studies indeed supplement for the variations in wetting properties of nanotubes. Thus extent of the hydrophobicity / hydrophilicity of the bucky paper can be tuned remarkably by surface functionalization using different routes. Surface roughness is engineered through a covalent coupling facilitating a change in both the surface chemical composition and the geometrical microstructure to generate hierarchical structures where the water contact angle (CA) can be anywhere between 40^o to 156^o. Secondly, we discuss the electrowetting of hydrophobic bucky papers of MWCNTs (prepared after ozonolysis), demonstrating an interesting transition from superhydrophobic, Cassie-Baxter to hydrophilic, Wenzel form. An initial contact angle of 156^o with slight pinning properties (roll off angle of 16^o) has been made superhydrophilic with an external electric field. In this regard, the effects of ionic strength, type of electrolyte and pH on the electrowetting of bucky paper have been systematically studied and modeled to deduce the differential capacitance at the bucky paper-liquid interface. Our results indicate that this type of controlling the hydrophobic surfaces of bucky papers on the side walls of MWCNTs could be useful for many potential applications due to the low surface energy with tunable contact angle.

4.2. Experimental Section

4.2.1. Materials

MWCNTs were prepared by a CVD method [36] using a ferrocene and xylene mixture at 700 ^oC with the help of the set-up mentioned in greater details in chapter 2. Tridecylamine (TDA), octadecylamine (ODA), sodium dodecyl sulphonate (SDS), potassium bromide (KBr; spectroscopy grade) and oxalyl chloride were used as received

from Aldrich (99.99%), while toluene, dichloromethane, acetone, tetrahydrofuran (THF), and nitric acid were used as received from Merck (AR grade), deionized water (16 MΩ) from a Milli-Q system was used for all experiments. Fuming sulphuric acid (oleum) obtained from s. d. fine chemicals and was used as received.

4.2.2. Fabrication of MWCNT Bucky Papers

In the first experimental approach, the surface of MWCNT was modified using different oxidizing treatments like ozonolysis (B), refluxing in 3:1 nitric acid (C), refluxing in 3:1 nitric acid followed by soaking in the same acid (D) for 30 days, refluxing in acid mixture (1:1 78% HNO_3 and 98% H_2SO_4: E), microwave treatment in presence of acid mixture (1:1 78% HNO_3 and fuming H_2SO_4: G) and covalent coupling with aliphatic mono (tridecylamine; F) and diamine (1,8-diaminooctane: H) respectively to create diverse surface functionalities, as summarized in Table 4.1 along with probable functional groups produced during these treatments.

Table 4.1. A summary of the functionalization procedures adopted for each sample along with dominant functional groups generated during this.

Sample	Treatment	Functional group	Number of acidic sites (g^{-1}) as estimated by acid-base titration
A	As synthesized sample	Graphitic C (sp^2)	-
B	Ozonolyzed MWCNTs	$-COOCH_3$	-
C	Refluxed in 3:1 nitric acid for 8 h	-OH (major), -COOH	2×10^{20}
D	Refluxing and soaking in 3:1 nitric acid	-OH (major), -COOH	$2\text{-}3 \times 10^{20}$
E	Refluxed in acid mixture (1:1 78% HNO_3 and 98% H_2SO_4)	-OH, -COOH	5×10^{20}
F	Covalent coupling with tridecylamine (TDA)	$-CONH(CH_2)_{12}-CH_3$	-
G	Microwave treatment in 1:1 78% HNO_3 and 98% H_2SO_4 for 4 min	-OH, -COO- (major), $-SO_3H$	50×10^{20}
H	Covalent coupling with 1,8-diaminooctane (DAO)	$-CONH(CH_2)_8-CONH_2$	-
I	Microwave treatment in 98% H_2SO_4 for 4 min	-COOH, $-SO_3H$	$4\text{-}5 \times 10^{20}$

The amount of acidic sites like –COOH, -SO_3H, were determined by a simple titration method using 0.05 M NaOH and 0.05 M HCl solutions and the results have been documented in the Table 4.1. In the second approach, the surface of MWCNTs was modified by varying the molecular level corrugation associated with the lesser amount of functional groups created by treatment with nitric acid. The pristine sample is designated as 'A'. Herein, we have used less crystalline CVD nanotubes (with varying diameter) for our measurements, although CNTs with more uniform diameter and well crystallinity (especially Arc derived) would have given more accurate results. The modified samples of carbon nanotube (bucky papers) were characterized using DRIFT, sessile drop water contact angle (CA) measurements, SEM, EDS, XPS and Raman spectroscopy.

[A] Pristine MWCNTs

MWCNTs used in this study were synthesized by a CVD process as mentioned in chapter 2 with purity >90% and diameter of 20- 30 nm. It also contains ~1% of bigger MWCNTs (100-150 nm, as determined from TEM analysis). A continuous film of MWCNTs was used for contact angle measurements after sticking to a two side tape.

[B] Ozonolysis

62 mg of pristine MWCNTs (above mentioned) was weighed and dispersed in 40 ml of dichloromethane (DCM). The resultant solution was sonicated for about half an hour to get a homogeneous dispersion, which was then subjected for ozonolysis in a suitable reactor (Fischer Ltd) for about an hour. The reaction was quenched using approximately 2 mL of dimethyl sulphide (DMS). The ozonolyzed CNTs were then filtered through a polytetrafluoroethylene (PTFE) membrane with a pore size of 0.2 μm and washed thoroughly to remove excess DMS by DCM. Finally the filtered sample, in the form of bucky paper (60 - 80 μm thick), was dried in vacuum at 100 ^{o}C to remove all solvent impurities. These ozonolyzed bucky papers were also used for electrowetting experiments. The quality of the bucky paper is one of the key factors in order to reproduce the results. Interestingly it has been observed that, the property of the paper is

influenced by the quality and concentration of the CNT dispersion prior to filtration. We find 100 mg per 40 mL of solvent as the optimal concentration of the MWCNTs in order to make smooth and flat bucky papers of 30 mm diameter and thickness of 50 – 60 μm. This condition gives macroscopically a smooth, homogeneous paper that offers better contact between the nanotubes that make up the bucky paper.

[C] Nitric acid treatment

About 60 mg of MWCNT was mixed with 50 mL of 3:1 HNO_3 in water and the mixture was then refluxed for 20 h at 60 ^oC in an oil bath in order to oxidize the graphitic sp^2 carbon to–COOH and -OH groups on the side walls of nanotubes. The acidified nanotubes were filtered through PTFE membrane with a pore size of 0.2 μm and washed thoroughly using deionized water (until the pH of the filtrate reaches 7). Finally, the carbon film (bucky paper) formed on the membrane was washed with acetone followed by drying at 100 ^oC in an oven to remove the moisture. Dried sample of bucky paper was then pressed at 0.2 bar/cm^2 and used for all further experiments.

[D] High Acid treatment

The nitric acid treated MWCNTs (above mentioned) were soaked for 30 days at room temperature in the acid solution. Then these acidified nanotubes were purified and casted in to the bucky paper by similar procedure as mentioned above.

[E] Acid Mixture

60 mg of MWCNT was mixed with 50 mL of 1:1 mixture of 98% H_2SO_4 and 70% HNO_3. The mixture was then refluxed for 24 h at 60 ^oC in an oil bath in order to oxidize the graphitic sp^2 carbon to convert into –COOH and -OH groups on the side walls of nanotubes. The acidified nanotubes were filtered, purified and casted in to the bucky paper by the similar procedure as mentioned above.

[F] MWCNTs-CONH$(CH_2)_{12}CH_3$

About 75 mg of nitric acid treated MWCNTs (dried sample) was mixed with 10 mL of oxalyl chloride and ultrasonicated for 10 min and the reaction was carried out in an argon atmosphere. The mixture was then refluxed for 24 h at 60 ^oC to obtain a higher degree of acylchloride functionalization (MWCNTs-COCl); excess of oxalyl chloride was removed under vacuum using rota-evaporation. MWCNTs-COCl was then mixed with 1 g solid tridecylamine (TDA; $CH_3(CH_2)_{12}NH_2$) and refluxed at 40 ^oC (m. p. of TDA: ~30 ^oC) for 40 h. The reaction mixture was then cooled and washed with copious amount of tetrahydrofuran (THF) with successive sonication and centrifugation to remove excess of TDA. The resulting MWCNTs-CONH$(CH_2)_{12}CH_3$, was then filtered through a PTFE membrane (0.2 μm pore size) and washed using copious amount of THF and a film of 60-80 μm thick bucky paper was casted and dried in an oven at 100 ^oC prior to the application of a pressure of 0.2 bar/cm^2.

[G] Microwave treated MWCNTs (s-MWCNTs)

The procedure described in sections 3.2.2.1 and 3.2.2.2 was repeated to obtain superhydrophilic bucky paper. Acidified nanotubes were filtered through a PTFE membrane with a pore size of 0.2 μm and washed thoroughly using deionized water. Finally, the carbon film (bucky paper) formed on the membrane was washed with acetone followed by drying at 100 ^oC in an oven to remove the moisture and used after pressing it at 0.2 bar/cm^2.

It is important to note that, all nanotube samples were dried at 100 ^oC (in vacuum) in order to avoid the contamination due to moisture (regardless of the removal of some functional groups on condensation) and hence all samples have undergone the same treatment. However, 100 ^oC or more in an oven often removes some of the acidic sites by condensation and hence drying the sample under vacuum at lower temperature has been preferred to avoid this damage.

[H] MWCNTs-CONH$(CH_2)_8NH_2$

About 60 mg of nitric acid treated MWCNTs was mixed with 10 mL of oxalyl chloride and ultrasonicated for 10 min in argon atmosphere. The mixture was then refluxed for 24 h at 60 ^{o}C to obtain MWCNTs-COCl, which was then mixed with 1 g solid 1,2 diaminooctane (DAO; $H_2N\ (CH_2)_8\ NH_2$) followed by heating at 60 ^{o}C (m. p. of DAO: ~50-52 ^{o}C) for about 40 h. The reaction mixture was then cooled, filtered through a PTFE membrane and washed with copious amount of tetrahydrofuran (THF) with successive sonication and centrifugation to remove the excess of DAO.

[I] Sulphonated MWCNTs

The procedure described in section 3.2.2.2 [G] was repeated with a minor change of only using 98% H_2SO_4 as an oxidizing agent for processing.

4.2.3. Characterization of Bucky Papers

4.2.3.1. Contact Angle Measurements

All contact angle measurements were performed on a GBX model (DIGIDROP contact angle instrument) using Windrop software. The sessile contact angle measurements were performed after fixing the bucky paper (thickness; 0.5 mm) on a cleaned, dry glass slide with double side stick-tape with no effect due to the tape. Extreme care has been taken in carrying out these measurements to monitor contact angle values within 2 - 3 min to avoid the evaporation effects. All contact angle measurements were carried out at room temperature (27 ^{o}C) and constant humidity (40-50%) with a standard deviation of $\pm 2^{o}$. However, the contact angle depends on the liquid purity, temperature, as well as the statistical errors in the actual reading of the contact angles by different peoples.

Elemental analysis was performed by CHNS-O EA1108-Elemental analyzer, Carloerba Instruments (Italy) with a precision of ±0.4%. Other characterization details like FT-IR (DRIFT mode), SEM, HR-TEM, XPS, Raman and TG analysis have been already described in chapter 3, section 3.2.2.

4.2.3.2. Electrowetting of Bucky Papers

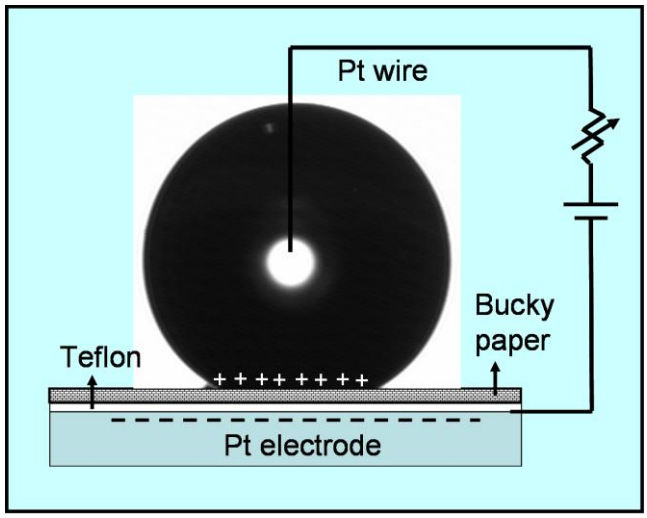

Scheme 4.1. Experimental configuration for electrowetting on superhydrophobic bucky paper (sample B) indicating charge separation on either sides of the dielectric medium (teflon); a Platinum wire (150 μm diameter) and Platinum plate act as anode and cathode respectively.

The electrowetting of bucky paper (especially sample B) of MWCNTs was carried out using various aqueous solutions of KCl, NaCl, Na_2SO_4 and $LiClO_4$ (0.05, 0.1. 0.5 and 1 M) by a sessile drop method. Effect of ionic strength was also studied by noting the contact angle variations of liquid droplet with different concentrations (0.05, 0.1, 0.5 and 1 M), as a function of voltage. Bucky paper prepared by ozonolysis (details are given in the section 4.2.2[B]) without using any surfactant, was pressed at 0.2 bar/cm^2 between two smooth stainless steel surfaces and then fixed to a platinum foil by a two-side tape. A thin film (50 μm) of a dielectric material like teflon was placed in between the Pt foil and bucky paper, in order to avoid the electrochemical reactions, typically called electrowetting on dielectric (EWOD) [38], although it changes the magnitude of applied field (as it has effect of dielectric thickness and permittivity too). Insertion of such a kind of thin insulating film between bucky paper and metal electrode can make a good charge separation of about few hundreds of micron, which could lead to large variations in the wettability with perhaps, greater reversibility and flexibility. In a typical electrowetting experiment, the contact angle was measured after putting a drop of deionized water (volume; 5 μL) on top of the bucky paper. Electrical contact to the liquid drop was given

by a Pt wire from the top as shown in scheme 4.1. All measurements were performed within 4 min in order to avoid the effect of natural evaporation since the water drop evaporates completely within 30 min for the ozonolyzed bucky paper. Nevertheless, it is important to note that the use of bucky paper as a substrate for the electrowetting has two main limitations, which determine the reproducibility of the results. The electrical contact to the substrate is one of the problems due to the colloidal nature of the silver paint, which is circumvented by using a combination of both Pt plate and silver paint. In order to achieve a conducting path for electrowetting, four point probe I/V measurements were carried out to reveal a conductivity of ~ 250 S/cm.

4.3. Results for the Characterization of Bucky Papers

4.3.1. FTIR Spectroscopy

The superimposed FTIR spectra (Figure 4.1) of both pristine and modified MWCNT samples give a clear evidence for surface modification. For example, in the high frequency region in Figure 4.1, a broad band at 3730 cm^{-1} corresponding to the free –O-H bonds is invariant with surface modification, although a slight shift (at 3636 cm^{-1}) in the case of sample G is observed which could be attributed to intermolecular bonding (H-bonding) among various functional groups on sidewalls. The fundamental bands corresponding to C=C (1525 cm^{-1}), C=O (broad 1860 cm^{-1}) and –O-H (phenolic; 1250 cm^{-1}) are also observed except in the case of sample G, where peaks due to C=O and –OH are absent and a new peak at 1595 cm^{-1} appears, attributed to –COO- groups. Nevertheless, structural information on the local molecular environment and hence sp^3 defect sites due to the functional groups on CNTs can be obtained, where the C-H stretching region (2800-3000 cm^{-1}) is particularly informative about the orientation of methylene chains. The bands at 2864 and 2921 cm^{-1} respectively, are due to C-H stretching vibrational modes produced during the reaction, strongly indicating the presence of sp^3 defects after functionalization of the MWCNTs surface. This region, for –CH stretching (both for $–CH_2$ and $–CH_3$) is more prominent in case of amine derivatized nanotubes (say for sample F and H), which is clearly seen in Figure 4.1.

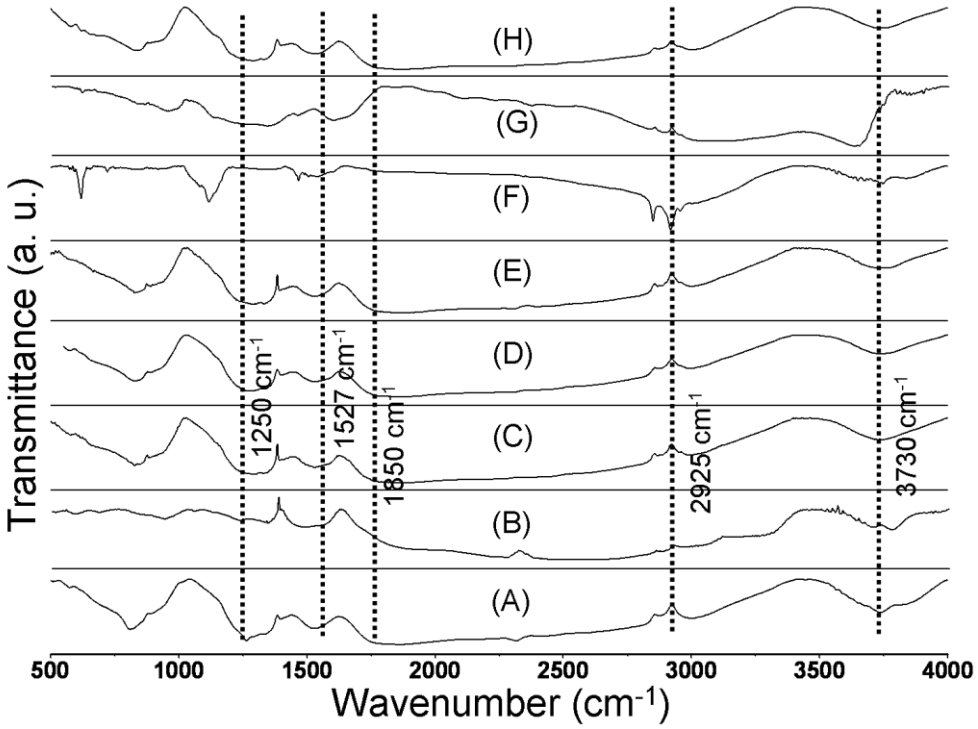

Figure 4.1. A comparison of the DRIFT spectra of pristine MWCNTs (A) and surface functionalized bucky paper samples (B-H), revealing the changes in surface functional groups, mainly the –CH stretching frequencies after covalent functionalization using amines (sample F and H).

In order to correlate these FTIR results, probable functional groups produced during these treatments have tentatively been described in Table 4.1. Although a very weak signal of –S-O stretching has been observed, due to $–SO_3H$ groups in sample G, the presence of such functional groups have been clearly indicated in other characterization techniques like XPS, which will be discussed at later parts of this chapter.

4.3.2. SEM Analysis

Interestingly, the surface topography of all the bucky papers is found to be changed after functionalization. For instance, Figure 4.2 shows a comparison of typical scanning electron microscopic image of all bucky papers (a-h) of samples from A to H, which

indicates the compact nature of bucky paper (film) clearly showing the difference in the image-contrast due to the variation in conductivities after modification.

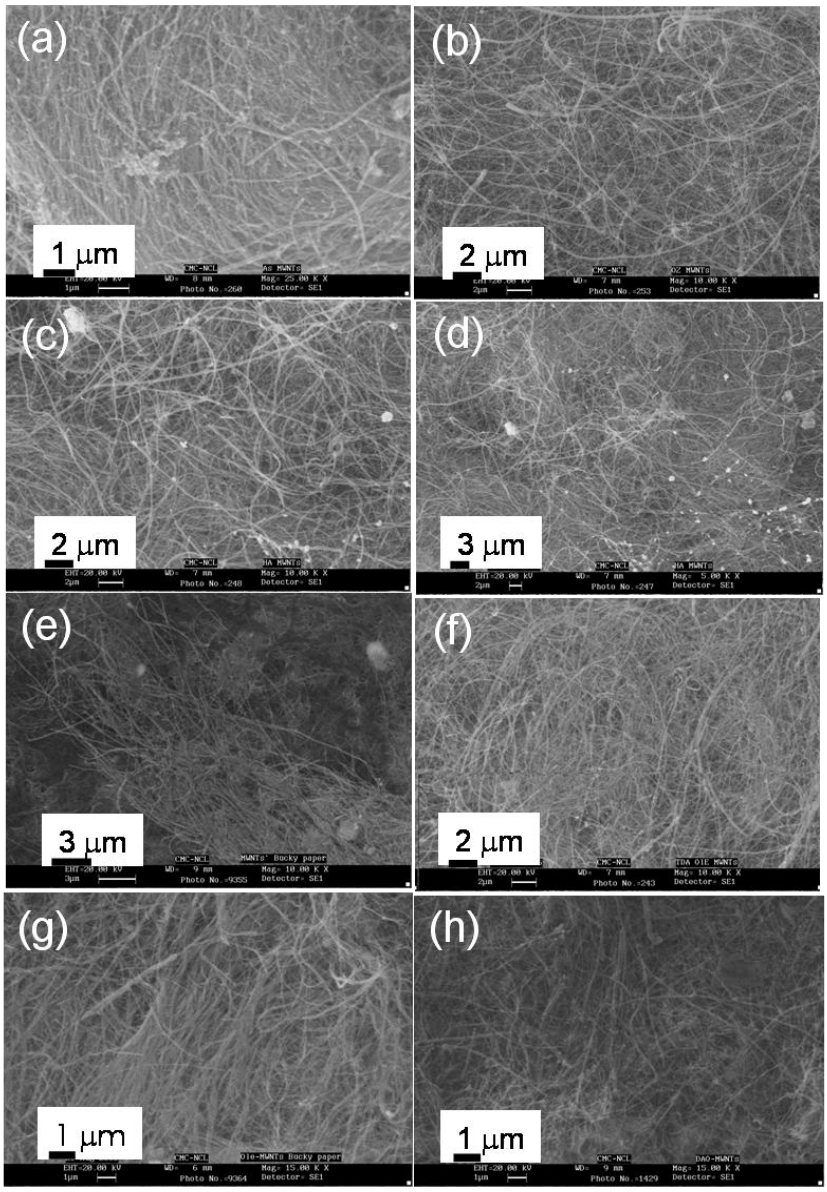

Figure 4.2. SEM images of pristine MWNTs **(a)** and modified bucky paper samples **(b-h)** of MWNTs showing compact films after surface modification.

Specifically, the image of sample G (i.e., image g) clearly shows some sort of alignment of nanotubes comprised in the bucky paper, which perhaps could be due to the intertubular interactions developed after microwave treatment (attributable to the

hydrophilic surface groups like –COO- and $–SO_3H$. This effect is clearly observed in case of SWCNTs, as discussed in the previous chapter.

4.3.3. HRTEM Analysis

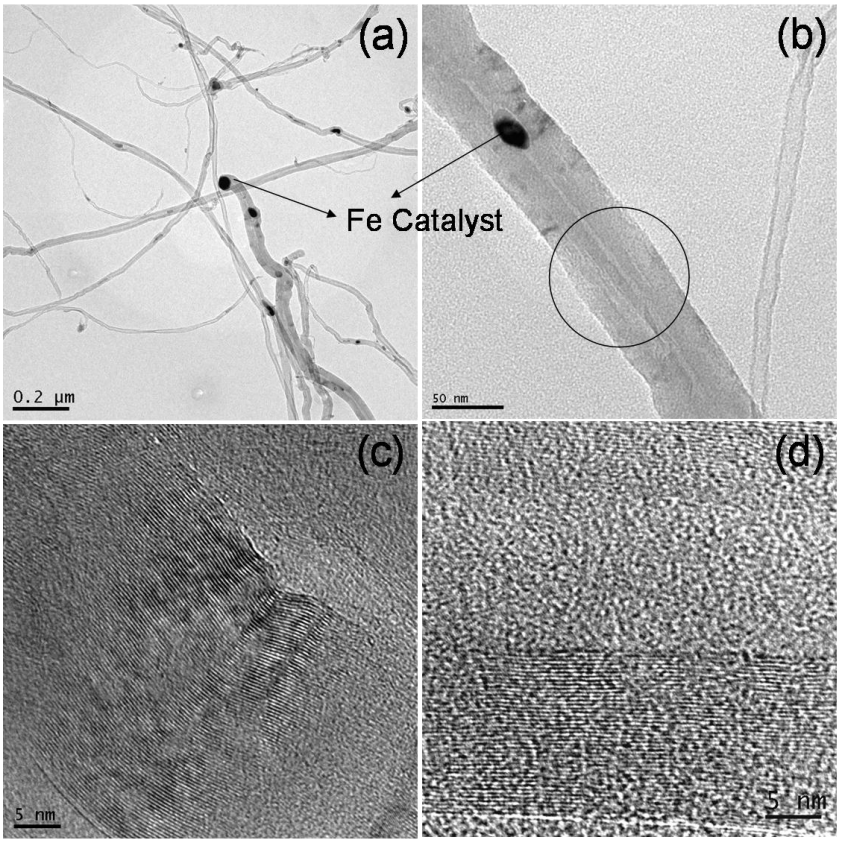

Figure 4.3. (a-b) Low resolution TEM images of pristine MWCNTs showing some catalyst and **(c-d)** HRTEM images of pristine MWCNTs, showing comparatively less defective side walls except at several places (uniformity in the lattice fringes and hence the crystallinity) due to the inherent CVD process limitations; encircled portion shows the defect sites in graphene stacking.

The surface corrugation or wall defects could clearly be studied by TEM analysis. During the refluxing stage with concentrated acids, the graphitic surface of the CVD grown MWCNTs gets severely damaged (unlike that of arc-MWCNTs). The surface of CNTs gets corrugated, the graphitic layers get fragmented and in many cases this causes roughness and mostly sp^3 disordered type surface is created which is well documented in the literature [37]. This has been confirmed by the HRTEM images as shown in Figure

4.3. These types of effect could be observed, especially, if we compare the microwave treated MWCNTs (in acid mixture) with pristine samples.

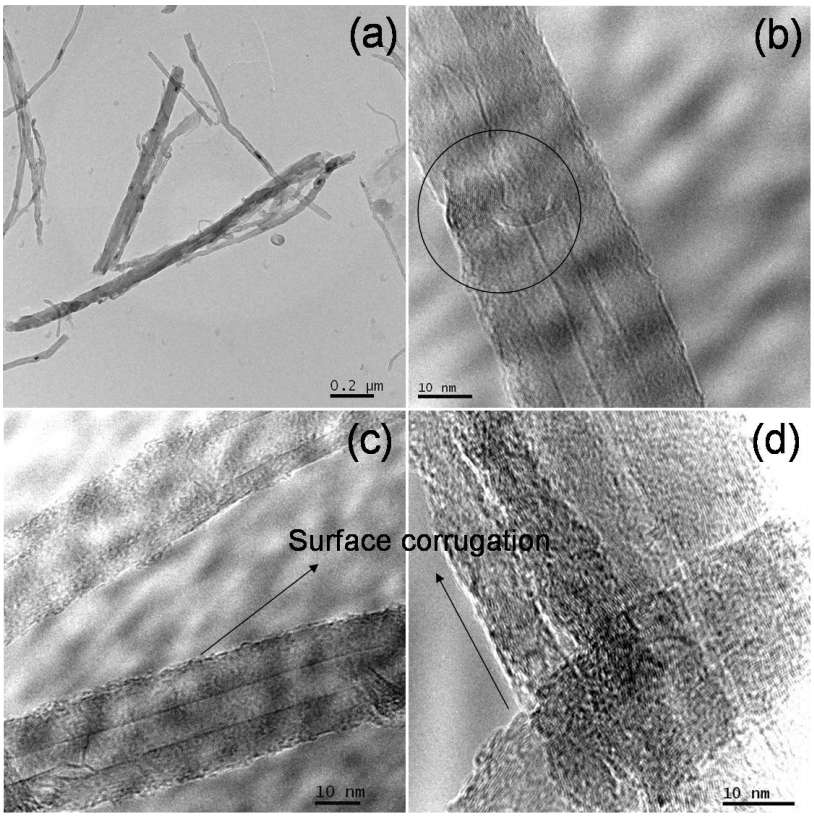

Figure 4.4. (a) Low resolution TEM images of sample G showing open ends of fullerene caps and **(b-d)** HRTEM images of sample G, showing more defective side walls (less uniformity in the lattice fringes and hence the crystallinity) due to the acid treatment leading to superhydrophilicity; encircled portion shows the severe defect sites in graphene stacking.

Accordingly, Figure 4.3(a-d) show the HRTEM images of pristine MWCNTs, where lesser extent of defects have been observed along with some catalyst particles. Such less defects on the side walls could be the consequence of the experimental conditions employed during the synthesis in a typical CVD process (over Arc method synthesis, where these defects could be eliminated, forming a stiffer and more perfect concentric graphitic tubule). Figure 4.3(c-d) also exhibits regular stacking of graphitic layers with minimal (or absence of) surface corrugation effects, leading to a superhydrophobic surface.

On the other hand, Figure 4.4(a-d) shows the HRTEM images of microwave treated MWCNT sample (G) under different resolutions, suggesting intense damage of the side walls which in turn, could facilitate both internal as well as external wetting. Interestingly, internal wetting would be observed more effectively, since most of the MWCNTs show open ends after microwave treatment, as shown in Figure 4.4(a). Encircled portion of Figure 4.4(b) shows some wall defects along with graphene miss-match regions facilitating the generation of sp^3 defect sites on the side walls as also evidenced in the FTIR spectra (with bands corresponding to –C-H stretching modes). These images also reveal surface corrugation effects perhaps due to such rigorous oxidizing conditions.

4.3.4. XPS Analysis

Analysis of the core level spectra of C1s and O1s of all bucky papers confirms the difference in local chemical environment upon various oxidative treatments [39]. For example, Figure 4.5 shows the corresponding XP spectra of C1s and O1s for all bucky samples, indicating few changes in higher binding energy in case of the C1s core level, especially for sample F, where the covalent coupling due to tridecylamine gives rise to another peak at 286.8 eV for aliphatic chains. Additionally, the peak broadening has been seen in case of samples B-H, which could be attributed to the random distribution of functional groups on the side walls. More interestingly, the O1s peak is affected seriously upon various oxidative treatments. Peak broadening along with differences in relative intensities has been observed in all the samples, revealing the presence of different functional groups. Although no quantitative relationship between the degree of functionalization and wettability is available, a systematic variation in the wetting has been observed by many groups [18]. Hence, this effect of tuning the wettability of bucky papers could be especially important when we compare the relative intensities of O1s peak in the XP spectra of these samples.

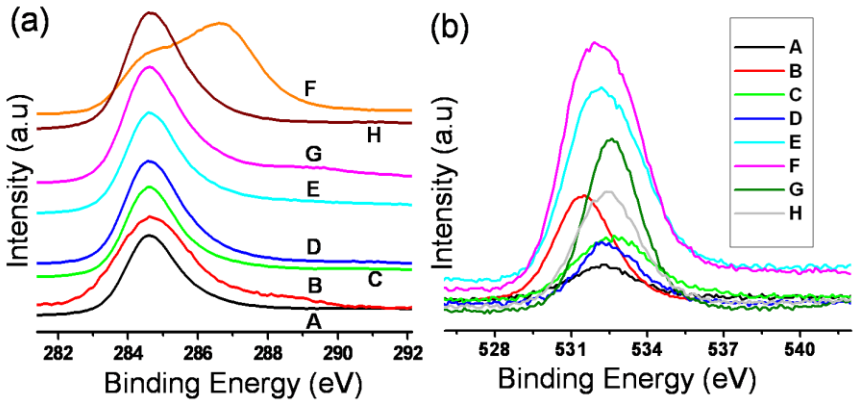

Figure 4.5. XP spectra for core level **(a)** C1s and **(b)** O1s for all bucky paper samples, revealing a prominent variation in the O1s intensities due to difference in the oxygen content of the surface of nanotube;. C1s peak of sample F is affected seriously due to additional sp^3 carbon chain formed due to the tridecylamine.

Table 4.2. Elemental analysis of all bucky paper samples, showing varying percentage of elements responsible for different extent of wetting.

Sample	Carbon	Hydrogen	Oxygen	Nitrogen	Sulphur
A	92.11	0.593	7.297	-	-
B	85.42	1.091	13.489	-	-
C	84.09	0.900	14.607	0.403	-
D	83.23	1.000	15.360	0.410	-
E	80.00	1.800	18.000	-	0.200
F	62.27	9.370	16.720	5.510	6.490
G	72.518	1.810	24.460	0.501	0.711
H	72.820	3.210	15.500	3.640	4.83
I	82.110	-	17.890	-	-

In order to substantiate these surface changes and give correlation to the XPS results, the elemental analysis is very useful. Accordingly Table 4.2 exhibits the elemental contents of all nanotube papers after various oxidation processes, although, an approximate estimate has only been obtained by this method. The presence of sulphonated functional groups surely helps to change the wetting behavior to an appreciable extent.

4.3.5. TG Analysis

Effect of thermal treatment on the bucky papers is generally very important for validating the purity of these samples [40]. Accordingly, Figure 4.6 exhibits the thermograms of all bucky samples performed in dry nitrogen at a heating rate of 10 ^{o}C/min. The initial slow weight loss, in all cases (except for sample H), up to 570 ^{o}C is attributed to adsorbed water (moisture) or molecular oxygen, whereas, the onset of weight loss at 600 ^{o}C could be attributed to the actual decomposition of carbon.

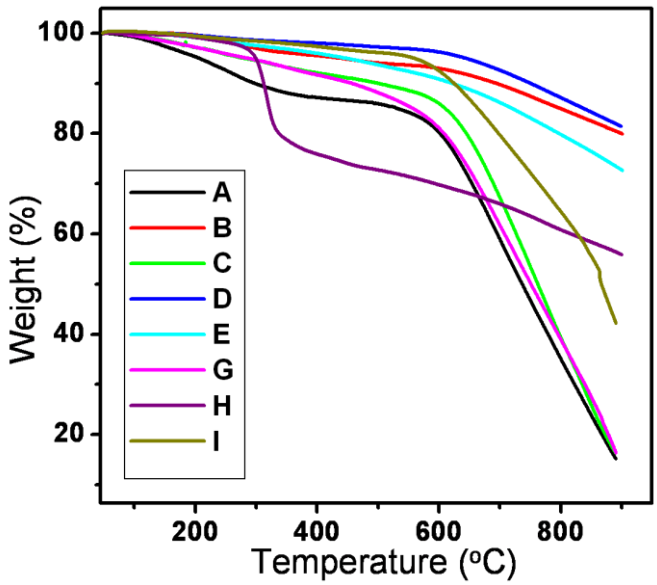

Figure 4.6. TG curves of all bucky paper samples (A-I) performed in dry N_2 at 10 ^{o}C/min, revealing almost similar trend in weight loss, due to strong sp^2 network of carbon.

The observed decomposition temperature of carbon match with that reported for MWCNTs (700 ^{o}C) [40a], although it is substantially greater than that of SWCNT (550^{o}C) prepared by similar method [40b]. A sharp and distinct single weight loss at 730 ^{o}C also suggests clear evidence for negligible amorphous carbon content in the as-synthesized sample. Both the weight losses for all samples are slightly different from each other, revealing varying extent of oxygenated species in all CNT samples. Further, the final weight losses also significantly differ, suggesting the presence of more or less oxygen necessary for their complete decomposition. Incidentally, the sample 'A' contains

plenty of moisture revealing almost 14% weight loss as compared to about less than 10% for other samples. The presence of 14% moisture is sufficient to decompose the total weight (even up to 85%), although not enough to complete the decomposition to 100%. Similarly, sample 'G' shows all parallel trends in the TG, perhaps due to the excess of hydrophilic groups generated during microwave irradiation. The only difference between the oxygen content in both the samples (A and G) is that, 'A' has adsorbed moisture, whereas, 'G' contains covalently linked oxygen and thus manifesting extreme wetting properties (i.e., 'A' is superhydrophobic while 'G' is superhydrophilic). In comparison, sample 'H' shows a sharp weight loss around 310 ^{o}C indicating the loss of diamino side chain upon heating, although the second decomposition is found to be very feeble, perhaps due to the absence of oxygen for decomposition. Such a variation in oxygenated functional groups on the CNT surface leads to a remarkable alteration in their wetting behavior.

4.3.6. Raman Analysis

In order to elaborate the electronic structural changes upon chemical functionalization of MWCNTs, Raman studies have been performed using an excitation from a 514.5 nm argon ion Laser [41]. Most of the graphitic materials are known to show a sharp and distinct band at 1350 cm^{-1} (D band), which is perceptible in accordance with some defect-induced double resonant Raman scattering, which originates from K point phonons and exhibit a resonant behavior [41e]. On the other hand, the G band (Tangential mode) corresponds to the stretching mode in the graphite plane, which is generally located at 1580 cm^{-1} [41f]. Accordingly, Figure 4.7 exhibits Raman spectra of all bucky paper samples, revealing two characteristic peaks at 1343 cm^{-1} and 1573 cm^{-1} corresponding to D and G bands respectively.

One of the important advantages of Raman for CNT is that, the intensity ratio I_D/I_G could be used to diagnose wall-defects and disorder in the graphitic structure. A comparatively larger I_D/I_G after various treatments indicates more strain on the sidewalls

of CNTs as compared to that on ideal defect-free CNT, which could be clearly seen in Figure 4.7.

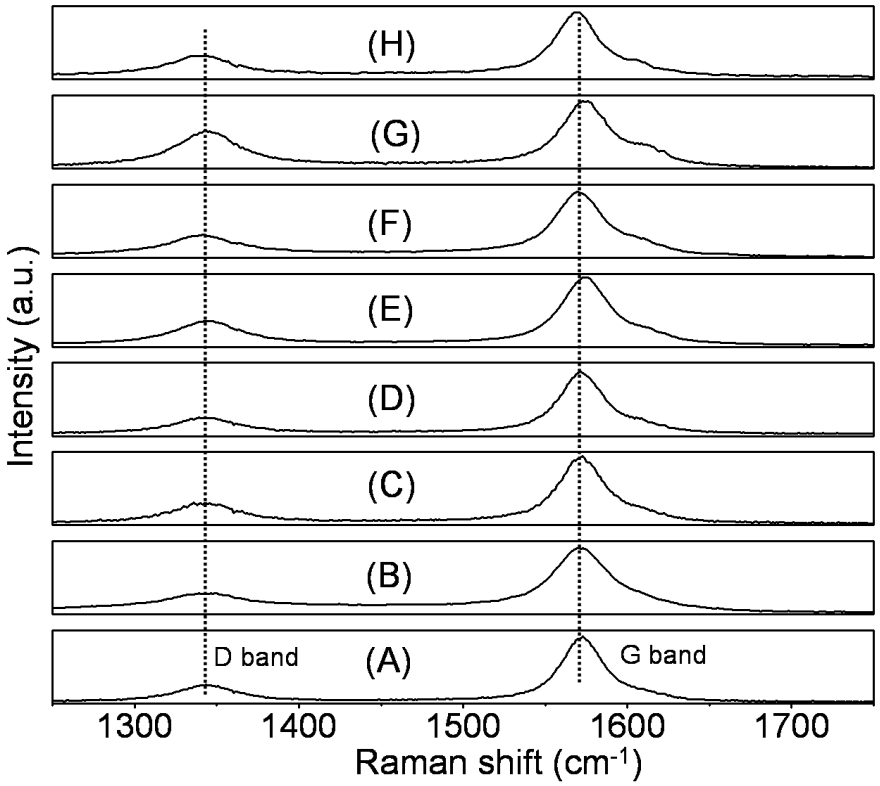

Figure 4.7. Raman spectra for all bucky paper samples (A-H), indicating a prominent variation in the G-band (tangential mode) due to difference in surface topography of nanotubes; the sample G shows an increased ratio of I_D/I_G, perhaps due to large number of hydrophilic groups like –COOH, -OH and $–SO_3H$ produced during pretreatment.

Interestingly, the G band (tangential mode) has been affected systematically after functionalization, especially for sample 'G' where the tangential band has been broadened to effect a splitting into several peaks upon deconvolution. The appearance of another peak around 1585 cm^{-1} suggests defect site generation on the side walls [41b], which is perceptible to the presence of large amount of hydrophilic functional groups and sp^3 defects on side walls. However, this kind of G-band splitting is not seen in case of pristine sample (A), showing a near perfect graphitic structure of nanotubes with superhydrophobic behavior. Sample 'B' (ozonolyzed bucky paper) on the other hand,

shows similar behavior as that of pristine CNTs, and hence this has been used for electrowetting measurements.

4.3.7. Wetting Behavior by Contact Angle Measurements

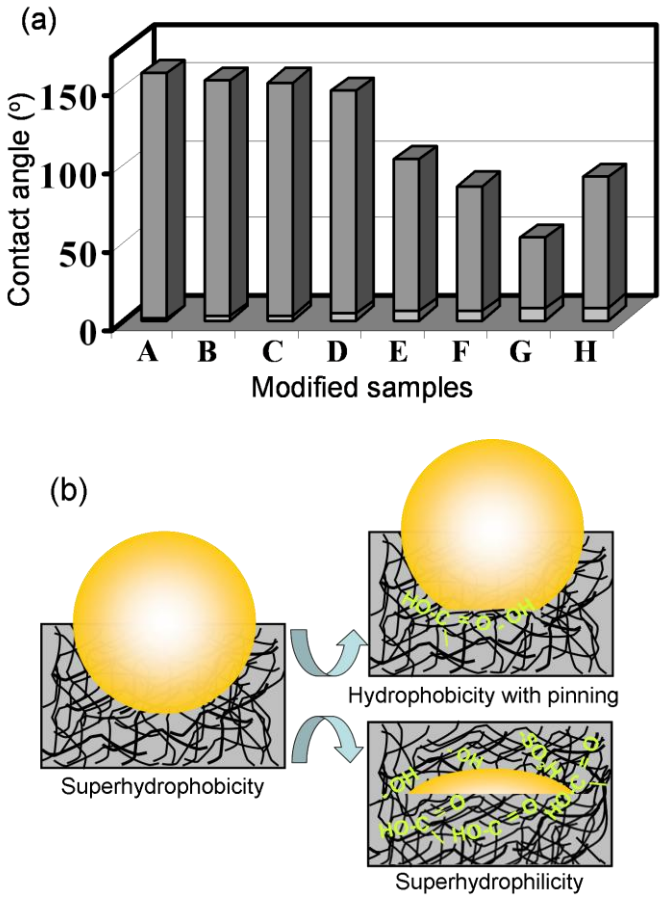

Figure 4.8. (a) Histogram exhibiting the variation in the contact angles (± 2°) of pristine MWCNT sample (A) and modified bucky paper samples (B-H), indicating the effect of surface functionalization on wetting behavior; **(b)** schematic of surface modification after chemical treatment, showing the pinning action as well as spreading of water drop on the bucky paper.

In order to understand the wettability of bucky papers, the contact angle measurements have been performed at 27 °C at constant humidity (40-60%). Accordingly, Figure 4.8(a) shows a histogram, exhibiting the contact angle of all modified MWCNT bucky paper samples. The advancing contact angle of pristine MWCNT (sample A is 156°) undergoes a systematic variation with respect to different

functionalization protocols. The poor wettability of the pristine CNT (sample A) is known to cause the drop to bounce back from the surface making it practically difficult to detach from the tip. The value of water contact angle on pristine sample is indeed smaller as compared to that on densely packed aligned CNTs (166^o) [25,27] due to random contacts between solid and liquid, affecting the contour, length and continuity of the triple contact line.

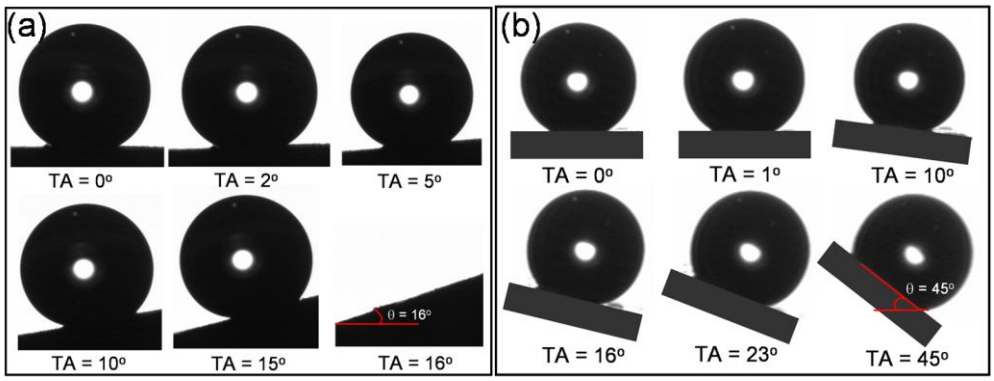

Figure 4.9. Water-drop profile at different tilt angles (TA) on **(a)** pristine MWCNT sample, revealing a surface pinning action up to 16^o (which is higher than ideal superhydrophobic surface; $\leq 3^o$) due to a lesser extent of surface functionalization, following Wenzel's model and **(b)** sample C showing the pinning action even at more than 45^o due to increased hydrophilic groups, but still on a hydrophobic surface (surface pinning).

Surfaces showing angle greater than 150° and lower than 30° are described by many as superhydrophobic and superhydrophilic respectively, although other diagnostic criteria such as low hysteresis and low rolling angle are also important to describe the extent of hydrophobicity [42]. It has also been observed that, the tilt angle over pristine sample (A) is 16^o, which is rather high as compared to that for an ideal superhydrophobic surface ($\leq 3^o$). This higher value of tilt angle (as shown in Figure 4.9(a)) could be attributed to the residual water content on the surface, which is clearly evidenced in the TGA and FTIR spectra. However, this water content in the sample 'A' is not sufficient to retain the drop for a longer period; it rolls off at an angle of 16^o, perhaps due to the physisorbed moisture (and not chemically bonded). Interestingly, Figure 4.9(b) exhibits the drop profile for sample C (nitric acid treated), where the hydrophobic drop has been

retained even beyond 45^{o} of tilt angle. This clearly supports the pinning action due to lesser extent of chemically bonded oxygenated functional groups, which bind the droplet without allowing it to spread or evaporate easily. The effect of droplet pinning along with hydrophobic surface is an indication of the Wenzel formalism, where it is assumed that the liquid fills up the space between the protrusions on the surface [43].

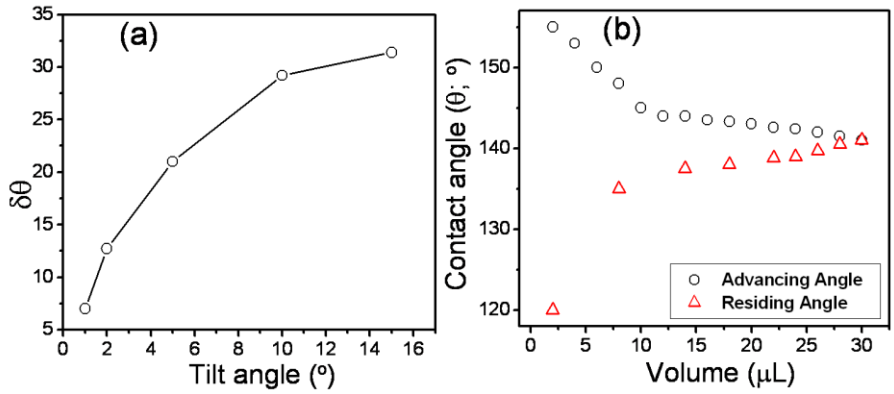

Figure 4.10. Hysteresis on the superhydrophobic bucky paper sample 'A' **(a)** δθ (=θa - θr) Vs. tilt angle showing a saturation limit after 14^{o} and **(b)** advancing (θa) and receding (θr) contact angle measurements of a Cassie drop, showing molecular level changes in the surface; final contact angle is about 110-120^{o}.

Further the hysteresis on the hydrophobic surface of pristine sample (A) shows critical values of advancing (θa) and receding (θr) contact angles [42k,44] (as shown in Figure 4.10(a)). Four positions for four different tilt angles and the arithmetic difference between θa and θr gives δθ (= θa - θr). An increasing value for δθ indicates a larger hysteresis (Figure 4.10(a)), perhaps due to the Wenzel mode of wetting, where the grooves or surface groups keep water intact. In addition, Figure 4.10(b) suggests an initial decrease in the advancing contact angle with increasing volume followed by an almost constant value. This is also clear from the hysteresis curve since, the droplet does not regain its original state. Hence, no conclusions could be drawn from the receding contact angle (Figure 4.10(b)) of a Wenzel drop, where the apparent contact angle decreases with a decrease in the volume up to the smallest drop possible. There is no constant apparent angle with decrease in the drop volume to imply that the Wenzel form, despite wetting of

the grooves, exhibits a very large hysteresis. However, this is undesirable for applications involving droplet motion.

Interestingly, the initial water contact angle of 156^{o} on pristine sample (A) for a droplet volume of 5 μL changes upon evaporation within 30 min followed by a constant contact angle (with a very small decrease in contact angle) until the weight of the drop decreases to an appreciable value and then follows the constant area mode below 90^{o} (Figure 4.11). However, sample after nitric acid treatment shows a advancing contact angle of only 145°, with a roll-off angle more than 45^{o} perhaps indicating the role of functional moieties present on the surface rather than the contribution from surface roughness.

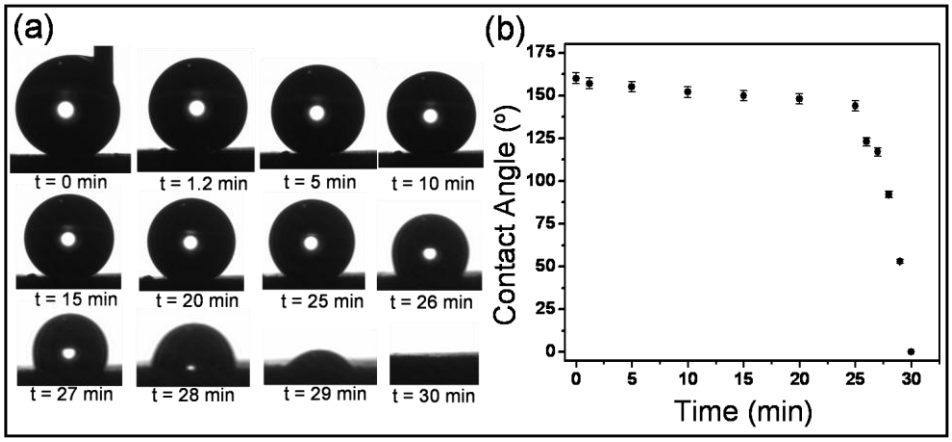

Figure 4.11. (a) Water drop evaporation profile on pristine MWCNTs sample, at room temperature (27 ^{o}C) and constant humidity (40-50%), revealing initial superhydrophobic surface with a very slight decrease in a contact angle (standard deviation ± 2^{o}) up to 23 - 25 min followed by sudden evaporation following constant area mode: **(b)** contact angle variation as a function of time.

Surprisingly, sample G shows an initial water contact angle of 40^{o}, although it spreads to 0^{o} within 2 seconds (shown in histogram of Figure 4.8(a)), indicating the formation of a 'superhydrophilic' surface. Such super-hydrophilic surface can be well understood by 2D [44] or 3D [42a,46] capillary effects on the hydrophilic surfaces. Hence, a microwave treatment for 5 min could make the CNT surface superhydrophilic, where the formation of more sidewall defects in the form of –COOH, -OH and -SO_3H

(~30 wt% oxygenated groups as judged from XPS studies) plays an important role in surface wettability (discussed in details in chapter 3).

More interestingly, the sample 'I' prepared by treatment with 3:1 H_2SO_4 shows an initial contact angle value of 145^o whereas, it spreads to 0^o within 6 min indicating surface pinning followed by absorption through capillary action. In sharp contrast to the pioneering work by Birdi and Vu [47], we find the initial water contact angle of 145^o (hydrophobic) diminishing linearly to 0^o (hydrophilic) despite following the constant area mode. These variations could be due to few limitations in their studies like, the use of different substrates and varying liquid drop (shape and volume).

We have adopted several functionalization strategies to tune the surface topography of the MWCNTs, which also leads to the decapping (breaking of the fullerene caps) during treatment in all cases. However, the presence of different amount of functional groups on the side walls as well as in the interior of the nanotubes contributes more to the variation in the wetting properties. When open nanotubes contact a liquid surface, the internal wetting force due to the liquid surface tension acting on the nanotube interior surface should be considered equally. Sample 'G' (microwave treated in presence of acid mixture) shows a superhydrophilic behavior due to the higher extent of internal wetting along with external wetting due to the presence of large amount of functional groups. However, sample 'C' (nitric acid treated) still shows superhydrophobic behavior, although a rolling angle of more than 45^o has been observed indicating a strong pinning action, which means a lower extent of functional groups on the side walls (as well as on the interior of the nanotubes) making the droplet to reside on the surface but resisting for a capillary action through the nanotube.

Recently, Barber et al, have shown an enhanced internal wetting for the open ended individual MWCNTs using Wilhelmy force balance method [48], where water exhibits a significantly larger interaction with the nanotube (as a function of nanotube diameter) as compared to other organic liquids such as polyethylene glycol and glycerol. However, in the present situation the contact angle measurements have been performed

on a MWCNT film comprising nanotubes with non-uniform diameter distribution, which could give an ensemble effect on wetting. Since, the defect sites increase with increase in the diameter [23], the wetting properties of CVD grown nanotubes (more strained walls) will be governed by the number of defects at the nanotube surface. In particular, in the case of pristine sample, the wide diameter distribution (20–100 nm) leads to the superhydrophobic behavior. On the other hand, in the case of sample 'G', CNTs with a larger diameter, containing a high degree of surface defects, a smaller contact angle is seen when compared to that of thinner nanotubes. All these observations suggest that, the uneven distribution of functional groups along the side-walls of individual CNTs plays a considerable role in wetting. Consequently, the interplay of all these factors on the contact angle of bucky paper prevents the quantification of contributions from capillarity and internal wetting. Thus, the variation in wetting properties of MWCNT bucky paper using such surface designing strategies provides controlled heterogeneity on the surface with no or minimal effect on surface roughness.

Thus these studies clearly demonstrate that, the presence of different functionalization groups on the surface of CNTs determines the surface topography and consequently the hydrophobicity/hydrophilicity (as demonstrated in schematic view of the bucky paper surface in Figure 4.8(b)). Thus, hierarchical structures created by sub-nanolevel manipulation of surface topology on CNT offer a novel approach to construct promising materials for various applications.

4.3.8. Electrowetting of Bucky Papers

Electrowetting is a fascinating approach to reduce the interfacial tension between a solid and a liquid by the application of electric field across the solid-liquid interface, which modifies the wetting properties of the liquid on the solid without changing the composition of both. Since our ability to tune CNT surface by surface functionalization has given a remarkable control on wettability, it is of immense interest to see the effect of electric field on the same. Accordingly, we find an interesting wetting behavior of these bucky surfaces in presence of electric field and demonstrate a transition from

superhydrophobic, Cassie-Baxter to hydrophilic, Wenzel form. More specifically, an initial contact angle of 155^{o} with slight pinning properties (roll off angle of 16^{o}) changes to superhydrophilic with an external electric field. A schematic of electrowetting experiment is shown in Scheme 4.1, where the charge separation across the dielectric medium is seen upon the application of applied field. Effect of critical parameters like concentration and pH of the drop has been systematically studied to deduce the differential capacitance at the bucky paper-liquid interface.

Accordingly, Figure 4.12 shows the droplet (deionized water) profile on the bucky paper surface as a function of voltage, which reveals the spreading of liquid in a systematic fashion. The observation of an initial contact angle of 155^{o} reveals the superhydrophobic nature of the bucky paper, perhaps due to the presence of several hydrophobic functional groups produced during the ozonolysis. A continuous decrease in the contact angle with respect to dc voltage shows a remarkable tuning of the surface properties of the nanotube paper, especially with respect to its change in its surface oxygen content, as explained in the latter discussion. The appearance of bubbles at about 15 V is indicative of the onset of electrolysis of water with subsequent reduction in the interfacial tension.

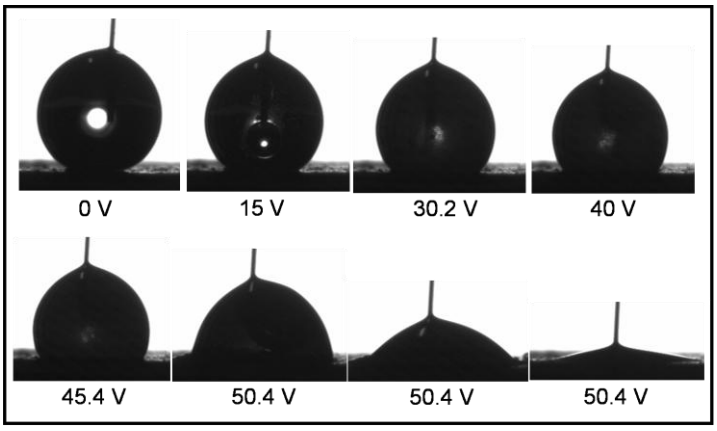

Figure 4.12. Droplet shape evolution during electrowetting on bucky paper using deionized water (5 μL drop size), indicating the onset of oxygen evolution at 15 V.

Before application of voltage, the liquid remains suspended at the top of the bucky paper and forms a stable "immobile ball" due to slight pinning action with an angle of

155^{o}. Interestingly, the application of electric field induces a transition from the superhydrophobic to the hydrophilic state where the immobile droplet undergoes a distortion which could be seen even with naked eye. However, some of the liquid penetrates through the bucky paper substrate as a result of this transition. Since the electrical energy could induce both external as well as internal wetting (capillarity) of the inner bore of the MWCNTs, an approximate estimation of the capillary rise (~0.49 mm) could be calculated as follows-

Assuming uniform inner diameter of MWCNTs and zero contact angle between inner walls of the capillary and water, we can use the relationship,

$\gamma = (1/2)\ \rho\ g\ r\ [h + (r/3)]$ ……. (4.1)

where, 'γ' is the surface tension of liquid at 25 ^{o}C (water; 71.97 dyne/cm), 'ρ' is the density of water at 25 ^{o}C (0.99707 g/cm^3), 'g' is the acceleration due to gravity (980.665 cm/s^2), 'r' is the average inner radius of the MWCNT (3 nm) and 'h' is the height of the water to be raised due to the capillary action. This capillarity effect (internal wetting) is clear even in the low resolution TEM images, as shown in Figure 4.13.

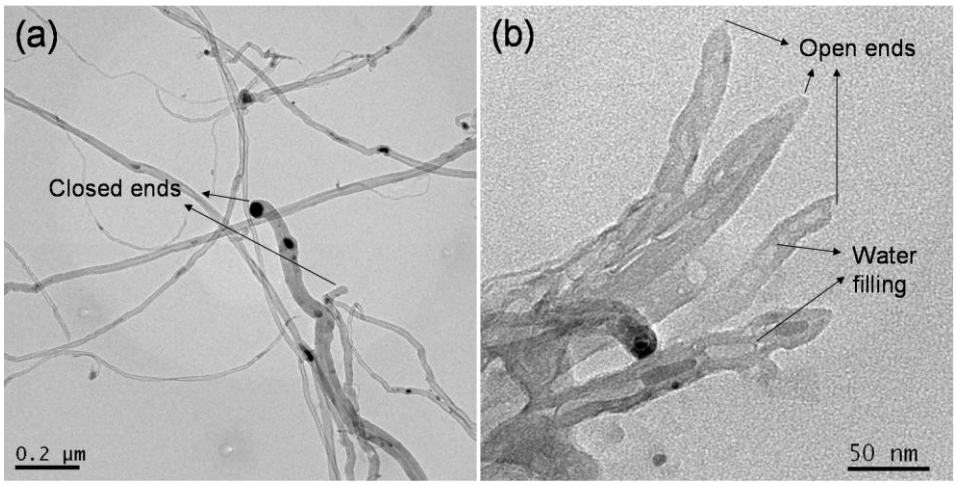

Figure 4.13. TEM images of **(a)** pristine MWCNTs and **(b)** after electrowetting experiment, revealing subtle changes; water capillarity through open ends of CNTs gives a water level of ~ 0.49 mm.

A similar capillary rise has been recently demonstrated by Prins et al, using electrowetting of single SWCNT by mercury through microchannels, although not at the nanoscale [19]. This effect of electrocapillarity is strictly based on electrostatic control of

the solid-liquid interfacial tension [32]. After the application of electric field, charge gets build up across the SWNT-water interface, causing repulsion between similar electric charges, which is believed to lower the surface tension [50]. Nevertheless, at a critical value of the applied potential, wetting commences to move up water along the CNT sidewalls, concomitantly filling the nanotube cores to show a capillary action. This is in excellent agreement with the recent observation of Barber et al, where an enhanced internal wetting for the open ended individual MWCNTs is demonstrated using a Wilhelmy force balance [48]. This also explains why water exhibits a significantly larger interaction with the nanotube (as a function of diameter) causing a unique behavior [19] as compared to what other organic liquids reveal under similar conditions.

4.3.8.1. Morphological Changes

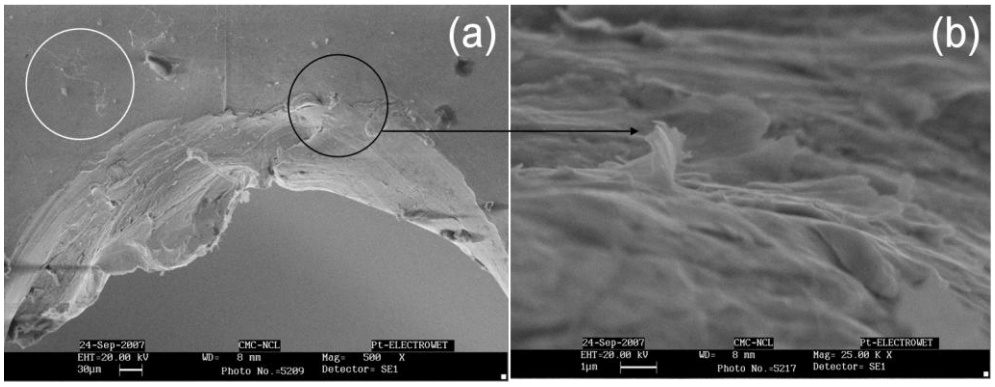

Figure 4.14. SEM images of bucky paper **(a)** showing both regions of, before (white circled) and after electrowetting (dotted region) experiment and **(b)** magnified portion of electrowetted area indicated as black circle in (a), revealing the surface corrugation effects after electrowetting.

Since, electrowetting does not provide a reconstruction of the surface and produce more surface roughness, the observed topographical changes need a satisfactorily explanation. Accordingly, Figure 4.14(a) clearly demonstrates the comparative surface topography (in SEM images) of bucky paper before (white circled) and after electrowetting (black circled) experiments. Figure 4.14(b) shows a magnified SEM image of the circled portion from Figure 4.14(a), which clearly reveals a surface roughness developed after electrowetting as compared to the portion shown in Figure 4.14(a) in

white circle. Upon the application of electric field, similar charges produced on CNTs (in presence of liquid) may exert repulsive forces among themselves, perhaps leading to the rearrangement of the surface.

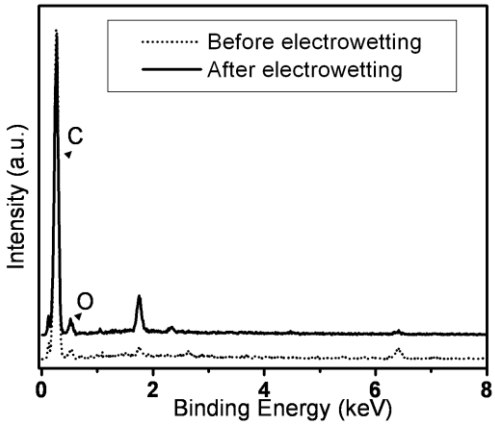

Figure 4.15. Energy dispersive (ED) x-ray analysis data of bucky paper, before and after electrowetting experiment, indicating the enhancement in the oxygen content after electrowetting.

The electrolysis of water might also play an important role for the topographical changes. Interestingly, the compositional variations have been clearly seen in energy dispersive analysis (ED) (Figure 4.15). Mainly, the oxygen peak has been severely affected by the electrowetting, since rupturing of graphitic structure of CNTs resulting in the formation of –C-O bonding. This also reveals the electric field induced functionalization of CNTs to develop more oxygenated functional groups on the side walls. Thus, the application of electric field could be an efficient route towards functionalization of nanotubes to overcome the surface inertness. Consequently, the C/O peak intensity ratio has been decreased, leading to the hydrophilic surface on the bucky paper. The dangling bonds present on the side walls of nanotubes with hydrogen atoms show probable variations in the surface tension perhaps due to the hydrogen bonding when the surface comes in contact with the droplet.

4.3.8.2. Effect of Ionic Strength

Since surface tension of a liquid depends on the concentration and conductivity, the variation of solid-liquid interfacial tension would be a function of the ionic strength. In

order to correlate the effect of ionic strength on wetting, electrowetting experiments have been carried out as a function of ionic strength.

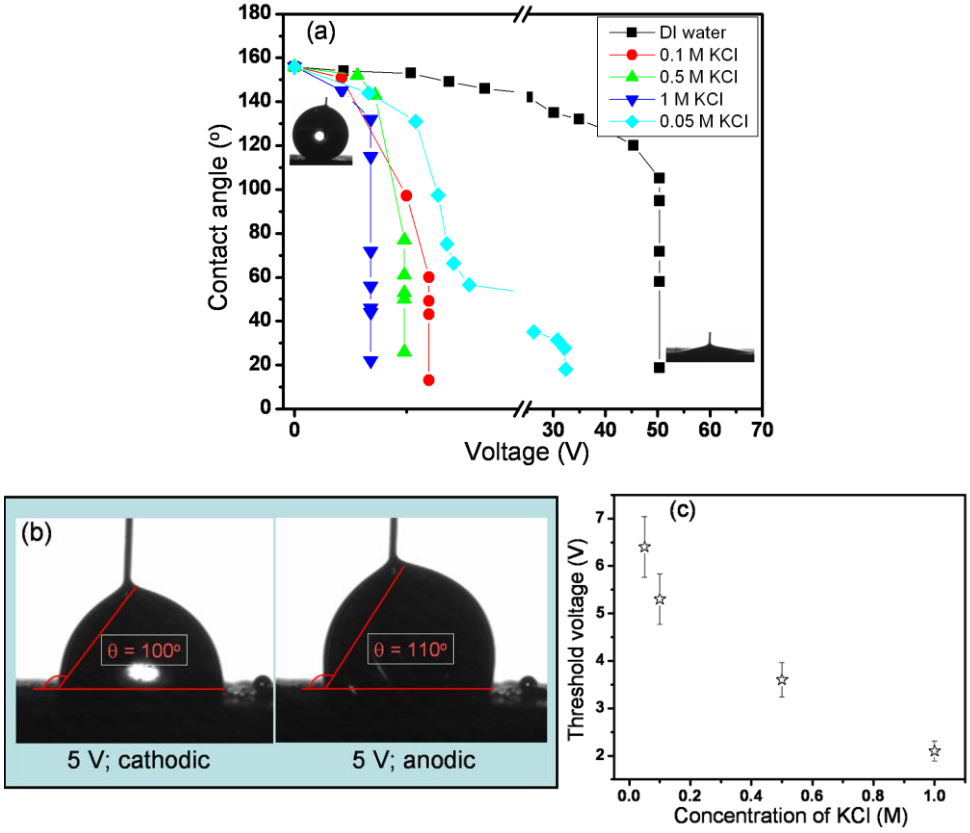

Figure 4.16. (a) Water droplet profile with respect to the ionic strength of liquid using various concentrations of KCl indicating that a very small amount of electrolyte could reduce the surface energy of the nanotubes; **(b)** reversible wetting and de-wetting of bucky paper using 0.1 M KCl, showing the tuning between the contact angle of 100^{o} (at cathodic potential) and 110^{o} (at anodic potential): **(c)** variation of threshold voltage for reversal of switching with ionic strength with a standard deviation of 10%.

Accordingly, Figure 4.16(a) shows the variation of electrowetting results with respect to the ionic strength of the solution where the contact angle decreases by increasing the concentration of the electrolyte. It means that a very small amount of electrolyte could reduce the surface energy of the nanotubes to an appreciable extent. In addition, the wetting could be reversed by changing the polarity as shown in Figure 4.16(b) (100^{o} become 110^{o} on reversal). Thus, the droplet behavior can be reversibly switched between the superhydrophobic, Cassie-Baxter state and the hydrophilic, Wenzel

state by the application of electric field. However, the hysteresis of pristine sample shows an appreciable extent of variation, since this reversal clearly exhibits a surface manipulation (contact angle of 110^o as compared to initial 155^o) due to the pinning action during both advancing and receding modes (as described in section 4.3.7). Interestingly, this reversal of switching is possible only when the voltage applied is lower than a threshold. Variation of this threshold voltage with ionic strength has been shown in Figure 4.16(c), where a gradual decrease in the threshold value could be observed with an increase in concentration of KCl, where the solution conductivity variation contributes substantially.

4.3.8.3. Effect of Electrolyte

The application of electric field as a function of the type of cation and anion also exhibits a remarkable change in the wetting behavior of bucky paper, since specific adsorption of these ions can vary significantly. For example, Figure 4.17(a) shows a systematic variation of the surface properties as a result of ionic size, especially the size of anion. A small amount of bigger sized SO_4^{2-} ions require a lower voltage for the liquid to spread over nanotube surface. Hence, the surface hydrophilicity could be enhanced by increasing the concentration of larger anions, where a possible trend in order to achieve a better hydrophilicity would be $SO_4^{2-} > ClO_4^- > Cl^-$. This effect of variation in the wettability with respect to various electrolytes could be attributed to the specific adsorption of anions, especially Cl^- and SO_4^{2-} shows dramatic change after adsorption on the anode (Cl^- ions adsorb strongly as compared to SO_4^{2-} ions). However, ClO_4^- ions show unusual behavior, since a lower stability of Li^+ salt might alter the results. Further, a reversal switching of surface property (hydrophilicity) is observed below a threshold voltage. A possible trend (with decreasing threshold voltage) using 0.05 M electrolytic concentration has been observed as $KCl > NaCl > LiClO_4 > Na_2SO_4$ (and shown in Figure 4.17(b)).

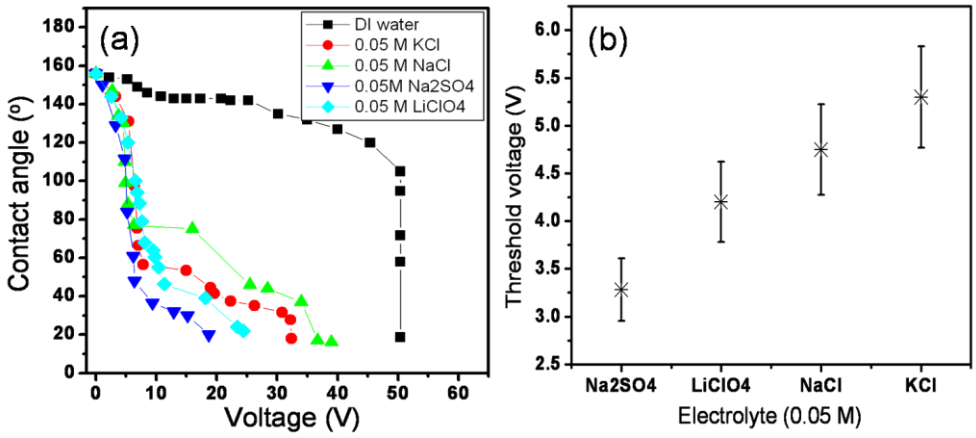

Figure 4.17. (a) Electrowetting as a function of the type of electrolyte showing a dramatic variation in the wetting behavior; **(b)** variation of the threshold value for reversal of switching with the type of electrolyte having a standard deviation of ±10%.

4.3.8.4. Effect of pH

Change in the wetting of the surface with pH is entirely dominated by the surface tension of solid-liquid interface (γ_{SL}) and not by that of liquid-vapor (γ_{LV}) and solid-vapor (γ_{SV}) interfaces, since γ_{SL} is determined by the energy of interaction of the liquid with a collection of groups on the exterior surface of the solid [51]. Hence molecular level changes with variation in pH is a direct consequence of ionization of surface functional groups and the surface does not reconstruct to its original state [51], which is confirmed by SEM analysis.

It is interesting to note that, the electrowetting results demonstrate more droplet stability at alkaline pH (= 12), whereas, at acidic pH (= 2) the stability of droplet is lower as compared to that of deionized water. Although, an initial sudden drop in the contact angle (up to 100^{o} at 10 V) in case of alkaline droplet causes further wetting slowly, a converse trend occurs for deionized water droplet (as shown in Figure 4.18). On the other hand, the acidic droplet shows a gradual wetting behavior with applied voltage, indicating easy surface manipulation in acidic media. It could also be explained by the fact that, during electrowetting the easy hydrolysis of the ester groups of nanotubes takes place in acidic pH rather than at alkaline pH. However, the exact reason is unknown for such

variations in the surface properties at different pH and more systematic studies are desired in this direction.

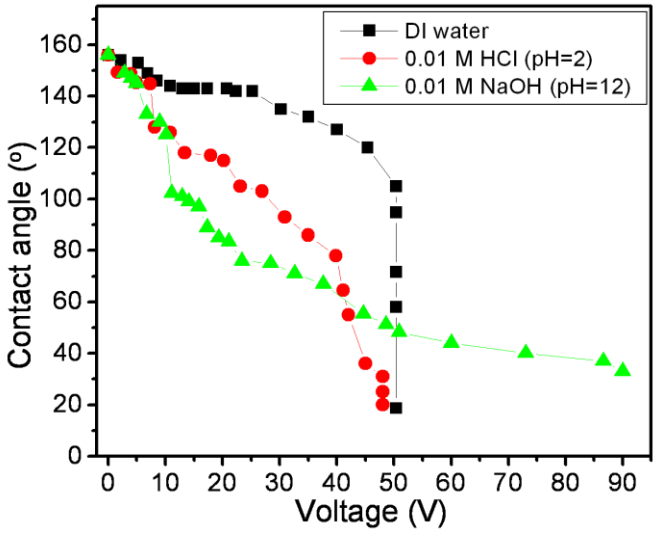

Figure 4.18. Electrowetting of bucky paper as a function of pH, showing a dramatic variation in the surface properties with better stability at alkaline pH.

4.3.8.5. Mechanism

This superhydrophobic to superhydrophilic transition, upon the application of electric field could be explained on the basis of two classical models like Wenzel and Cassie.

According to former, the apparent contact angle is given by-

$\cos\theta_w = r \cos\theta o$ ……(4.2)

where, θ_w and θo are Wenzel apparent and ideal Young angle respectively and r is the surface roughness, which is defined as the ratio of the actual area of the solid surface to the projected area on the horizontal plane. This equation is notably valid for the case of homogeneous wetting of the surface [27,31]. On the other hand, the Cassie model can be considered for a system where the air between the liquid drop and grooves of the surfaces plays a key role. According to Cassie model-

$\cos\theta_C = \phi_S \cos\theta o + \phi_S - 1$ ..... (4.3)

where θ_C is the Cassie apparent contact angle and ϕ_S is the fraction of the projected area of the solid surface wetted by the liquid.

Assuming analogous behavior of CNT surfaces with that of graphite (surface tension of ~35 mN/m) [53], the contact angle of CNT/water system could be determined by knowing the interfacial tension between these two [54] as-

$\gamma_{SL} = [(\gamma_{SV})^{1/2} - (\gamma_{LV})^{1/2}]^2 / [1 - 0.015 (\gamma_{SV} . \gamma_{LV})^{1/2}]$ ..... (4.4)

By knowing 'γ_{SV}' for Carbon nanotubes (27.8 mN/m) [49] and 'γ_{LV}' as 71.97 at 25 ^oC for water/vapor equilibrium, 'γ_{SL}' can be determined as 31.33 mN/m. Hence, by substituting this value in Young's equation,

$\gamma_{LV} \cos\theta = \gamma_{SV} - \gamma_{SL}$ ..... (4.5)

we get, the value of contact angle between CNT and water is 92.81^o. However, the observed superhydrophobic contact angle of 155^o could be due to the compact nature of bucky paper. Additionally, a combination of wide diameter distribution of CNTs along with molecular changes as a consequence of functional groups also affects the contact angle.

We assume the Cassie model to be valid for wetting in the present situation (since there could be trapped air under the liquid drop). Now the application of voltage to the water droplet changes its shape and spreads on the bucky surface. Consequently, equation (4.3) would be modified for the transformation from superhydrophobic to hydrophilic surface as-

$\cos\theta_T = r_S \phi_S \cos\theta o + \phi_S - 1$ .....(4.6)

As the electric field decreases, the variation of interfacial tension between bucky paper and liquid could be understood by the combination of equation (4.3) with the voltage-dependence of contact angle [6].

$\cos\theta = \cos\theta o + (1/2) (C/\gamma_{LV}) V^2$ ..... (4.7), which could be expressed as,

$\cos\theta_T = a + bV^2$ ..... (4.8)

where, $a = r_S \phi_S \cos\theta o + \phi_S - 1$ and $b = (½) r_S \phi_S (C/\gamma_{LV})$. By using $\cos\theta$ Vs. voltage plots, it is convenient to determine the differential capacitance where 'a' and 'b' are the fitting parameters and 'γ_{LV}' is the surface tension of water (taken as 71.97 mN/m at 25 ^oC).

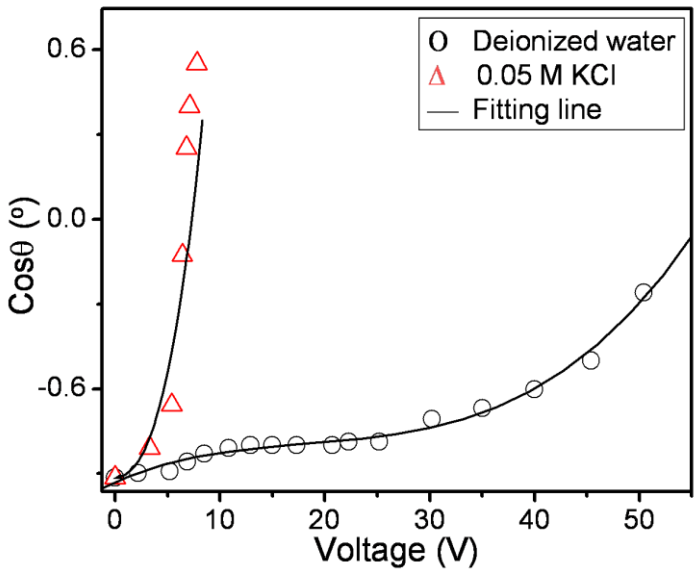

Figure 4.19. Contact angle (cosθ) variation with voltage for deionized water (O) and 0.05 M KCl (Δ), indicating a polynomial fit; $\cos\theta = a + bV^2$; continuous lines represent the fitting lines.

Accordingly, Figure 4.19 shows the fitting curves for both deionized water and 0.05 M KCl indicating the poor fitting at initial and final values of contact angle, where 'γ_{SL}' increases with the application of voltage since the liquid tends to wet the bucky paper surface. Similar approaches developed by Morcos et al, [53] and Zhu et al, [27] have been used to describe the present system, where the ϕ_S (= 0.09853; fraction of projected area of bucky surface wetted by the liquid) is determined from the magnitude of fitting parameters 'a' and 'b'. The parameters θ_C and θo have been taken as 155°, 92.81° respectively (by solving for 'a' and 'b'). The values of 'a' and 'b' for deionized water and 0.05 M KCl are given in Table 4.3.

Table 4.3. Fitting parameters determined from the cosθ Vs. voltage plot for both deionized water and 0.05 M KCl, assuming the polynomial as $\cos\theta = a + bV^2$.

Liquid	a	b	r_S	C (μF/cm^2)
Deionized water	-0.92	-0.8587	3.83	0.026
0.05 M KCl	-0.007	-0.052	8.85	0.858

Figure 4.19 also depicts that, the saturation limit has not been reached even when the voltage exceeds 6 and 80 V for 0.05 M KCl and deionized water respectively, probably due to the porous nature of the substrate. Indeed, capillary effects along with water spreading through the porous bucky paper (formed due to the wide diameter distribution of MWCNTs) are expected to show a transition from Cassie state to the Wenzel state [30]. The capacitance value from the above treatment indicates that as per Gouy-Chapmen model of the electrical double layer, the Debye length varies with concentration of the ions [54]. The higher capacitance possibly results in a higher surface charge density, which is responsible for the reduction of the solid/liquid interfacial tension. The experimental values of interfacial capacitance using deionized water and 0.05 M KCl are 0.026 $\mu F/cm^2$ and 0.858 $\mu F/cm^2$ respectively. In comparison, the values obtained by the electrowetting studies of aligned forest of MWCNTs are 0.07 and 0.311 $\mu F/cm^2$ respectively for deionized water and 0.03 M KCl [27]. The slight difference in the capacitance values could be attributed to the geometrical effects, where compact nature of bucky film is primarily responsible.

Thus, a control of the wetting behavior of functionalized bucky papers of MWCNTs has been demonstrated using both surface functionalization as well as by electric field.

4.4. Conclusions

The achievements of tuning the wetting characteristics of MWCNT surfaces described in this chapter imply that the fabrication of CNT papers with an amazing range of superhydrophobic to superhydrophilic properties could be realized by improving the surface functionalization strategies. Practical utilization of such tunable CNT surfaces to make high performance polymer composites (e.g., controlling the interfacial adhesion between CNT surface and polymer) would significantly open up new perspectives in the preparation of various polymer composites extending the range of their possible applications. Such capabilities would allow one to construct much more sophisticated architectures from MWCNTs, including electronic interconnects, robust nanocomposites

and structured thin films. Thus, the fabrication of hierarchical structures of bucky papers using unique functionalization strategies without using surfactants causes fascinating wetting behavior like transition from superhydrophobic to hydrophilic MWCNT bucky paper, as a function of electric field. More significantly, the reversal of switching of droplet behavior between superhydrophobic, Cassie-Baxter state to hydrophilic, Wenzel state is studied. Our present findings may have important benefits for a wide range of applications of CNT surfaces such as design of biosensors, smart composites, variable lenses and display screen.

4.5. References

1. Blossey, R. *Nat. Mater.* **2003**, *2*, 301.
2. Feng, L.; Li, S.; Li, Y.; Li, H.; Zhang, L.; Zhai, J.; Song, Y.; Liu, B.; Jiang, L.; Zhu, D. *Adv. Mater. (Weinheim, Ger.)* **2002**, *14*, 1857.
3. Barthlott W.; Neinhuis, C. *Planta* **1997**, *202*, 1.
4. Gao X.; Jiang, L. *Nature* **2004**, *432*, 36.
5. Feng, L.; Zhang, Z.; Mai, Z.; Ma, Y.; Liu, B.; Jiang, L.; Zhu, D. *Angew. Chem., Int. Ed.* **2004**, *43*, 2012.
6. McHale, G.; Schirtcliffe, N. J.; Aqil, S.; Perry, C. C.; Newton, M. I. *Phys. Rev. Lett.* **2004**, *93*, 036102.
7. Oner, D.; McCarthy, T. J. *Langmuir* **2000**, *16*, 7777.
8. Erbil, H. Y. ; Demirel, A. L. ; Avci, Y. ; Mert, O. *Science* **2003**, *299*, 1377.
9. Odom, T. W. ; Huang, J. -L. ; Kim, P. ; Lieber, C. M. *J. Phys. Chem. B* **2000**, *104*, 2794.
10. Chen, W.; Fadeev, A. Y.; Heieh, M. C.; Öner, D.; Youngblood, J.; McCarthy, T. J. *Langmuir* **1999**, *15*, 3395.
11. Wu, Y.; Sugimura, H.; Inoue, Y.; Takai, O. *Chem. Vap. Deposition* **2002**, *8*, 47.
12. Tsujii, K.; Yamamoto, T.; Onda, T.; Shibuchi, S. *Angew. Chem. Int. Ed. Engl.* **1997**, *36*, 1011.
13. Tadanaga, K.; Katata, N.; Minami, T. *J. Am. Ceram. Soc.* **1997**, *80*, 3213.
14. Nakajima, A.; Abe, K.; Hashimoto, K.; Watanabe, T. *Thin Solid Films* **2000**, *376*, 140.
15. Bico, J.; Marzolin, C.; Quéré, D. *Europhys. Lett.* **1999**, *47*, 220.
16. Xiao, W.; Huang, Z.; He, Z. *Appl. Phys. Lett.* **2006**, *89*, 083101.
17. Wang, J.; Wen, Y.; Hu, J.; Song, Y.; Jiang, L. *Adv. Funct. Mater*. **2007**, *17*, 219.
18. (a) Woodward, J. T.; Gwin, H.; Schwartz, D. K. *Langmuir*, **2000**, *16*, 2957. (b) Sun, T.; Song, W.; Jiang, L. *Chem. Commun.* **2005**, 1723. (c) Wang, S.; Feng, L.; Liu, H.; Sun, T.; Zhang, X.; Jiang, L.; Zhu, D. *Chem. Phys. Chem*, **2005**, *6*, 1475. (d) Genzer, J.; Efimenko, K. *Science*, **2000**, *290*, 2130. (e) Schondelmaier,

D.; Cramm, S.; Klingeler, R.; Morenzin, J.; Zilkens, Ch.; Eberhardt, W. *Langmuir*, **2002**, *18*, 6242. (f) Kong, H.; Gao, C.; Yan, D. *J. Am. Chem. Soc.* **2004**, *126*, 412 (g) Baskaran, D.; Mays, J. W.; Bratcher, M. S. *Angew. Chem., Int. Ed.*, **2004**, *43*, 2138. (h) Liu, J.; Rinzler, A. G.; Dai, H.; Hafner, J. H.; Bradley, R. K.; Boul, P. J.; Lu, A.; Iverson, T.; Shelimov, K.; Huffman, C. B.; Rodriguez-Macias, F.; Shon, Y. S.; Lee, T. R.; Colbert, D. T.; Smalley, R. E. *Science*, **1998**, *280*, 1253. (i) Khare, B. N.; Meyyappan, M.; Kralj, J.; Wilhite, P.; Sisay, M.; Imanaka, H.; Koehne, J.; Baushchilcher, C. W. *Appl. Phys. Lett.* **2002**, *81*, 5237. (j) Ni, B.; Andrews, R.; Jacques, D.; Qian, D.; Wijesundara, M. B. J.; Choi, Y.; Hanley, L.; Sinnott, S. B. *J. Phys. Chem. B* **2001**, *105*, 12719. (k) Tada, H.; Nagayama, H. *Langmuir* **1995**, *11*, 136. (l) Nishino, T.; Meguro, M.; Nakamae, K.; Matsushita, M. *Langmuir*, **1999**, *15*, 4321. (m) Anton, D. *Adv. Mater*. **1998**, *10*, 1197.

19. Ghosh, S.; Sood, A. K.; Kumar, N. *Science* **2003**, *299*, 1042.
20. Dujardin, E.; Ebbesen, T. W.; Hiura, H.; Tanigaki, K. *Science* **1994**, *265*, 1850.
21. Dujardin, E.; Ebbesen, T. W.; Krishnan, A.; Treacy, M. M. J. *Adv. Mater.* **1998**, *10*, 1472.
22. Ebbesen, T. W. *J. Phys. Chem. Sol.* **1996**, *57*, 951.
23. Neimark, A. V. *J. Adhesion Sci. Technol.* **1999**, *13*, 1137.
24. Mattia, D.; Bau, H. H.; Gogotsi, Y. *Langmuir* **2006**, *22*, 1789.
25. (a) Feng, L.; Li, S. H.; Li, Y. S.; Li, H. J.; Zhang, L. J.; Zhai, J.; Song, Y. L.; Liu, B. Q.; Jiang, L.; Zhu, D. B. *Adv. Mater*. **2002**, *14*, 1857. (b) Shibuichi, S.; Onda, T.; Satoh, N.; Tsujii, K. *J. Phys. Chem.* **1996**, *100*, 19512. (c) Shibuichi, S.; Yamamoto, T.; Onda, T.; Tsujii, K. *J. Colloid Interface Sci.* **1998**, *208*, 287. (d) Miwa, M.; Nakajima, A.; Fujishima, A.; Hashimoto, K.; Watanabe, T. *Langmuir* **2000**, *16*, 5754.
26. (a) Ichimura, K.; Oh, S.-K.; Nakagawa, M. *Science* **2000**, *288*, 1624. (b) Lahann, J.; Mitragotri, S.; Tran, T.-N.; Kaido, H.; Sundaram, J.; Choi, I. S.; Hoffer, S.; Somorjai, G.; Langer, R. *Science* **2003**, *299*, 371. (c) Isaakson, J.; Tengstedt, C.;

Fahlman, M.; Robinson, N.; Berggren, M. *Adv. Mater.* **2004**, *16*, 316.

27. Zhu, L.; Xu, J.; Xiu, Y.; Sun, Y.; Hess, D. W.; Wong C. *J. Phys. Chem. B* **2006**, *110,* 15945.
28. Krupenkin, T.; Taylor, J.; Schneider, T.; Yang, S. *Langmuir* **2004**, *20*, 3824.
29. Chen, J. Y.; Kutana, A.; Collier, C. P.; Giapis. K. P. *Science* **2005**, 310, 1480.
30. Bockrath, M.; Cobden, D. H.; Lu, J.; Rinzler, A G.; Smalley, R. E.; Balents, L.; McEuen. P. L. *Nature* **1999**, 397, 598.
31. Liu, H.; Zhai, J.; Jiang, L. *Soft Matter* **2006**, *2*, 811.
32. Froumkine A. *Actualites Scientifiques* **1976**, *373*, 5.
33. Lippman G. *Ann. Chim. Phys.* **1875,** *5*, 495.
34. Sondag-Huethorst J. A. M.; Fokkink L. G. J. *Langmuir* **1994**, *10*, 4380.
35. Wang, Z.; Ou, Y.; Lu, T.-M.; Koratkar N. *J. Phys. Chem. B* **2007**, *111,* 4296.
36. Andrews, R.; Jacques, D.; Rao, A. M.; Derbyshire, F.; Qian, D.; Fan, X.; Dickey, E.C.; Chen, J. *Chem. Phys. Lett.* **1999,** *303*, 467.
37. (a) Chen, J.; Hamon, M. A.; Hu, H.; Chen, Y.; Rao, A. M.; Eklund, P. C.; Haddon, R. C. *Science* **1998**, *282*, 95. (b) Fu, K.; Huang, W.; Lin, Y.; Riddle, L. A.; Carroll, d. L.; Sun, Y.-P. *Nano Lett.* **2001**, *1*, 439 (c) Hudson, J. L.; Casavant, M. J.; Tour, J. M. *J. Am. Chem. Soc.* **2004**, *126*, 11158.
38. (a) Shamai, R.; Andelman, D.; Berge, B.; Hayes, R. *Soft Matter* **2008**, *4*, 38. (b) Quilliet, C.; Berge, B. *Current Opinion in Colloid and Interface Science,* **2001**, *6*, 34.
39. (a) Darmstadt, H.; Roy , C.; Kaliaguine, S.; Choi, S. J.; Ryoo. R. *Carbon* **2002**, *40*, 2673 (b) http://srdata.nist.gov/xps/elm_in_comp_res. (c) Choi, H. C.; Kim, S. Y. ; Jang, W. S.; Bae, J. P.; Kim, K. L.; Kim, K. *Chem. Phys. Lett.* **2004**, *399*, 255. (d) Kasuya, S.; Sasaki, Y.; Tohji, K.; Nishina, Y. *Phys. Rev. Lett.* **1997**, *78*, 4434. (e) Rao, A. M.; Eklund, P. C.; Bandow, S.; Thess, A.; Smalley, R. E. *Nature* **1997**, *388*, 257. (f) Bubert, H.; Haiber, S.; Brandl, W.; Marginean, G.; Heintze, M.; Brüser, V. *Diamond and Related Materials* **2003**, *12*, 811. (g) Haiber, S.; Xingtao, A.; Bubert, H.; Heintze, M.; Brüser, V.; Brandl, W.;

Marginean, G. *Anal Bioanal Chem.* **2003**, *375*, 875. (h) Felten, A. ; Bittencourt, C. ; Pireaux, J. J. ; Van Lier, G. ; Charlier, J. C. *J. Appl. Phys.* **2005,** *98*, 074308. (i) Pirlot, C.; Willems, I.; Fonseca, A.; Nagy, J. B.; Delhalle, J. *Advanced Engineering Materials*, **2002**, *4*, 109. (j) Ago, H.; Kugler, T.; Cacialli, F.; Salaneck, W. R.; Shaffer, M. S. P.; Windle, A. H.; Friend, R. H. *J. Phys. Chem. B* **1999,** *103*, 8116. (k) Wang, Y. Q.; Sherwood, P. M. A. *Chem. Mater.*, **2004**, *16*, 5427. (l) Parekh, B. D. T.; Knight, P.; Santhanam, K.S.V.; Takacs, G. A *J. Adhesion Sci. Technol.* **2006,** *20*, 1833.

40. (a) Lee C. J.; Park, J. H.; Huh, Y.; Lee, J. Y. *Chem. Phys. Lett.* **2001,** *343*, 33. (b) Chiang, I. W.; Brinson, B. E.; Huang, A. Y.; Willis, P. A. ; Bronikowski, M. J. ; Margrave, J. L. ; Smalley, R. E. ; Hauge, R. H. *J. Phys. Chem. B* **2001**, *105*, 8297.
41. (a) Rao, A. M.; Jorio, A.; Pimenta, M. A.; Dantas, M. S. S.; Saito, R.; Dresselhaus, G.; Dresselhaus, M. S. *Phys. Rev. Lett.* **2000**, *84*, 1820. (b) Zhao, X.; Ando, Y.; Qin, L.-C.; Kataura, H.; Maniwa, Y.; Saito, R. *Physica B* **2002**, *323*, 265. (c) Bacsa, R. R.; Flahaut, E.; Laurent, Ch.; Peigney, A.; Aloni, S.; Puech, P. et. al. *New J. Phys.* **2003**, *5*, 131.1- 1.9. (d) Matthews, M. J.; Pimenta, M. A.; Dresselhaus, G; Dresselhaus, M. S.; Endo, M. *Phys. Rev. B* **1999**, *59*, R6585. (e) Brar, V. W.; Samsonidze, G. G.; Dresselhuas, G.; Saito, R.; Swan, A. K.; Unlu, M. S.; Goldberg, B. B.; Souza, F. A. G.; Jorio, A. *Phys Rev. B* **2002**, *66*, 155418. (f) Chen, C. M.; Dai, Y. M.; Huang, J.G.; Jehng, J. M. *Carbon* **2006,** *44*, 1808.
42. (a) Martines, E.; Seunarine, K.; Morgan, H.; Gadegaard, N.; Wilkinson, C. D. W. ; Riehle M. O. *Nano Lett.* **2005**, *5*, 2097. (b) Extrand C. W. *Langmuir* **2004**, *20*, 4017. (c) Gao, L.; McCarthy T. J. *Langmuir* **2006**, *22*, 6234. (d) McHale, G.; Shirtcliffe, N. J.; Newton M. I.*Langmuir* **2004**, *20*, 10146. (e) He, B.; Lee, J.; Patankar N. A. *Colloids and Surfaces A: Physicochem. Eng. Aspects* **2004**, *248*, 101. (f) Li, W.; Amirfazli A. *J. Coll. Inter. Sci.* **2005**, *292*, 195. (g) McHale, G.; Shirtcliffe, N. J.; Aqil, S.; Perry, C. C.; Newton. M. I. *Phys. Rev. Lett.* **2004**, *93*,

036102-1. (h) Rio, E.; Daerr, A.; Andreotti, B.; Limat, L. *Phys. Rev. Lett.* **2005**, *94*, 024503. (i) Baret J.-C.*Phys. Rev. Lett.* **2006**, *96*, 016106. (j) Dorrer, C.; Ru¨he J.; *Langmuir* **2006**, *22*, 7652. (k) Extrand, C. W.; Kumagai, Y. *J. Coll. Inter. Sci.* **1997**, *191*, 378. (l) Baret, J. –C.; Brinkmann, M. *Phys. Rev. Lett.* **2006**, *96*, 146106.

43. Wenzel, R. N. *Ind. Eng. Chem.* **1936**, *40*, 988.
44. MacDougall, G.; Okrent, C. *Proc. R. Soc. London A* **1942**, *180*, 151.
45. (a) Wang, R.; Hashimoto, K.; Fujishima, A.; Chikuni, M.; Kojima, E.; Kitamura, A.; Shimohigoshi, M.; Watanabe, T. *Nature* **1997**, *388*, 431. (b) Sakai, N.; Wang, R.; Fujishima, A.; Watanabe, T.; Hashimoto, K. *Langmuir* **1999**, *14*, 5918.
46. (a) Harminghaus, S. *Europhys. Lett.* **2000**, *52*, 165.
47. (a) Birdi, K. S.; Vu, D. T. *J. Phys. Chem.* **1989**, *93*, 3702. (b) Birdi, K. S. ; Vu, D. T. *J. Adhesion Sci. Technol.* **1993**, *7*, 485.
48. Barber, A. H.; Cohen, S. R.; Wagner, H. D. *Phys. Rev. B:* **2005**, *71*, 115443/1.
49. Prins, M. W. J.; Welters, W. J. J.; Weekamp, J. W. *Science* **2001**, *291*, 277.
50. Adam, N. K. *The Physics and Chemistry of Surfaces* (Dover, New York, **1968**).
51. (a) Holmes-Farley, S. R.; Reamey, R. H.; McCarthy, T. J.; Deutch, J.; Whitesides, G. M. *Langmuir* **1985**, *1*, 725. (b) Holmes-Farley, S. R.; Bain, C. D.; Whitesides, G. M. *Langmuir* **1988**, *4*, 921. (c) Quinn, A.; Sedev, R.; Ralston, J. *J. Phys. Che. B* **2005**, *109*, 6268.
52. Morcos, I. *J. Chem. Phys.* 1972, 57, 1801.
53. Morcos, I. *J. Chem. Phys.* 1972, *76*, 2750.
54. Bard, A. J.; Faulkner, L. R. *Electrochemical Methods, Fundamentals and Applications (2nd Edition)*, Brijbasi Art Press Ltd., Noida, India.

CHAPTER 5

Rhodium Nanoparticles Supported on Multiwalled Carbon Nanotubes*

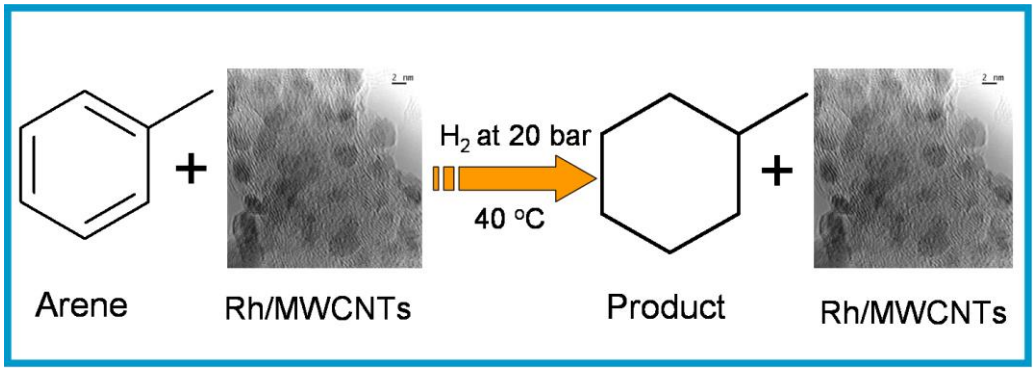

Monodispersed Rhodium nanoclusters protected by tridecyl amine (4.9 ± 0.2 nm) have been synthesized in a simple bi-phasic mixture, which show a quantized double layer charging behavior typically in this size regime. Differential pulse (DPV), cyclic voltammetry (CV) and linear sweep voltammetry (LSV) demonstrate 13 consecutive charging peaks with ΔV of 80 mV in the E_{PZC} (0.012 V) region. However, when these Rhodium nanoparticles, are anchored to the Multiwalled carbon nanotubes by a simple microwave treatment, they no longer show such unusual behavior in the same electrolyte although interestingly exhibit a remarkable catalytic activity for arene hydrogenation with an enhanced turn over number of ~10000; indeed, di-substituted arenes show selective conversion of thermodynamically less favorable *cis*-products (>80%). A series of arenes have been tested using various Rh based catalysts and a comparison of the results with that of reported rhodium catalysts shows unique selectivity under mild conditions.

*A part of the work discussed in this chapter has been published in: **"***Adv. Mater.* **2007,** *19*, 272 and another part in *J. Nanosci. Nanotechnol.* **2007**, *7*, 2870".

5.1. Introduction

Recently, a large amount of effort has been focused to understand the structure and properties of nanometer sized metallic and semiconducting quantum dots due to their promising applications as building blocks for nanoelectronic circuit components like molecular switches, single electron transistors, field effect transistors and resonant tunneling diodes [1-5]. Surface passivation or stabilization of these Q-dots by various organic molecules, such as aliphatic or aromatic thiols, amines etc. has been used by many groups, which in turn provides a great flexibility to tune their size and shape, and hence electronic properties and chemical reactivities [6-10].

The confinement of electronic wave function in these regime causes discreteness of energy levels and more importantly, the average spacing of successive quantum levels (Kubo gap, δ) can be controlled to make a system metallic or nonmetallic. Since δ is approximately given by $4E_f/3n$, where E_f is the Fermi energy of bulk metal and n is the number of valence electrons in Q-dots, a change in 'n' by size tuning can lead to the control of δ compared to the value of thermal energy [11-15]. The scanning tunneling microscopic (STM) studies at low temperature of both isolated and organized Q-dots show Coulomb Blockade effect, where dielectric organic molecules act as tunnel barriers for the electron transfer [16,17]. Consequently, in order to tunnel across the barrier, the electron should have to overcome the Q-dot charging energy (E_c), i.e., $E_c = e^2/2C_{CLU}$, where e is the electronic charge and C_{CLU} is the capacitance of the individual cluster [16, 17].

Pioneering work by Murray and co-workers have shown that freely diffusing (in solution) or organized ultra small Q-dots on electrode surface have multivalent redox property due to their sub-atto farad charge storage capability [18-20]. These Q-dots show consecutive single electron charging in voltammetric experiments as current peaks at an equal potential interval ($\Delta V=e/C_{CLU}$; $E_c >> k_BT$); popularly known as quantized double layer (QDL) charging, analogous to the STM based "Coulomb Staircase" or "Coulomb Blockade" behavior [18,19]. The capacitance is associated with the ionic space charge formed around each Q-dots dissolved in the electrolyte solution, where electrostatic

principles govern the charging of the core. Although this QDL charging has been reported for both metal (Au, Ag, Pd, Cu etc.) and semiconductor (Si, CdS, PbS, CdTe etc.) Q-dots, most of these reports are restricted in 1-3 nm size regime and some of them are observed only at low temperature [18-27]. This is because of several limitations in synthetic procedures like polydispersity, use of interfering phase transfer agents and tedious methods of purification and size sieving [27-30]. Most of these synthetic procedures involve the use of ammonium salts, whose complete removal from the particle surface is very troublesome [27-35]. Thus, the development of low cost synthetic procedure to prepare size selective MPCs by avoiding the use of quaternary-ammonium salts is important for their practical applications. Interestingly, the semiconductor like nature of these Q-dots shows a large ΔV spacing near E_{pzc} region, where E_{pzc} is the formal potential of the zero charge for these Q-dots, ("Electrochemical Band Gap") analogous to their HOMO-LUMO gap [18-20]. A theoretical calculation based on the model proposed by Chen et al. predicts that bigger sized Q-dots (>3 nm diameters) have higher capacitance value and hence it is possible to observe a larger number of discrete charging events at a smaller potential window in solution electrochemistry [36]. On the other hand, previous effort from our group has shown some success to correlate this prediction for larger sized AuMPCs (~Au_{1400}, Au_{2869}), where the surface adsorption plays an important role [37]. However, no report of both solution phase as well as solid state coulomb Blockade effects is available in case of transition metal nanoclusters like Pt, Ru and Rh to date, despite their significance in various field of energy technology like fuel cell and catalysis [38]. Consequently, there is an urgent need to explore synthetic procedures in order to get monodispersed nanoclusters of Rh and other similar systems to its importance of tuning their size and shape dependent properties.

One of the important applications of such Rh nanoparticles is in catalysis, where a remarkable performance for hydrogenation for various compounds has been observed [39]. Selective hydrogenation of arenes is a crucial step in the preparation of a wide variety of organic compounds of commercial interest such as the synthesis of cyclohexane (a precursor to adipic acid for producing nylon) [40], removal of aromatic compounds from fuels [41], and finally as a way to prevent paper from yellowing without

the addition of bleaches [42]. Many important results have been observed for hydrogenation by soluble metal clusters, especially using Rh and Ru. Some of the prominent ones are as follows- (i) soluble nanocluster catalysts are implicated as the true catalysts in many putatively "homogeneous" arene hydrogenations; (ii) with few exceptions, nanocluster catalysts for arene hydrogenation are poorly characterized; (iii) soluble nanocluster catalysts for arene hydrogenation have modest activity and lifetime; (iv) Rh and Ru are used almost exclusively as the active metals; (v) two catalyst systems, one developed by Roucoux and co-workers [43] and the other by Finke and co-workers [44], show remarkable activity and lifetime, (vi) selective arene hydrogenation, especially for the synthesis of the all-*cis* diastereomer of substituted cyclohexanes, has received considerable attention and is a promising area for future study and, perhaps, for fine chemical applications. However, some of these nanoparticles are kinetically unstable since they undergo agglomeration after several cycling, resulting in the deactivation. Mechanistic details on their thermal stability, catalyst isolation and precipitation during polarity changes have not been understood adequately till date, despite the significance of soluble metal nanoparticles [45].

In order to avoid such difficulties in using soluble metal catalysts, metal nanoparticles on high surface area support would be a better option. More interestingly, much attention has been focused on strong-metal support interaction (SMSI), which occurs when a metal is supported on a reduced metal oxide [46]. However, the effect of SMSI on catalysis depends on the type of reaction. For example, the effect could be very pronounced for reactions involving carbon-carbon bond breaking, but is generally rather small for hydrogenation reactions [46]. Traditionally, arene hydrogenation has been performed with heterogeneous catalysts such as Rh/Al_2O_3, Raney nickel, and metal sulfide under drastic reaction conditions [47]. For example, Rothwell et al. have used homogenous niobium and tantalum catalysts for the hydrogenation of arenes and arylphosphines [48], while Finke et al. have utilized metal nanoparticles as catalysts for similar reactions [49]. As recyclable catalyst in the form of molecular rhodium tethered to a palladium-silica support [50] or ionic copolymer [51] has been reported. Arene hydrogenation has been performed under various conditions such as liquid-liquid

biphasic conditions [52], ionic liquid conditions [53] and supercritical CO_2 conditions [54].

Recently, the use of carbon nanotubes (CNT) as a support in heterogeneous catalysis has garnered much attention due to their favorable characteristics such as high surface area, mechanically stable and inert carbon network and chemically tunable topography. These also show catalytic properties superior to those of catalysts prepared on activated carbon, soot, or graphite [55]. While carbon nanofibers consist of graphite sheets arranged in various orientations along the central axis in which the planes are stacked up like a fishbone, with lot of edges, SWCNTs and MWCNTs show a concentric wall structure consisting of ordered graphite platelets. The morphology and the size of the above supports, especially since they present higher length to diameter ratio, can play a significant role in catalytic applications owing to their ability to disperse the active phase. Their electronic properties are also of primary importance [56] and their mechanical strength makes them resistant in view of recycling. A recent comparison between the interaction of transition metal atoms with carbon nanotube walls and with graphite indicates major differences in bonding sites, magnetic moments and charge-transfer direction [57].

Accordingly, several efforts have been attempted to explore the catalytic activity of metal nanoparticles anchored on CNTs [57b,58]. For example, CNT supported Rh, Pd and Pd/Rh nanoparticle catalysts synthesized by microemulsion-template show a higher yield in Heck coupling reaction, although a drastic change in conditions like pressure have been employed with the metal content more than 5 wt% [59]. However, most of these reports deal with tedious synthetic procedures involving supercritical conditions of solvents with more than 20% catalyst loading.

In the previous chapter (i.e., chapter 4), we have discussed the unique functionalization strategy for both SWCNTs and MWCNTs by covalent route in order to enhance their solubility, which could be a pre-requisite for composite preparation. To extend our studies in catalytic properties of MWCNTs, the present chapter deals with the synthesis, characterization and catalytic performance of Rhodium nanoparticles supported MWCNTs. We also describe the electrochemical QDL charging behavior of

RhMPCs (ca. 4.9 ± 0.2 nm) passivated with tridecylamine by differential pulse and cyclic voltammetry at 298 K. In this size domain the QDL property is restored as reflected by 13 numbers of discrete charging events in a narrow potential range (-0.6 to +0.6 V) with equidistant ΔV ($\approx$ 80 mV) spacing. Further, comparative catalytic properties of these RhMPCs along with Rhodium-MWCNT based catalysts have been studied with respect to their Turn over number (TON). All these Rhodium based catalysts thus prepared, were characterized by HRTEM, SEM, XRD, TGA, XPS and BET isotherm in order to explore their structural changes after decoration.

5.2. Experimental Section

5.2.1. Materials

Tridecylamine (99%), $NaBH_4$ and tetrabutylammoniumhexaflurophosphate (TBAHFP) and Rhodium (II) acetate dimer ($Rh_2(OOCCH_3)_4 .2H_2O$) were obtained from Aldrich, whereas acetone, hexane and dichloromethane were of AR grade from Merck and were used after further purification. MWCNTs were synthesized by CVD method as discussed in chapter 2. All arenes like benzene, phenol, anisole, diphenyl ether, anthracene, naphthalene, xylenes and acetophenone (AR grade from Merck) were used without further purification. Vulcan XC-72 amorphous carbon obtained from Arora Matthey Ltd. India, was used as received. In all these experiments deionized water (16 MΩ) from Milli-Q system was used. A detailed description of MWCNT synthetic procedure is mentioned in chapter 2.

5.2.2. Preparation of Rhodium Nanoclusters

Monolayer protected Rhodium nanoclusters (RhMPCs) of size of 4.9 ± 0.2 nm have been synthesized using a modified form of Brust synthesis [6,38] and digestive ripening process [34a,b]. In brief, RhMPCs were obtained in a water-toluene (v/v; 1:1; 50 mL each) biphasic mixture using a 1:3 mole ratio of rhodium (II) acetate to tridecylamine in ambient conditions. The formation of RhMPCs takes place through a rosy red

intermediate Rh complex (due to dimeric Rh-Rh bonding) in the organic layer with subsequent reduction using an aqueous $NaBH_4$ solution. The formation of the intermediate Rh complex is a crucial step during the synthesis as the size of the nanoparticles can effectively be tuned by varying the reaction conditions like temperature and pH, since higher activation barrier at lower temperature prohibits the formation of complex, which consequently leads to a sluggish reaction. The Rh salt-to-amine ratio was kept constant, because the core size is mainly controlled by the Rh / amine stoichiometry. The mixture was stirred for 10 min and subsequently reduced using the dropwise addition of 10 mL of aqueous 0.1 M $NaBH_4$ solution, where upon the red color of Rh complex was transformed to brown-black. This indicates the formation of Rh(0) cluster, and after rigorous stirring for 1 h, most of the Rh species were found to be converted to Rh(0) turning the upper layer brown-black. After separation of the non-aqueous portion from the aqueous layer, the non-aqueous layer was rota-vapped at 313 K. This procedure was repeated 10 times to collect a large amount of sample. The dark powder of toluene-soluble MPCs was precipitated by the addition of an excess volume of acetone (500 mL). The particles were allowed to settle, and excess acetone was decanted to reduce the volume to 20 mL, followed by repeated centrifugation (8-10 times) and decantation to remove excess unbound amine and other unwanted reaction byproducts like borate and unreacted amine which act as deleterious impurities. The RhMPCs produced by this method were of size 4.9 ± 0.2 nm and free from the presence of any phase-transfer catalyst, which might otherwise affect their behavior.

5.2.3. Preparation of Rhodium Catalysts

[a] Rh/MWCNTs1

A weighed quantity (125 mg) of MWCNTs was subjected to microwave treatment for 5 min in concentrated acid mixture (H_2SO_4 + HNO_3) for developing functional groups on the side walls. A detailed procedure of the MWCNT functionalization has been described in the previous chapter [section 4.2.2[G]]. About 100 mg of these functionalized nanotubes was dispersed in 50 mL toluene under ultrasonication (33 kHz) for 10 min, till

a stable dispersion of nanotubes was prepared in order to achieve a homogeneous mixing of metal nanoparticles on the CNTs. About 1.6 mg of RhMPCs, containing ca, 60% of rhodium (deduced from the TG analysis described in the section 5.3.5) was added in MWCNTs dispersion and irradiated with microwave for 1 min (50% of 700 W) followed by stirring for 10 min. Decoloration (initial dark brown) of solution after stirring indicated complete impregnation or adsorption of RhMPCs on MWCNTs, which could be due to more defect sites and active $–COO^-$ groups on the side walls. The excess toluene (colorless solution indicated complete adsorption of RhMPCs on MWCNTs) was removed by filtration through PTFE membrane (0.2 μm pore size). The RhMPC/MWCNTs hybrid material was then calcined at 300 ^oC in argon atmosphere (100 sccm) for 2 h in order to remove the organic capping layer of tridecylamine and subsequently to create more catalytically active sites for Rh nanoparticles.

[b] Rh/MWCNTs2

Initially, 40 mL of 1 mM rhodium acetate solution was mixed with 40 mg of p-aminobenzoic acid (ABA) and stirred for 20 min. To this, 5 mL of 0.1 M $NaBH_4$ was added dropwise in order to reduce Rh(+2) to Rh(0), and the formation of a dark brown color indicated the generation of Rh nanoclusters stabilized by ABA, designated RhABA. The solution of RhABA was further stirred for 10-15 min to allow complete reduction of Rh(+2) ions and the excess of ABA was removed by successive centrifugation and decantation using acetone.

About 100 mg of microwave treated MWCNT was mixed with 40 mL of deionized water and ultrasonicated for 10 min to get a good dispersion. 3 mL of aqueous RhABA (containing 1 mg of Rhodium) solution was added to this before irradiation with microwave for 2 min followed by stirring for further 15 min. Decoloration (initial dark brown) of solution after stirring indicated a complete impregnation or adsorption of RhABA nanoclusters on MWCNTs (preferably on side walls), which could be due to more defect sites and active –COO- groups on the side walls of MWCNTs. Excess water was removed by filtration through a PTFE membrane (0.2 μm pore size). The

RhABA/MWCNTs hybrid material was then calcined at 300 ^{o}C in argon atmosphere for 2 h in order to remove the organic capping layer of ABA. The resultant catalyst was designated as Rh/MWCNTs2.

[c] Rh3

This catalyst was prepared by direct reduction of Rhodium acetate solution (50 mL, 1 mM) using 0.1 M $NaBH_4$ aqueous solution under constant stirring. A black precipitate of Rh(0), thus obtained, was washed with copious amount of water and the solid catalyst was isolated (designated as Rh3).

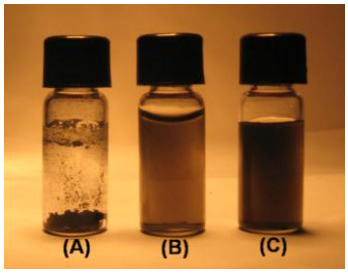

Photograph 5.1. Simple optical images of **(A)** pristine MWCNTs in water after 2 h ultrasonication **(B)** Rh/MWCNTs1 in toluene and **(C)** Rh/MWCNTs2 in water indicating two different catalyst with entirely different surface properties. The approximate solubility in (B) and (C) are 0.05 mg/mL and 0.15 mg/mL respectively.

[d] Rh/VulcanXC

Similar procedure was employed to prepare the Rhodium supported carbon catalyst, as described in section 5.2.3.1. The carbon support in this case was Vulcan XC 72 with surface area 250 m^2/g and particle size distribution of 10 - 15 nm [43c]. Similar pre-treatment was also given to the Vulcan XC amorphous carbon prior to preparing the catalyst and its catalytic activity was compared with those samples mentioned above.

All the above catalysts were prepared with the composition of 1 wt% of Rhodium content for comparing their catalytic performance.

5.2.4. Characterization Techniques

Details pertaining to the characterization tools like XRD, HR-TEM, XPS, FT-IR, Raman and TG-DTA have been already described in chapter 3, (section 3.2.2). Further, the surface area of the catalyst was determined by Brunauer Emmett Teller (BET) method using Quantachrome Autosorb Automated Gas Sorption System with N_2 gas adsorption–desorption measurements at 77 ^{o}C and 100 ^{o}C respectively.

5.2.5. Electrochemical Measurements

All electrochemical measurements were carried out in a mixture (3:1) of acetonitrile and toluene using 0.1 M tetrabutylammoniumhexaflurophosphate (TBAHFP) as the supporting electrolyte at 298 K using a standard three electrode cell comprising Pt disc working electrode (0.5 mm; with area 7.855×10^{-3} cm^2), a Pt wire counter electrode and another Pt wire as quasi reference electrode (calibrated independently with an internal standard of ferrocene/ferrocenium cation redox couple) unless mentioned separately. A weighed quantity (10.0 mg) of thoroughly purified RhMPCs was dissolved in 5.0 mL of electrolyte and Differential pulse (modulation time 200 ms, interval time 0.01 s, step potential 0.025 V and modulation amplitude 0.025 V) voltammetry, and cyclic voltammetry were performed on an Autolab PGSTAT30 (ECO CHEMIE) instrument.

5.2.6. Catalytic Hydrogenation

An autoclave was charged with the appropriate amount of a selected sample of Rh catalyst (5 mg) to the desired amount of substrate (5 mmol) in *n*-hexane (50 mL). This was pressurized with H_2 to the desired level, heated to 40 °C, and then stirred at 400 rpm. The reaction was monitored by gas chromatography (GC) and the products were analyzed by GC/MS. After completion of the reaction, the autoclave was cooled and the reaction mixture was filtered and washed with hexane 3 times (50 mL). The filtrate was activated at 150 °C for 5 h and used in the next cycle. The efficacy of the catalyst was assessed using the hydrogenation of several arenes. Toluene was chosen as the test substrate and heterogeneous selective hydrogenation was carried out with a substrate to catalyst molar ratio of 10000:1 in hexane at 40 °C and at 20 bar H_2. All results of catalysis were

compared in terms of their Turn over numbers (TON)[#] and Turn over frequency (TOF)[#]. Hydrogenation of arenes was studied in details using the catalyst Rh/MWCNTs1 due to its remarkable activity.

5.3. Results and Discussion

5.3.1. Results for the Characterization of RhMPCs

5.3.1.1. Uv-vis Analysis

The color of the nanoparticles has fascinated researchers from ancient time, which originates due to the surface plasmon resonance of the particles [60]. Mie was the first to describe them quantitatively by solving Maxwell's equations with the appropriate boundary conditions for spherical particles [61]. The total extinction cross section composed of absorption and scattering is given as a summation over all electric and magnetic multipole oscillations.

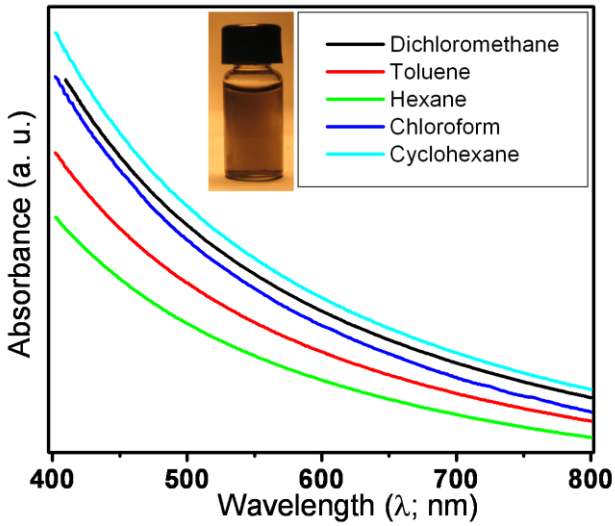

Figure 5.1. UV-vis absorption spectra of 4.9 ± 0.2 nm sized RhMPCs in five different solvents; the absorption spectra are nearly featureless and the broad spectrum over the entire visible region is consistent with the dark brownish-black color of the MPCs, shown in inset.

[#] TON is the mole substrate converted per mole of Rhodium, whereas, TOF is the mole of substrate converted per mole of Rh per h.

For particles with smaller sizes than the wavelength (λ) of the excitation light ($\lambda >> 2r$, and when $2r < 25$ nm, where r is the radius) [62] only the dipole absorption of the Mie equation contributes to the extinction cross section (σ_{ext}) of the nanoparticles. The Mie theory then reduces to the following relationship (quasi-static or dipole approximation):

$$\sigma_{ext} = (9V_P\varepsilon_m^{3/2}/c).[\omega\varepsilon_2(\omega)/\{\varepsilon_1(\omega) + 2\,\varepsilon_m\}^2 + \varepsilon_2(\omega 2)^2] \qquad (5.1)$$

where V_P is the spherical particle volume, c is the speed of light, ω is the angular frequency of the exciting radiation, and ε_m is the dielectric constant of the surrounding medium (assumed to be frequency independent) [63]. $\varepsilon_1(\omega)$ and $\varepsilon_2(\omega)$ denote the real and imaginary part of the dielectric function of the particle, respectively [$\varepsilon(\omega) = \varepsilon_1(\omega) + i\varepsilon_2(\omega)$]. This shows that the surface plasmon band position strongly depends on the particle size and on the dielectric function of the materials and its surrounding medium [60-63].

Figure 5.1 shows the UV-vis spectra of 4.9 nm sized RhMPCs in various solvents such as dichloromethane, toluene, hexane, chloroform and cyclohexane to account the effect of solvent refractive index, where the absorptions have been shown along the arbitrary y-axis. The absorption spectra are nearly featureless and the broad spectrum over the entire visible region is consistent with the dark brownish-black color of the MPCs, shown in the inset of Figure 5.1. Apparently there is no significant change as a function of the solvent refractive index.

5.3.1.2. TEM Analysis

The size distribution and regular arrangement are evident from a comparison of the TEM images of these particles. For example, Figure 5.2 (a-b) shows a high population of uniformly sized particles with an average size of 4.9 ± 0.2 nm along with their statistical distribution (Gaussian) as an inset of Figure 5.2(e), which is the analysis of more than 100 spherical particles, verified from four different samples. More specifically, the high-

resolution images as shown in Figure 5.2 (a-b) depict the lattice fringes for these particles, whereas hexagonal close packed structure is clearly evident in these figures. The composition of these RhMPCs are also approximated from the TEM results by calculating the nearest stable magic numbers as full shell clusters, since certain magic numbers are known to be stable [64]. The average composition of these MPCs are summarized as $Rh_{2057}(TDA)_{321}$ by assuming the shape of these particles as spherical, radius of Rh atom as 173 pm, perfect fcc packing (74% packing) and further considering one N atom per two Rh atoms on the surface as reported for two dimensional SAM formation of long chain amines on single crystal metal surfaces [1,30]. Finally, the bright field selected area diffraction (SAED) pattern shows a crystalline nature of the RhMPCs exhibiting dominant reflections corresponding to (111), (200), (220) and (311) planes as indicated in the Figure 5.2(f).

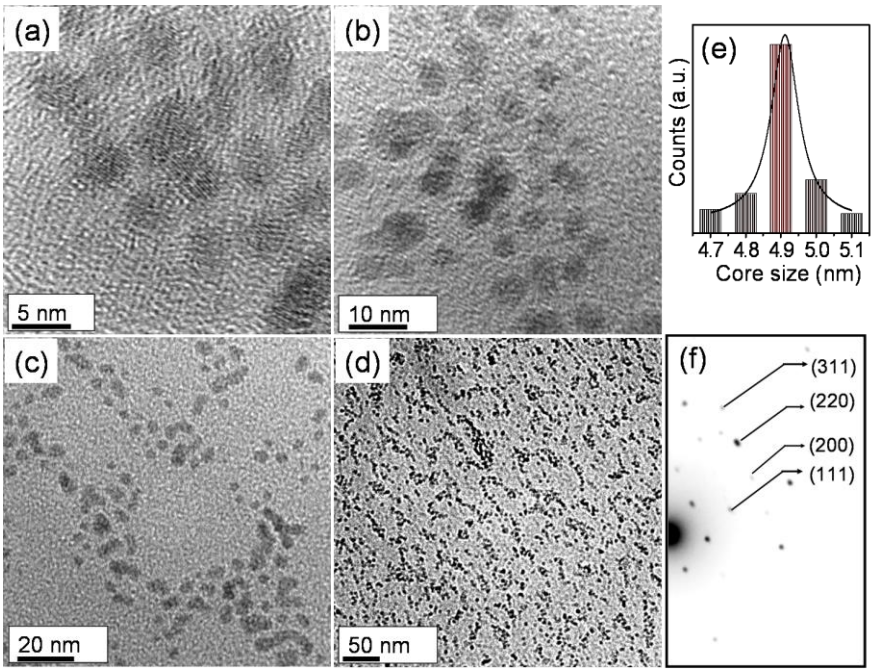

Figure 5.2. (a-b) High resolution TEM images of purified RhMPCs corresponding to $Rh_{2057}(TDA)_{321}$ after repeated solvent extraction and careful fractionation experiments revealing the particle size of 4.9 ± 0.2 nm [distribution in (e)]; the lattice fringes are visible in micrograph **(c-d)** low resolution TEM images show monodispersed nanoparticles; **(f)** shows bright field SAED pattern of the RhMPCs indicating the crystalline nature with dominant reflections.

5.3.1.3. XRD Analysis

XRD studies have been carried out to investigate the crystallinity of these MPCs. Accordingly, Figure 5.3 shows respective XRD patterns of these MPCs along with simulated patterns based on the space group Fm3m (space group number: 225), assuming a perfect fcc structure. This reveals bulk fcc crystal structure for these MPCs, which is in agreement with previous reports [65] and the corresponding lattice planes are marked in the figure; the slight variations in the positions perhaps arise due to lattice miss matching due to low dimensionality.

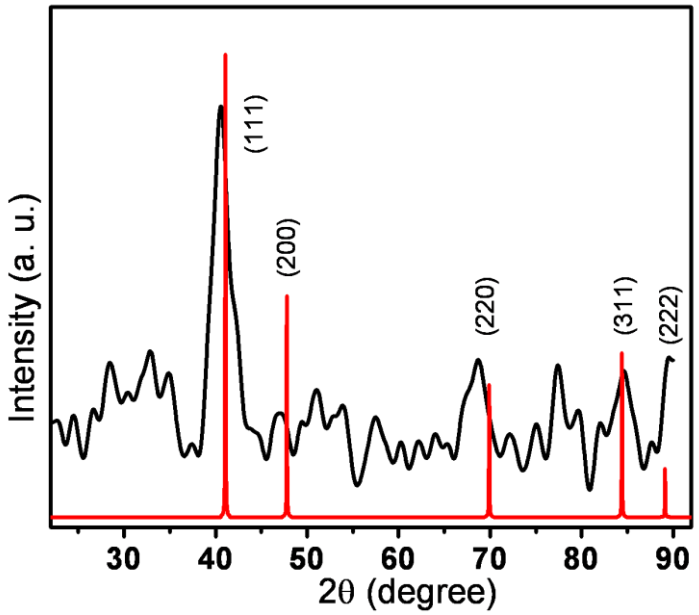

Figure 5.3. XRD patterns of RhMPCs (black line) and simulated curve based on the space group Fm3m (space group number: 225) assuming a perfect fcc structure (red line); XRD pattern with corresponding lattice planes of the RhMPC clearly show a bulk fcc crystal structure with slight variations in the positions, perhaps due to lattice miss-matching.

Crystallite size is also calculated from the full width at the half maxima (FWHM) of the (111) peak using Scherrer formula as given by:

$$\text{Particle Size} = K\lambda / B\cos\theta \qquad (5.2)$$

Where, K is Scherrer constant (0.9 for spherical particles), λ is wavelength of the X-ray

diffraction (1.54 Å for CuK_α), B is the FWHM of the peak and θ is diffraction angle [66]. The calculated crystallite size (~ 3.8 nm) is comparable with the size obtained from TEM analysis.

5.3.1.4. NMR Analysis

The surface passivation along with the purity of these MPCs has been examined with the help of ^1H NMR analysis as shown in Figure 5.4. These spectra show distinct multiplets (three) corresponding to the protons at C_2, $C_{3\text{-}12}$ and C_{13} carbons at ~1.73, ~1.26 and ~0.89 ppm respectively. The individual peak positions are similar, despite broadening compared to that of pure alkanes, [29a] and integration of the peaks gives rise to the total of 27 protons corresponding to the aliphatic chain of the tridecylamine. Interestingly, the proton at C_1 position is not observed due to the effective capping through N atom, which causes inhomogeneity in the local chemical environment. In particular, the absence of prominent resonance at 2.7 ppm corresponding to the protons at C_1 position indicates a strong interaction with the metal surface as well as the purity of the samples [29a].

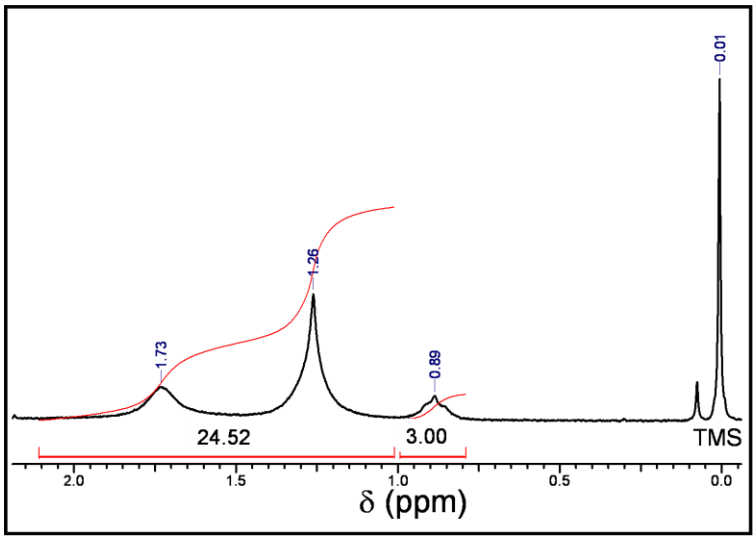

Figure 5.4. ^1H NMR response of purified RhMPCs in $CDCl_3$, revealing that the peaks are significantly broadened and shifted from their ideal position due to surface passivation of the Rh core.

5.3.1.5. FTIR Analysis

The local molecular environment of the passivating ligands on these MPCs can be obtained from the FTIR analysis (as shown in Figure 5.5(a)), where the C-H stretching region (2800- 3000 cm^{-1}) is particularly informative about the orientation of methylene chains. For example, Figure 5.5(b) shows the superimposed FTIR spectra of C-H stretching region corresponding to TDA (black curve) and RhMPCs (red curve), where four peaks are evident corresponding to symmetric (d^+) and asymmetric (d^-) CH_2 stretching modes, asymmetric in plane (r^-) and symmetric (r^+) stretching mode of terminal methyl groups.

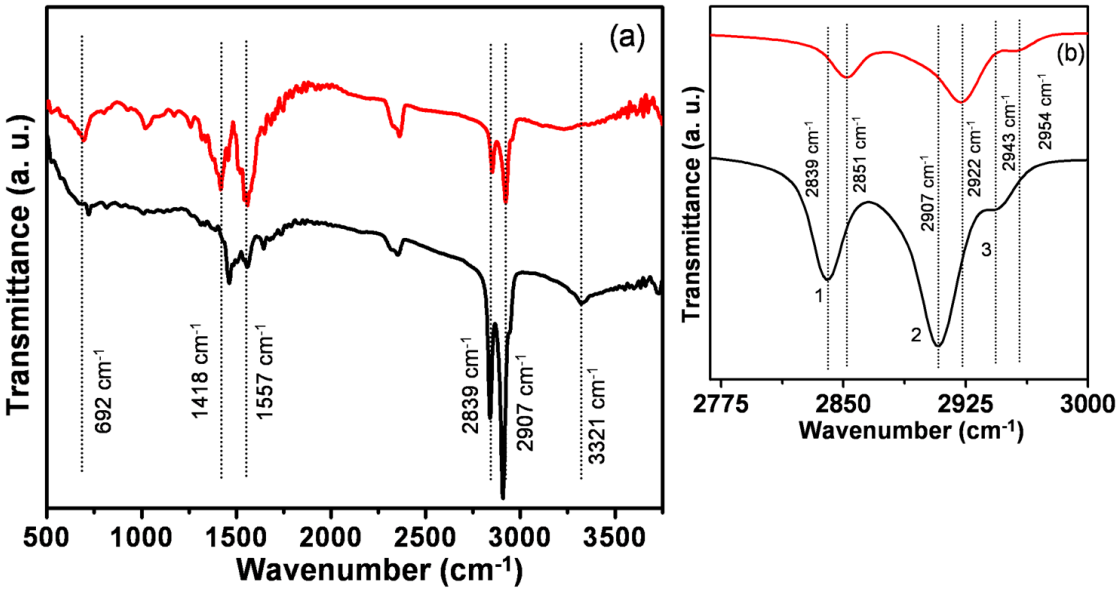

Figure 5.5 (a) Superimposed FTIR spectra of tridecylamine (black line) and RhMPC (red line) showing the capping of tridecylamine **(b)** C-H stretching region, where three peaks are evident corresponding to symmetric (d^+) and asymmetric (d^-) CH_2 stretching modes, and asymmetric in-plane (r^-) stretching mode of terminal methyl groups. A blue shift of 12 cm^{-1} in all these positions indicates the increment of capping and disordering in monolayer. FTIR was performed using a single crystal of NaCl.

The ordering of the alkyl chains is best evident by the peak values of d^+ and d^- CH_2 stretching vibrations, whereas r^+ and r^- stretching modes are indicative for orientational freedom of the chain termini. The corresponding positions of these

stretching modes are summarized in Table 5.1 for both tridecylamine and TDA capped RhMPCs. Most importantly, we find the d^+ and d^- values for particle are red shifted as compared to that of the bulk alkanes. However, the red shift of d^+ and d^- stretching modes indicates the presence of a high percentage of all-trans conformations, especially characteristic of crystalline alkanes, whereas the blue shift corresponds to a greater number of gauche defects [67,68]. Interestingly, all these stretching modes are blue shitted as shown in Figure 5.5 (b), where (1-3) correspond to d^+, d^- and r^- in similar order. Nevertheless, the symmetric in plane stretching modes for methyl groups have not been observed in both the cases. More specifically, this blue shift of stretching modes illustrates the decrease of alkyl chain order along with a concomitant increment of gauche defects, thus, indicating the presence of a higher number of ligands facilitating disorder.

Table 5.1. FTIR results of tridecylamine and RhMPCs, especially showing variation of d^+, d^- and r^- stretching modes after capping.

Sample	**(1) d^+ (cm^{-1})**	**(2) d^- (cm^{-1})**	**(3) r^- (cm^{-1})**
Tridecylamine	2839	2907	2943
RhMPC	2851	2922	2954

All other bands are assigned on the basis of n-alkane vibrations as shown in Figure 5.5(a), The scissoring motion (δ) of an 'all-trans' methylene chains for tridecylamine is apparent at ~1456 cm^{-1}, which is broadened after capping, due to the overlap of other vibrational modes such as scissoring motion of a methylene group next to a gauche bond, and the methyl antisymmetric bending vibration. In addition, Figure 5.5(a) reveals that the capping agent is pretty intact except for the disappearance of a peak due to –N-H stretching at 3321 cm^{-1} after anchoring to Rh surface. Appearance of additional strong bands at 572 cm^{-1} is attributed to the presence of Rh-N bond [69]. A few sharp bands near 1030 and 1358 cm^{-1}, which are absent in the spectra of TDA, could be ascribed to the coordinated N species. In addition, a broad band at 2320 cm^{-1} suggests

the presence of N as a charged amine species (-NH^+), indicating the involvement of electrostatic interactions, especially with the nanoparticle surface [69,70]. Therefore, it is likely that RhMPC surface already has a complex like environment of R-amine after the reduction due to the presence of few coordinate Rh-N bonds in axial position [69,71].

5.3.1.6. TG-DT Analysis

The relationship between core size and percentage of weight loss of organic capping can be analyzed by TG [28]. For example, two step decomposition (as shown in Figure 5.6) reveals a two-step loss of weight due to uncapped (physisorbed / complexed / excess) and capped tridecylamine (primary layer) respectively. Accordingly, the observed ~18% weight loss due to organic capping supports the approximate particle composition, which also agrees well with the magic number calculations.

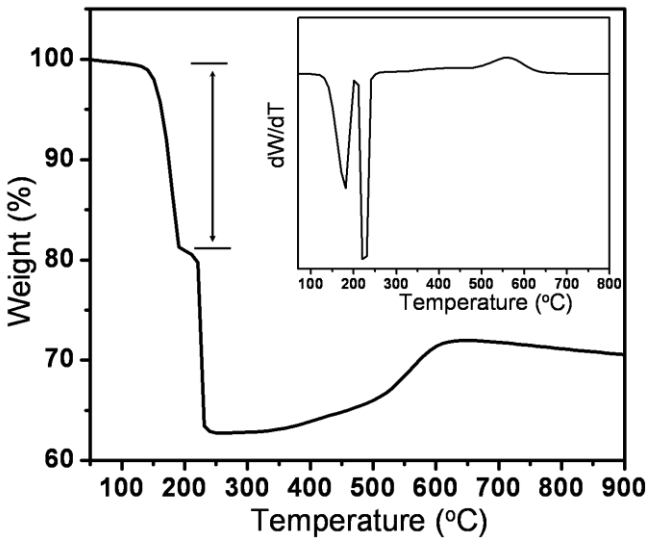

Figure 5.6. TG curve of RhMPCs revealing two inflexions due to free (uncapped) and capped TDA molecules, where the organic capping corresponding to ~18% weight loss reveals Rh: N ratio of 2:1; the DT curve for the RhMPCs with two sharp inflexions, as given in the inset.

The DTG curve (shown in inset) clearly exhibits two distinct weight losses; weight increase after 550 ^oC corresponding to ca. 9% is indicative of the formation of RhO_2 leading finally to Rh_2O_3 (a gradual weight loss after 630 ^oC corresponds to Rh(IV) to Rh(III)) in the end [28e].

5.3.1.7. XPS Analysis

XPS analysis of core level spectra of Rh 3d, C 1s and N 1s confirms the formation of Rh nanoclusters with the surface passivation of tridecylamine. The peak position, line shape and peak to peak separation (≈ 4.7 eV) are standard measures of the Rh oxidation state [Figure 5.7(a)] [72a]. The B.E. for Rh 3d doublet (307.8 and 312.5 eV) is consistent with Rh(0) oxidation state [72a], while another Rh 3d doublet (309.3 and 314.1 eV) is consistent with the Rh(+4) oxidation state [72b].

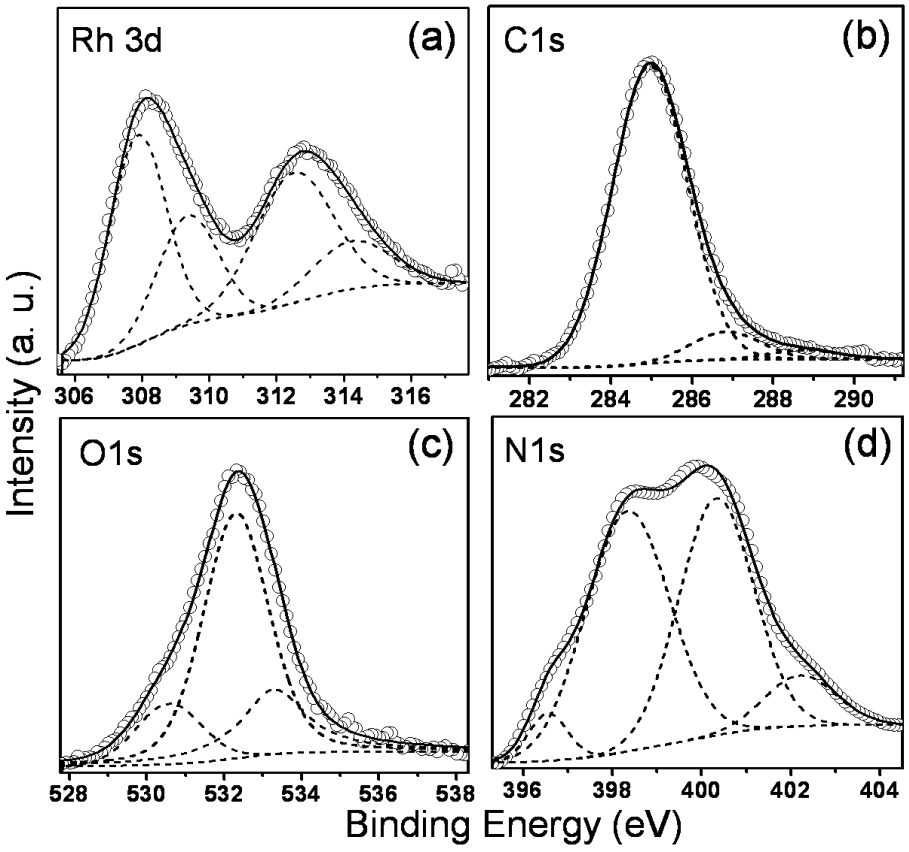

Figure 5.7. Representative X-ray photoelectron spectra of TDA capped Rh nanoparticles revealing core level information of (a) Rh3d, (b) C1s, (c) O1s and (d) N1s (experimental data points are shown as circles, resultant fitting curve as continuous line and individual fitted curves as dashed lines deconvulated by using Shirley background fitting).

This suggests that, the binding energy (BE) of $3d_{5/2}$ peak, 308.2 eV, is the typical value expected for self assembled monolayers modified on Rh or for few complexes of

Rh formed by exchange of bridging ligands. On the other hand, N 1s core level (Figure 5.7(d)) exhibits a quadruplet and the BE corresponding to bonded amine falls in the range of 398 - 400 eV. Therefore, the peak at 398.3 eV could be attributed to bonded amine in the MPCs. The peak at 396.5 could also reveal the formation of Rh-TDA complex (two TDA ligands in the axial position of Rh acetate gives rosy red color) due to the presence of Rh-Rh (2.3855 Å) bonding. Another peak of lower intensity at around 402.3 eV indicates the presence of a charged species of nitrogen ($-NH_2^+$) or its analogues.

Figure 5.7(b) shows C1s XP spectrum, where the deconvolution of the peak with respect to Gaussian fitting shows two distinct peaks at 286.8 and 285 eV respectively [72]. Considering 284.5 eV peak as the reference, peak at 286.8 eV is attributed to the C1s peak for C-N linkages, while a minor peak at 288.7 eV may be due to the presence of carbide species, originating from differential sample charging. Since the peak positions are assigned on the basis of the C1s peak at 285 eV, it does not affect the other B.E. values. The XPS results are in good agreement with FTIR results, which confirms the presence of TDA molecules on the surface of RhMPCs.

Thus, we have successfully described the synthesis of RhMPCs without using quaternary-ammonium salts or any tedious separation steps. These particles are thoroughly characterized by Uv-vis, TEM, XRD, ^{1}H NMR, FTIR, TG-DTA and XPS to depict their size, crystallinity and surface passivation. These results clearly show that the ordering of the passivating alkyl chains decreases slightly after its capping to the Rh surface compared to free amine.

5.3.1.8. Single Electron Transfer Behavior / Quantized Double Layer Charging

Nanoclusters below a critical size are known to show a novel electrochemical phenomenon called single electron transfer due to their size confinement effects [18-27]. The consecutive one electron QDL peaks observed in solution are analogous to the current peaks seen in traditional redox reactions [30]. Thus, MPCs in solution can be viewed as mixed-valent ensembles of clusters with adjacent state of core charges, where

the QDL charging process is diffusion controlled and obeys the Nernst equation with respect to the average core potential [36]. Accordingly, these peak potentials can be taken as the formal redox potential $E^{o'}$ for each ($z/z \pm 1$) "redox couple or charge state couple" and is given by the DPV peak potentials [73]. The formal redox potential $E^{o'}$ can be described by:

$$E^{o'}_{z/z+1} = E_{PZC} + (z - {}^{1}/_{2})e/C_{CLU} \qquad (5.3)$$

where E_{PZC} is the potential of zero charge (i.e., $z = 0$) of the MPC, and z is assigned such that $z > 0$ and $z < 0$ corresponding to core "oxidation" and "reduction" respectively and C_{CLU} is the capacitance of the MPC. More specifically, the C_{CLU} is associated with the ionic space charge formed around an MPC dissolved in the electrolyte solution, upon electronic charging of the core, whose charging is controlled by electrostatic (i.e., double layer) principles [73]. The above equation predicts a linear plot of $E^{o'}_{z/z+1}$ vs charge state (popularly known as "Z-plot"), which can be used to determine C_{CLU} from the slope [20-23,73,74]. Typical values are of the order of attofarad (10^{-18} farads) for 2-3 nm clusters.

Figure 5.8 (a) shows the DPV response (anodic scan) of 2 mg RhMPC per ml in 0.1 M TBAHFP in 3:1 acetonitrile – toluene mixture, where a large population of evenly spaced current peaks are observed (charging states are marked in Figure 5.8 (b) following $z/z\pm1$ fashion) [74]. Interestingly, peak potentials for a given cluster change approximately in a linear manner with a variation in its core charge state, as predicted by the theory [36], which also could help to determine the values of absolute standard redox potentials with respect to various charge states [75]. The blank response is also superimposed with this curve in identical conditions (shown as red curve in the Figure 5.8(a)). Here, as prepared RhMPCs are assigned the charge state of $z = -1$, which is reasonable since a very strong reducing agent like $NaBH_4$ is used for MPC preparation, and thus one expects the MPC formed to be in the reduced form at the prevailing pH conditions of the synthesis [20]. Hence, -1/0 and -2/-1 are the first oxidation and reduction processes respectively. The -1/0 and 0/1 charge steps are marked for comparison with respect to the potential measured using a Pt quasi reference electrode.

$Rh_{2057}(TDA)_{321}$ nanoclusters with a tiny metallic core (4.9 ± 0.2 nm) is shown to behave like a capacitor in the atto-farad range by separating it with another cluster using two to three molecular thick TDA spacing. Interestingly, Figure 5.8(c) shows the superimposed behavior of both anodic and cathodic response, which reveals equally spaced currents steps as good as mirror images with an average current peak ratio of unity.

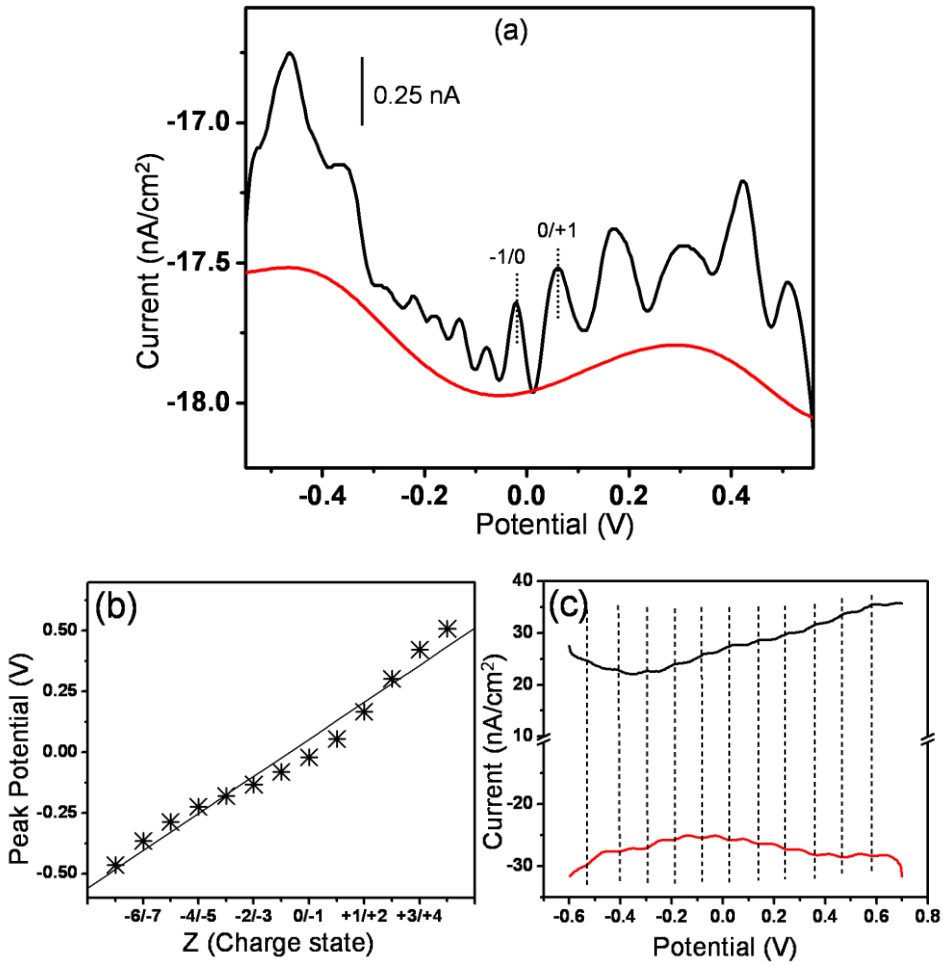

Figure 5.8. (a) Differential pulse voltammetric curve of RhMPCs (black curve) in 0.1 M TBAHFP solution containing 1:3 mixture of toluene and acetonitrile at ambient temperature (Pulse amplitude 25 mV, pulse width 10 ms, modulation period 200 ms, step potential 25 mV/s) and Pt disc (area 7.855×10^{-3} cm^2) as a working electrode in a concentration of 2 mg/mL of RhMPCs; red curve indicates the DPV response in absence of RhMPCs with identical conditions **(b)** charge state variations with peak potentials (Z-plot) and **(c)** superimposed DPV of both anodic and cathodic response revealing equally spaced currents steps under similar conditions except the modulation period of 100 ms and step potential of 40 mV.

A spacing (ΔV) of 80 mV has been observed near E_{PZC} region, which reveals a capacitance of 1.93 aF due to charging of transported and specifically oriented clusters towards the electrode interface. This comparatively lower ΔV could be attributed to the higher core size and the E_{PZC} is observed to be 0.012 V. This capacitance (C_{CLU}) of Q-dots can be estimated with the help of a concentric sphere capacitance model, as

$$C_{CLU} = (4 \pi\varepsilon_o\varepsilon_r) [r(r + d)/d] \quad (5.4)$$

where, ε_o is the permittivity of free space, ε_r is the dielectric constant of the medium respectively (taken as 3) [76], 'r' is the radius of the Q-dot core and 'd' is the length of the passivating agent, using Bain's empirical formula as, d = (0.25 + 0.127n), where 'n' is the number of methylene groups [76c]. According to this model, the capacitance of the 4.9 nm sized Q-dot is estimated to be of 1.93 aF, which matches very well with the experimentally calculated value. Moreover, the charging energy ($E_c = e^2/2C$) is found to be of 41 meV for our Q-dots, satisfying the theoretical single electron transfer criteria as $E_c >> k_BT_{298}$.

Interestingly, the full width at half maximum (FWHM) of each peak is found to be of ca. 50-55 mV in the positive potential region whereas, a FWHM of 30-35 mV is observed in reverse direction, particularly signifying the QDL process for these larger MPCs, which differs from the earlier reports of smaller sized AuMPCs (110-115 mV) or ideal (90.6 mV) one electron transfer process for conventional redox species [20-24,77,78]. The reason for the unusual variation in the FWHM for both cathodic and anodic regions is not clear although several factors including reorganization or disproportionation of charged clusters during electron transfer process [78] and more complex geometrical effects of tridecylamine might be responsible. For example, these MPCs can be viewed as assembly of mixed valent redox centers at the electrode solution interfaces during electrochemical process. These resemble the case of conducting polymers, where the occupied site interaction energies (in the order of *k*T) substantially cause change in redox capacity with the magnitude and types of interactions. This type of interaction is also widely known for electroactive films or adsorption electrochemistry, where substantial broadening or sharpening of the voltammetric peaks are observed

depending on the degree of the adsorbate-adsorbate interaction [78]. Another possibility is the interdigitation of the hydrocarbon chains effectively leading to closer distance between MPCs as if there is an attractive interaction caused by the soft organic matrix. Furthermore, there are also possibilities for the reorganization of charges among clusters by electron self-exchange or disproportionation.

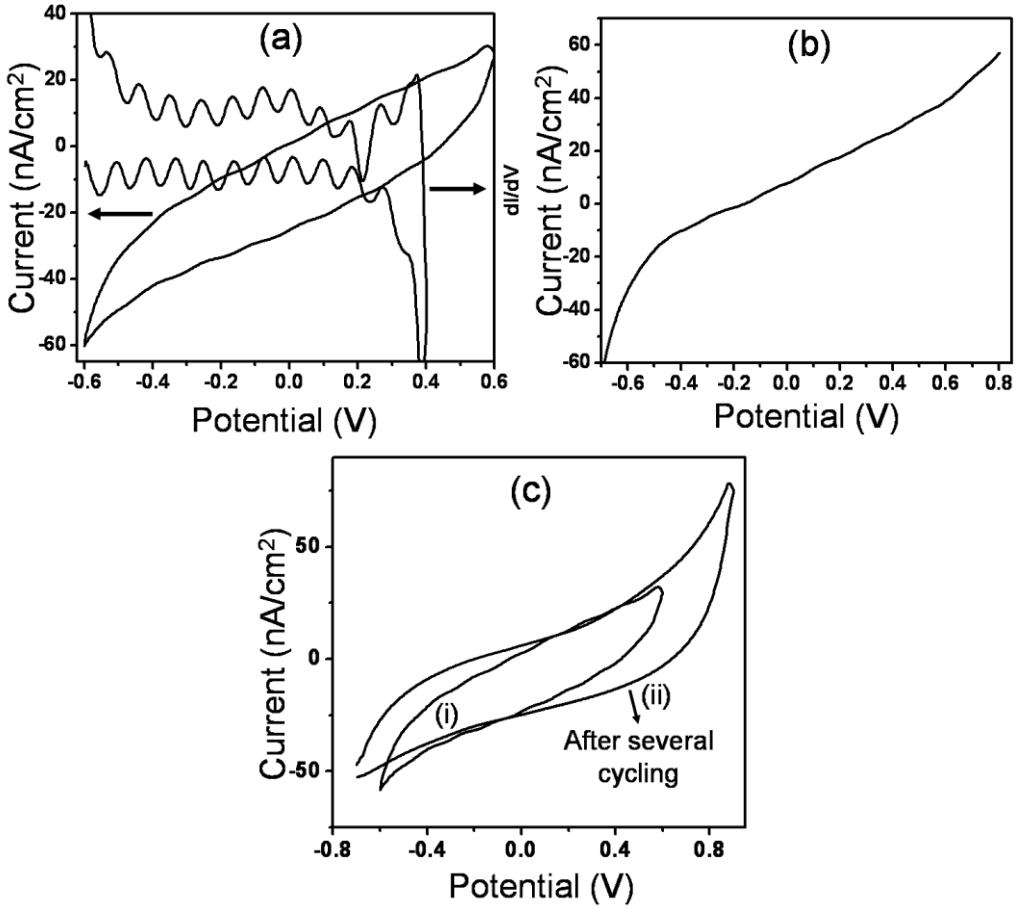

Figure 5.9. (a) Cyclic voltammetric response along with its derivative curve and **(b)** linear sweep voltammetric behavior of RhMPCs in 0.1 M TBAHFP solution containing 1:3 mixture of toluene and acetonitrile at ambient temperature (CV and LSV; scan rate 125 mV/s) **(c)** superimposed CVs of RhMPCs at **(i)** initial period and **(ii)** after several cycling showing strong adsorption, resulting in the disappearance of electron transfer events; (Pt disc of area 7.855×10^{-3} cm^2 working electrode in a concentration of 2 mg/mL of RhMPCs).

A slightly less monodispersity in the core size also directly affects on the capacitance of the particles at various charge states, which could clearly be observed in the DPV. Also, the core diameter of the MPCs is calculated by transmission electron

microscopy and also confirmed by the DPV technique, since the HOMO-LUMO energy corresponding to ΔV is related to the size and composition of the nanoparticle assuming spherical geometry of the particle [20].

Most interestingly, the variation in the FWHM in both, DPV and CV (or LSV), could arise due to the different rates of processes (diffusion and adsorption), since more population of charge steps in Figure 5.8(a) is affected by the electron transfer of adsorbed species, while, the minor population in the Figure 5.9(a) and (b) might be attributed to the diffusion of charged clusters towards electrode surface.

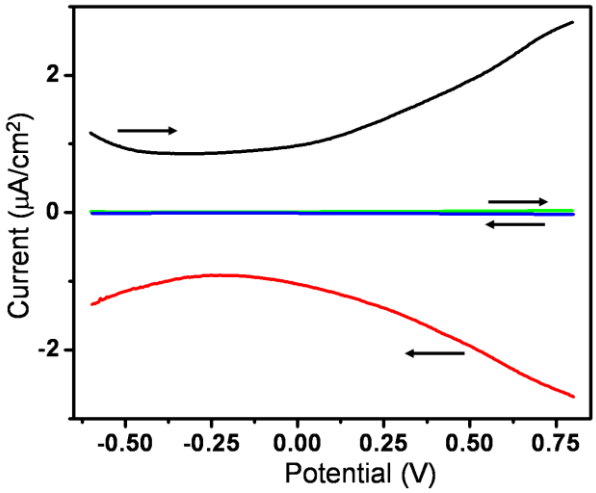

Figure 5.10. Superimposed differential pulse voltammetric curves (both anodic: black curve and cathodic: red curve) of RhMPC-MWCNTs in 0.1 M TBAHFP solution containing 1:3 mixture of toluene and acetonitrile at ambient temperature (Pulse amplitude 25 mV, pulse width 10 ms, modulation period 200 ms, step potential 25 mV/s) and Pt (diameter 25 μm) as a working electrode; blue and green curves are superimposed DPV curves (cathodic and anodic respectively) of s-MWCNTs under similar conditions; the arrow indicated the direction of scan.

It is interesting to see the effect of anchoring such RhMPCs on the side walls of MWCNTs on single electron transfer behavior of nanoclusters, since the fascinating electronic properties of nanotube could furnish remarkable variations in presence of such tiny clusters of Rhodium. Accordingly, Figure 5.10 shows a comparative differential pulse voltammetric behavior of s-MWCNTs (microwave treated MWCNTs) and RhMPC anchored MWCNTs performed in 1:3 mixture of toluene and acetonitrile using 0.1 M TBAHFP as supporting electrolyte. DPV and CV have been recorded after depositing

nanotube sample on the Pt working electrode (RhMPCs, in previous cases, have been taken in solution).

Figure 5.10 shows superimposed DPV curves for RhMPC-MWCNTs and s-MWCNTs (both anodic and cathodic), where a large background current indicates the non-faradaic contribution from nanotube and thus not exhibiting any quantized single electron transfer events in both the cases. Further, this charging behavior is attributable to the deposited nanotube sample, since an entirely different double layer charging has been possible as compared to that of soluble species (similar to one shown in Figure 5.8(a)). Figure 5.10 also shows three orders of increase in current due to the anchoring of RhMPCs to the side walls of nanotubes. This is because of the fact that, RhMPCs on the side-walls modify the geometry for double layer of nanotubes. Thus, single electron transfer events have not been observed after immobilization of such RhMPCs on the nanotubes despite an enhancement in their double layer capacitance.

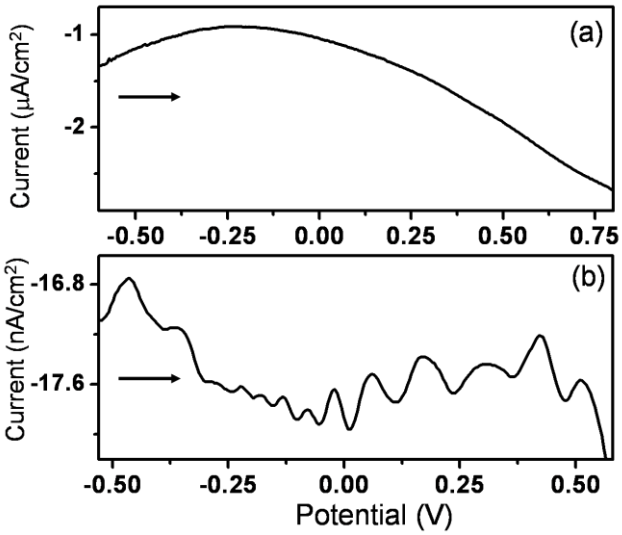

Figure 5.11. (a) cathodic DPV curve for RhMPC-MWCNTs in 0.1 M TBAHFP solution containing 1:3 mixture of toluene and acetonitrile at ambient temperature (Pulse amplitude 25 mV, pulse width 10 ms, modulation period 200 ms, step potential 25 mV/s) and Pt (diameter 25 μm) as a working electrode; **(b)** cathodic DPV curve of RhMPCs under similar conditions except the dimensions of Pt electrode (area 7.855×10^{-3} cm^2).

Further, comparing the DPV response of both RhMPCs and RhMPC-MWCNTs (as shown in Figure 5.11), it clearly reveals the disappearance of discrete electron transfer

after immobilization of RhMPCs on nanotubes along with increase in charging current. This effect could also be attributed to the inhomogeneous coating of MPCs on the side walls and the interaction between RhMPC and CNT.

This effect is also seen in cyclic voltammetric results shown in Figure 5.12. Accordingly, Figure 5.12(a) shows the superimposed cyclic voltammograms of blank Pt microelectrode, s-MWCNTs and RhMPC-MWCNTs performed in 1:3 mixture of toluene and acetonitrile with 0.1 M TBAHFP. An increase in capacitance is observed due to anchoring of RhMPCs on side-walls of nanotubes, since the geometry of double layer changes from cylindrical to complex cylindrical. Scan rate dependent voltammograms of RhMPC-MWCNT also show no special features except a resistive behavior at negative direction, perhaps due to capping molecules of tridecylamine.

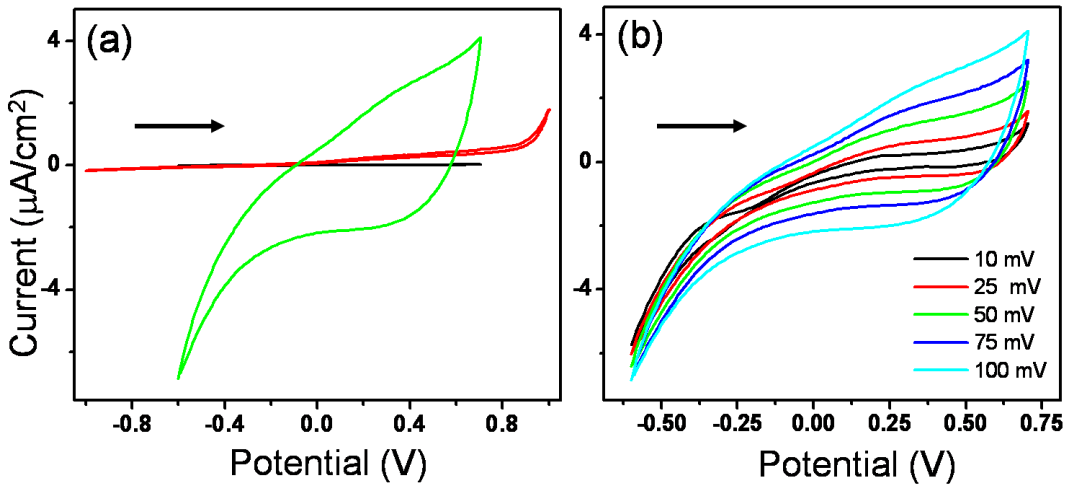

Figure 5.12. (a) superimposed cyclic voltammetric response of blank Pt electrode (black curve), s-MWCNTs (red curve) and RhMPC-MWCNTs (green curve) **(b)** Scan rate dependent voltammograms of RhMPC-MWCNTs performed in 0.1 M TBAHFP solution containing 1:3 mixture of toluene and acetonitrile at ambient temperature (scan rate 125 mV/s); (sample has been drop-coated on Pt microelectrode with diameter 25 μm).

A simple method for the synthesis of monodispersed Rhodium nanoclusters stabilized by tridecylamine at room temperature has been discussed along with their electronic behavior of Coulomb blockade in electrochemical techniques like DPV, CV and LSV. We hope our experimental results will fill up the lacuna for the size effect on

single electron transfer features, which can be useful for designing size selective catalysts, ultrasmall supercapacitors or circuit components for nanoelectronic devices.

5.3.2. Results for the Characterization of Rhodium Catalysts

5.3.2.1. TEM Analysis

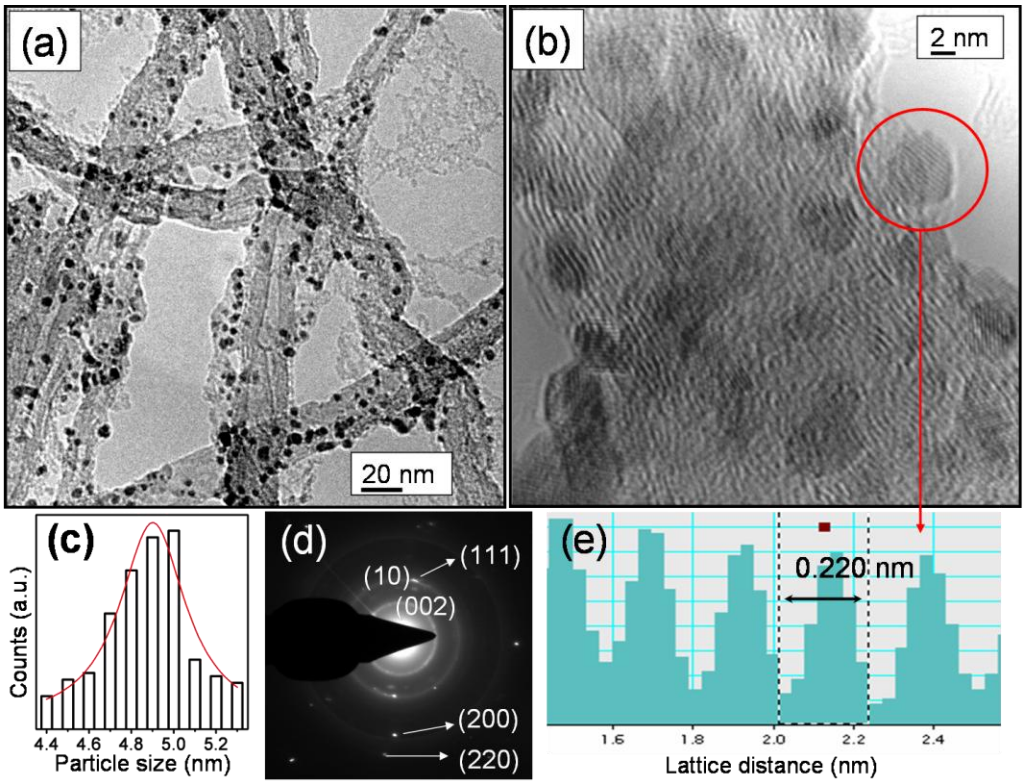

Figure 5.13. (a) TEM image of Rh/MWCNTs1 hybrid material prepared by *ex-situ* method, revealing a uniform distribution of Rh nanoparticles on MWCNTs; **(b)** High resolution TEM image of Rh nanoparticles on CNT with lattice fringes of (111) plane; **(c)** histogram indicating an average size of 4.9 ± 0.4 nm; **(d)** dark field SAED pattern revealing spots corresponding to Rh nanoparticles and bright rings corresponding (002) and turbostratic (10) planes due to MWCNTs and **(e)** profile of lattice fringes of Rh(111) encircled in (b), clearly exhibiting a distance of 0.220 nm.

The size distribution and particle arrangements are evident from a comparison of the TEM images. For example, Figure 5.13(a) shows the low resolution image of Rh/MWCNTs1, which exhibits a high population of uniformly sized particles on MWCNTs with an average size of 4.9 ± 0.4 nm along with their statistical distribution

(Gaussian) as Figure 5.13(c), which is the analysis of more than 100 spherical particles, from four different regions in a single Cu grid. This particle size variation could be attributed to the calcination effect, where few particles would have been fragmented into smaller sizes. More specifically, the high-resolution images as shown in Figure 5.13(b) depict the lattice fringes for these particles corresponding to (111) plane with an interplanar distance of 0.22 nm along with a hexagonal closed packed structure. Also, the lattice fringes due to CNTs corresponding to (002) lattice planes are clearly seen in the Figure 5.13(b), where a slight distortion in the graphene layers have been observed, perhaps due to the harsh oxidative pre-treatment. It also could be explained as a result of electron beam induced damaging of side walls during imaging, since energy of ca. 100 keV is reported to be sufficient to damage the graphene structure [79].

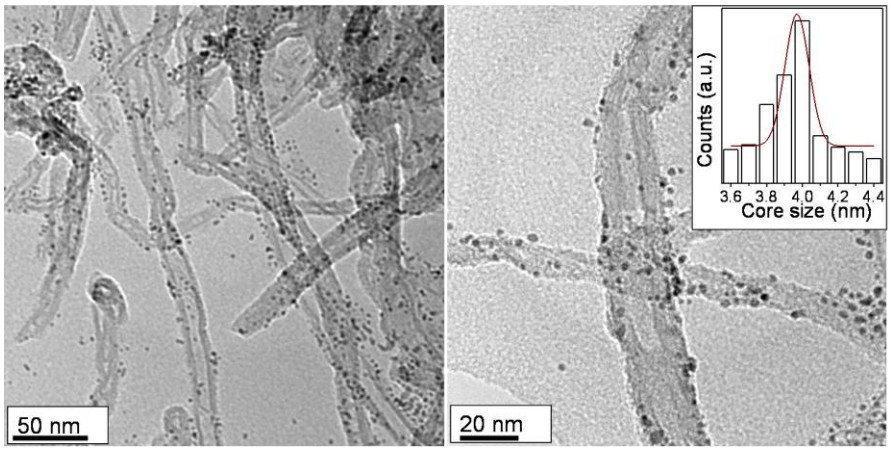

Figure 5.14. TEM images of Rh/MWCNTs2 at two magnifications revealing the decoration of Rh nanoparticles with size of 4.0 ± 0.5 nm; the particle size distribution is shown in the inset.

Selected area diffraction (SAED) pattern shows a crystalline nature of the RhMPCs exhibiting dominant reflections corresponding to (111), (200) and (220) planes as indicated in Figure 5.13(d); other reflections are rather insignificant. SAED pattern also reveals two bright rings matching with (002) and turbostratic (10) planes of MWCNTs.

In addition, Figure 5.14 exhibits TEM images of the catalyst Rh/MWCNTs2, where the Rh nanoparticles with a size distribution of 4.0 ± 0.5 nm have been seen along

with a histogram (inset) indicating a narrow distribution of nanoparticles on the side walls.

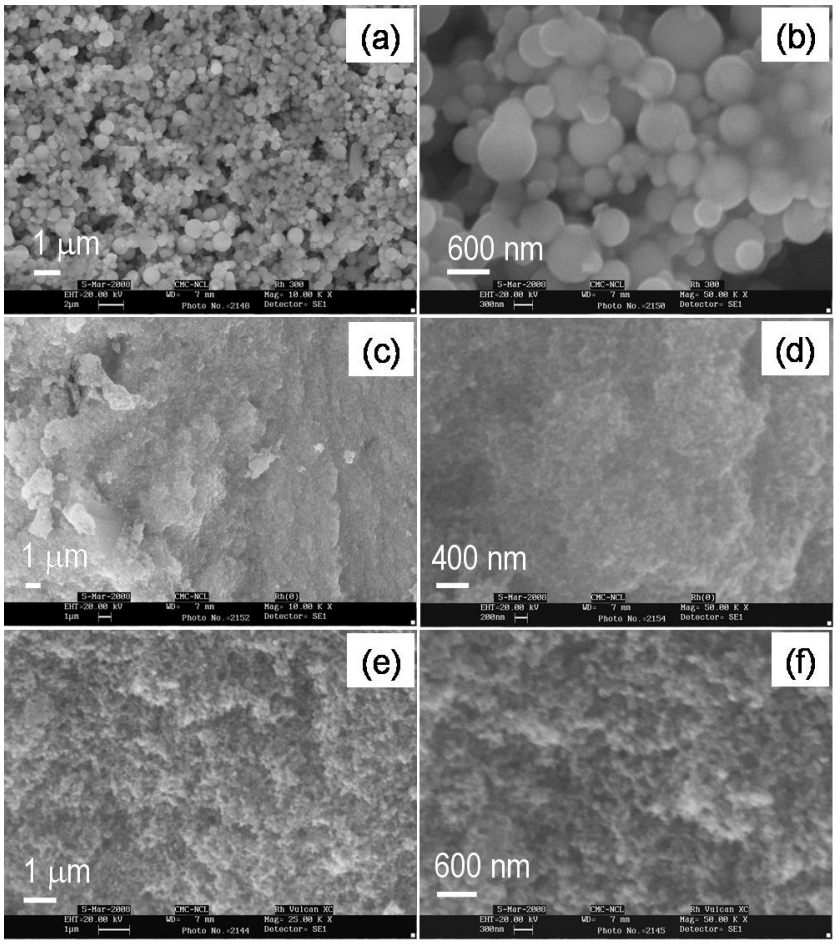

Figure 5.15. SEM images of the catalyst **(a-b)** Rh3 **(c-d)** RhMPCs and **(e-f)** Rh/Vulcan XC, revealing spherical aggregates of nanoparticles for Rh3 with size ranging from 10-15 nm; catalyst RhMPCs and Rh/Vulcan XC show monodispersed particles, although poor resolution of the images makes it difficult to discern their size distribution.

The morphology of other Rh based catalysts as revealed by SEM images 'a-f' of Figure 5.15 is also interesting. For example, Images 'a' and 'b' exhibit two different magnifications of spherical aggregates of Rh3 with size from 10-15 nm. While, images (c and d) and also (e and f) show RhMPCs and Rh/vulcan XC respectively having monodispersed particles, although low resolution of the images makes it difficult to

discern their size distribution. However, the morphology of RhMPCs has clearly been shown in Figure 5.2 (section 5.3.1.2.).

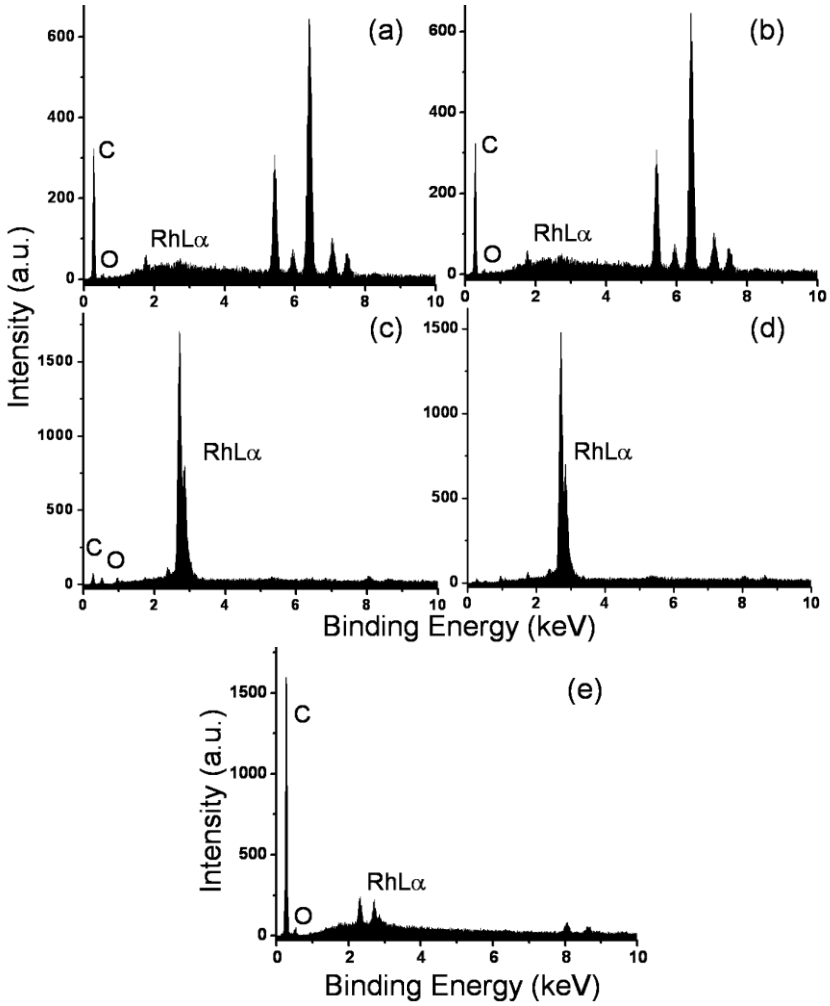

Figure 5.16. Compositional variation of Rhodium in the catalyst **(a)** Rh/MWCNTs1, **(b)** Rh/MWCNTs2, **(c)** Rh3, **(d)** RhMPCs and **(e)** Rh/Vulcan XC, where the peaks corresponding to the C, O and RhLα have been shown in the ED spectra; catalyst Rh3 and RhMPCs clearly show the presence of metallic Rhodium.

Since the amount of Rhodium in the catalyst affects the catalytic efficiency, there is a strong need to determine this accurately prior to the reactions and in this context, EDX spectrum is particularly valuable. Accordingly, Figure 5.16(a-e) shows EDX spectra of all catalysts, exhibiting strong signal corresponding to C to Rh in case of Rh/MWCNTs1, Rh/MWCNTs2 and Rh/Vulcan XC with only 1 wt% of Rh present in the

substrate of carbon (Figure 5.16(a, b and e) respectively). However, Rh3 and RhMPCs show 98 wt% and 60 wt% of Rhodium metal respectively, as revealed from the strong signal corresponding to RhLα.

5.3.2.2. XRD Analysis

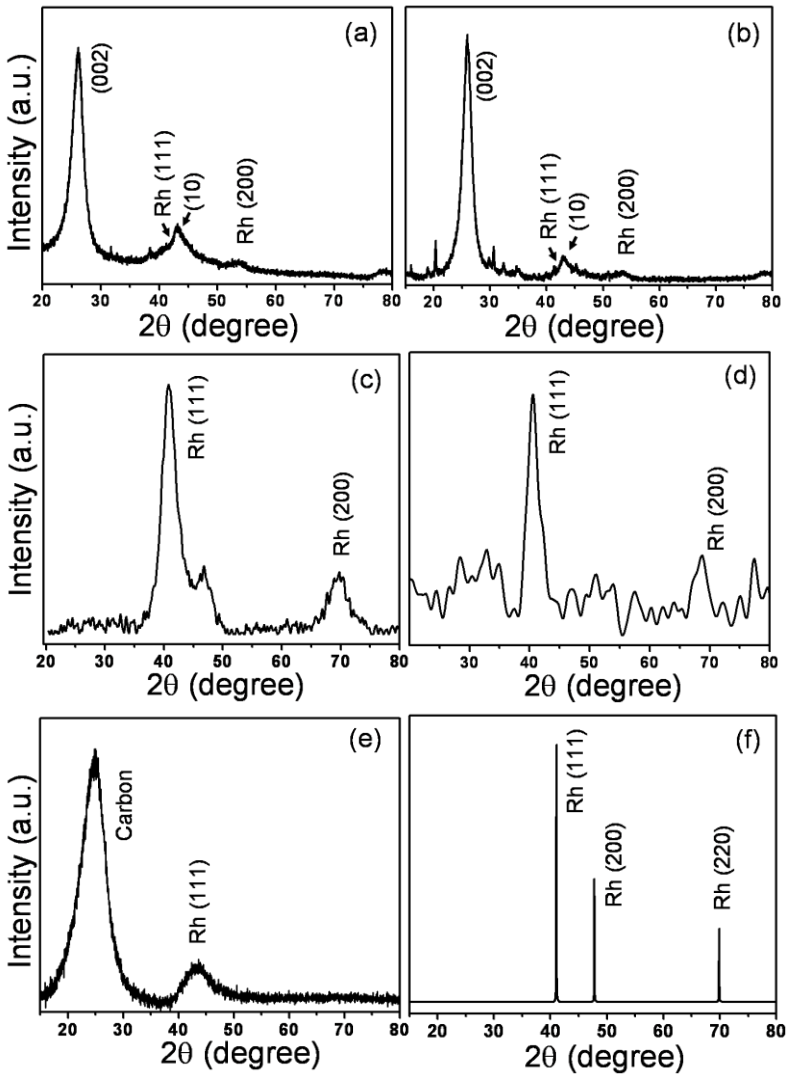

Figure 5.17. A comparison of the XRD patterns of catalysts (a) Rh/MWCNTs1 (b) Rh/MWCNTs2 (c) Rh3 (d) RhMPCs (e) Rh/Vulcan XC and (f) simulated curve based on the space group Fm3m (space group number: 225) and a perfect fcc structure. XRD pattern of Rh clearly shows a bulk fcc crystal structure with slight variations in the positions, perhaps due to lattice miss-matching at lower dimensions; the corresponding lattice planes are marked in the figure.

XRD analysis provides valuable information on the difference in crystallinity along with some idea on their size distribution. Accordingly, Figure 5.17(a-e) shows a comparison of the respective XRD pattern of these catalysts along with simulated curve (f) based on the space group Fm3m (space group number: 225) and a perfect fcc structure. The XRD comparatively, reveals bulk fcc crystal structure for these MPCs and the corresponding lattice planes are marked in the figure, which is in excellent agreement with that of previous reports [80].

The reflections corresponding to Rh clearly show fcc crystal structure in all cases with a slight variation in the position, perhaps due to lattice miss-matching arising from lower dimensionality. Figure 5.17 (a, b and c) clearly shows a very small hump corresponding to the Rh(111) reflection indicating a very low metal content in these samples.

Table 5.2. Crystallite sizes of Rh particles closely resembling that from TEM analysis

Sample number	Catalyst	Particle size from TEM (nm)	Crystallite size from XRD (nm)
(a)	Rh/MWCNTs1	4.9 ± 0.50	5.36
(b)	Rh/MWCNTs2	4.0 ± 0.50	4.40
(c)	Rh3	10-15	2.97
(d)	RhMPCs	4.9 ± 0.20	3.80
(e)	Rh/Vulcan XC	10-12	2.20

Crystallite size is also calculated from the FWHM of the (111) peak using Scherrer formula [80c] as described in equation 5.2 and a comparison is shown in Table 5.2 along with that calculated from TEM.

5.3.2.3. TG-DT Analysis

The relationship between percentage of Rhodium metal content and nanotube could be substantiated using TG analysis. The presence of a single step decomposition (as shown in Figure 5.18) reveals that a majority of weight loss indeed, corresponds to the presence of nanotube substrate. In case of Rh/MWCNTs1, a decomposition of more than 95% of the catalyst occurs at 570 ^{o}C, whereas it occurs as early as at 460 ^{o}C in the case of Rh/MWCNTs2.

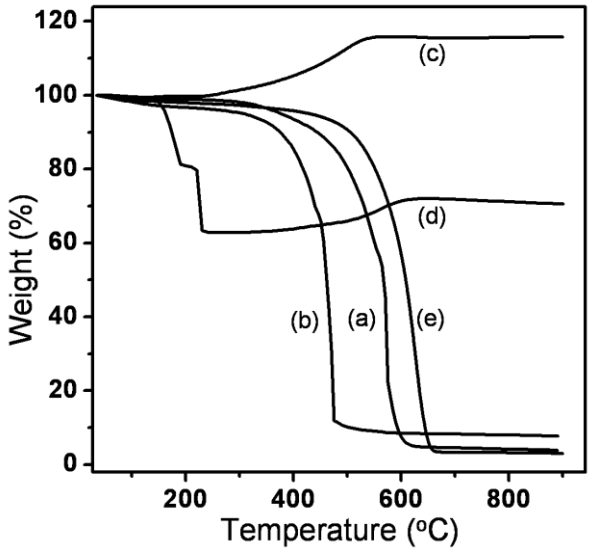

Figure 5.18. A comparison of TG profiles of **(a)** Rh/MWCNTs1, **(b)** Rh/MWCNTs2, **(c)** Rh3 **(d)** RhMPCs and **(e)** Rh/VulcanXC, showing similar trend in case of catalysts (a, b and e), whereas more metal content is evident for sample (c); all thermograms have been recorded in dry oxygen at 10 ^{o}C/min.

This variation of the decomposition of CNT substrate could be attributed to the structural changes during the synthesis of both catalysts. The final residue corresponding to the Rhodium metal has been clearly seen in Figure 5.18 while interesting thermal profiles, 'c' and 'd' show thermograms of the catalysts Rh3 and RhMPCs, revealing a significant variation in the weight loss, presumably due to more metal content of catalysts; Rh3 clearly shows a gradual weight gain (15%) due to the oxide formation. On the other hand, Rh/Vulcan XC shows a similar trend in the weight loss as in the case of Rh/MWCNTs1 and Rh/MWCNTs2. The observation of more than 96% weight loss at

610 ^{o}C is attributed to the preponderance of amorphous carbon in Vulcan XC (Figure 5.18(e)), which is used as the substrate.

5.3.2.4. XPS Analysis

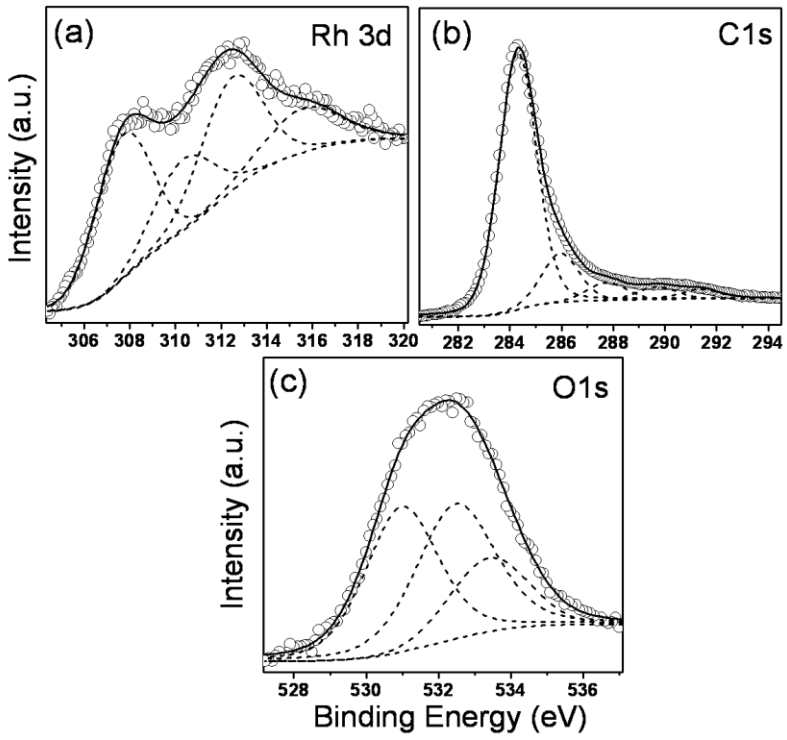

Figure 5.19. Representative X-ray photoelectron spectra of catalyst Rh/MWCNTs1 revealing core level information of (a) Rh3d, (b) C1s, and (c) O1s (experimental data points are shown as circles, resultant fitting curve as continuous line and individual fitted curves as dashed lines deconvulated by using Shirley fitting algorithm).

XPS analysis of core level spectra of Rh 3d and C1s confirms the formation of Rh – CNT hybrid catalyst. The peak position, line shape and peak to peak separation (≈ 3.4 eV) are the standard measure of the Rh oxidation state [Figure 5.19(a)] [80a]. For example, the B.E. for Rh 3d doublet (307.8 and 311.3 eV) is consistent with Rh^{o} oxidation state [80a], while another Rh3d doublet (312.1 and 315.5 eV) is consistent with the Rh(+4) oxidation state as RhO_2 [81]. The formation of a smaller amount of RhO_2 on the active Rh(0) catalyst could affect the catalytic activity. Interestingly, this analysis suggests that, a slight shift in the binding energy (BE) of $3d_{5/2}$ peak (307.8 eV) occurs

due to the CNT support, where a charge transfer could occur from the electron rich nanotube network to the Rhodium metal [57,82].

Figure 5.19(b) shows C1s XP spectrum, where the deconvolution with respect to Gaussian fitting shows two distinct peaks at 284.5 and 286.1 eV respectively [58,83]. We have taken 284.5 eV peak as the reference peak for sp^2 carbon of nanotubes, while peak at 286.0 eV is attributed to the C1s peak for physisorbed C-Rh(0) linkage. Three minor peaks at 287.8, 289.7 and 291.3 eV may be due to the presence of other oxygenated functional groups on the nanotube side walls and since, the peak positions are assigned on the basis of the C1s peak at 284.5 eV, all these do not affect the other B.E. values.

Table 5.3. A comparison of the binding energy positions of C1s, Rh3d and O1s present in different catalysts.

Species		**Binding Energy (eV)**				
		Rh/MWCNTs1	**Rh/MWCNTs2**	**Rh3**	**RhMPCs**	**Rh/Vulcan XC**
C1s		284.5	285.5	(minor)	284.5	284.5
		286.0	286.1	-	286.8	286.3
		287.8	287.3	-	288.7	288.0
		289.7	288.5	-	-	289.2
		291.3	289.8	-	-	290.5
Rh	$3d_{5/2}$	307.8	307.1	307.0	307.8	307.9
		310.7	310.5	310.8	309.3	310.4
	$3d_{3/2}$	312.4	312.0	312.6	312.5	312.2
		315.6	315.4	315.8	314.1	315.3
O1s		531.0	529.6	530.5	530.5	531.3
		532.5	532.1	532.5	532	532.5
		533.5	534.1	(minor)	533.3	533.4

Similarly, the XP spectra for other catalysts have been analyzed based on Shirley fitting and the binding energies of C1s, Rh3d and O1s for all catalyst samples have been documented in Table 5.3. The B.E. values of Rh3d and O1s for all samples along with

their intensities clearly suggest the formation of less amount of oxide on active sites of the catalyst. Catalyst Rh3 shows a minor peak corresponding to the chamber carbon from the instrument with no signatures of other carbon species, indicating a pure Rh(0) phase with small quantity of its oxides. Comparative XP results for all Rh based catalyst (except Rh3) reveal almost a similar chemical environment for all elements, although their surface properties could cause a dramatic changes in their catalytic behavior.

5.3.2.5. BET Surface Area

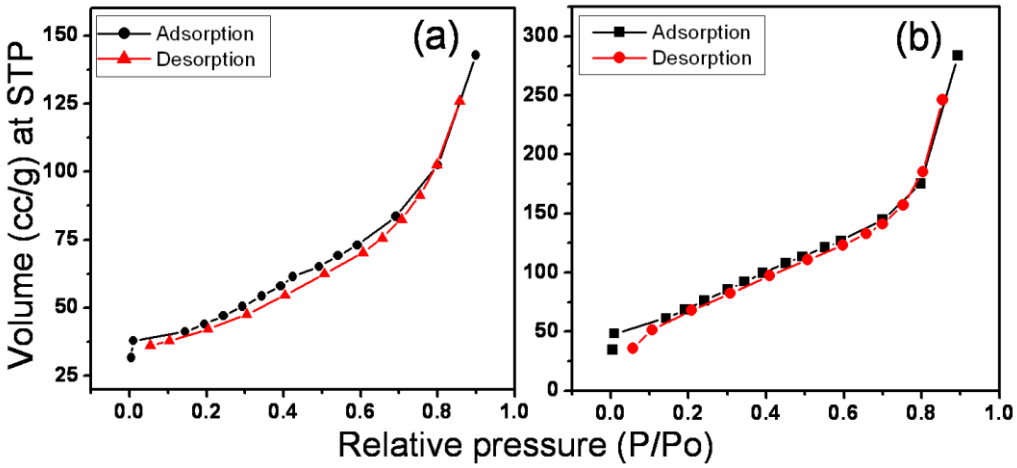

Figure 5.20. Nitrogen adsorption-desorption results for **(a)** Rh/MWCNTs1 and **(b)** Rh/MWCNTs2 revealing less hysteresis corresponding to a homogeneous pore size distribution in both the cases (temperature of 77 ^{o}C).

Adsorption-desorption studies are very valuable for analyzing the change in surface area along with pore size distribution. For example, Figure 5.20 reveals less hysteresis for N_2 adsorption indicating a homogeneous pore size distribution in case of both Rh/MWCNTs1 and Rh/MWCNTs2, while Table 5.4 confirms a narrower pore size distribution, perhaps contributing from the inner diameter of the MWCNTs (at 77 ^{o}C). Comparatively, a slightly lesser value of pore size distribution in case of Rh/MWCNTs1 could be attributed to the effective blocking of inner bore of the CNTs by nanoparticles.

Interestingly, the catalytic activities of Rh/MWCNTs1 have been found to be surprisingly enhanced as compared to that of Rh/MWCNTs2, despite the lower surface area and pore volume. This effect is attributed to the improved surface properties of the

catalysts like hydrophilicity or hydrophobicity, which remain inherent due to different treatment procedures [84].

Table 5.4. A comparative surface area and pore size distribution of MWCNTs, Rh/MWCNTs1, Rh/MWCNTs2, and Rh/vulcan XC, based on BET measurements.

Sample ID	Surface area by BET isotherm (m^2/g)	Pore volume (cc/g)	Average pore diameter (nm)
MWCNTs	380.4	0.501	6.82
Rh/MWCNTs1	162.4	0.221	5.44
Rh/MWCNTs2	281.6	0.438	6.23
Rh/vulcan XC	220.0	0.301	4.50

More significantly, the textural properties of Rh heterogenized MWCNT (both samples 1 and 2) show a decrease in surface area and pore volume compared to the parent MWCNTs [85]. This indicates that the Rh nanoparticles are well dispersed inside the channels, defect sites as well as in the inner core of nanotubes. This is also in agreement with the data shown in Figure 5.20 where, after the heterogenization of Rh into nanotubes and even after calcination, the mesostructure is retained without any change in morphology.

5.3.3. Hydrogenation of Arenes

Toluene is chosen as the test substrate for the heterogeneous selective hydrogenation and the reaction is carried out with a substrate to catalyst molar ratio of 10000:1 in hexane at 40 °C using 20 bar H_2. The details of the preparation of catalyst Rh/MWCNTs1 along with its reaction using toluene is demonstrated in Scheme 5.1, where, the results are compared in terms of their Turn over numbers (TON) and Turn over frequency (TOF). Interestingly, methylcyclohexane is found to be the only product after 2 h with a TOF of 4950. Further, hydrogenation of several arenes has been studied using the catalyst Rh/MWCNTs1due to its remarkable activity.

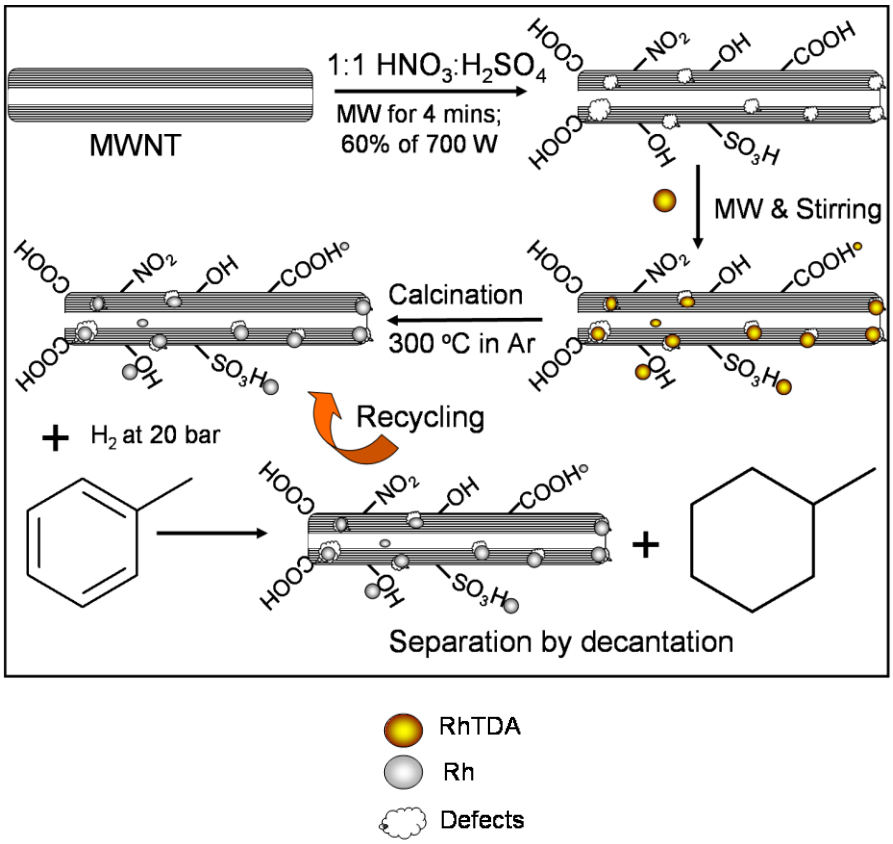

Scheme 5.1. A schematic of the preparation of Rh/MWCNTs1 and its activity for the hydrogenation of toluene at selected conditions; (MW represent microwave treatment); greater extent of functional groups and defect sites due to the MW treatment leads to the formation of Rh-CNT hybrid materials.

5.3.3.1. Effect of Temperature

Figure 5.21 shows the variation of conversion (%) with time as a function of temperature. A variation of reaction temperature reveals that the conversion of toluene increases with the increase in temperature upto 60 ^{o}C, and an optimum of 40 ^{o}C has been selected for all further hydrogenation studies. A gradual increase in the conversion at lower temperature indicates a sluggish reaction with no obvious saturation limit, thus requiring infinite time to convert all reactants to the desired products.

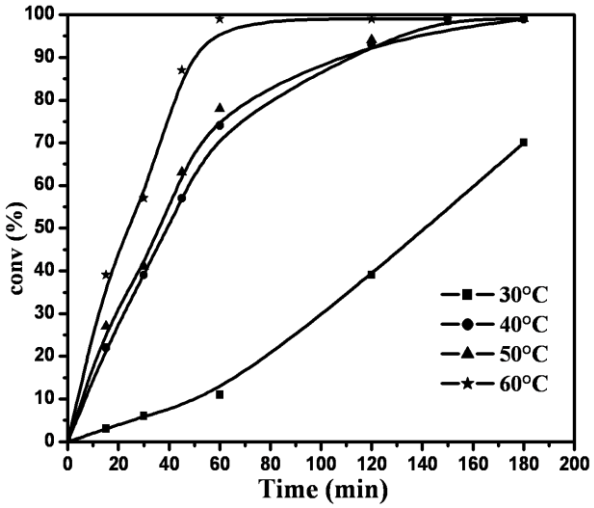

Figure 5.21. Variation of conversion with temperature, where an optimum of 40 ^{o}C shows a maximum conversion of toluene to cyclohexane using Rh/MWCNTs1.

5.3.3.2. Effect of Pressure

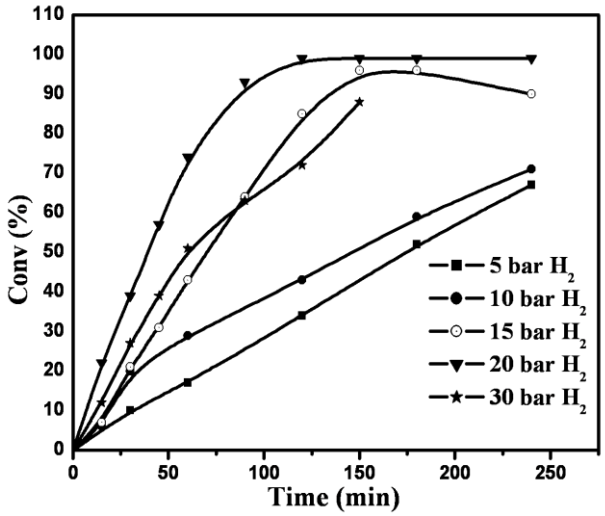

Figure 5.22. Variation of conversion with pressure, where an optimum of 20 bar shows a maximum conversion of toluene to cyclohexane using Rh/MWCNTs1.

Variation of conversion with pressure reveals that the conversion of toluene increases with increase in pressure upto 20 bar H_2 followed by a decrease in activity at higher pressures. Figure 5.22 shows such a variation of conversion with time as a function of temperature revealing an optimum of 20 bar necessary to carry out the

reaction. At initial pressure, the conversion is poor and a gradual increase in conversion with time (at different pressures) requires infinite time for a saturation limit.

The recyclability of Rh/MWCNTs1 catalyst has been tested for the hydrogenation of toluene by conducting five successive runs. After each run, the catalyst has been repeatedly washed with hexane, dried at 150 °C for 5 h and then used with a fresh reaction mixture. The conversion of toluene is practically the same (99%) in first five cycles with a marginal decrease at the fifth cycle as indicated in Table 5.5.

Table 5.5. Recyclability of the Rh/MWCNTs1 catalyst for hydrogenation of toluene, showing a very small decrease in its activity after 5^{th} cycle; (reaction condition: 5 mmol of substrate, 5 mg catalyst (0.0005 mmol), hexane 50 ml, at 40 °C and at 20 bar H_2).

Entry	Cycle	Time (h)	Conversion (%)	TON	TOF
1.	Fresh	2	99	9900	4950
2.	1^{st}	2	99	9900	4950
3.	2^{nd}	2	97	9700	4850
4.	3^{rd}	2	97	9700	4850
5.	4^{th}	2	97	9700	4850
6.	5^{th}	2	94	9400	4700

Further experiments have been conducted using a range of arenes with Rh/MWCNTs1 showing excellent activity under selected conditions of temperature and pressure (40 ^{o}C and 20 bar). Hydrogenation products along with their conversion and TON (TOF) have also been included in Table 5.6.

Rh/MWCNTs1 show excellent activity with a wide range of arenes under selected conditions. In particular, benzene shows a similar trend as that of toluene but showing enhanced conversion within 1.5 h with TOF of 6600, whereas naphthalene and anthracene show less reactivity for the selected reaction conditions, producing tetrahydro derivative as the major products.

Table 5.6. Efficiency of the **Rh/MWCNTs1** catalyst for arene hydrogenation under selected conditions (5 mmol of substrate, 5 mg catalyst (0.0005 mmol), hexane 50 mL, 40° C and at 20 bar H_2); TON (turn over number) mole substrate converted per mole of Rh; TOF (turn over frequency) mole of substrate converted per mole of Rh per h; (* the reaction was carried out in methanol as solvent).

Entry	Substrate	Product	Time (h)	Conversion (%)	Selectivity		TON	TOF
1.	Toluene	Methyl cyclohexane	2	99	-	-	9900	4950
2.	Benzene	Cyclohexane	1.5	99	-	-	9900	6600
3.	Phenol	Cyclohexanol	10	98	-	-	9800	980
4.	Anisole	Methoxycyclohexane	5	44	-	-	4400	880
5.	Diphenyl ether	Cyclohexyl phenol ether (major), dicyclohexyl ether	7	60	69	31	6000	857
6.*	Anthracene	Tetrahydroanthracene(major), octahydroanthracene(minor)	22	15	98	2	1500	68
7.	Naphthalene	Tetrahydronaphthalene (major) Octahydronaphthalene (minor)	13	17	97	3	1700	130
8.	m-xylene	1,3-dimethylcyclohexane	4	99	82 (cis)	18 (trans)	9900	2475
9.	p-xylene	1,4-dimethylcyclohexane	4	99	72 (cis)	28 (trans)	9900	2475
10.	o-xylene	1,2-dimethylcyclohexane	4	96	91 (cis)	9 (trans)	9600	2400
11.	p-cresol	4-methylcyclohexanol	4	87	97 (cis)	3 (trans)	8700	2175
12.	Acetophenone	Cyclohexylethanol (minor),1-cyclohexylethanol (major) benzenemethanol	3	84	50 (major)	20 (minor) 30	8400	2800

Hydrogenation of anisole (entry 4, Table 5.6) gives a single product, methoxycyclohexane with a TOF of 880, while that of dipenyl ether (entry 5, Table 5.6) generates cyclohexyl phenol ether as the major product and dicyclohexyl as a minor product. On the other hand, hydrogenation of p-cresol gives cis 4-methylcyclohexanol as major product (entry 11, Table 5.6), while that of acetophenone generates three products with cyclohexylethanol as the major product. By continuing the reaction for more time (8 h), cyclohexylethanol is the only product at the end.

More interesting are the hydrogenation results of disubstituted benzene derivatives such as xylenes, since these give selective conversion to *cis*-dimethylcyclohexane, a thermodynamically less favorable product. Similar selective formation of *cis* products has been reported in literature on rhodium-catalyzed hydrogenation reactions performed with homogeneous [86], biphasic [87], gas/solid [88] and liquid/solid [89] catalytic systems. Formation of the *cis* isomer is generally interpreted as the addition of six hydrogen atoms from the metal surface (in hydride form) to the aromatic ring from the same face, whereas, the *trans* compounds (commonly observed as minor products) are related to the outcome of the partially hydrogenated intermediates. Indeed, these are formed when a dimethylcyclohexene derivative dissociates from the catalyst surface and then re-associates with the opposite "face" before further hydrogenation.

A comparative study reveals that, despite a greater Rh loading in case of Rh/MWCNTs2, the conversion of toluene is less than that in case of Rh/MWCNTs1 (Table 5.7), perhaps due to the difference in the hydrophobic/hydrophilic properties of catalysts [47]. This has also been confirmed by BET adsorption studies (section 5.3.2.5), where a comparatively lower surface area of Rh/MWCNTs1 has been observed due to the homogeneous coverage of nanoparticles through the pores/defect sites. However, Rh3, and RhMPCs show rather inferior conversion as compared to that of Rh/MWCNTs1 as shown in Table 5.7. It could be due to the fact that the high surface area CNT provide a better support and also due to contributing factors such as the wall defects on CNTs (produced during pretreatment), acid-base and wetting properties of catalyst, etc. Surprisingly, Rh/vulcan XC shows higher efficiency (TOF; 6500 for benzene), although

the reaction gets stopped after 1 h. The deactivation of the catalyst takes place after 1 h, perhaps due to the blocking of active sites of Rhodium. Hence in comparison, Rh/MWCNTs1 shows remarkably higher efficiency in terms of both conversion efficiency and better recyclability.

Table 5.7. Catalytic activity of various Rh based catalysts for toluene under identical conditions (5 mmol of substrate, 5 mg catalyst (0.0005 mmol), hexane 50 mL, 40 °C, 20 bar H_2; (* benzene has been used as substrate).

Catalyst	Product	Time (h)	Conversion (%)	TON	TOF
Rh/MWCNTs1	Methyl cyclohexane	2	99	9900	4950
Rh/MWCNTs1	Cyclohexane*	1.5	99	9900	6600
Rh/MWCNTs2	Methyl cyclohexane	12	53	5300	442
Rh3	Methyl cyclohexane	2	52	2800	1300
RhMPCs	Methyl cyclohexane	2	72	3600	1800
Rh/Vulcan XC	Methyl cyclohexane	1	63	6300	6300
Rh/Vulcan XC	Cyclohexane*	1	65	6500	6500

In order to check the leaching of Rh nanoparticles into the reaction mixture, the reaction has been also carried out for 1 h under selected conditions using fresh Rh/MWCNTs1 at 40 ^{o}C and at 20 bar in hexane. The reaction has been stopped after 1 h and the catalyst has been separated by filtration and then the filtrate has been stirred further for 2 h. In the absence of the catalyst, there is no further increase in the conversion of toluene, which indicates the absence of leaching of any Rh metal into the reaction mixture. This observation confirms that the reaction is catalyzed heterogeneously. However, further studies including a rigorous evaluation of the chemical stability, durability, cost effectiveness and finally a possible mechanism are necessary if these advantages are to be commercially exploited.

5.4. Conclusions

A simple method for the synthesis of the monodispersed Rhodium nanoclusters stabilized by tridecylamine at room temperature has been discussed in this chapter along with their coulomb blockade behavior using electrochemical techniques like DPV, CV and LSV. The capacitance calculated from these experimental techniques is in good agreement with the results of the theoretical calculations. However, when these Rhodium nanoparticles (4.9 ± 0.2 nm) are anchored to the Multiwalled carbon nanotubes by simple microwave treatment, they no longer show such unusual behavior in the same electrolyte although interestingly, exhibit a remarkable catalytic activity for arene hydrogenation. The approach of using such Rh/MWCNTs for arene hydrogenation offers an unprecedented opportunity to obviate many limitations of currently used heterogeneous catalysts, opening new possibilities for manipulating the properties and stability to give enhanced catalytic performance. Apart from a remarkable conversion of products, these hybrid materials are also capable of increasing the thermal stability that could arise from the incorporation of Rhodium. However, several challenges have to be overcome before these advantages could be commercially exploited including a rigorous evaluation of the chemical stability, durability and cost effectiveness. Nevertheless, these results raise enough scope to design heterogeneous catalysis with better overall system efficiencies, recyclability and simplified balance of plant using these new generation of hybrid materials.

5.5. References

1. Templeton, A. C.; Wuelfing, W. P.; Murray, R. W. *Acc. Chem. Res.* **2000**, *33*, 27.
2. Xia,Y.; Gates, B.; Yin, Y. Lu, Y. *Adv. Mater. 12*, **2000**, 693.
3. Markovich, G.; Collier, C. P.; Heath, J. M. *Phys. Rev. Lett.* **1998**, *80*, 3807.
4. Dorogi, M.; Gomez, J.; Osifchin, R.; Andres, R. P.; Reifenberger, R. *Phy. Rev. B* **1995**, *52*, 9071.
5. Gittins,D. I.; Bethell, D.; Schiffrin, D. J.; Nichols, R. J. *Nature* **2000**, *408*, 67.
6. Brust, M.; Walker, M.; Bethell, D.; Schiffrin, D. J.; Whyman, R. *J. Chem. Soc. Chem. Commun* **1994**, 801.
7. Manna, A.; Kulkarni, B. D.; Bandyopadhyay, K.; Vijayamohanan, K. *Chem. Mater*. **1997**, *9*, 3032.
8. Crispin, X.; Bureau, C.; Geskin, V.; Lazzaroni, R.; Brédas, *Eurp. J. Inorg. Chem.* **1999**, *349*, 1999.
9. Balogh, L.; Tomalia, D. A. *J. Am. Chem. Soc.* **1998**, *120*, 7355.
10. Yeh, M.; Yang, Y.; Lee, Y.; Lee, H; Yeh, Y.; Chen-Sheng, Y. *J. Phys. Chem. B* **1999**, *103*, 6851.
11. Rao, C. N. R.; Kulkarni, G. U.; Thomas, P. J.; Edwards, P. P. *Chem. Soc. Rev.* **2000**, *29*, 27.
12. Schmid, G.; Chi, L. F.; *Adv. Mater.* **1998**, *10*, 515.
13. Collier, C. P.; Saykally, R. J.; Shiang, J. J.; Henrichs, S. E.; Heath, J. R. *Science* **1997**, *277*, 1978.
14. Chaki, N. K.; Gopakumar, T. G.; Maddanimath, T.; Aslam, M.; Vijayamohanan, K. *J. App. Phys.* **2003**, *94*, 3663.
15. Aslam, M. ; Mulla, I. S. ; Vijayamohanan, K. ; *App. Phy. Lett.* **2001**, *79*, 689.
16. Andres, R. P.; Bein, T.; Dorogi, M.; Feng, S.; Henderson, J. I.; Kubiak, C. P.; Mahoney, W.; Osifchin, R. G.; Reifenberger, R. *Science* **1996**, *272*, 1323.
17. Thomas, P. J.; Kulkarni, G. U.; Rao, C. N. R. *Chem. Phys. Lett.* **2000**, *321*, 163.
18. Chen, S.; Ingram, R. S.; Hostetler, M. J.; Pietron, J. J.; Murray, R. W.; Schaaff,

T. G.; Khoury, J. T.; Alvarez, M. M.; Whetten, R. L. *Science* **1998**, *280*, 2098.

19. Ingram, R. S. ; Hostetler, M. J. ; Murray, R. W. ; Schaaff, T. G. ; Khoury, J. ; Whetten, R. L. ; Bigioni, T. P. ; Guthrie, D. K. ; First, P. N. ; *J. Am. Chem. Soc.* **1997**, *119*, 9279.
20. (a) Quinn, B. M.; Lijeroth, P.; Ruiz, V.; Kaaksonen, T.; Kontturi, K. *J. Am. Chem. Soc.* **2003**, *125*, 6644. (b) D. Lee, R. L. Donkers, G. Wang, A. S. Harper, R. W. Murray, *J. Am. Chem. Soc.* **2004**, *126*, 6193.
21. Chen, S. ; Sommers, J. M. *J. Phys. Chem. B* **2001**, *105*, 8816.
22. Ding, Z. ; Quinn, B.M. ; Haram, S.K. ; Pell, L.E. ; Korgel, B.A. ; Bard, A.J. *Science* **2002**, *296*, 1293.
23. Cheng, W.; Dong, S.; Wang, E. *Electrochem. Commun*. **2002**, *4*, 412.
24. Chen, S.; Huang, K.; Stearns, J. A. *Chem. Mater*. **2000**, *12***,** 540.
25. Haram, S. K.; Quinn, B. M.; Bard, A. J. *J. Am. Chem. Soc.* **2001**, *123*, 8860.
26. Bae, Y.; Myung, Y.; Bard, A. J. *Nano Lett.* **2004**, *4*, 1153.
27. Chen, S.; Truax, L. A.; Sommers, J. M. *Chem. Mater*. **2000**,*12*, 3864.
28. (a) Templeton, A. C.; Wuelfing, W. P.; Murray, R. W. *Acc. Chem. Res*. **2000**, *33*, 27. (b) Terrill, R. H.; Postelethwaite, T. A.; Chen, C.; Poon, C. D.; Terzis, A.; Chen, A.; Hutchison, J. E.; Clark, M. R.; Wignall, G.; Londono, J. D.; Superfine, R.; Falvo, M.; Johnson, C. H., Jr.; Samulski, E. T.; Murray, R. W. *J. Am. Chem. Soc*. **1995**, *117*, 12537. (c) Chen, S.; Murray, R. W. *Langmuir* **1999**, *15*, 682. (d) Hostetler, M. J.; Wingate, J. E.; Zhong, C. -J.; Harris, J. E.; Vachet, R. W.; Clark, M. R.; Londono, J. D.; Green, S. J.; Stokes, J. J.; Wignall, G. D.; Glish, G. L.; Porter, M. D.; Evans. N. D.; Murray, R. W. *Langmuir* **1998**, *14*, 17. (e) Fouad, N.; Mohamed, A. A.; Zaki, M. I.; Knozinger, H. *J. Anal. Appl. Pyro.* **2000**, *53*, 185.
29. (a) Leff, D. V.; Brandt, L.; Heath, J. R. *Langmuir* **1995**, *12*, 4723. (b) Vijaya Sarathy, K.; Kulkarni, G. U.; Rao, C. N. R. *Chem. Commun.* **1997**, 537. (c) Shenhar, R.; Rotello, V. M. *Acc. Chem. Res.* **2003**, *36*, 549. (d) Cliffel, D. E.; Zamborini, F. P.; Gross, S. M.; Murray, R. W. *Langmuir*, **2000**, *16*, 9699. (e)

Schaaff, T. G.; Shafigullin, M. N.; Khoury, J. T.; Vezmar, I.; Whetten, R. L. *J. Phys. Chem. B* **2001**, *105*, 8785.

30. (a) Vijaya Sarathy, K.; Raina, G.; Yadav, R. T.; Kulkarni, G. U.; Rao, C. N. R. *J. Phys. Chem. B* **1997**, *101*, 9876. (b) Chen, S.; Sommers, J. M. *J. Phys. Chem. B* **2001**, *105*, 8816. (c) Zamborini, F. P.; Gross, S. M.; Murray, R. W. *Langmuir*, **2001**, *17*, 481. (d) Balogh, L.; Tomalia, D. A. *J. Am. Chem. Soc.* **1998**, *120*, 7355. (e) Yeh, M.; Yang, Y.; Lee, Y.; Lee, H; Yeh, Y.; Chen-Sheng, Y. *J. Phys. Chem. B* **1999**, *103*, 6851. (f) Hostetler, M. J.; Zhong, C. -J.; Yen, B. K. H.; Anderegg, J.; Gross, S. M.; Evans, N. D.; Porter, M.; Murray, R. W. *J. Am. Chem. Soc.* **1998**, *120*, 9396. (g) Sandhyarani, N.; Pradeep, T. *Chem. Mater.* **2000**, *12*, 1755.
31. Daniel, M. -C.; Astruc, D. *Chem. Rev.* **2004**, *104*, 293.
32. (a) Tanori, J.; Pileni, M. P., *Adv. Mater.* **1995**, *7*, 862. (b) Lisiek, I.; Pileni, M. P. *J. Phy. Chem.* **1995**, *99*, 5077. (c) Pileni, M. P. *J. Phy. Chem.B* **2001**, *104*, 3358.
33. (a) Manna, A.; Kulkarni, B. D.; Bandyopadhyay, K.; Vijayamohanan, K. *Chem. Mater.* **1997**, *9*, 3032. (b) Manna, A.; Imae, T.; Iida, M.; Hisamatsu, N. *Langmuir* **2001**, *17*, 6000. (c) Wang, W.; Chen, X.; Efrima, S. *J. Phys. Chem. B* **1999**, *103*, 7238. (d) Kim, S. -W.; Park, J.; Jang, Y.; Chung, Y.; Hwang, S.; Hyeon, T.; Kim, Y. W. *Nano Lett.* **2003**, *3*, 1289. (e) Wilcoxon, J. P.; Williamson, R. L.; Baughman, R. *J. Chem. Phys.* **1993**, *98*, 9933.
34. (a) Lin, X. M.; Wang, G. M.; Sorensen, C. M.; Klabunde, K. J. *J. Phys. Chem. B* **1999**, *103*, 5488. (b) Prasad, B. L. V.; Stoeva, S. I.; Sorensen, C. M.; Klabunde, K. J. *Chem. Mater.* **2003**, *15*, 935. (c) Teranishi, T.; Kiyokawa, I.; Miyake, M. *Adv. Mater.* **1998**, *10*, 596.
35. (a) Jana, N. R.; Peng, X. G. *J. Am. Chem. Soc.* **2003**, *125*, 14280. (b) Hiramatsu, H.; Osterloh, F. E. *Chem. Mater.* **2004**, *16*, 2509. (c) Green, M.; O'Brien, P. *Chem. Commun.* **2000**, 183.
36. Chen, S.; Murray, R. W.; Feldberg, S. W. *J. Phys. Chem. B* **1998**,*102*, 9898.
37. (a) Chaki, N. K.; Singh, P.; Dharmdhikari, C. V.; Vijayamohanan, K. *Langmuir*

2004, *20*, 10208. (b) Chaki, N. K.; Kakade, B.; Sharma, J.; Mahima, S.; Vijayamohanan, K. P.; Haram, S. K. *J. Appl. Phys.* **2004**, *96*, 9632. (c) Chaki, N. K.; Kakade, B. A.; Pillai, K. V.; Singh, P.; Dharmadhikari, C. V. *Phys. Chem. Chem. Phys.* **2006**, *8*, 1837.

38. Mu, X.; Meng, J.; Li, Z.; Kou, Y. *J. Am. Chem. Soc.* **2005**, *127*, 9694.
39. (a) Roucoux, A. ; Schulz, J. ; Patin, H. *Chem. Rev.* **2002**, *102*, 3757. (b) Rioux, R.M.; Song, H. J.; Hoefelmeyer, D.; Yang, P.; Somorjai, G. A. *J. Phys. Chem. B* **2005**, *109*, 2192. (c) Yang, C. ; Kalwei, M.; Schüth, F.; Chao, K. *Appl. Catal.* **2003**, *254*, 289. (d) Chatterjee, M.; Ikushima, Y.; Hakutaa, Y.; Kawanami, H. *Adv. Synth. Catal.* **2006**, *348*, 1580.
40. Weissermel, K.; Arpe, H.-J. *Industrial Organic Chemistry*, VCH, New York, **1993**.
41. Corma, A.; Martı´nez, A.; Martı´nez-Soria, V. *J. Catal.* **1997,** *169*, 480.
42. James, B.R.; Wang, Y.; Hu, T.Q. *Chem. Ind.* **1996**, *68* , 423.
43. (a) Schulz, J.; Roucoux, A.; Patin, H. *Chem. Commun.* **1999**, 535. (b) Schulz, J. ; Roucoux, A.; Patin, H.*Chem. Eur. J.* **2000**, *6*, 618. (c) Arico, A. S.; Srinivasan, S.; Antonucci, V. *Fuel Cells* **2001**, *1*, 133.
44. (a) Collman, J. P.; Hegedus, L.S.; Norton, J.R.; Finke, R.G. *Principles and Applications of Organotransition Metal Chemistry*, University Science Book, Mill Valley, **1987** (Chapter 10). (b) Weddle, K.S.; Aiken III, J.D.; Finke, R.G. *J. Am. Chem. Soc.* **1998,** *120*, 5653. (c) Collman, J. P.; Kosydar, K.M.; Bressan, M.; Lamanna, W.; Garrett, T. *J. Am. Chem. Soc.* **1984,** *106*, 2569. (d) James, B. R.; Wang, Y.; Alexander, C. S.; Hu, T. Q. *Chem. Ind.* **1998,** *75*, 233. (e) R.G. Finke, in: D.L. Feldheim, C.A. Foss Jr. (Eds.), *Metal Nanoparticles: Synthesis, Characterization, and Applications*, Marcel Dekker, New York, **2001** (Chapter 2).
45. Dyson, P. J. *Dalton Trans*. **2003**, 2964.
46. (a) Tauster, S. J.; Fung, S. C.; Garten, R. L. *J. Am. Chem. Soc.* **1978**, *100*, 170. (b) Tauster, S. J.; Fung, S. G. *J.Catal.*, **1978,** *55*, 29. (c) Cheetham, A. K.; Day,

P. *Solid State Chemistry Compounds* (Oxford Science Publications **1993**)

47. (a) Augustine, R. L. *Heterogeneous Catalysis for the Synthetic Chemistry*, Chap. 17, M. Dekker, New York, **1996**. (b) Eisen, M. S.; Marks, T. J. *J. Am. Chem. Soc.* **1992**, *114*, 10358. (c) Keane, M. A. *J. Catal.* **1997**, *166*, 347.
48. Rothwell, I. P. *Chem. Commun.* **1997**, 1331.
49. (a) Weddle, K. S. ; Aiken III, J. D. ; Finke, R. G. *J. Am. Chem. Soc.* **1998**, *120*, 5653. (b) Widegren, J. A.; Finke, R. G. *Inorg. Chem.* **2002**, *41*, 1558. (c) Hornstein, B. J.; Aiken III, J. D.; Finke, R. G. *Inorg. Chem.* **2002**, *41*, 1625. (d) Widegren, J. A.; Finke, R. G. *J. Mol. Catal. A* **2003**, *191*, 187. (e) Widegren, J. A.; Finke, R. G. *J. Mol. Catal. A* **2003**, *191*, 317. (f) Widegren, J. A.; Bennett, M. A.; Finke, R. G. *J. Am. Chem. Soc.* **2003**, *125*, 10301. (g) Hagen, C. M.; Widegren, J. A.; Maitlis, P. M.; Finke, R. G. *J. Am. Chem. Soc.* **2005**, *127*, 4423. (h) Qzkar, S.; Finke, R. G. *J. Am. Chem. Soc.* **2005**, *127*, 4800.
50. (a) Gao, H.; Angelici, R. J. *J. Am. Chem. Soc.* **1997,** *119*, 6937. (b) Yang, H.; Gao, H.; Angelici, R. J. *Organometallics* **2000**, *19*, 622.
51. Mu, X.; Meng, J.; Li, Z.; Kou, Y. *J. Am. Chem. Soc.* 2005, *127*, 9694.
52. (a) Schulz, J. ; Roucoux, A. ; Patin, H. *Chem. Commun.* **1999**, 535. (b) Schulz, J.; Roucoux, A.; Patin, H. *Chem. Eur. J.* **2000**, *6*, 618. (c) Pellegatta, J. ; Blandy, C.; ColliRre, V.; Choukroun, R.; Chadret, B.; Cheng, P. ; Philippot, K. ; *J. Mol. Catal. A* **2002**, *178*, 55. (d) Schulz, J.; Levigne, S.; Roucoux, A.; Patin, H. *Adv. Synth. Catal.* **2002**, *344*, 266. (e) Roucoux, A.; Schulz, J.; Patin, H. *Adv. Synth. Catal.* **2003**, *345*, 222. (f) MSvellec, V.; Roucoux, A.; Ramirez, E.; Philippot, K.; Chaudret, B. *Adv. Synth. Catal.* **2004**, *346*, 72. (g) Lu, F.; Liu, J.; Xu, J. *Adv. Synth. Catal.* **2006,** *348*, 857.
53. (a) Dyson, P. J.; Ellis, D. J.; Parker, D. G.; Welton, T. *Chem. Commun.* **1999**, 25. (b) Boxwell, C. J.; Dyson, P. J.; Ellis, D. J.; Welton, T. *J. Am. Chem. Soc.* **2002**, *124*, 9334. (c) Dupont, J.; Fonseca, G. S.; Umpierre, A. P.; Fichtner, P. F. P.; Teixeira, S. R. *J. Am. Chem. Soc.* **2002**, *124*, 4228. (d) Fonseca, G. S.; Umpierre, A. P.; Fichtner, P. F. P.; Teixeira, S. R.; Dupont, J. *Chem. Eur. J.* **2003**, *9*, 3263.

(e) Dyson, P. J.; Ellis, D. J. ; Henderson, W.; Laurenczy, G. *Adv. Synth. Catal.* **2003**, *345*, 216. (f) Fonseca, G. S. ; Scholten, J. D. ; Dupont, J. *Synlett* **2004**, *9*, 1525. (g) Silveira, E. T.; Umpierre, A. P.; Rossi, L. M.; Machado, G.; Morais, J.; Soares, G. V.; Baumvol, I. J. R.; Teixeira, S. R.; Fichtner, P. F. P.; Dupont, J. *Chem. Eur. J.* **2004**, *10*, 3734. (h) Geldbach, T. J.; Dyson, P. J. *J. Organomet. Chem.* **2005**, *690*, 3552. (i) Miao, S.; Liu, Z.; Han, B.; Huang, J.; Sun, Z.; Zhang, J.; Jiang, T. *Angew. Chem. Int. Ed.* **2006**, *45*, 266. (j) Migowski, P.; Dupont, J. *Chem. Eur. J.* **2007**, *13*, 32.

54. (a) Bonilla, R. J.; James, B. R.; Jessop, P. G. *Chem. Commun.* **2000**, 941. (b) Ohde, M.; Ohde, H.; Wai, C. M. *Chem. Commun.* **2002**, 2388. (c) Rode, C. V.; Joshi, U. D.; Sato, O.; Shirai, M. *Chem. Commun.* **2003**, 1960. (d) Ohde, H.; Ohde, M.; Wai, C. M. *Chem. Commun.* **2004**, 930.
55. Auer, E.; Freund, A.; Pietsch, J.; Tacke, T. *Appl. Catal. A* **1998**, *173*, 259.
56. Fischer, J. E.; Johnson, A. T. *Curr. Opin. Solid State Mater. Sci.* **1999**, *4*, 28.
57. (a) Menon, M.; Andriotis, A. N.; Froudakis, G. E. *Chem. Phys.Lett.* **2000**, *320*, 425. (b) Georgakilas, V.; Gournis, D.; Tzitzios, V.; Pasquato, L.; Guldi, D. M.; Prato, M. *J. Mater. Chem.* **2007**, *17*, 2679.
58. (a) Planeix, J. M.; Coustel, N.; Coq, B.; Brotons, V.; Kumbhar, P. S.; Dutartre, R.; Geneste, P.; Bernier, P.; Ajayan, P. M. *J. Am. Chem. Soc.* **1994,** *116*, 7935. (b) Ebbesen, T. W.; Hiura, H.; Bisher, M. E.; Treacy, M. M. J.; Shreeve-Keyer, J. L.; Haushalter, R. C. *Adv. Mater.* **1996,** *8*, 155. (c) Ang, L. M.; Hor, T. S. A.; Xu, G. Q.; Tung, C. H.; Zhao, S.; Wang, J. L. S. *Chem. Mater.* **1999** *11*, 2115. (d) Ye, X. R.; Lin, Y. H.; Wai, C. M. *Chem. Commun.* **2003**, 642. (e) Yen, C. H.; Cui, X.; Pan, H. -B.; Wang, S.; Lin, Y.; Wai, C. M. *J. Nanosci. Nanotechnol.* **2005,** *5*, 1852. (f) Ye, X. R.; Lin, Y.; Wai, C. M.; Talbot, J. B.; Jin, S. *J. Nanosci. Nanotechnol.* **2005**, *5*, 964. (g) Giordano, R.; Serp, P.; Kalck, P.; Kihn, Y.; Schreiber, J.; Marhic, C.; Duvail J. *Eur. J. Inorg. Chem.* **2003**, 610. (h) Rodriguez, N. M.; Kim, M.; Baker, R. T. K. *J. Phys. Chem.* **1994**, *98*, 13108. (i) Salman, F.; Park, C.; Baker, R. T. K. *Catal. Today* **1999**, *53*, 385. (j) Park, C.;

Baker, R. T. K. *J. Phys. Chem. B* **1998**, *102*, 5168. (k) Pham-Huu, C.; Keller, N.; Charbonnie`re, L. J.; Ziessel, R.; Ledoux, M. J. *Chem. Commun.* **2000**, 1871. (l) Pham- Huu, C.; Keller, N.; Erhet, G.; Charbonnie`re, L. J.; Ziessel, R.; Ledoux, M. J. *J. Mol. Cat.* **2001**, *170*, 155. (m) Gao, R.; Tan, C. D.; Baker, R. T. K. *Catal. Today* **2001**, *65*, 19. (n) Chen, P.; Wu, X.; Lin, J.; Tan, K. L. *J. Phys. Chem.* **1999**, *103*, 4559. (o) Planeix, J. M.; Coustel, N.; Coq, B.; Brotons, V.; Kumbhar, P. S.; Dutartre, R.; Geneste, P.; Bernier, P.; Ajayan, P. M. *J. Am. Chem. Soc.* **1994**, *116*, 7935. (p) Chen, H.; Lin, J.; Cai, Y.; Wang, X.; Yi, J.; Wang, J.; Wei, G.; Lin, Y.; Liao, D. *Appl. Surf. Sci.* **2001**, *180*, 328.

59. Yoon, B.; Wai, C. *J. Am. Chem. Soc.* **2005**, *127*, 17174.
60. El-Sayed, M. A. *Acc. Chem. Res.* **2001**, *34*, 257 and references there in.
61. Mie, G. *Ann. Physik* **1908**, *25*, 377.
62. Kreibig, U.; Vollmer, M. *Optical Properties of Metal Clusters;* Springer: Berlin, **1995**.
63. (a) Papavassiliou, G. C. *Prog. Solid State Chem.* **1980**, *12*, 185. (b) Kerker, M. *The Scattering of Light and Other Electromagnetic Radiation,* Academic Press: New York, **1969**. (c) Bohren, C. F.; Huffman, D. R. *Absorption and Scattering of Light by Small Particles,* Wiley: New York, **1983**. (d) Creighton, J. A.; Eadon, D. G. *J. Chem. Soc. Faraday Trans.* **1991**, *87*, 3881.
64. Aiken III, J. D.; Finke, R. G. *J. Mol. Cata. A:Chem.* **1999**, *145*, 1.
65. (a) Hoefelmeyer, J. D.; Niesz, K.; Somorjai, G. A.; Tilley, T. D. *Nano Lett.* **2005**, *5*, 435. (b) Ewers, T. D.; Sra, A. K.; Norris, B. C.; Cable, R. E.; Cheng, C.; Shantz, D. F.; Schaak, R. E. *Chem. Mater.* **2005**, *17*, 514.
66. Culllity, B. D.; Stock, S. R. *Elements of X-ray Diffraction, 3rd Edition*, Englewood Cliffs, N. J: Prince-Hall, **2001**.
67. (a) Sandhyarani, N.; Resmi, M. R.; Unnikrishnan, R.; Vidyasagar, K.; Ma, S.; Antony, M. P.; Selvaam, G. P.; Visalakshi, V., Kumar, N. C.; Pandian, K.; Tao, Y. T.; Pradeep, T. *Chem. Mater*, **2000**, *12*, 104. (b) Sandhyarani, N.; Pradeep, T.; Chakrabarti, J.; Yousuf, M.; Sahu, H. K. *Phys. Rev.B*, **2000**, *62*, 739. (c)

Sandhyarani, N.; Pradeep, T. *Chem. Mater*, **2000**, *12*, 1755. (d) Mitra, S.; Nair, B.; Pradeep, T.; Goyal, P. S.; Mukhopadhyay, R. *J. Phys.Chem. B* **2002**, *106*, 3960. (e) Sandhyarani, N.; Pradeep, T.; Antony, M. P.; Selvam, G. P. *J. Chem. Phys.* **2000**, *113*, 9794. (f) Pradeep, T.; Mitra, S.; Nair, A. S.; Mukhopadhyay, R. *J. Phys. Chem. B.* **2004,** *108*, 7012**.**

68. Hostetler, M. J.; Stokes, J. J.; Murray, R. W. *Langmuir* **1996**, *12*, 3604.
69. Frolov, V. M.; Shuikina, L. P.; Turisbekova, K. K.; Bondarenko G. N., *Kinet. Catal. (Eng. Trans.)* **1994**, *35*, 800.
70. *NIST Vibrational Spectroscopy Database* (via Internet: http://srdata.nist.gov/vb.)
71. Koh, Y. B.; Christoph, G. G. *Inorg. Chem.* **1978**, *17*, 2590.
72. (a) http://srdata.nist.gov/xps/elm_in_comp_res. (b) Weng-Sieh, Z.; Gronsky, R.; Bell, A. T. *J. Catal.* **1997**, *170*, 62. (c) Rubel, M.; Pszonicka, M.; Palczewska, W. *J. Mater. Sci.* **1985**, *20*, 3639.
73. (a) Pietron, J. J.; Hicks, J. F.; Murray, R. W. *J. Am. Chem. Soc.* **1999**, *121*, 5565. (b) Miles, D. T.; Murray, R. W. *Anal. Chem.* **2003**, *75*, 1251.
74. (a) Li, D.; Li, J. *Chem. Phys. Lett.* **2003**, *372*, 668. (b) Yang, Y.; Chen, S. *Nano Lett.* **2003**, *3*, 75.
75. Su, B.; Girault, H. H. *J. Phys. Chem. B* **2005**, *109*, 11427.
76. (a) Holmlin, R. E.; Haag, R.; Chabinyc, M. L.; Ismagilov, R. F.; Cohen, A. E.; Terfort, A.; Rampi, M. A.; Whitesides, G. M. *J. Am. Chem. Soc.* **2001**, *123*, 5075. (b) Rampi, M. A.; Schueller, O. J. A.; Whitesides, G. M. *Appl. Phys. Lett.* **1998**, *72*, 1781. (c) Bain C. D.; Whitesides G. M. *J. Am. Chem. Soc.* **1989**, *111*, 7164. (d) CRC Handbook of Chemistry and Physics, 85th Edition, [Editor-in-Chief- David R. Lide] CRC press. 2004-2005.
77. Bard, A. J.; Faulkner, L. R. *Electrochemical Methods, Fundamentals and Applications; 2nd ed,* John Wiley & Sons: New York, **2001**.
78. (a) Hicks, J. F.; Zamborini, F. P.; Osisek, A. J.; Murray, R. W. *J. Am. Chem. Soc.* **2001**, *123*, 7048. (b) Chidsey, C. E. D.; Murray, R. W. *J. Phys. Chem.* **1986**,

90, 1479. (c) Laviron, E. *J. Electroanal. Chem.* **1981**, *122*, 37.

79. (a) Chopra, N. G.; Ross, F. M.; Zettl, A. *Chem. Phys. Lett*. **1996**, *256*, 241. (b) Crespi, V. H.; Chopra, N. G.; Cohen, M. L.; Zettl, A.; Louie, S. G. *Phys. Rev. B: Condens. Mater*. **1996**, *54*, 5927.
80. (a) Hoefelmeyer, J. D.; Niesz, K.; Somorjai, G. A.; Tilley, T. D. *Nano Lett.* **2005**, *5*, 435. (b) Ewers, T. D.; Sra, A. K.; Norris, B. C.; Cable, R. E.; Cheng, C.; Shantz, D. F.; Schaak, R. E. *Chem. Mater.* **2005**, *17*, 514. (c) Culllity, B. D.; Stock, S. R. *Elements of X-ray Diffraction, 3rd Edition*, Englewood Cliffs, N. J: Prince-Hall, **2001**.
81. (a) http://srdata.nist.gov/xps/elm_in_comp_res. (b) Weng-Sieh, Z.; Gronsky, R.; Bell, A. T. *J. Catal.* **1997**, *170*, 62. (c) Rubel, M.; Pszonicka, M.; Palczewska, W. *J. Mater. Sci.* **1985**, *20*, 3639.
82. Lee, K. Y.; Kim, M.; Lee, Y. W.; Lee, J.-J.; Han, S. W. *Chem. Phys. Lett.* **2007**, *440*, 249.
83. (a) Rao, A. M.; Eklund, P. C.; Bandow, S.; Thess, A.; Smalley, R. E. *Nature* **1997**, *388*, 257. (b) Bubert, H.; Haiber, S.; Brandl, W.; Marginean, G.; Heintze, M.; Brüser, V.; *Diam. Rel. Mater.* **2003**, *12*, 811. (c) Haiber, S.; Xingtao, A.; Bubert, H.; Heintze, M.; Brüser, V.; Brandl, W.; Marginean, G. *Anal Bioanal Chem.*, **2003,** *375*, 875. (d) Felten, A.; Bittencourt, C.; Pireaux, J. J.; Van Lier, G.; Charlier, J. C. *J. Appl. Phys.* **2005,** *98*, 074308. (e) Pirlot, C.; Willems, I.; Fonseca, A.; Nagy, J. B.; Delhalle, J. *Adv. Eng. Mater.* **2002,** *4*, 109. (f) Ago, H.; Kugler, T.; Cacialli, F.; Salaneck, W. R.; Shaffer, M. S. P.; Windle, A. H.; Friend, R. H. *J. Phys. Chem. B* **1999,** *103*, 8116. (g) Wang, Y. Q.; Sherwood, P. M. A. *Chem. Mater.* **2004,** *16*, 5427. (h) Parekh, B. D. T.; Knight, P.; Santhanam, K.S.V.; Takacs, G. A J. *Adhesion Sci. Technol.* **2006,** *20*, 1833.
84. Kyotani, T.; Nakazaki, S.; Xu, W. –H.; Tomita, A. *Carbon* **2001**, *39*, 782.
85. Kim, D. Y.; Yang, C.-M.; Park, Y. S.; Kim, K. K.; Jeong, S. Y.; Han, J. H.; Lee, Y. H. *Chem. Phys. Lett.* **2005**, *413*, 135.
86. Fonseca, G. S.; Umpierre, A. P.; Fichtner, P. F. P.; Teixeira, S. R.; Dupont, J.

Chem. Eur. J. **2003,** *9,* 3263.

87. Bonilla, R. J.; James, B.R.; Jessop, P. G. *Chem. Commun.* **2000,** 941.
88. (a) Neyestanaki, A. K.; M.aki-Arvela, P.; Backman, H.; Karhu, H.; Salmi, T.; V¨ayrynen, J.; Murzin, D. Y. *J. Catal.* **2003,** *218,* 267. (b) Park, I. S.; Kwon, M.S.; Kim, N.; Lee, J. S.; Kang, K.Y.; Park, J. *Chem. Commun.* **2005,** 5667.
89. (a) Park, K. H.; Jang, K.; Kim, H. J.; So, S. U. *Angew. Chem. Int.Ed.* **2007**, *46*, 1152. (b) Landre, P. D.; Richard, D.; Draye, M.; Gallezot, P.; Lemair, M. *J. Catal.* **1994**, *147*, 214.

CHAPTER 6

Conclusions and Future Prospects*

This chapter deals with the significant conclusions of the present study. It also outlines several limitations of CNT based materials along with few suggestions for their improvement. Related promising developments and daunting challenges in this broad area are also discussed to extend the applications of these fascinating carbonaceous nanomaterials in view of the fundamental and technological interest by physicists, chemists, biologists and engineers. Finally, some of the future prospects and precautions for processing carbon nanotubes and contiguous materials like graphene are also explained within the broad perspective of nanotechnology and its societal impact.

* The images in this cover picture have been adopted from [1] and [2].

Carbon Nanotubes (CNTs) are unique materials with remarkable electronic and mechanical properties, some stemming from their close relationship to graphite, while others from their one-dimensional aspects. CNTs continued to generate great interest because of their exotic electronic structure. As many other intriguing properties have been slowly unravelled including their fascinating electronic transport, unique Raman spectra and unusual mechanical properties, interest has grown in their potential applications in nanoelectronics and in a variety of other applications. Structurally, CNTs could be considered as a new man-made polymer consisting of discrete sp^2-carbon atoms with all possible strength and more importantly this stiffest, toughest molecule that could ever be produced acts also as best possible molecular conductor of both heat and electricity.

Various procedures such as Laser ablation, Arc discharge, High pressure carbon monoxide (HiPCO) process and thermal chemical vapor deposition (CVD) have been developed for the preparation of CNTs [3]. Among these, CVD has been more extensively used to grow a variety of carbon nanostructures due to its simpler design and easier instrumentation for control. One of the important prerequisites during CNT synthesis is the precise control of temperature of the reaction zone because of its direct influence on the CNT diameter-distribution. Growth by CVD and its variants enable to deal effectively this at a relatively lower temperature range, viz. 700 – 1200 ^{o}C, using various hydrocarbons in presence of suitable catalysts. Accordingly, several models have been developed, in order to explain the growth mechanism under different synthetic conditions (Chapter 1). Nevertheless, no report exists on the preparation of carbon nanostructures under a temperature ramp, which could be helpful in understanding possible transformations in their growth mechanism. As a result, we have successfully demonstrated this effect on synthesis, where the morphology of CNTs could be tuned under a constant temperature ramp facilitating the scroll formation. The mechanism of formation of such unique carbon nanostructures constituting a large amount of MWCNTs has been explained on the basis of thermal expansion coefficient in Chapter 2.

Although, considerable efforts have been expended recently in functionalizing carbon nanotubes, several important aspects related to their extent of selective

functionalization, purity, and its relation to the wetting behavior remain unaddressed. Accordingly, we have discussed a simple and novel method of solubilizing SWCNTs using a microwave treatment in Chapter 3. This also includes a strategy for an efficient phase transfer of SWCNTs from an aqueous to non-aqueous media using a unique amino functionalization route, where the water soluble SWNTs (2.6 mg/mL) could be transferred to solvents like chloroform, toluene and carbon disulphide (CS_2). A comparative study using two different functionalization strategies is discussed along with their merits and limitations. The usefulness of microwave functionalization has been highlighted especially in terms of the extent of functionalization, relative purity and the solubility.

Although many functionalization treatments have been recently carried out on both single and multiwalled nanotubes, no report is available to date, on their functionalization-dependent tuning of wetting behavior, despite their importance for a variety of applications like superhydrophobic coating and polymer nanocomposites. On the other hand, surface properties of CNTs, especially if they are in the form of paper or mats, offer the exciting possibility of using them in a more compact form for easy processing. In order to understand the effect of functionalization on wetting behavior of CNTs, we have demonstrated a simple strategy for controlling the wettability of MWNT films (bucky papers) from superhydorphobic (with water CA; 156^o) to nearly hydrophilic (CA; 40^o). Since CNT has a perfect graphitic network of sp^2 carbon, it exhibits intrinsic hydrophilic behavior (CA < 90^o), where further functionalization could facilitate easier control of their wetting properties [4]. Accordingly, various methods of acid functionalization have been employed to render effective modification of nanotube surfaces and the effect has been monitored by contact angle measurements. In addition, the wetting properties of such superhydrophobic surfaces have also been controlled using external electric field. A tentative mechanism for electrowetting of CNT paper has also been discussed in Chapter 4, in conjunction with results by varying key parameters like pH, ionic strength and size of cations/anions.

The use of CNT as a substrate in heterogeneous catalysis has garnered much attention due to their favorable characteristics such as high surface area, mechanical

stability due to the presence of an inert carbon network and more importantly their chemically tunable topography. They also show catalytic properties often many times superior to those of conventional catalysts on activated carbon or graphite [5]. If such high aspect ratio carbon nanostructures could be coupled with metallic nanoparticles (e.g., Rhodium), an improved catalytic activity for many of the important reactions like hydrogenation of olefin and arenes could be achieved. Consequently, a novel synthetic procedure has been demonstrated in Chapter 5, to anchor monodispersed nanoclusters of Rhodium on CNT surface due to their importance in size and shape dependent catalysis. More significantly, a unique electron transfer behavior of these Rhodium nanoparticles stabilized by tridecylamine (4.9± 0.2 nm) has also been discussed using electrochemical measurements at room temperature. This chapter also indicates that, Rh/MWNTs could be a good option for hydrogenation of arenes like disubstituted benzene derivatives (e.g., xylene), since it gives selective formation of thermodynamically less favorable, cis-dimethylcyclohexane as the main product with enhanced turn over numbers.

Thus, the main results of this thesis unravel few issues in the field of Carbon nanotubes with particular emphasis on their preparation, functionalization and tuning of their wetting properties for selected applications. Unique tunability of CNT with respect to their structure, property and application by chemical functionalization is expected to facilitate the prospect of this material for many more tangible applications. More specifically, since these nanostructures act as indispensable building blocks for creating designer materials, processing them into robust polymer composite thin films (after successfully overcoming barriers in dispersion) is essential for the fabrication of devices. Although, many well-established methods to synthesize and understand the properties of SWCNTs have been developed recently, several daunting challenges such as the difficulty of precisely controlling their aspect ratio, lack of well defined methods for the separation of metallic and semiconducting nanotubes, limitations of scale-up, issues of cost effectiveness and environmental effects still exist, demanding breakthroughs to utilize their complete technological and social benefits in the area of electronics, energy storage, water purification and so on. In addition, several existing gaps in our understanding need to be filled by urgent investigations focusing on atomically precise

manufacturing new materials and their structure-property correlations. For example, nanotubes synthesized by CVD always contain other unwanted structures, whose removal is often troublesome. Also, the effect of temperature on the preparation is rather crucial to design these nanostructures in a desired manner and hence finally to our in-depth understanding and control of their formation and interfacial chemistry. All of these challenges lie before us, especially since impure carbon nanotubes still cost more than that of gold!

Environmental impact of the usage of CNTs in particular and nanomaterials in general, has recently caused several important concerns due to increased public and media attention. It has been suggested that one reasonably close to market application is the use of carbon nanotubes in displays and the environmental impact of this has to be evaluated. Researchers are keen to discover if nanotubes have similar properties of asbestos, the ability to fix them in a polymer matrix will make them not air-borne thus reducing the risk. However, lack of systematic data in many of these areas is a common concern [6]. Therefore the social and environmental issues of nanotechnology have to be critically examined before delivering CNT based technology as several frightening (although exaggerated) consequences have been proposed recently [7]. Also, depending on the results of toxicity studies, disposal or recycling of products containing nanotubes may need to be carefully regulated to ensure containment. In addition, following points need to be understood along with the effectiveness of the technology solutions-

- What health, safety and environmental issues arise from applications of carbon nanotubes, and what will be the benefits and risks?
- Is there a need for new regulations especially with respect to biological applications of CNTs?
- What are the social and ethical issues of making new from of CNT based hybrid materials, such as CNT-DNA hybrid?
- What other public perceptions would influence the development of this type of nanotechnology?

A detailed understanding of the fundamental aspects of these materials would enable several fascinating nanoelectronic circuitry, while composites would be used as materials for making smart devices. Several technologies would be expected to revolutionize applications (e.g., UN Millennium Development Goals) including, information, computer, energy and biotechnology along with their global impact on health, food, water and medicine concerning our daily life [8]. For example, CANAPE (Carbon Nanotubes for Applications in Electronics, Catalysis, Composites and Nano-Biology) intends to exploit the full potential of carbon nanotubes by developing their most promising applications. The first large scale economic and environmental impact is recognized by the use of carbon nanostructures as a catalyst for styrene production, allowing the reaction to run at least 100 °C cooler and avoiding the hazardous waste created by the present catalyst Fe-K [6]. Accordingly, the cost and energy conservation for creating nanoarchitectures have also to be reduced along with ensuring their reproducibility and understanding the properties of CNT is essential for achieving many of these objectives..

Major accomplishments of the present investigations could be summarized as follows-

- Synthesis of the MWCNTs in the form of large scrolled mats under unique temperature conditions
- Development of a higher, yet quantitative, degree of solubility of SWCNTs and MWCNTs using simple and rapid microwave irradiation
- An efficient phase-transfer of SWCNTs from an aqueous to non-aqueous media using a unique amidation route
- Tuning the wetting behavior of thin films of MWCNTs using various chemical functionalization strategies
- Electric field induced reversible switching in wetting of bucky papers of MWCNTs
- Preparation and characterization of Rhodium nanoclusters/MWCNT hybrid materials

- An enhanced catalytic efficiency of these Rhodium/MWCNT hybrid materials for the hydrogenation of various arenes

In brief, our approach of such novel methods of CNT preparation and its processing offers an unprecedented opportunity to obviate many limitations of currently employed materials, opening new possibilities of manipulating the properties and stability to give enhanced performance. However, several limitations need to be mentioned before these results could commercially be exploited.

- The scrolled mats produced in these studies are very fragile as compared to bucky papers prepared by chemical methods and hence these need to be processed prior to discerning their properties.
- The increase in the solubility of SWCNTs obtained by using microwave irradiation could give different results, since the mixture of nanotubes with different aspect ratio could provide different solubility.
- The exact mechanism of change in wettability of bucky papers has not been explored, although a spectroscopic evidence based explanation could have been possible to unravel the interfacial phenomenon.
- A rigorous evaluation of the chemical stability of the Rhodium/CNT based catalysts, durability, cost effectiveness and finally elucidation of possible mechanism of conversion have to be carried out in a systematic manner.

Nevertheless, present results offer enough scope to design novel CNT based nanomaterials with better overall system efficiencies, recyclability and simplified functionalization chemistry using these new generation of hybrid materials. For example, in recent years, graphene has attracted great interest of both condensed matter physicist and materials scientists due to a variety of fascinating properties [9]. This strictly two-dimensional (2-D) carbonaceous material exhibits exceptionally high crystallinity and electronic structure, which reveals a wealth of new physics and potential applications, despite having a short history. More generally, graphene represents a conceptually new class of materials that are only one atom thick, offers new inroads into low-dimensional physics in which charge carriers can travel thousands of interatomic distances without scattering. Graphene's potential for electronics is usually justified by high mobility of its

charge carriers, capable of exhibiting anomalous Quantum Hall effect. However, the truly exceptional feature of graphene is that carrier mobility (μ) remains high even at highest electric-field-induced concentrations ($>10^{13}$), and seems to be little affected by chemical doping [10]. This translates into ballistic transport on a submicrometre scale at 300 K. A room-temperature ballistic transistor has long been an enticing but elusive dream and graphene could make it really possible. Nevertheless, the research directions should persuade even die-hard sceptics that graphene is not a fleeting fancy but here to stay, bringing up both more exciting physics, and perhaps applications in energy storage, electronics, and composites. Some of our findings are also valid for graphene and related structures (e.g., functionalized graphene sheets offer many multifunctional composites within polymer matrix) [11] and it is hoped that more studies would contribute significantly in the years to come.

References

1. Coluci, V. R.; Calvao, D. S.; Jorio, A. *Nanotechnology* **2006**, *17*, 617.
2. Cover page of '*American Scientist*', July **1997** (American Research society).
3. Dresselhaus, M. S. ; Dresselhaus, G. ; Avouris, Ph. (Eds.) *Carbon Nanotubes; Synthesis, Structure, Properties and Applications*, (Springer-Verlag Berlin Heidelberg New York **2001**).
4. Liu, H.; Zhai, J.; Jiang, L. *Soft Matter* **2006**, *2*, 811 and the references therein.
5. E. Auer, A. Freund, J. Pietsch, T. Tacke, *Appl. Catal. A* **1998**, *173*, 259-271.
6. (a) http://www.the-scientist.com/2004/02/16/8/1/ (b) http://www.the-scientist.com/2004/02/16/8/1/. (c) Springer Handbook of Nanotechnology, Bharat Bushan (Ed.) Springer-Verlag Berlin Heidelberg, New York **2004,** chapter 38, Part F edited by Bainbridge, W. S.
7. Roco, M. C., Karn, B. *Environ. Sci. Technol. A - Pages* **2005**, *39*, 106A and reference there in.
8. (a) *Societal Implications of Nanoscience and Nanotechnology*; Roco, M. C., Bainbridge, W. S. Eds. National Science Foundation Report: Arlington, VA; Kluwer Academic Publishers: Boston, MA, 2001. (b) *Nanotube paper based medical devices* US patent No. 217, 037, 3197. (c) UN Millennium Development Goals, http://www.un.org/ga/president/62/letters/bckgeducation.pdf. (d)http://www.un.org/ga/president/62/ThematicDebates/mdgthematicdebate.shtml.
9. (a) Geim, A. K.; Novoselov, K. S. *Nature Mater.* **2007**, *6*, 183. (b) http://physicsworld.com/cws/article/news/25385. (c) http://physicsworld.com/cws/article/print/1761.
10. Schedin, F. *et al.* http://arxiv.org/abs/cond-mat/0610809 (2006).
11. Hayamizu, Y.; Yamada, T.; Mizuno, K.; Davis, R. C.; Futaba, D. N.; Yumura, M.; Hata, K. *Nature Nanotech.* **2008**, *3*, 289.

List of Publications

1. *High-Purity Synthesis of Scrolled Mats of Multi-walled Carbon Nanotubes using Temperature Modulation* **Bhalchandra A. Kakade**, Hatem Allouche, Subhramania Mahima, Bhaskar R. Sathe, Vijayamohanan K Pillai *Carbon* **2008,** *46*, 567**.**

2. *Quantized Double Layer Charging Behavior of $Rh_{2057}(TDA)_{321}$ Clusters using Differential Pulse and Cyclic Voltammetry* **Bhalchandra A. Kakade**, Shashidhar Shintri, Bhaskar Sathe, S. B. Halligudi, and Vijayamohanan K. Pillai**.** *Adv. Mater.* **2007***, 19*, 272.

3. *Enhanced performance of polymer electrolyte fuel cells with Nafion based composite electrolytes using Sulfonic acid functionalized single wall carbon nanotubes* Ramaiyan Kannan, **Bhalchandra A. Kakade**, Vijayamohanan K. Pillai *Angew. Chem. Int. Ed.* **2008,** *47*, 1.

4. *Tuning the Wetting behavior of Multiwalled Carbon Nanotubes* **Bhalchandra A. Kakade,** Vijayamohanan K. Pillai *J. Phys Chem.* C **2008,** *112*, 3183.

5. *An efficient route towards the covalent functionalization of Single walled carbon nanotubes* **Bhalchandra A. Kakade**, Vijayamohanan K. Pillai *Appl. Sur. Sci.* **2008,** *254*, 4936.

6. *Highly Selective Catalytic Hydrogenation of Arenes using Rhodium Nanoparticle Supported Multiwalled Carbon Nanotubes* **Bhalchandra A. Kakade**, Suman Sahoo, Shivappa B. Halligudi, Vijayamohanan K. Pillai (*Under review Adv. Mater.* **2008**).

7. *Electric Field Induced, Superhydrophobic to Superhydrophilic Switching in Multiwalled Carbon Nanotube papers* **Bhalchandra Kakade**, Rutvik Mehta, Apurva Durge, Sneha Kulkarni, Vijayamohanan Pillai*" (Under Review Nano Lett.* **2008**).

8. *Enhanced Field Emission from Hexagonal Rhodium Nanostructures* Bhaskar Sathe, **Bhalchandra A. Kakade**, Imtiaz S. Mulla, Vijayamohanan K. Pillai, Dattatray J. Late, Mahendra A. More, Dilip S. Joag *Appl. Phys. Lett.* **2008** (In press).

9. *Tuning the Transport Properties of poly(oxyethylene)bis amine-Nafion Polyelectrolyte Complexes by Dielectric Manipulation* Meera Parthasarathy, **Bhalchandra Kakade**, Vijayamohanan Pillai *Macromolecules* **2008** (In press).

10. *Ultrafast switching time and third order nonlinear coefficients of microwave treated single walled carbon nanotube suspensions* N. Kamaraju, Sunil Kumar, B. Karthikeyan, **Bhalchandra Kakade**, Vijayamohanan K. Pillai, A. K. Sood **(***Under Review J. Nanosci. Nanotechnol.* **2008).**

11. *Near-Complete Phase Transfer of Single-Wall Carbon Nanotubes by Covalent Functionalization using Oxalyl Chloride* **Bhalchandra A. Kakade**, Sanjay D. Patil, Bhaskar R. Sathe, Suresh P. Gokhale, Vijayamohanan K. Pillai *J. Chem. Sci.* **2008** (In press).

12. *Nanometer Sized Tridecylamine Capped Rhodium Dispersed on High Surface Area Support: Catalytic Investigations* Trissa Joseph, Shashidhar Shintri, **Bhalchandra Kakade**, Vijayamohanan Pillai., Shivappa Halligudi *J. Nanosci. Nanotechnol.* **2007**, *7*, 2870.

13. *Role of Polyfunctional Organic Molecules in the Synthesis and Assembly of Metal Nanoparticles* Jadab Sharma, **Bhalchandra Kakade**, Nirmalya Chaki, S. Mahima, Vijayamohanan K. Pillai *J. Nanosci. Nanotechnol.* **2007**, *7*, 2139.

14. *Synthesis and characterization of mesoporous carbon through inexpensive mesoporous silica as template* Karandikar, P., Patil, K. R., Mitra, A., **Kakade, Bhalchandra**, Chandwadkar, A. *J. Microporous and Mesoporous Materials* **2007**, *98*, 189.

15. *Suppression of electron-transfer characteristics of ferrocene by OTS monolayer on a silicon/electrolyte interface* Sneha Kulkarni, **Bhalchandra Kakade**, Imtiaz Mulla, Vijayamohanan Pillai, *J. Coll. Int. Sci.* **2006**, *299*, 777.

16. *Electrochemical organization of monolayer protected gold nanoclusters on single-walled carbon nanotubes: Significantly enhanced double layer capacitance* Mahima, S., Nirmalya Chaki, Jadab Sharma, **Bhalchandra Kakade,** Renu Pasricha, Appa Rao, Vijayamohanan Pillai *J. Nanosci. Nanotechnol.* **2006,** *6*, 1387.

17. *Investigation of interparticle interactions of larger (4.63 nm) monolayer protected gold clusters during quantized double layer charging* Nirmalya Chaki, **Bhalchandra Kakade,** Vijayamohanan Pillai, Poonam Singh, C. Dharmadhikari, *Phys. Chem. Chem. Phys.* **2006**, *8*, 1837.

18. *Eu^{3+} doped lanthanum oxide nanowhiskers: Microwave hydrothermal synthesis, characterization and photoluminescence properties* Vadivel Murugan, Kasi Viswanath, **Bhalchandra Kakade,** V. Ravi, V. Saaminathan, *J. Phys. D: Applied Physics* **2006**, *39*, 3974.

19. *Quantized double layer charging of dodecanethiol protected larger Au nanoclusters: combined investigations using differential pulse voltammetry, cyclic voltammetry and impedance technique* Nirmalya K. Chaki**, Bhalchandra Kakade,** Vijayamohanan Pillai *Electrochem. Commun.* **2004,** *6*, 661.

20. *Highly resolved quantized double-layer charging of relatively larger dodecanethiol-passivated gold quantum dots* Chaki, N. K., **Bhalchandra Kakade,** Jadab Sharma, S. Mahima, Vijayamohanan Pillai, Santosh Haram, *J. Appl. Phys.* **2004**, *96*, 5032.

21. *Solvent-assisted one-pot synthesis and self-assembly of 4-aminothiophenol-capped gold nanoparticles* Jadab Sharma, S. Mahima, **Bhalchandra Kakade,** Renu Pasricha, A. B. Mandale, Vijayamohanan Pillai *J. Phys. Chem. B,* **2004**, *108*, 13280.

22. *Photoluminescence studies of Eu3+ doped Y_2O_3 nanophosphor prepared by microwave hydrothermal method* Vadivel Murugan, A. Viswanath, V. Ravi, **Bhalchandra Kakade,** V. Saaminathan, *Appl. Phys. Lett.* **2004**, *89*, 123120.

Erratum